The Dissertation Committee for Xiaoyan Chen Certifies that this is the approved version of the following dissertation:

Luminescent and Magnetic Materials Based on Conducting Metallopolymers

Committee:

Bradley J. Holliday, Supervisor

Alan Campion

Alan H. Cowley

Christopher J. Ellison

Richard A. Jones

Luminescent and Magnetic Materials Based on Conducting Metallopolymers

by

Xiaoyan Chen, B.S., Ph.D.

Dissertation

Presented to the Faculty of the Graduate School of

The University of Texas at Austin

in Partial Fulfillment

of the Requirements

for the Degree of

Doctor of Philosophy

The University of Texas at Austin

August, 2011

Dedication

For my husband, my son, and my parents. Thank you for all of your love, support, and sacrifice throughout my life.

Acknowledgements

First and foremost, I would like to thank my advisor Dr. Bradley J. Holliday for his direction and discussion. Without him I would not have achieved my goals for this dissertation. His knowledge, guidance, patience, and mentorship make my Ph.D. experience productive and stimulating. In addition, I'd like to thank my committee: Dr. Alan Campion, Dr. Alan H. Cowley, Dr. Christopher J. Ellison, and Dr. Richard A. Jones for their support and suggestions to my research projects. I would also like to thank Dr. Allen J. Bard and Dr. Jianshi Zhou for all of their assistance and advice with electrogenerated chemiluminescence experiments and magnetic susceptibility measurements.

I would also like to thank my co-workers, especially Michelle Mejia, Kristen Milum, Travis Hesterberg, and Matt Raiford for all of their help and suggestions. You all make my five years here wonderful.

I would like to thank my family members, especially my father Changfa Chen, and my mother Guiying Tang. Without them I would not have made it this far in life. They have been there for me every step of the way, have always loved me unconditionally, and have aided me through all of my tough decisions.

Finally, I would like to thank my husband, Yihua Zhao, whom without his full love, support, and sacrifice I never would have realized my full potential. I thank him everyday of my life.

Luminescent and Magnetic Materials Based on Conducting Metallopolymers

Publication No._____

Xiaoyan Chen, Ph.D.

The University of Texas at Austin, 2011

Supervisor: Bradley J. Holliday

Conducting metallopolymers are a new and fascinating class of materials that incorporate metals into conducting polymer systems. These new materials combine the processing advantages of polymers with the electronic, optical and catalytic properties provided by the presence of metal centers. A large number of conducting metallopolymers have been synthesized and studied and have found applications in areas such as sensors, memory and light-emitting devices, solar cells, and catalysis. Among the various applications, conducting metallopolymers as emitting layers in high-efficiency polymer light-emitting diodes (PLEDs) attract great research interest. In order to get PLEDs with long lifetime, high quantum efficiency, and excellent color purity, we have developed an approach to synthesize well-defined conducting metallopolymers that incorporate lanthanide complexes in an inner sphere fashion. As such, we aim to take full advantage of the properties of both organic and inorganic components with high efficiency due to the direct electronic interface this configuration creates. Lanthanide complexes with polymerizable groups have been synthesized, characterized and utilized

as precursors for conducting metallopolymers. These lanthanide monomers and corresponding metallopolymers display visible and near-infrared luminescence at room temperature that is consistent with efficient energy transfer from the organic polymer matrix to the lanthanide metal ion followed by lanthanide luminescence.

As a second but closely related area, electrogenerated chemiluminescence (ECL) of polymers is attractive for light-emitting devices. Up to now, there are limited studies dealing with ECL from pure active materials deposited as solid films on electrodes. The operation theory and degradation mechanism are still under investigation. To advance the development of ECL of conducting metallopolymers, we prepared cyclometalated Pt(II) complexes with polythiophene system. Conducting metallopolymer films are prepared through controlled electropolymerization. ECL of the Pt(II) containing conducting polymers are observed for the first time.

Finally, a preliminary study of magnetism and conductivity of conducting metallopolymers has been done. We incorporate Fe(II)/Fe(III) into our newly designed ligand systems with polymerizable thiophene derivatives. Three complexes show spin crossover (SCO) phenomena with the highest transition temperature at 265 K, which are further verified by variable temperature electron paramagnetic resonance spectra.

Table of Contents

List of Tables

List of Figures

List of Schemes

Chapter 1: Synthesis, Characterization, and Application of Conducting Metallopolymers

INTRODUCTION

Conducting polymers are organic polymers that exhibit near metallic electrical conductivity while maintain the unique features of polymer materials, such as high mechanical strength, flexibility, low weight, and ease of processing. These materials were proclaimed as futuristic new polymeric materials that would lead to the next generation of electronic and optical devices. The first conducting polymer, poly(acetylene), was synthesized by Natta *et al.* as black powder in 1958.[1] Although Prof. Heeger *et al.* announced the discovery of the ability to dope poly(acetylene) over the full range from insulator to metal in 1977,[2] commercialization of conducting polymers was impeded by poor stability, and research activity decreased until a light-emitting diode with poly(*p*-phenylenevinylene) as the light-emitting layer was reported in 1990.[3] Since then, a tidal wave of renewed and amplified interest in these materials has catalyzed many new developments both on a fundamental level and from the manufacturing side. Conducting polymers provide benefits to industries such as electronics by shielding against electromagnetic interference.[4] Conducting polymers are also already used in devices that detect environmentally hazardous chemicals, factory emissions, and flavors or aromas in food products.[5] Recently, their conductivity is being explored in electrostatic materials, conducting adhesives, electromagnetic shielding, artificial nerves, aircraft structures, diodes, and transistors.[6] Notably, the most exciting application of conducting polymers is the use of them in polymer light-emitting diodes (PLEDs), replacing silicon as the traditional substrate material for clock radios, audio equipments, televisions, cellular telephones, automotive dashboard displays, and aircraft cockpit displays.[6]

While many advances have been made, long-standing issues including limited lifetime, low quantum efficiencies, and poor color purity continue to plague many conjugated polymer materials/devices. The internal quantum efficiency of the PLED device with poly(*p*-phenylenevinylene) mentioned above was as low as 0.01%. Among the various efforts made towards the goal of high efficiency PLEDs, the combination of organic polymers and inorganic metals into the same molecular backbone has captivated many groups and is likely to lead to a wide variety of advanced materials.[7-9] The introduction of metals into conducting polymer systems can be achieved in different ways. The two main routes to include metals into polymers are:

(1) Dissolution or dispersion of discrete metal complexes in the polymer matrix. The materials synthesized by this approach should be more accurately defined as inorganic/organic composite materials. The metallic centers in these systems are appended to the polymer backbone in such a manner that little if any direct electronic communication between the metal and the polymer's extended π-system can exist. This approach offers the advantage of versatility. Both the polymer matrix and the metal complexes can be chosen independently. For example by varying the metal centers, luminescent materials emitting at different wavelengths can be produced: when red emissive europium *β*-diketonate complexes were blended with a blue-emitting, alkoxy nitrile-functionalized, polyphenylene host, red emission was observed.[10] When a lissamine complex of Nd^{3+} is mixed with a blue-emitting polyfluorene-based copolymer host, near-infrared (NIR) emission can be observed.[11] But it is difficult to obtain a uniform distribution of the metal complex in the polymer matrix. Some problems including concentration limitation of entrapped species, inhomogeneous dispersion of both components and leaching of metal complexes can not be avoided due to the weak interaction between the metal complex and the polymer matrix.[12,13] In the case of

lanthanide/polymer composites, the nonhomogeneous distribution of lanthanides leads to clustering of lanthanide ions and hence a decrease of the luminescent intensity.[14,15]

(2) Attachment of metal complexes to the polymer matrix through covalent bonds. This route rules out phase separation or aggregation during device processing/operation. Furthermore, energy transfer in a covalently bound system is anticipated to be more efficient due to the close proximity of the two components. In many cases, an increase in structural complexity gives rise to new properties, which cannot be foreseen on the basis of the independent constituting moieties.[16,17] The covalently bound metals impart many properties including luminescence, electro- and photochemistry, catalysis, charge, magnetism, and thermochromism.[18] A new category of materials emerges as conducting metallopolymers, which are conducting polymers containing metal atoms in the repeating monomer, either as part of the backbone or in the side chains. The incorporation of

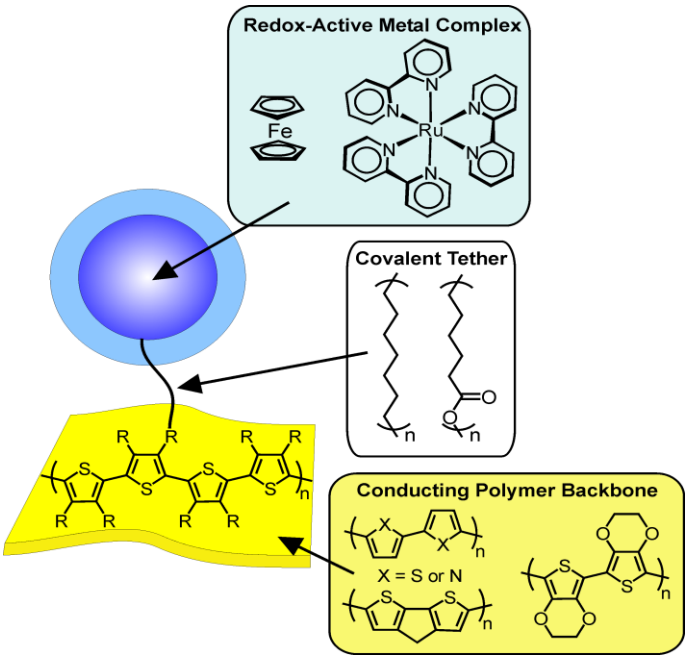

Scheme 1. Outer sphere conducting metallopolymer. Diagram adapted from reference 19.

metals greatly expands the function and ultimate applications of conducting polymer systems. For example, the incorporation of redox-active metal centers into conducting polymer structures can create highly efficient redox conductivity for sensory, catalytic, photochemical, and photoelectronic applications.[19] During the development of conducting metallopolymers, a central issue is to understand the nature of the interactions of the metal centers with the conducting organic polymer and how the interactions between the associated metal centers affect the overall bulk conductive property of the polymer. Based on the degree of interaction between the metal and the organic π systems, conducting metallopolymers can be divided into two groups, outer sphere and inner sphere conducting metallopolymers.

In outer sphere conducting metallopolymers, the metal is linked to the polymer chain through a non-π-conjugated linker resulting in indirect communication between the π electrons of the conducting polymer and the metal center (Scheme 1).[19] The outer sphere conducting metallopolymers are more widely studied compared with inner sphere ones. In the outer sphere arrangement although the metal complexes are not directly involved in the conductivity pathway, in many cases the metal centers remain in

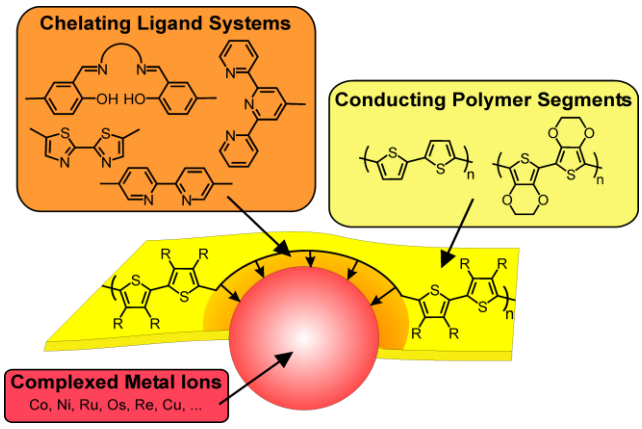

Scheme 2. Inner sphere conducting metallopolymer. Diagram adapted from reference 19.

electronic communication with the conducting polymer backbone through inductive effects. As shown in Scheme 1, the length and nature of the tether has been varied as well as the nature of the conducting polymer backbone. In most cases, a saturated tether has been employed resulting in electronic isolation of the metal complexes from the polymer backbone.

In the inner sphere conducting metallopolymers, the metal is bound to the polymer chain by a π-conjugated linker (Scheme 2). The metal is inserted into the polymer main chain, or binds directly to the polymer chain via metal-carbon or metal-heteroatom bonds. In this way, the metal centers are part of intrapolymer conductive pathway. Although the inner sphere conducting metallopolymers are less explored, there are a handful of structural varieties. As shown in Scheme 2, different types of chelating ligands have been adopted as metal binding groups, such as schiff base ligands, 2,2'-bipyridine, and 2,2';6',2"-terpyridine.

Our interest is focused on the inner sphere conducting metallopolymers because these polymers can take full advantage of the properties of both components with high efficiency due to the direct electronic interface this configuration creates. Herein I will discuss the synthesis, characterization, and application of conducting metallopolymers based on lanthanides, platinum and other transition metals. Specifically this dissertation will focus on the photoluminescence, electrogenerated chemiluminescence and magnetic properties of conducting metallopolymers.

CONDUCTING METALLOPOLYMERS WITH LANTHANIDE IONS

Lanthanide Complex Luminescence

The lanthanide elements are those in which the 4*f* orbitals are sequentially filled, thus possessing accessible 4*f* energy levels.[20] The lanthanides are unique in that they have

very similar properties across the series, such as hydration enthalpies, common oxidation states, ionic radius, and wide range of coordination numbers (i.e. 2 - 12) with an empirical tendency towards high coordination numbers of 8 and 9.[21] One significant aspect of the lanthanides is their unusual spectroscopic properties. Trivalent cations of lanthanides display absorption and emission bands that correspond to Laporte-forbidden (transition between *d* orbitals are forbidden in octahedral complexes) *f-f* transitions. Additionally, these *f-f* transitions are parity forbidden (electronic transitions with a change of multiplicity are forbidden), resulting in very long lived excited states, with typical luminescence lifetimes on the micro- to millisecond timescale. Since 4*f* orbitals are effectively shielded from the influence of the external forces by the overlying $5s^2$ and $5p^6$ orbitals, the various excited states arising from the f^n configurations are splitted by external fields only to the extent of 100 cm^{-1}. Therefore, emission bands as well as absorption bands (*f–f* transitions) are extremely sharp when electronic transitions occur from one *J* state of an f^n configuration to another *J* state of the same configuration.[22] Unfortunately, as another consequence of the parity (Laporte) forbidden nature of the 4*f* transitions, the lanthanide absorptions have very low molar absorptivity (less than 1 $M^{-1}cm^{-1}$) which makes the direct excitation of lanthanides very difficult, thus limiting their practical use. In order to circumvent these low extinction coefficients, the luminescent lanthanide ion can be chelated to a chromophore-containing group which functions as an 'antenna' absorbing incident light then transferring energy to the Ln(III), thus populating the metal centered excited state, which can then deactivate by undergoing its typical luminescent emission (Figure 1).[23] In addition to directing energy to the metal, chelation also serves to exclude solvent molecules from the first coordination sphere, which is essential to avoid quenching of the lanthanide luminescence through non-radiative decay

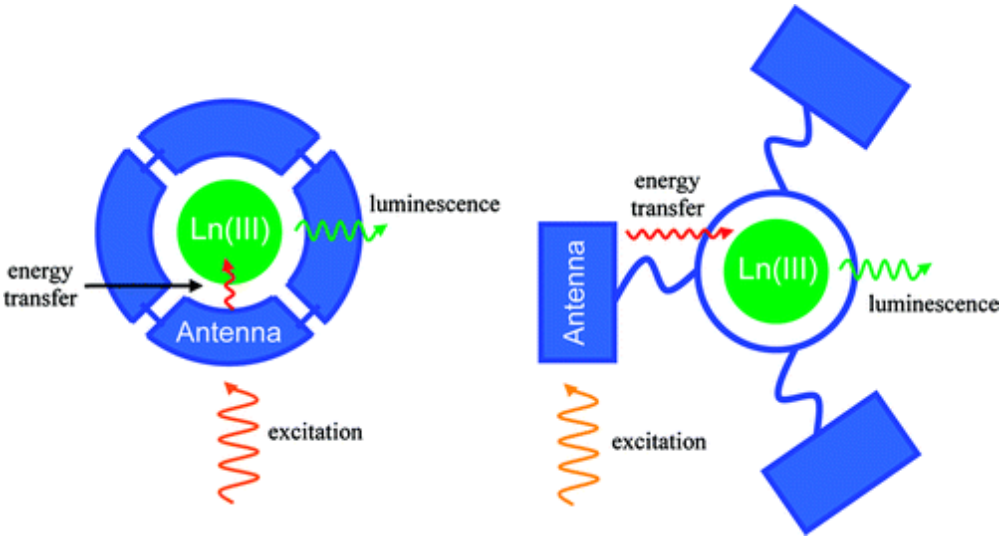

Figure 1. The antenna effect for Ln(III) sensitization, illustrated using the chromophoric chelate (left) and pendant chromophore (right) ligand designs. Illustration adapted from reference 23.

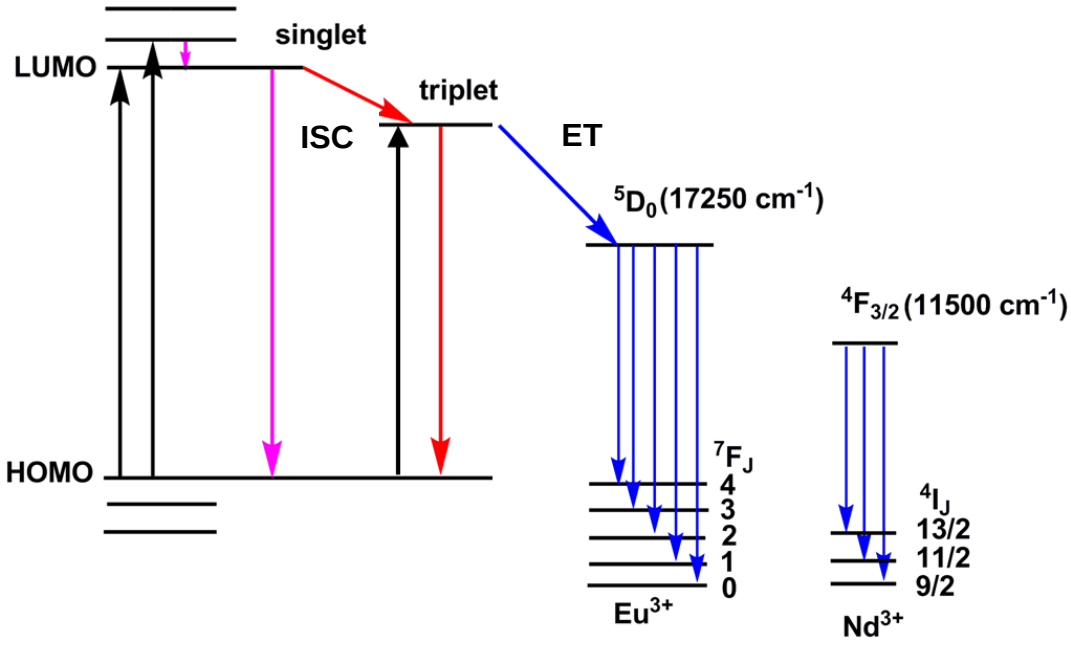

Figure 2. The antenna effect of excitation in lanthanide complexes.

via vibronic coupling to vibrational states of O-H and N-H bonds, and also to provide stable metal complexes.

The excitation mechanism of lanthanide differs from organic compounds. The energy transfer in lanthanide complexes is shown in Figure 2. During the photoluminescence process, the ground state of the organic compound is excited to the singlet excited state by absorption of energy. The singlet excited state may return to the ground state by reemission called fluorescence, or undergo a change of spin to the triplet called intersystem crossing (ISC). The energy of triplet excited state can be degraded through thermal deactivation process without the emission of photons. During electroluminescence, the singlet state and triplet are excited at the same time. According to spin statistics, the internal quantum efficiency for light-emitting diode devices using organic fluorescent compounds is limited to 25%.[24] In contrast, for lanthanide complexes,

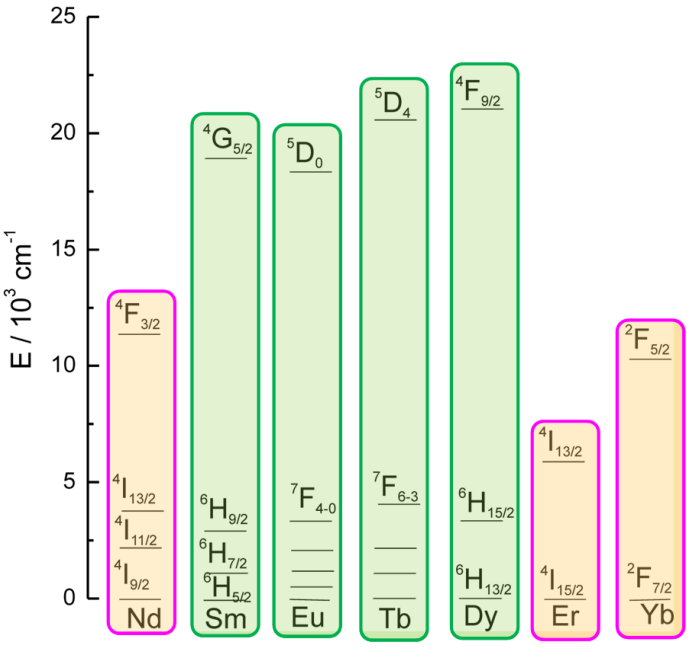

Figure 3. Ground and excited states for Ln(III).

lanthanide ions are excited via intramolecular energy transfer (ET) from the triplet excited state of the organic ligand. So the typically non-emissive triplet excited state energy can be transferred to *f* levels of the lanthanides to emit light. In theory internal quantum efficiencies of 100% should thus be possible in electroluminescent stimulation sceneries.[25]

Based on the emission wavelength, lanthanides can be generally divided into two categories: visible emitting lanthanides (Sm, Eu, Tb, Dy) and near-infrared emitting (NIR) lanthanides (Nd, Er, Yb). The ground and excited states of these lanthanides are shown in Figure 3.

Incorporation of Lanthanide Ions into Light-emitting Diodes (LEDs)

The unique photophysical properties of lanthanide ions triggered efforts to use them as the emissive materials in LEDs.[26] Due to the intrinsic and characteristic emission of lanthanide ions, they are excellent candidates for this application. First, the emission from organic compounds and transition metal complexes is usually broad, thus requiring filters to get monochromatic color. Also tuning the parameters of the devices can change the color. The lanthanide metal ions exhibit extremely sharp emission bands due to the well-shielded 4*f* electrons. Little vibrational coupling with the environment is seen, and the emission bands are narrow and ion specific. Next, the energy of the singlets and triplets that form on the ligands can be transferred to the *f* levels of the lanthanide ion to generate light. Theoretically, we can obtain an internal quantum efficiency of 100% due to spin statistics (see above).

Numerous studies about organo lanthanide complexes for electroluminescent materials have been done. We will only give a few examples here. Kido *et al*. reported the first OLED containing Tb-tris-(acetylacetonato), $Tb(acac)_3$ in 1990.[27] This report

detailed a double-layer device with *N*-*N*′-diphenyl-*N*,*N*′-(bis(3-methylphenyl)-1,1′-biphenyl-4,4′-diamine (TPD) as the hole-transport layer, i.e. ITO/TPD/$Tb(acac)_3$/Al. Bright green emission was observed from the OLED when operated in a continuous dc mode (biased Al negative). The device showed a luminance of 7 cd m^{-2} at a current density of 0.4 mA cm^{-2}. In the following year Kido *et al*. discussed the electroluminescent properties of $Eu(TTA)_3$ (TTA = thenoyltrifluoroacetone) incorporated into a device. Red emission was observed with a turn-on voltage of 12 V and a maximum intensity of 0.3 cd m^{-2} at 18 V.[28] Takada and co-workers have also developed a similar OLED based on a sublimable Eu complex, $Eu(TTA)_3(Phen)$.[29] The device utilized a microcavity design with a cell structure of (SiO_2/TiO_2 bilayers)/ITO/TPD/Eu complex/Alq_3/Mg:Ag. This device showed a line emission from the Eu complex with a maximum brightness value greater than 100 cd/m^2. These visible luminescence lanthanides have the potential for television screens and LEDs,[30-34] in liquid crystals,[35] as well as in fluoroimmunoassays[36] and in biophysical applications.[37-40]

NIR electroluminescence has become increasingly important, as materials capable of emitting in this region of the spectrum can be utilized in the area of telecommunications and optical amplifiers.[41-43] Nd-containing systems are regarded as the most promising NIR luminescent materials for application in laser systems. Additionally, the relative transparency of human tissue at ~1000 nm suggests the luminescent probes at this wavelength could have diagnostic value.[44,45] The NIR emission at 1530 nm of the Er ion is particularly interesting for fiber-optic communications, because of the narrow line width of the emission at room temperature and the high bandwidth capacity.[46]

Several investigators have fabricated NIR OLEDs containing Nd, Er, and Yb ions. Yanagida *et al*. reported an OLED based on $Nd(DBM)_3$bath (DBM =

dibenzoylmethanido, bath = bathophenanthroline) as the emitting material. TPD and Alq_3 were used as the hole- and electrontransport materials, respectively.[47] Sharp NIR emission bands corresponding to *f-f* transitions of the Nd ion were obtained. However, the device degraded during the measurement. Gillin and Curry fabricated an Er-containing OLED with Er-tris(8-hydroxyquinoline) complex as the emitting material.[48] They observed 1540 nm sharp emission due to the 4*f* transition of the Er ion at room temperature.

With regard to OLED fabrication, researchers quickly realized that the use of pure compounds can lead to concentration quenching effects in addition to compromising the long term stability of the device due to recrystallization tendencies of the complexes. Thus, for practical applications in optical devices, it is advantageous to embed lanthanide complexes in a matrix. These matrices can be sol-gel glasses, inorganic-organic hybrid materials, polymers or liquid crystals.[49-53] These matrices can additionally act as charge-transport layers to facilitate the formation and confinement of excitons. Using polymer materials can also make the preparation of light-emitting films easier by allowing the use of solution processes, such as spin coating, screen printing, and ink-jet printing.

Bazan and co-workers reported a series of Eu(β-diketonate)$_3$Phen complexes incorporated into poly[2-(6'-cyano-6'-methyl-heptyloxy)-1,4-phenylene] (CN-PPP) which leads to LEDs with photoluminescence efficiencies in the range 17 - 27%. Devices with the configuration ITO/PVK/2 wt% complex in CN-PPP/cathode displayed turn-on voltages around 20 V and highest electroluminescence efficiencies of 1.1%. Reynolds *et al*. reported NIR LEDs based on poly(phenylene)/Yb-tris(β-diketonate) complexes. The maximum NIR external efficiencies of the devices with Yb(DBM)$_3$phen and Yb(DNM)$_3$phen (DNM = dinaphthoylmethane) are 7×10^{-5} (at 6 V, and 0.81 mA mm^{-2}) and 4×10^{-4} (at 7 V, and 0.74 mA mm^{-2}) , respectively.[49]

Considering the phase separation or aggregation problems when metals were blended with matrices, more recently, efforts in the utilization of polymers with covalently attached emitting complexes have been studied to avoid phase separation during operation and subsequent loss of the light emission. Despite the potential advantages, very few metallopolymers with lanthanide complexes linked through covalent bonds have been explored. Some representative examples are shown in Figure 4.[50-53]

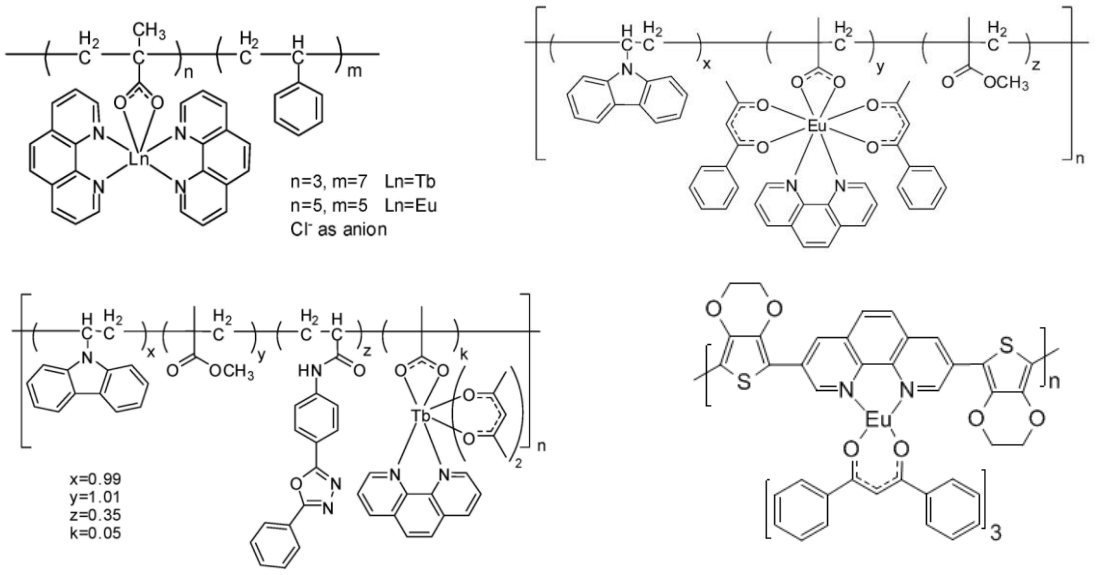

Figure 4. Lanthanide containing metallopolymers.

CONDUCTING METALLOPOLYMERS WITH TRANSITION METALS

Light-Emitting Materials

Transition metals are elements in the *d* block of the periodic table. Since lanthanides have been discussed as a special section above, in this section we will focus on transition metals other than lanthanides. Transition metal compounds with organic ligands or organometallic compounds find an increasing level of interest due to their

large potential for new photophysical and photochemical applications, especially as triplet emitters where emission colors vary from blue to red and also are observed in the NIR. The lifetime of transition metal emission is usually orders of magnitude longer than that of purely organic singlet emitters. The compounds are often photo-redox active which is important in systems that convert solar energy into electrical or chemical energy.[54-56] Moreover, emission wavelengths and/or excited state decay times of the organometallic compounds are often sensitive to environmental factors, such as oxygen, water, rigidity of the environment, nature of the coordination environment, pH value, specific organic vapors, concentration of glucose, or simply vary with temperature, etc. Thus, these compounds also find applications in the field of luminescence sensors.[57-59]

As discussed previously, the triplet excited states of the emitting materials play an essential role in OLEDs. Specifically, by use of transition metal compounds, in principle it is possible to obtain an electroluminescence efficiency that is up to four times higher than with typical singlet emitters. This efficiency enhancement, also called triplet harvesting, is due to enhanced spin-orbit coupling in the presence of transition metals.[60] We can explain this by comparing the efficiency which is obtainable with a purely organic molecule to the efficiency achievable with a transition metal complex. For organic molecule, the initial process of exciton formation occurs statistically with respect to the spin orientations, one obtains 25% of excitons with singlet character and 75% with triplet character. As discussed previously, the lowest excited singlet and triplet states are populated. The organic molecule can exhibit emission as the singlet excited state returns to the ground state via fluorescence. The deactivation of the triplet excited state normally occurs non-radiatively at ambient temperature. Therefore, 75% of the triplet excitons (which is a bound state of an electron and hole which are attracted to each other by the electrostatic Coulomb force) are lost. The conditions are more favorable for transition

metal complexes, in which the central metal ion carries significant spin-orbit coupling. This is particularly valid for metal ions of the second and third row transition metals as spin-orbit coupling scales with atomic number. Fast intersystem crossing induced by spin-orbit coupling effectively depopulates the singlet excited state into the lowest triplet excited state. Again, due to spin-orbit coupling, the triplet excited state can decay radiatively as phosphorescence, even with high emission quantum yield at ambient temperature. By this process of triplet harvesting one can in principle obtain a four times larger electro-luminescence efficiency for triplet emitters than for singlet emitters.

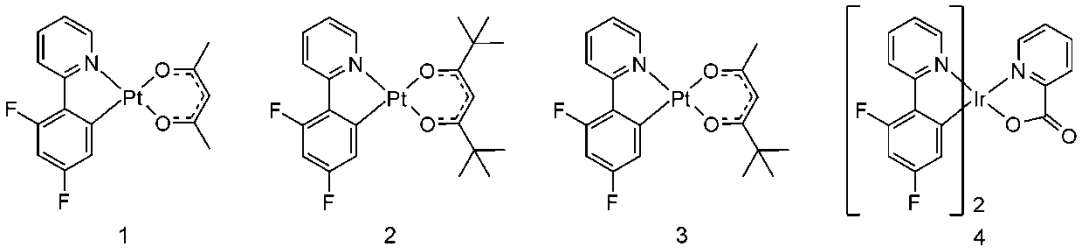

Figure 5. Molecular structure of some triplet emitters.

The intense tunable phosphorescence of the [Pt(C^N^N)(C≡CR)] complexes, and their neutrality and stability under vacuum deposition conditions, render them good candidates as emitters for high-efficiency OLEDs.[61,62] A maximum luminance of 3100 cd m^{-2} at 12 V and a maximum efficiency of 1.0 cd A^{-1} at 30 mA cm^{-2} were observed for a device using [Pt(C^3^N^N)(C≡CC_6H_4Me-4)] (HC^3^N^N = 6-(2'-thienyl)-2,2'-bipyridine). These values are comparable with the best red light OLEDs in the literature[63] and demonstrate the potential of these platinum(II)-alkynyl complexes as electrophosphorescent emitters. Forrest and Thompson have demonstrated high-efficiency, high-brightness red phosphorescent OLEDs employing cyclometalated benzothienylpyridine (btp) iridium and platinum complexes, such as (2-(2'-benzo[4,5-α]thienyl)pyridinato-N,$C^{3'}$)platinum(acetylacetonate).[64] Thompson has reported the

synthesis and photophysical properties of a series of phosphorescent cyclometalated platinum complexes, [(C^N)Pt(O^O)] (complexes 1 - 3 in Figure 5). Their emission characteristics are governed by the nature of the cyclometalating ligand through modifying the 2-phenylpyridyl group with electron-donating or withdrawing substituents. Incorporating electronegative atoms such as fluorine onto the phenyl ring blue-shifts the emission while substituting with electron-donating methoxy group gives a pronounced red shift. This allows the emission to be tuned in energy with λ_{max} in the range of 456 - 600 nm.[65] Iridium(III) cyclometalated complexes are also attracting widespread interest because of their unique photophysical properties and applications in organic light-emitting diodes (OLEDs). Several groups have extensively used neutral Ir cyclometalated complexes in OLEDs and obtained up to 19% external quantum efficiency, which require a complicated multilayered structure for charge injection, transport, and light emission.[66-68] Forrest reported the use of the phosphorescent excimer arising from the phosphor 1 (Figure 5), coupled with blue monomer emission from either 3 or iridium-bis(4,6-difluorophenylpyridinato-N,C^2)-picolinate 4, to achieve efficient electrophosphorescent white light OLEDs.[69]

As discussed in the previous section, polymers have many advantages over small molecules in the manufacturing procedures. Similarly, metal complexes can offer much to these areas by virtue of their easily tunable electronic structures and intrinsically low ionization energies. In principle, the advantages of both polymers and metals in this area can be utilized simply by blending an appropriate metal complex into an organic polymer matrix. Since these systems suffer from severe problems associated with phase separation, these systems will not be discussed further.

The harvesting of triplet excitons via the spin-orbit coupling of heavy transition metals can also be achieved by the incorporation of transition metal complexes into

groups pendant to the polymer main chain. Polymers containing Ir centers (Figure 6) have shown much promise as electrophosphorescent materials. Changing the ligand set around the Ir center has been shown to change the wavelength of the emission, and drawing from knowledge of the photophysics of molecular Ir^{3+} analogues, red, blue, and green electrophosphorescent polymers have been prepared.

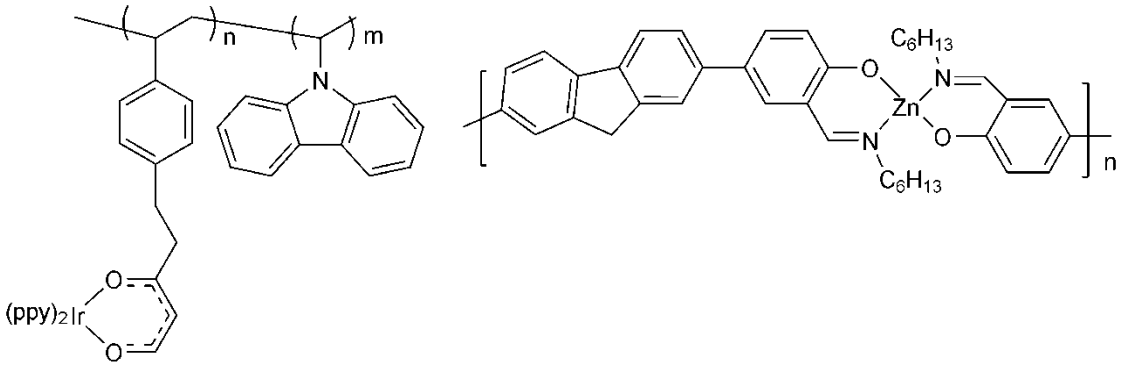

Figure 6. Molecular structure of metallopolymers containing Ir(III) and Zn(II).

The incorporation of zinc-salen complexes into the backbone of organic polymers has also afforded luminescent materials, as shown in Figure 6.[70] The physical properties of the polymer could be varied easily by exchanging the substituent on the imine nitrogen. In addition, it was noted that incorporation of the zinc-salen unit into the polymer resulted in an increase in the thermal stability of the resulting polymer. When cast as films, these materials emitted yellowish-orange light under photoluminescence conditions. Two specific devices were fabricated in PLEDs with the configuration ITO/PEDOT:PSS/polymer/BCP/Alq_3/LiF/Al (PEDOT = poly(3,4-ethylenedioxythiophene), PPS = poly(styrenesulfonate), BCP = 2,9-dimethyl-4,7-diphenyl-1,10-phenanthroline). Their electroluminescence was studied, which differed in

wavelength from that of the photoluminescence, suggesting that the former should not be assigned to the intra-ligand $^1\pi^*-^1\pi$ fluorescence.

Sensors and Memory Devices

The incorporation of metals into the main chain of a polymer might be expected naturally to enhance the conductivity of the system. Unlike carbon, transition metals can readily change coordination number or oxidation state, and when these elements are incorporated into polymers, these processes can modulate the system between states of relative high and low conductivity. It is this type of response that enables conducting metallopolymers to act as sensors.

Through a fundamental understanding of the mechanism for conduction in metallopolymers, Swager *et al*. have developed materials that can sense particular analytes by changes in resistivity. Transition metals can reversibly bind small molecules which alter the energy levels of the metal-based orbitals. Consequently, the presence of an analyte will change the efficiency by which electrons are transported along the polymer chain and hence the conductivity. For example, a monomer incorporating a cobalt(II)-salen fragment between two electropolymerizable 3,4-(ethylenedioxy)thiophene units was polymerized between two electrodes, to form a sensor (Figure 7).[71] When exposed to a 7 mM solution of NO, the electrode confined polymer exhibits a specific 30% increase in its in situ conductivity. Furthermore, no

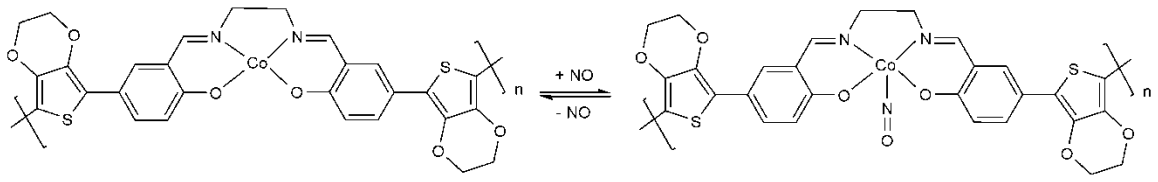

Figure 7. Chemical sensor based on reversible bonding of NO.

response was observed when the device was exposed to O_2, CO and CO_2.

In related work Choi *et al*. have prepared conjugated metallopolymers for memory applications (Figure 8) with a redox-active iron center in the main chain. By switching the oxidation state between Fe(II) and Fe(III), the resistance of the film can be changed reversibly.[72] Initially the device was at the low-conductivity state (off-state). Then the current abruptly increased at −1.9 V implying a transition from the off-state to a high-conductivity on-state presumably because of the oxidation of the ferrocene groups. This observation can be viewed as ferrocene acting like a voltage-dependent in-situ dopant resulting in the enhancement of the conductivity of the polymer film. This on-state persisted until the device was switched back to the off-state at the positive bias of 1.4 V. This provides nonvolatile memory behavior and preliminary work enables data to be stored as '0' or '1' for over 7 hours. A nonvolatile polymer memory device has also been prepared using a redox-active copolymer with carbazole electron donors and Eu-complex electron acceptors (Figure 8).[73] Current density increases progressively with the applied bias. A sharp decrease in injection current occurs at 4 V, indicating the transition of the device from high conductivity on-state to low conductivity off-state. The off-state can be recovered by the simple application of a reverse voltage pulse. The device remains in either state even after the power has been turned off.

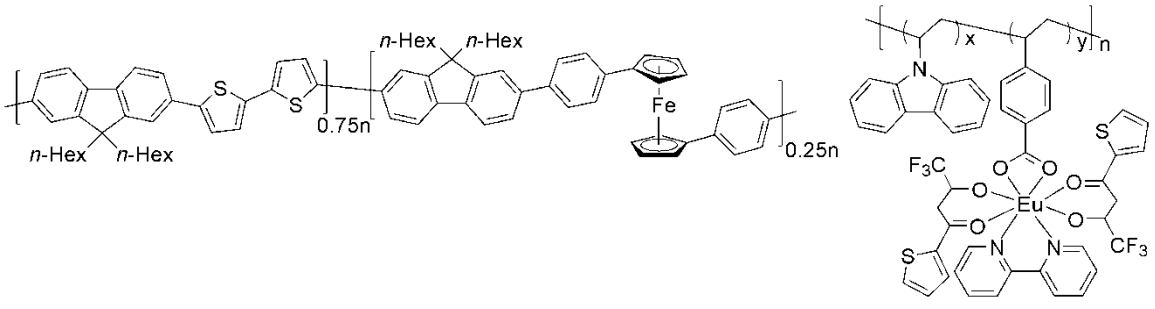

Figure 8. Structure of conducting metallopolymers used as memory devices.

Photovoltaic Materials

Harvesting energy directly from the sunlight using photovoltaic technology is increasingly recognized as a solution to the world's energy problem. Solar cells based on solution-processable organic semiconducting polymers have attracted considerable interest as a low-cost alternative to inorganic semiconductors for large-area and lightweight applications. However, novel materials with lower energy gaps need to be developed to improve the coverage of the solar spectrum and consequently improve the efficiency.[71] Therefore, great effort has been made to optimize the spectral response of polymer photovoltaic cells by extending the absorption to longer wavelengths, as absorption of the active layer must cover most of the solar spectrum. Conducting metallopolymers have demonstrated exceptional promise in the creation of high-efficiency polymer solar cells. Especially, platinum alkynyls have been a popular candidate for inclusion into such a polymeric backbone. The irradiation of the platinum polyyne, $[–C{\equiv}C–C_6H_4–C{\equiv}C–Pt(P\textit{n}\text{-}Bu_3)]_n$ (Figure 9, polymer 1), encased between ITO and Al electrodes afforded a device that had a quantum efficiency of 0.03% under short-circuit conditions.[74] Operation under forward bias, consequently, increased the quantum efficiency of the device to 0.6%. Further improvements in efficiency were made by doping the platinum polyyne film. The addition of 10% by weight of the electron-acceptor, C_{60}, to the polymer afforded, when assembled as above, a two order of magnitude increase in quantum yield (0.01 to 1.6%). This increase was attributed to the efficient quenching of the long-lived triplet excited state of the polyyne by C_{60}.

Wong *et al*. reported metalated conjugated polymers which demonstrated exceptional promise in the creation of high-efficiency polymer solar cells.[75] The metallopolymer structure is shown in Figure 9 as polymer 2. The solar cell, containing metallopolyyne/fullerene derivative blends, shows an unoptimized power-conversion

efficiency of 4.1%, which is comparable to that of poly(3-hexylthiophene), a thoroughly developed organic polymer for such applications.

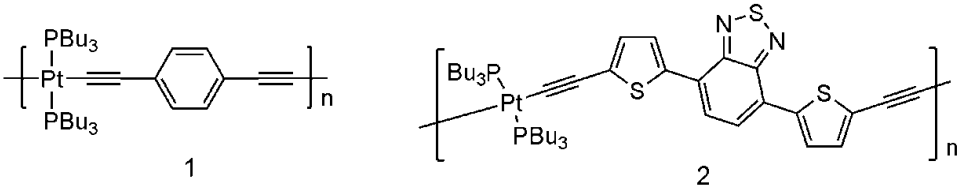

Figure 9. Platinum polyynes for solar cell applications.

Magnetic Conducting Metallopolymers

In addition to the various physical phenomena currently related to conjugated polymers, magnetism is one of the latest properties found in polymers. Magnetism traditionally has been restricted to compounds containing metal ions, but a team of chemists at the University of Nebraska-Lincoln created the world's first conjugated organic magnet in 2001.[76] A report in 2007 even reveals the coexistence of conducting and magnetic electrons based on molecular π-electrons in supramolecular anion radical salt (Me-3,5-DIP)[Ni(dmit)$_2$]$_2$ (Me-3,5-DIP = *N*-methyl-3,5-diiodopyridinium and dmit = 1,3-dithiole-2-thione-4,5-dithiolate),[77] in which one kind of molecule plays two contrasting roles: metallic conduction and paramagnetism with antiferromagnetic interactions. In contrast to discrete organic radicals, in conducting polymers, the magnetic moments are created upon doping. When doped with an electron or hole a conjugated polymer with a nondegenerate ground state produces a polaron, an ion radical self-trapped in a local lattice distortion. A polaron has spin 1/2 and charge e (for hole doping). If the polymer is heavily doped, two polarons may form a bipolaron with zero spin and charge 2e. In the partially doped state, superexchange interaction occurs between the

polarons formed in the polymeric chain via the dopant anions. The polaron formation in the conducting polymer forecasts the theoretical possibility of ferromagnetic behavior in conducting polymers.[78]

Accordingly, Fukutome proposed a new class of ferromagnetic conjugated polymers as a 'polaronic ferromagnet' (ferromagnetism interactions between polarons) in 1987. These polymers have an A-B-A-B structure, where the A units are organic blocks which carry polarons upon doping (spin containing units, SCU). The B units are blocks which couple A-block polaron spins in a ferromagnetic fashion (ferromagnetic coupling units, FCU). Fukutome suggested the use of oligomeric fragments of conducting polymers as SCUs, for example, polyparaphenylene, polypyrrole or polythiophene, which all have degenerate or nearly degenerate band structures. The polaronic approach overcomes the problems of instability associated with 'built-in' radicals. By separating the polymer synthesis stage from the introduction of spins, this design allows full characterization of the polymers, and hence ensures that the desired topology for ferromagnetic coupling has been created, prior to the introduction of spins. According to the polaronic ferromagnet theory developed by Fukutome, some pioneering research on polaronic ferromagnet has been reported (Figure 10).[79-82]

Surprisingly, however, the spin concentration in these polaronic polymer chains was extremely low. Only a few percent of the doped monomer units actually carried an unpaired electron. This kind of low spin concentration can be explained by the spinless bipolarons mentioned above. Additionally, it has been firmly established that cation radicals of oligopyrroles and oligothiophenes can form diamagnetic π-dimers in the solid state and in solution at low temperature.[83-85] Obviously, π-dimerization and the associated antiferromagnetic pairing of unpaired electrons would be detrimental for high-spin polymers via the polaronic chain concept. This also accounts for the previous observation

of low spin concentration in polaronic ferromagnetic chains, which has limited the applications of these structures as magnetic materials.

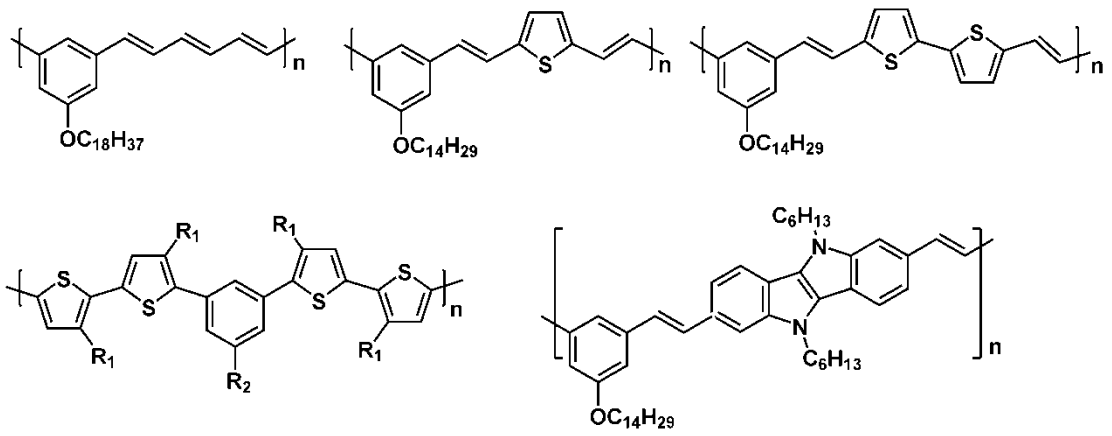

Figure 10. Polaronic ferromagnets based on conducting polymers.

Relatively few studies have been concerned with the design of metallopolymer based magnetic materials. Incorporation of paramagnetic metal centers within a polymer matrix offers an important opportunity to study a variety of electronic processes such as long-range magnetic interaction and delocalization. There are a few pioneering reports about this combination of disparate properties. A particularly intriguing class includes materials with the potential to exhibit both switching magnetic properties and electrical conductivity, with the goal of using the bistable magnetic property to control the extent of conductivity. For example, Takahashi *et al*. reported some iron(III) spin crossover (SCO) conductors including ionic complexes that contain iron SCO cations and conducting anionic components in the same lattice, such as $[Fe(qsal)_2][Ni(dmit)_2]_3 \cdot CH_3CN \cdot H_2O$ (qsalH = *N*-(8-quinolyl)salicylaldimine) which behaved as a SCO molecular conductor.[86]

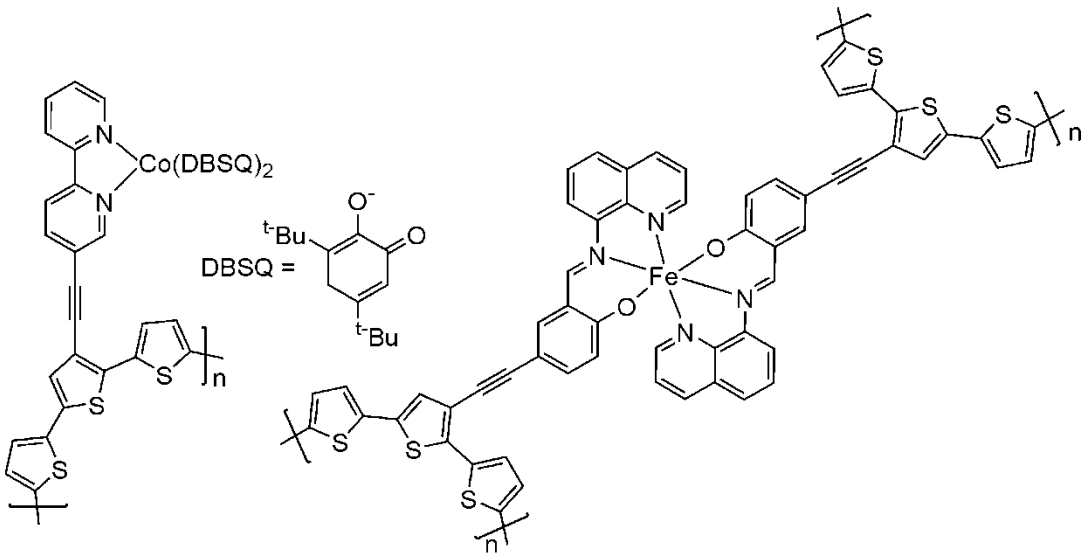

Figure 11. Molecular structures of magnetic conducting metallopolymers.

Lemaire *et al*. reported a conducting metallopolymer featuring valence tautomerism. In 2009 they described the variable temperature magnetic properties of poly(terthiophene) containing a pendant cobalt-semiquinone coordination complex in which temperature-dependent valence tautomerism was observed in the polymer film (Figure 11).[87] In the same year, they reported one conducting metallopolymer with SCO Fe(III) centers covalently bonded to the conducting polymer backbone (Figure 11).[88] Variable temperature magnetic susceptibility measurements demonstrate that SCO is operative in the polymer film. The conductivity of the resulting polymer is on the same order of magnitude as other poly(terthiophene) materials (approximately 10 - 100 $S \cdot cm^{-1}$), which is significantly more conductive than other reported SCO conductors. The unusual and dramatic differences were observed between cooling and warming measurements of the conductivity, which may result from structural changes that originate at the pendant coordination complex caused by SCO.

SCOPE OF DISSERTATION

Over the past decade conducting metallopolymers have been a topic of intense research activity as a consequence of both synthetic breakthroughs and in-depth studies of polymer properties. The combination of functionality provided by metal centers and the easy processing of polymer materials allows the creation of new functional materials with a range of properties and emerging applications. The future for conducting metallopolymers clearly holds much promise. Important future applications can be imagined in areas such as polymer light-emitting diodes, intrinsically magnetic polymers, high density magnetic data storage arrays, metallopolymer-biopolymer hybrids and molecular machines. To access the conducting metallopolymers needed to bring many of these examples to fruition, the synthetic control of these materials must be taken to a new level. Beyond self-assembly, the ability to create functional materials by combining organic polymer chemistry with metal ion properties will be important for continuing innovation. The general availability of conducting metallopolymers will be critical to their applications in novel devices.

We seek to develop solid state light-emitting materials and our approach involves the design and synthesis of well defined conducting metallopolymers that incorporate visible and NIR emitting lanthanide complexes in an inner sphere fashion. As such, we aim to take full advantage of the properties of both organic and inorganic components with high efficiency due to the direct electronic interface this configuration creates. New ligand systems based on 2,2'-bipyridine and 1,10-phenanthroline with polymerizable thiophene derivatives have been synthesized. The coordination chemistry of these ligands with lanthanide ions has been investigated. The oxidative electrochemical polymerization of the monomer complexes leads to the formation of inner sphere conducting metallopolymers. The electrochemistry and photophysical properties of the monomers

and corresponding conducting metallopolymers have been studied which represents a novel perspective on the use of luminescent conducting metallopolymers for a wide range of light-emitting applications.

We have also prepared a new type of cyclometalated Pt(N^C^N)Cl complexes based on 1,3-di(pyridin-2-yl)benzene and 1,3-di(1H-pyrazol-1-yl)benzene derivatives. The solubility of the complexes is improved by using the alkylated terthiophene groups. The photophysical properties of the Pt(II) complexes and the corresponding polymers have been studied. The electrogenerated chemiluminescence (ECL) of the conducting metallopolymers with cyclometalated Pt(II) has been studied to seek new types of phosphorescent materials for potential electroluminescence applications.

In the previous studies, coexistence of conducting electrons and localized spins leads to numerous intriguing phenomena, for example paramagnetic superconductor, antiferromagnetic superconductor and magnetic field induced superconductor. The most prominent aspect of these materials is that they are all bifunctional. These studies initiate our interest in magnetic conducting polymers for their potential application in electromagnetic interference shielding, microwave absorption materials, nonlinear optical systems, and magnetic storage materials. Herein we will discuss a rational synthetic route to prepare well-defined magnetic conducting polymers with inorganic metal centers covalently linked to the conducting polymer backbone. This strategy permits a higher concentration of the metals, which will lead to better microwave absorption properties and thus more effective electromagnetic shielding. The well defined and ordered polymeric structure and homomorphology of the material also offers the promise of achieving high conductivity. We have synthesized ligand systems with four different metal binding groups as 2,6-di(1H-pyrazol-1-yl)pyridine, 2,6-bis((1H-pyrazol-1-yl)methyl)pyridine, 2,4-di(1H-pyrazol-1-yl)-1,3,5-triazine, and tris(1H-pyrazol-1-

yl)methane. The inorganic metal centers of Fe(II)/(III) and Cu(II) have been incorporated into the organic backbone via covalent bonds. These complexes have been investigated by X-ray diffraction analysis, electrochemistry, variable temperature magnetic susceptibility and in situ conductivity measurements.

REFERENCES

1. Natta, G.; Mazzanti, G.; Corradini, P. *Atti. Acad. Naz. Lincei, Cl. Sci. Fis. Mat. Rend.* **1958**, *25*, 3.
2. Chiang, C. K.; Fincher, Jr., C. R.; Park, Y. W.; Heeger, A. J.; Shirakawa, H.; Louis, E. J.; Gau, S. C.; MacDiarmid, A. G. *Phys. Rev. Lett.* **1977**, *39*, 1098.
3. Burroughes, J. H.; Bradley, D. D. C.; Brown, A. R.; Marks, R. N.; MacKay, K.; Friend, R. H.; Burn, P. L.; Holmes, A. B. *Nature* **1990**, *347*, 539.
4. Duan, Y.; Liu, S.; Guan, H. *Sci. Technol. Adv. Mater.* **2005**, *6*, 513.
5. Nambiar, S.; Yeow, J. T. W. *Biosens Bioelectron* **2011**, *26*, 1825.
6. *Conjugated Polymers: Processing and Applications*; Skotheim, T. A.; Reynolds, J. R., Eds.; Hoboken CRC Press, 2006.
7. *Frontiers in Transition Metal-Containing Polymers*; Abd-El-Aziz, A. S.; Manners, I., Eds.; John Wiley & Sons, Inc, New Jersey, 2007.
8. *Synthetic Metal-Containing Polymers*; Manners, I., Ed.; Wiley-VCH, New York, 2004.
9. *Supramolecular Chemistry-Concepts and Prospectives*; Lehn, J.-M., Ed.; VCH, Weinheim, 1995.
10. McGehee, M. D.; Bergstedt, T.; Zhang, C.; Saab, A. P.; O'Regan, M. B.; Bazan, G. C.; Srdanov, V. I.; Heeger, A. J. *Adv. Mater.* **1999**, *11*, 1349.
11. Slooff, L. H.; Polman, A.; Cacialli, F.; Friend, R. H.; Hebbink, G. A.; van Veggel, F. C. J. M.; Reinhoudt, D. N. *Appl. Phys. Lett.* **2001**, *78*, 2122.
12. Li, H. R.; Fu, L. S.; Lin, J.; Zhang, H. J. *Thin Solid Films* **2002**, *416*, 197.
13. Du, C. X.; Ma, L.; Xu, Y.; Li, W. L. *J. Appl. Polym. Sci.* **1997**, *66*, 1405.
14. Strek, W.; Legendziewicz, J.; Lukowiak, E.; Maruszewski, K.; Sokolnicki, J.; Boiko, A. A.; Borzechowska, M. *Spectrochim. Acta, Part A* **1998**, *54*, 2215.
15. Wang, Q. M.; Yan, B. *J. Mater. Chem.* **2004**, *14*, 2450.
16. Shunmugam, R.; Tew, G. N. *Maccromol. Rapid Commun.* **2008**, *29*, 1355.
17. Shunmugam, R.; Tew, G. N. *J. Am. Chem. Soc.* **2005**, *127*, 13567.
18. Balzani, V.; Juris, A.; Venturi, M.; Campagna, S.; Serroni, S. *Chem. Rev.* **1996**, *96*, 759.
19. Holliday, B. J.; Swager, T. M. *Chem. Commun.* **2005**, 23.
20. *Handbook on the Physics and Chemistry of Rare Earths*; Gschneidner, K. A.; Eyring, L., Eds.; Elsevier Science Publisher, New York, 1987.
21. *Lanthanide and Actinide Chemistry*; Cotton, S., Ed.; John Wiley & Sons, Ltd., 2007.
22. *Complexes of the Rare Earth*; Sinha, S. P., Ed.; Progamon: London, 1966.
23. Moore, E. G.; Samuel, A. P. S.; Raymond, K. N. *Acc. Chem. Res.* **2009**, *42*, 542.
24. Segal, M.; Baldo, M. A.; Holmes, R. J.; Forrest, S. R.; Soos, Z. G. *Phys. Rev. B* **2003**, *68*, 075211/1.
25. D'Aleo, A.; Picot, A.; Beeby, A.; Williams, J. A. G.; Le Guennic, B.; Andraud, C.; Maury, O. *Inorg. Chem.* **2008**, *47*, 10258.
26. Kido, J.; Okamoto, Y. *Chem. Rev.* **2002**, *102*, 2357.
27. Kido, J.; Nagai, K.; Ohashi, Y. *Chem. Lett.* **1990**, 657.
28. Kido, J.; Nagai, K.; Okamoto, Y.; Skotheim, T. *Chem. Lett.* **1991**, 1267.

29. Takada, N.; Tsutsui, T.; Saito, S. *Jpn. J. Appl. Phys.* **1994**, *33*, 863.
30. *Lanthanide Probes in Life, Chemical and Earth Sciences - Theory and Practice*; Bünzli, J.-C. G.; Choppin, G. R., Eds.; Elsevier, Amsterdam, 1989.
31. *Solid State Luminescence - Theory, Materials and Devices*; Kitai, A. H., Ed.; Chapman & Hall, London, 1993.
32. *Luminescent Materials*; Blasse, G.; Grabmaier, B. C., Eds.; Springer Verlag, Berlin, New York, 1994.
33. Armelao, L.; Quici, S.; Barigelletti, F.; Accorsi, G.; Bottaro, G.; Cavazzini, M.; Tondello, E. *Coord. Chem. Rev.* **2010**, *254*, 487.
34. Binnemans, K. *Chem. Rev.* **2009**, *109*, 4283.
35. Binnemans, K. *Chem. Rev.* **2005**, *105*, 4148.
36. Hemmila, I. J. *Alloys Compd.* **1995**, *225*, 480.
37. Selvin, P. R. *Annu. Rev. Biophys. Biomol. Struct.* **2002**, *31*, 275.
38. Tremblay, M. S.; Zhu, Q.; Marti, A. A.; Dyer, J.; Halim, M.; Jockusch, S.; Turro, N. J.; Sames, D. *Org. Lett.* **2006**, *8*, 2723.
39. Sculimbrene, B. R.; Imperiali, B. *J. Am. Chem. Soc.* **2006**, *128*, 7346.
40. Mondry, A.; Janicki, R. *Dalton Trans.* **2006**, 4702.
41. Wang, B. S.; Andrejco, M. J. *Proc. SPIE-Int. Soc. Opt. Eng.* **2005**, *6019*, 601911.
42. Weissleder, R.; Tung, C.-H.; Mahmood, U.; Bogdanov, A. *Nat. Biotechnol.* **1999**, *17*, 375.
43. Hebbink, G. A.; Stouwdam, J. W.; Reinhoudt, D. N.; Van Veggel, F. C. J. M. *Adv. Mater.* **2002**, *14*, 1147.
44. Shah, K. *Cancer Biol. Ther.* **2005**, *4*, 518.
45. Zimmer, J. P.; Kim, S.-W.; Ohnishi, S.; Tanaka, E.; Frangioni, J. V.; Bawendi, M. G. *J. Am. Chem. Soc.* **2006**, *128*, 2526.
46. Ennen, H.; Pomrenke, G.; Axmann, A.; Eisele, K.; Haydl, W.; Schneider, J. *App. Phys. Lett.* **1985**, *46*, 381.
47. Kawamura, Y.; Wada, Y.; Hasegawa, Y.; Iwamuro, M.; Kitamura, T.; Yanagida, S. *Appl. Phys. Lett.* **1999**, *74*, 3245.
48. Gillin, W. P.; Curry, R. J. *Appl. Phys. Lett.* **1999**, *74*, 798.
49. Kang, T.-S.; Harrison, B. S.; Bouguettaya, M.; Foley, T. J.; Boncella, J. M.; Schanze, K. S.; Reynolds, J. R. *Adv. Funct. Mater.* **2003**, *13*, 205.
50. Wang, D.; Zhang, J.; Lin, Q.; Fu, L.; Zhang, H.; Yang, B. *J. Mater. Chem.* **2003**, *13*, 2279.
51. Chen, J.; Liu, X.; Fan, X.; Lin, Q.; Gu, P.; Tang, J. *Proc. SPIE-Int. Soc. Opt. Eng.* **2000**, *4220*, 255.
52. Zheng, L.; Yang, M.; Wu, P.; Ye, H.; Liu, X. *Synth. Met.* **2004**, *144*, 259.
53. Chen, X. Y.; Yang, X. P.; Holliday, B. J. *J. Am. Chem. Soc.* **2008**, *130*, 1548.
54. Hagfeldt, A.; Grätzel, M. *Acc. Chem. Res.* **2000**, *33*, 269.
55. Kuciauskas, D.; Freund, M. S.; Gray, H . B.; Winkler, J. R.; Lewis, N. S. *J. Phys. Chem. B.* **2001**, *105*, 392.
56. Tai, W. P.; Inoue, K.; Oh, J. H. *Sol. Energy Mater.* **2002**, *71*, 553.
57. Demas, J. N.; DeGraff, B. A. *Coord. Chem. Rev.* **2001**, *211*, 317.

58. Buss, C. E.; Mann, K. R. *J. Am. Chem. Soc.* **2002**, *124*, 1031.
59. Higgins, B.; DeGraff, B. A. *Inorg. Chem.* **2005**, *44*, 6662.
60. *Photofunctional Transition Metal Cmplexes*; Yam, V. W. W.; Balch, A. L., Eds.; Springer Verlag, Berlin; New York, 2007.
61. Lu, W.; Mi, B. X.; Chan, M. C. W.; Hui, Z.; Zhu, N.; Lee, S. T.; Che, C. M. *Chem. Commun.* **2002**, 206.
62. Lu, W.; Mi, B. X.; Chan, M. C. W.; Hui, Z.; Che, C. M.; Zhu, N.; Lee, S. T. *J. Am. Chem. Soc.* **2004**, *126*, 4958.
63. Baldo, M. A.; O'Brien, D. F.; You, Y.; Shoustikov, A.; Sibley, S.; Thompson, M. E.; Forrest, S. R. *Nature* **1998**, *395*, 151.
64. Adachi, C.; Baldo, M. A.; Forrest, S. R.; Lamansky, S.; Thompson, M. E.; Kwong, R. C. *Appl. Phys. Lett.* **2001**, *78*, 1622.
65. Brooks, J.; Babayan, Y.; Lamansky, S.; Djurovich, P. I.; Tsyba, I.; Bau, R.; Thompson, M. E. *Inorg. Chem.* **2002**, *41*, 3055.
66. Adachi, C.; Baldo, M. A.; Thompson, M. E.; Forrest, S. R. *J. Appl. Phys.* **2001**, *90*, 5048.
67. Ikai, M.; Tokito, S.; Sakamoto, Y.; Suzuki, T.; Taga, Y. *Appl. Phys. Lett.* **2001**, *79*, 156.
68. Nazeeruddin, M. K.; Humphry-Baker, R. *J. Am. Chem. Soc.* **2003**, *125*, 8790.
69. D'Andrade, B. W.; Brooks, J.; Adamovich, V.; Thompson, M. E.; Forrest, S. R. *Adv. Mater.* **2002**, *14*, 1032.
70. Kwok, C.-C.; Yu, S.-C.; Sham, I. H. T.; Che, C.-M. *Chem. Commun.* **2004**, 2758.
71. Holliday, B. J.; Stanford, T. B.; Swager, T. M. *Chem. Mater.* **2006**, *18*, 5649.
72. Choi, T. L.; Lee, K. H.; Joo, W. J.; Lee, S.; Lee, T. W.; Chae, M. Y. *J. Am. Chem. Soc.* **2007**, *129*, 9842.
73. Ling, Q. D.; Song, Y.; Ding, S. J.; Zhu, C. X.; Chan, D. S. H.; Kwong, D. L.; Kang, E. T.; Neoh, K. G. *Adv. Mater.* **2005**, *17*, 455.
74. Köhler, A.; Wittmann, H. F.; Friend, R. H.; Khan, M. S.; Lewis, J. *Synth. Met.* **1996**, *77*, 147.
75. Wong, W. Y.; Wang, X. Z.; He, Z.; Djurisic, A. B.; Yip, C. T.; Cheung, K. Y.; Wang, H.; Mak, C. S. K.; Chan, W. K. *Nat. Mater.* **2007**, *6*, 521.
76. Rajca, A.; Wongsriratanakul, J.; Rajca, S. *Science* **2001**, *294*, 1503.
77. Kosaka, Y.; Yamamoto, H. M.; Nakao, A.; Tamura, M.; Kato, R. *J. Am. Chem. Soc.* **2007**, *129*, 3054.
78. Fukutome, H.; Takahashi, A.; Ozaki, M. *Chem. Phys. Lett.* **1987**, *133*, 34.
79. Yoshizawa, K.; Tanaka, K.; Yamato, T.; Yamauchi, J. *J. Chem. Phys.* **1992**, *96*, 5516.
80. Devine, J. N.; Crayston, J. A.; Walton, J. C. *Synth. Met.* **1999**, *103*, 2294.
81. Murray, M. M.; Kaszynski, P.; Kaisaki, D. A.; Chang, W.; Dougherty, D. A. *J. Am. Chem. Soc.* **1994**, *116*, 8152.
82. van Haare, J. A. E. H.; van Boxtel, M.; Janssen, R. A. *J. Chem. Mater.* **1998**, *10*, 1166.
83. Hill, M. G.; Mann, K. R.; Miller, L. L.; Penneau, J.-P. *J. Am. Chem. Soc.* **1992**, *114*, 2728.

84. Bäuerle, P.; Segelbacher, U.; Gaudl, K. U.; Huttenlocher, D.; Mehring, M. *Angew. Chem., Int. Ed. Engl.* **1993**, *32*, 76.
85. van Haare, J. A. E. H.; Groenendaal, L.; Havinga, E. E.; Jassen, R. A. J.; Meijer, E. W. *Angew. Chem., Int. Ed. Engl.* **1996**, *35*, 638.
86. Takahashi, K.; Cui, H.-B.; Okano, Y.; Kobayashi, H.; Einaga, Y.; Sato, O. *Inorg. Chem.* **2006**, *45*, 5739.
87. O'Sullivan, T. J.; Djukic, B.; Dube, P. A.; Lemaire, M. T. *Chem. Commun.* **2009**, *14*, 1903.
88. Djukic, B.; Lemaire, M. T. *Inorg. Chem.* **2009**, *48*, 10489.

Chapter 2: Synthesis and Characterization of Visible Emitting Lanthanide Containing Conducting Metallopolymers

INTRODUCTION

Lanthanide complexes have attracted intense research interest due to their unique electronic properties, large stokes shift, long lived luminescence lifetime and sharp emission spectra. In the past decades, much work on light-emitting diodes using lanthanide complexes as the emitting materials has been reported. As far as lanthanide complexes developed for electroluminescent devices are concerned, [Ln(β-diketonate)$_3$L] type complexes (L = bidentate neutral heterocyclic ligand) have played an important role due to the following advantages.[1-8] The β-diketone ligand has strong absorption within a large wavelength range from its π-π^* transition and consequently has been targeted for its ability to sensitize the luminescence of the Ln^{3+} ions. Further, the β-diketone has the ability to form stable and strong adducts with Ln^{3+} ions, which can be of practical usage.[1,2] Lastly, the introduction of the bidentate neutral heterocyclic ligands increases the coordination number, protecting lanthanide ions from vibrational coupling with ancillary ligands and increasing their light absorption cross section by the 'antenna effect'.

We aim to attach lanthanide tris-β-diketonate complexes into a polymer matrix by covalent bonds, which will lead to a one-component material, thus ruling out phase separation or segregation during material processing and device operation. Besides, instead of the intermolecular energy transfer from a conjugated polymer host to a lanthanide complex dopant, in the covalently bound system, the energy transfer should be intramolecular energy transfer which is anticipated to be more efficient. Our initial studies start from lanthanide complexes with polymerizable ligands, which can be used as monomer precursors of conducting polymers via electropolymerization. Considering the

rich literature base of lanthanide(III)-β-diketone complexes with 2,2'-bipyridine and 1,10-phenanthroline, we have attempted to functionalize these bidentate nitrogen donor ligands by attaching polymerizable thiophene derivatives to obtain a new series of lanthanide(III)-β-diketone complexes.

EXPERIMENTAL

General Methods

Air- and moisture-sensitive reactions were carried out in oven-dried glassware using standard Schlenk techniques under an inert atmosphere of dry argon. Dry DMF was used from EMD as sure-seal bottles. Bromine was obtained from EMD. 1,10-Phenanthroline and tri-*n*-butyltin chloride were purchased from Alfa Aesar. Trans-dichlorobis(triphenylphosphine)palladium(II) was obtained from STREM. THF was dried by conventional methods and distilled under argon. CH_2Cl_2 was dried using a double-column anhydrous solvent system (Innovative Technologies, Newburyport, MA) and further degassed via nitrogen purge prior to use. Other reagents were used as received from Aldrich. 5,5'-Dibromopyridine and 3,8-dibromo-1,10-phenanthroline were prepared according to the published procedures.[9,10] 2-(Tributylstannyl)-thiophene and 2-(tributylstannyl)-3,4-(ethylenedioxy)thiophene were prepared by Swager's method.[11]

^1H and $^{13}C\{^1H\}$ NMR spectra were recorded with Varian 400 MHz spectrometer. Low-res and high-res mass spectrometry were carried out by Thermo Finngan TSQ 700 and Waters Autospec Ultima, respectively. Elemental analysis was performed by QTI, Whitehouse, NJ (www.qtionline.com). X-ray photoelectron spectroscopy (XPS) was carried out on a PHI 5700 XPS system equipped with a dual Mg X-ray source and monochromatic Al X-ray source complete with depth profile and angle-resolved capabilities.

Crystal Structure Determination

Suitable crystals were mounted on a glass fiber and placed in the low-temperature nitrogen stream. The data were collected on a Nonius Kappa CCD diffractometer using a graphite monochromator with MoKα radiation (λ = 0.71073Å). Data reduction were performed using DENZO-SMN.[12] The structure was solved by direct methods using SIR97[13] and refined by full-matrix least-squares on F^2 with anisotropic displacement parameters for the non-H atoms using SHELXL-97.[14] The hydrogen atoms on carbon were calculated in ideal positions with isotropic displacement parameters set to 1.2 × Ueq of the attached atom (1.5 × Ueq for methyl hydrogen atoms).

The disorder of benzene solvent molecule in the structures of **2** and **3** was modeled by assigning the variable x to the site occupancy factor for one orientation. The variable (1-x) was assigned to the site occupancy factor for the alternate orientation. The geometry of the two rings was constrained to be an ideal hexagon. A common isotropic displacement parameter was refined for the twelve carbon atoms. The variable x refined to a value very close to 1/2. Therefore, the site occupancy factors for the two components of the disorder were fixed at 1/2 for the remainder of the refinement. The toluene solvent molecule in the structures of **1** and **12** was disordered around a crystallographic inversion center at ½, ½, ½. The molecule could not be adequately modeled. As a result, the contributions to the scattering factors due to this solvent molecule was removed by use of the utility SQUEEZE in PLATON98.[15] PLATON98 was used as incorporated in WinGX.[16]

In addition to the solvent disorder, one of the thiophene moieties in the structures of **2** and **3** was found to be disordered by rotation about the C-C bond connecting the thiophene ring to the bipyridyl ring system. The disorder was modeled as described above except that the geometry of the two rings was restrained to be equal. The site occupancy

factor for the major component of the disorder refined to 0.83(1) for **2** and 0.81(1) for **3**, respectively.

UV-Vis and Luminescent Measurements

Absorption spectra were recorded on a Varian Cary 5000 or 6000i Spectrometer with Starna Quartz Fluorometer Cells with a pathlength of 10 mm for the ligand and 0.1 mm for the complexes, respectively. Samples were prepared by dissolving the crystals in the anhydrous CH_2Cl_2. Luminescent measurements were recorded on a Spex Fluorolog.

Electrochemistry

Electrochemical syntheses and studies were performed in a dry-box under a nitrogen atmosphere using a GPES system from Eco. Chemie B. V.. All the electrochemical experiments were carried out in a three-electrode cell with a $Ag/AgNO_3$ reference electrode (silver wire dipped in a 0.01 M silver nitrate solution with 0.1 M [(*n*-$Bu)_4N][PF_6]$ ($TBAPF_6$) in CH_3CN), a Pt button working electrode, and a Pt wire coil counter electrode. Potentials were relative to this 0.01 M $Ag/AgNO_3$ reference electrode. Ferrocene was used as an external reference to calibrate the reference electrode before and after experiments were performed and that value was used to correct the measured potentials. The supporting electrolyte was 0.1 M $TBAPF_6$ that was purified by recrystallization three times from hot ethanol before being dried for 3 days at 100 ^oC under active vacuum.

Synthesis

Synthesis of Ligand

5,5'-Bis(thiophen-2',2''-yl)-2,2'-bipyridine (**L1**) was prepared according to literature procedure.[11]

3,8-Bis(thiophen-2',2''-yl)-1,10-phenanthroline (**L2**). 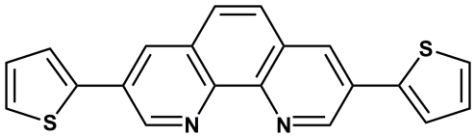 A solution of $Pd(PPh_3)_2Cl_2$ (0.31 g, 0.44 mmol) in 5 mL of dry THF was cooled in a dry ice/acetone bath, and *n*-butyllithium (550 μL of a 1.6 M solution in hexane) was added. The cooling bath was removed after stirring for 20 min. When it reached room temperature, the yellow mixture turned into a clear dark blue solution, which was cannula transferred to a solution of 3,8-dibromo-1,10-phenanthroline (1.56 g, 4.6 mmol) and 2-(tributylstannyl)-thiophene (4.04 g, 10.8 mmol) in 60 mL of dry DMF. The reaction mixture was heated for 18 h at 130 °C. After cooling, 100 mL of CH_2Cl_2 was added into the resulting red solution. The solution was then washed with saturated $NH_4Cl_{(aq)}$ and H_2O. The separated organic phase was evaporated to get the crude residue. Ethyl acetate (100 mL) was added to the above residue to get a yellow solid, which was filtered, washed with ethyl acetate and hexanes. The product was dissolved in a mixture of THF and saturated $Na_2EDTA_{(aq)}$ solution. The above mixture was stirred overnight, then extracted with CH_2Cl_2. Evaporation of the solvent yielded a yellow powder (730 mg, 46%). ^1H NMR ($CDCl_3$): δ (ppm) = 9.45 (dd, *J* = 1.2, 2.4, 2H), 8.35 (dd, *J* = 1.2, 2.0, 2H), 7.83 (d, *J* = 0.8, 2H), 7.60 (dd, *J* =1.2, 3.6, 2H), 7.45 (dd, *J* =1.2, 5.2, 2H), 7.20 (t, *J* = 6.0, 2H). Elemental anal. calcd. (Found) for **L2**, $C_{20}H_{12}N_2S_2$: C, 69.74 (69.19); H, 3.51 (3.34); N, 8.13 (7.36).

3,8-Bis(3,4-(ethylenedioxy)thien-2-yl)-1,10-phenanthroline (L3). 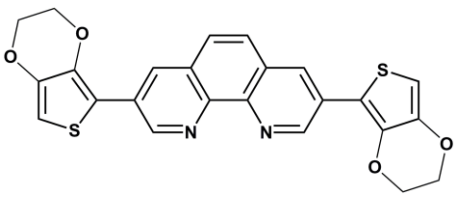 A solution of $Pd(PPh_3)_2Cl_2$ (0.31 g, 0.44 mmol) in 5 mL of dry THF was cooled in a dry ice/acetone bath, and *n*-butyllithium (550 μL of a 1.6 M solution in hexane) was added. The cooling bath was removed after stirring for 20 min. When it reached room temperature, the yellow mixture

turned into a clear dark blue solution, which was cannula transferred to a solution of 3,8-dibromo-1,10-phenanthroline (1.56 g, 4.6 mmol) and 2-(tributylstannyl)-3,4-(ethylenedioxy)thiophene (4.64 g, 10.8 mmol) in 60 mL of dry DMF. The reaction mixture was heated for 15 h at 130 °C. After cooling, 100 mL of CH_2Cl_2 was added to the resulting red solution. The solution was then washed with saturated $NH_4Cl_{(aq)}$ $Na_2(EDTA)_{(aq)}$, and H_2O. The separated organic phase was evaporated to give the crude residue. Ethyl acetate (100 mL) was added to the above residue to get a yellow solid, which was filtered, washed with ethyl acetate, hexanes, and dried under vacuum (yield: 1.14 g, 53%). ^{1}H NMR (400 MHz, $CDCl_3$): δ (ppm) = 9.46 (d, J = 2.4, 2H), 8.48 (d, J = 2.4, 2H), 7.77 (s, 2H), 6.45 (s, 2H), 4.42 (m, 2H), 4.31 (m, 2H). $^{13}C\{^1H\}$ NMR (100 MHz, $CDCl_3$): δ (ppm) = 148.3, 142.7, 140.2, 131.4, 128.7, 128.5, 127.3, 113.2, 99.8, 77.4, 65.2, 64.7. LRMS (CI) calcd. for $C_{24}H_{17}N_2O_4S_2$ m/z 461.52 ([**L3** + H]$^+$), found 461. Elemental anal. calcd. (Found) for **L3**·$2H_2O$, $C_{24}H_{20}N_2O_6S_2$: C, 58.05 (58.01); H, 4.06 (3.51); N, 5.64 (5.36).

General Procedure for Complexation

Ln(*β*-diketonate)$_3$(H_2O)$_2$[17] (0.05 mmol) was added into a suspension of ligand (0.05 mmol) in benzene or toluene (5.0 mL). The mixture was refluxed to get a clear yellow solution. After filtration, the solution was slowly cooled to room temperature and stored at the refrigerator (~ -20 °C). Yellow crystals suitable for X-ray diffraction analysis were obtained after a few days.

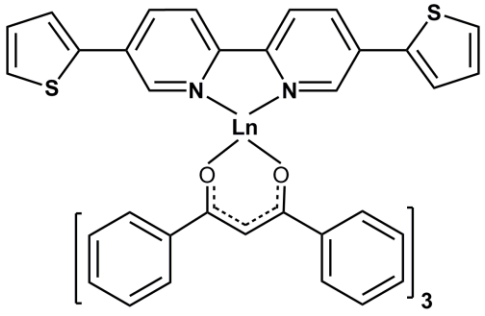

[Sm(DBM)$_3$L1]·C_7H_8 (1, DBM = dibenzoylmethanido). Yield: 26.1 mg, 42.4%; Elemental anal. calcd. (Found) for **1**, $C_{70}H_{53}N_2O_6S_2Sm$: C, 68.21 (67.39); H, 4.33

(3.71); N, 2.27 (2.35). CI-MS (CH_2Cl_2) m/z: 1141 [**1** + H - C_7H_8]$^+$. mp 283 °C.

[Eu(DBM)$_3$L1]·C$_6$H$_6$ (2). Yield: 28.7 mg, 47.0%; Elemental anal. calcd. (Found) for [**2** - C_6H_6], $C_{63}H_{45}EuN_2O_6S_2$: C, 66.25 (66.29); H, 3.97 (4.12); N, 2.45 (2.36). ^{1}H NMR (CD_2Cl_2): δ (ppm) = 14.52 (s, 2H), 10.13 (s, 2H), 9.41 (s, 2H), 7.77 (d, J = 3.6, 4H), 7.05 (m, 18H), 6.96 (s, 6H), 6.29 (s, 6H), 5.36 (s, 2H), 2.73 (s, 3H). CI-MS (CH_2Cl_2) m/z: 1143 [**2** + H - C_6H_6]$^+$. mp 280 °C.

[Tb(DBM)$_3$L1]·C$_6$H$_6$ (3). Yield: 30.0 mg, 48.9%; Elemental anal. calcd. (Found) for [**3** - C_6H_6], $C_{63}H_{45}N_2O_6S_2Tb$: C, 65.85 (66.14); H, 3.95 (4.16); N, 2.44 (2.22). CI-MS (CH_2Cl_2) m/z: 1150 [**3** + H - C_6H_6]$^+$. mp 290 °C.

[Dy(DBM)$_3$L1]·C$_7$H$_8$ (4). Yield: 22.7 mg, 41.7%; Elemental anal. calcd. (Found) for **4**, $C_{70}H_{53}DyN_2O_6S_2$: C, 67.54 (67.19); H, 4.29 (3.80); N, 2.25 (2.31). CI-MS (CH_2Cl_2) m/z: 1154 [**4** + H - C_7H_8]$^+$. mp 300 °C.

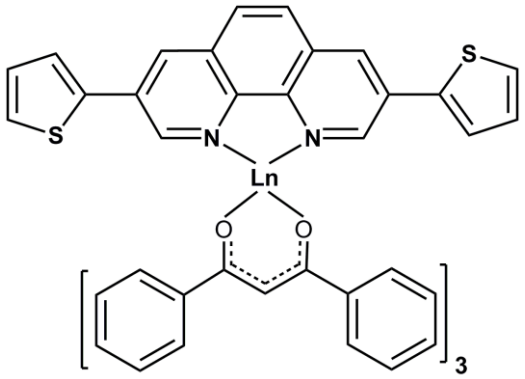

Sm(DBM)$_3$L2 (5). Yield: 21.6 mg, 37.1%; Elemental anal. calcd. (Found) for **5**, $C_{65}H_{45}N_2O_6S_2Sm$: C, 67.04 (67.38); H, 3.89 (3.96); N, 2.41 (2.28). CI-MS (CH_2Cl_2) m/z: 1166 [**5** + H]$^+$. mp 250 °C.

[Eu(DBM)$_3$L2]·1.25C$_7$H$_8$, (6). Yield: 19.4 mg, 30.3%; Elemental anal. calcd. (Found) for [**6** - 1.25C_7H_8], $C_{65}H_{45}EuN_2O_6S_2$: C, 66.95 (67.04); H, 3.89 (3.95); N, 2.40 (2.27). ^{1}H NMR (CD_2Cl_2): δ (ppm) = 11.42 (s, 2H), 10.45 (s, 2H), 9.15 (br, 2H), 7.61 (d, J = 4.0, 2H), 7.14 (d, J = 3.6, 4H), 6.85 (br, 18H), 6.03 (br, 12H), 3.0 (s, 3H). CI-MS (CH_2Cl_2) m/z: 1167 [**6** + H - 1.25C_7H_8]$^+$. mp 255 °C.

Tb(DBM)$_3$L2 (7). Yield: 18.7 mg, 31.9%; Elemental anal. calcd. (Found) for **7**, $C_{65}H_{45}N_2O_6S_2Tb$: C, 66.55 (65.73); H, 3.87 (3.82); N, 2.39 (2.27). CI-MS (CH_2Cl_2) m/z: 1174 [**7** + H]$^+$. mp 265 ^{o}C.

Dy(DBM)$_3$L2 (8). Yield: 21.3 mg, 36.2%; Elemental anal. calcd. (Found) for **8**, $C_{65}H_{45}DyN_2O_6S_2$: C, 66.35 (65.94); H, 3.85 (3.70); N, 2.38 (2.25). CI-MS (CH_2Cl_2) m/z: 1178 [**8** + H]$^+$. mp 280 ^{o}C.

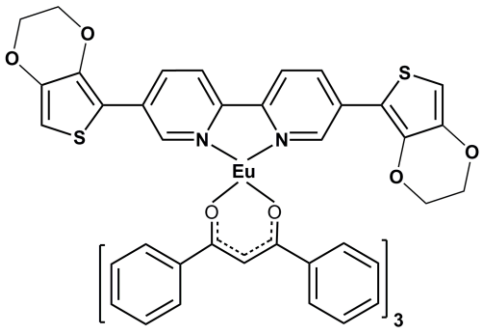

Eu(DBM)$_3$L3 (9). Yield: 21.8 mg, 34%. ^{1}H NMR (400 MHz, CD_2Cl_2): δ (ppm) = 11.41 (s, 2H), 10.82 (br, 2H), 10.49 (s, 2H), 6.86 (m, 18H), 6.19 (d, J = 9.2, 12H), 4.22 (m, 2H), 4.02 (m, 2H), 2.73 (s, 3H). HRMS (CI): calcd. for $C_{69}H_{49}EuN_2O_{10}S_2$ m/z 1282.2041 [**9**]$^+$, found 1282.2040. Elemental anal. calcd. (Found) for **9**, $C_{69}H_{49}EuN_2O_{10}S_2$: C, 64.63 (64.50); H, 3.85 (3.49); N, 2.18 (2.11).

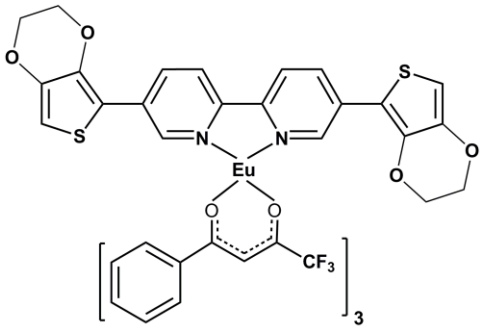

[Eu(BTFA)$_3$L3]·2C$_7$H$_8$ (10, BTFA = 4,4,4-trifluoro-1-phenyl-1,3-butanedione). Yield: 25.8 mg, 41%; Elemental anal. calcd. (Found) for [**10** - 2C_7H_8], $C_{54}H_{34}EuF_9N_2O_{10}S_2$: C, 51.56 (51.78); H, 2.72 (3.20); N, 2.23 (2.44). CI-MS (CH_2Cl_2) m/z: 1259 [**10** + H - 2C_7H_8]$^+$.

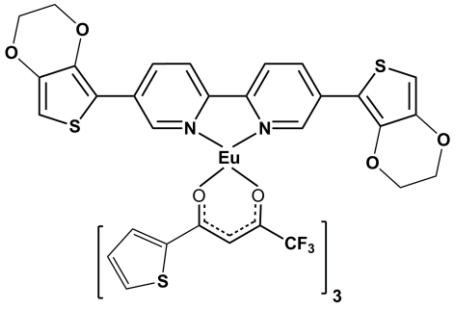

Eu(TTA)$_3$L3 (11, TTA =

thenoyltrifluoroacetone). Yield: 24.9 mg, 39%; Elemental anal. calcd. (Found) for **11**, $C_{48}H_{28}EuF_9N_2O_{10}S_5$: C, 45.18 (45.56); H, 2.21 (2.66); N, 2.20 (2.39). CI-MS (CH_2Cl_2) *m*/*z*: 1276 [**11**]$^+$.

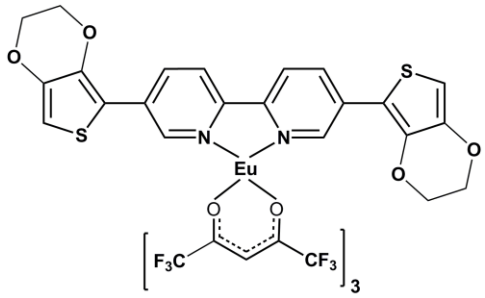

[Eu(HFPD)$_3$L3]·0.5C$_7$H$_8$ (12, HFPD = 1,1,1,5,5,5-hexafluoro-2,4-pentanedione). Yield: 16.1 mg, 25.2%; Elemental anal. calcd. (Found) for [**12** - 0.5C_7H_8], $C_{39}H_{19}EuF_{18}N_2O_{10}S_2$: C, 37.97 (37.61); H, 1.55 (1.88); N, 2.27 (2.12). CI-MS (CH_2Cl_2) *m*/*z*: 1235 [**12** + H - 0.5C_7H_8]$^+$.

RESULTS AND DISCUSSION

Lanthanide Complexes Based on L1 and L2

Crystal Structure of Ln(DBM)$_3$L1 (Ln = Eu (2), Tb (3))

Complex **2** crystallizes in the monoclinic space group $P2_1/n$. The coordination environment of Eu^{3+} in **2** with atom labeling scheme is shown in Figure 12. The Eu^{3+} ion is octa-coordinated by six oxygen atoms from three DBM ligands and two nitrogen atoms from the **L1** ligand. The coordination sphere of the Eu^{3+} center can be best described as a slightly distorted square antiprism from the coordination site angles (Figure 12). The O and N atoms lie at the apexes of the distorted square antiprism. One of the two planes of the square antiprism is formed exclusively by oxygen atoms (O1A, O1C, O2A and O2C) with the mean deviation of 0.0082 Å and the other one by two nitrogen atoms and two oxygen atoms (N1, N2, O1B, and O2B) with the largest deviation of 0.0327 Å for N2. The two square planes are almost parallel to each other, as shown by the dihedral angle of 1.8° between the two mean planes. The average Eu-N bond distance (2.6205(2) Å) is longer than the Eu-O bonds (2.3443(18) Å) of DBM ligands as observed in the X-ray

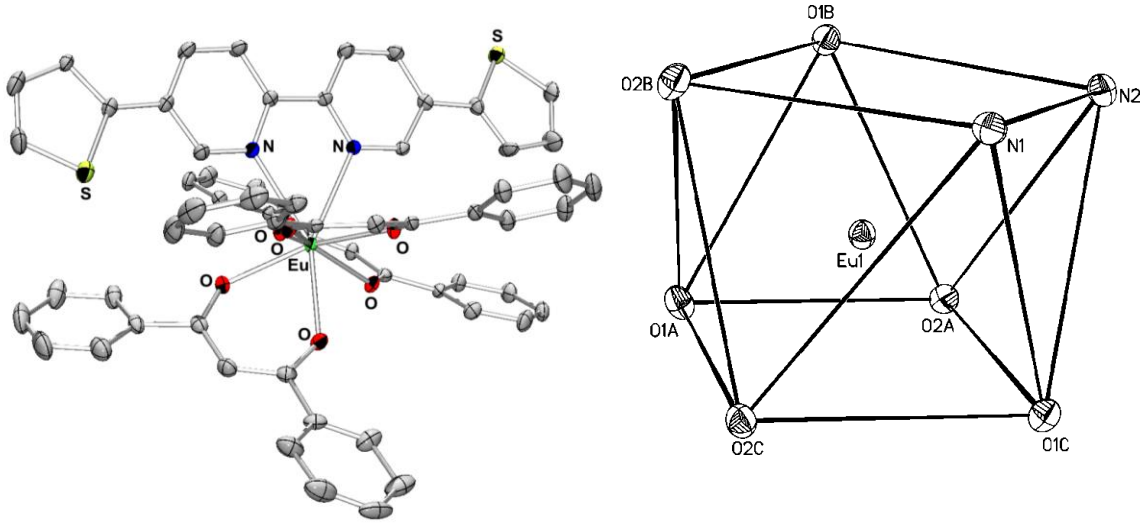

Figure 12. Left: ORTEP plot for **2** with ellipsoids drawn at the 30% probability level. The hydrogen atoms have been removed for clarity. The lower occupancy atoms of the disordered thiophene rings are not shown. Right: Coordination polyhedron of the Eu^{3+} ion in complex **2**.

single crystal data of the complex (2,2'-bipyridine)tris(dibenzoylmethane)europium.[18] In the *β*-diketone rings of complex **2**, all of the average carbon-carbon and carbon-oxygen bond lengths are between the single bond distance and the double bond distance. This can be explained by the fact that there exists conjugated structure between the phenyl ring and the coordinated *β*-diketonate, which leads to the delocalization of the electron density of the coordinated *β*-diketonate chelating ring. In the coordinated **L1** ligand, one of the thiophene moieties containing S1 was found to be disordered by rotation about the C-C bond connecting the thiophene ring to the bipyridal ring system. The other thiophene ring is planar with an average standard deviation from planarity of 0.0042 Å. The C-C bond lengths in the thienyl ring are very similar to those of the corresponding C-C bond distances in free thiophene. The average C-S bond distance (1.699(7) Å) is somewhat

shorter than a normal Csp^2-S single bond length (1.759(8) Å), and is comparable with the corresponding C-S distance of free thiophene (1.714(1) Å).[19] Therefore, the thiophene ring structure indicates some delocalization of the π-electrons, as what is found in free thiophene. The two pyridine planes in bpy are twisted by 6.7°, and the dihedral angle between the thiophene ring and the connected pyridine ring is 8.6°.

Complex **3** is isostructural with **2**. The lanthanide centers are both eight-coordinate showing the square antiprism geometry. The average Ln-O and Ln-N bond lengths of complex **3** (Ln-$O_{av.}$ = 2.319(2) and Ln-$N_{av.}$ = 2.593(3) Å) are shorter than those of complex **2**. These regular changes result from the decreasing sizes of these ions caused by the lanthanide contraction.[20]

Crystal Structure of [Eu(DBM)$_3$L2]·1.25C$_7$H$_8$ (6)

Structure characterization of **6** reveals a similar structure to that of **2** (Figure 13). The central Eu^{3+} ion adopts an eight-coordinate geometry with six oxygen atoms from three DBM ligands and two nitrogen atoms from the **L2** ligand, yet the polyhedron of coordination can be regarded most accurately as a dodecahedron. The different coordination geometry results from the distinct nature of 1,10-phenanthroline which has a rigid structure imposed by the central ring, such that the two nitrogen atoms are always in juxtaposition, whereas, for **L1**, the free rotation of the pyridyl rings about the linking bond allows the two nitrogen atoms to deviate from planarity. The structural data further support this idea. In **2**, the two pyridine planes in bpy are twisted by 6.7°, while in **6**, the phenanthroline fragment is almost planar with the largest deviation from the mean plane of 0.08 Å. In **6**, the Eu-O distances vary between 2.337(3) and 2.392(3) Å, whereas the Eu-N distances are 2.634(4) and 2.643(4) Å, respectively. The thiophene ring structure

also shows some delocalization of the π-electrons determined by the C-C and C-S bond lengths.

It should be noted that **L1** and **L2** have been previously reported but these studies focused on the coordination chemistry of **L1** and **L2** with Ru(II),[11,21] and contained no X-ray diffraction analysis data. Herein, we structurally characterized the eight-coordinate lanthanide complexes with the bulky bis-thiophene substituted ligands for the first time, which sheds light on further electropolymerization of them.

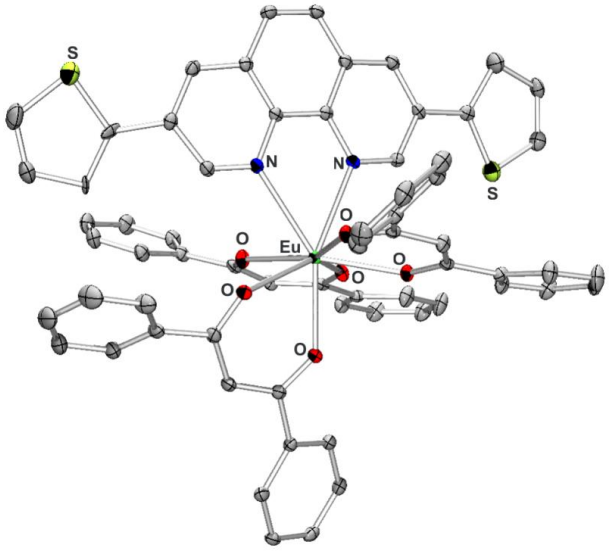

Figure 13. ORTEP plot for **6** with ellipsoids drawn at the 30% probability level. The hydrogen atoms and solvent molecules have been removed for clarity. The lower occupancy atoms of the disordered thiophene rings are not shown.

UV-Vis Absorption Spectra

Absorption spectra of **L1**, **L2**, complex **2** and **6** in dichloromethane at room temperature are presented in Figure 14. The UV absorption spectrum of **L1** shows one π-π^* absorption peak at 350 nm, which is nearly the same as the absorption of the uncoordinated DBM ligand.[22] For **L2**, two strong absorption peaks at 280 and 350 nm attributed to the π-π^* transitions are observed. The molar absorption coefficients of **L1**

and **L2** at 350 nm are 5.3×10^4 and 2.7×10^4 L mol^{-1} cm^{-1}, respectively, showing the strong ability of these ligands to absorb light. Absorption spectra of the complexes **1** - **4** show one principal absorption peak at 350 nm with the molar absorption coefficients around 10^5 L mol^{-1} cm^{-1} (9.7×10^4, 9.1×10^4, 10.2×10^4 and 9.4×10^4 L mol^{-1} cm^{-1}). The increased molar absorption coefficients of the complexes compared to the $Eu(DBM)_3(H_2O)_2$ precursor (6.9×10^4 L mol^{-1} cm^{-1}) indicate the complexation of the ligands to the metal center. Similarly, the high molar absorption coefficient values of complexes **5** and **6** at 350 nm (10.0×10^4 and 10.2×10^4 L mol^{-1} cm^{-1}) are also observed, which reveal the strong ability of these complexes to absorb light.

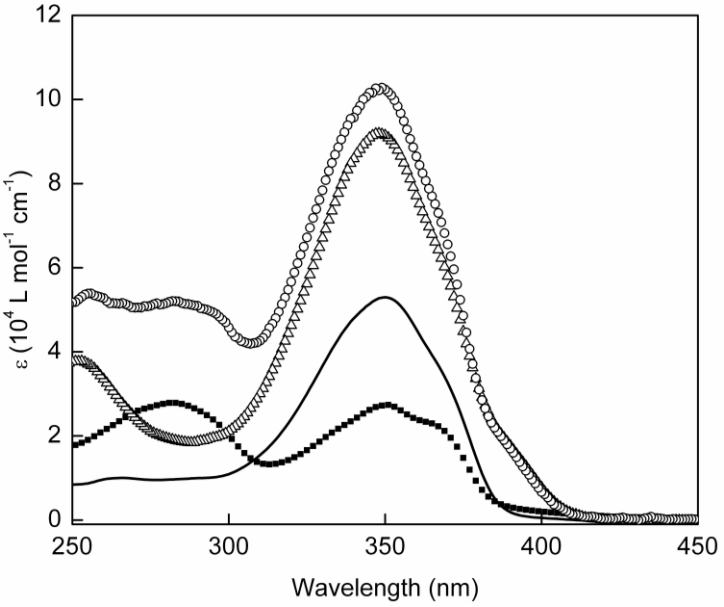

Figure 14. UV-Vis absorption spectra of **L1** (-), **L2** (■), **2** (Δ) and **6** (○) in CH_2Cl_2 solution.

Photoluminescence of Ln(DBM)$_3$L1 Complexes

Photoluminescent emission of the Sm^{3+} ion is very weak in complex **1** in toluene solution (10^{-3} M) or in the solid state at room temperature. At 77 K in toluene solution,

the Sm^{3+} emission is also weak. However at 77 K in the solid state, the Sm^{3+} emission is easily observable with two minor peaks at 563 ($^4G_{5/2} \rightarrow {}^6H_{5/2}$) and 606 nm ($^4G_{5/2} \rightarrow {}^6H_{7/2}$) and a relatively intense peak at 643 nm ($^4G_{5/2} \rightarrow {}^6H_{9/2}$) (Figure 15).

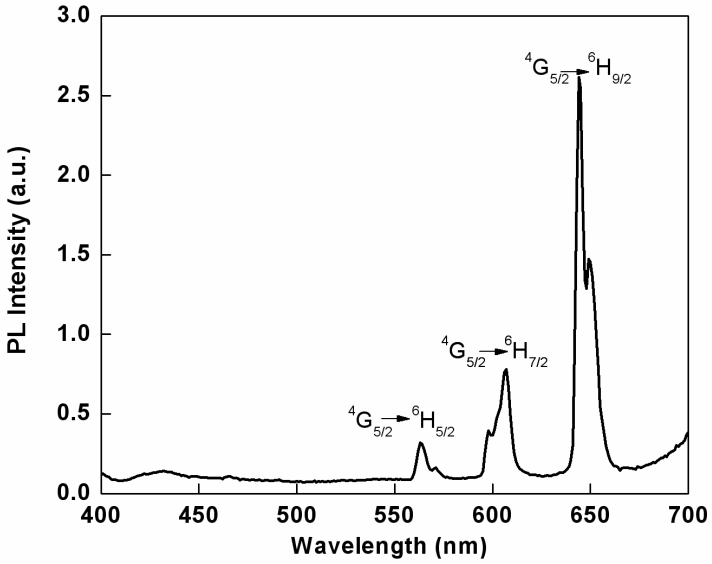

Figure 15. Emission spectrum of **1** at 77 K in the solid state.

The normalized excitation spectrum of **2** in toluene at room temperature, obtained by monitoring the peak of the intense $^5D_0 \rightarrow {}^7F_2$ transition of the Eu^{3+} ion, shows features similar to the absorption spectrum of **2**. The excitation maximum is red shifted by 55 nm (Figure 16) which indicates the indirect excitation by energy transfer from the ligands to Eu^{3+} ion. At 77 K, the excitation spectrum is blue shifted to 392 nm with a new shoulder at 370 nm. The room temperature normalized emission spectrum of **2** is shown in Figure 16. The emission spectrum of **2** displays a broad band centered at 436 nm, derived from the fluorescence of the coordinated ligand, and characteristic Eu^{3+} ($^5D_0 \rightarrow {}^7F_J$, J = 0 - 4) transitions dominated by the transition to the $^7F_2$ sublevel at 610 nm. The symmetry forbidden emission $^5D_0 \rightarrow {}^7F_0$ at 576 nm can be found in **2**. It is well known that the $^5D_0$

$\rightarrow {}^7F_0$ transition is strictly forbidden in a field of symmetry. Thus the above result reveals that the Eu^{3+} ion in **2** occupies a site with low symmetry and without an inversion center. The ${}^5D_0 \rightarrow {}^7F_1$ transition is a magnetic dipole transition, and its intensity varies with the crystal field strength acting on Eu^{3+}. On the other hand the ${}^5D_0 \rightarrow {}^7F_2$ transition increases as the site symmetry of Eu^{3+} decreases. Therefore the intensity ratio of the ${}^5D_0 \rightarrow {}^7F_2$ transition to the ${}^5D_0 \rightarrow {}^7F_1$ transition is widely used as a measurement of the coordination state and the site symmetry of the rare earth elements.[23] For complex **2**, the intensity ratio $I({}^5D_0 \rightarrow {}^7F_2) / I({}^5D_0 \rightarrow {}^7F_1)$ is equal to ca. 10, which also suggests the very low site symmetry of the Eu^{3+} in **2**. The overall luminescent quantum yields for the emissions from the Eu^{3+} ion and the coordinated ligand in toluene are 9.4% and 12.1%, respectively (λ_{ex} = 390 nm, room temperature). When the temperature was cooled to 77 K, the ligand

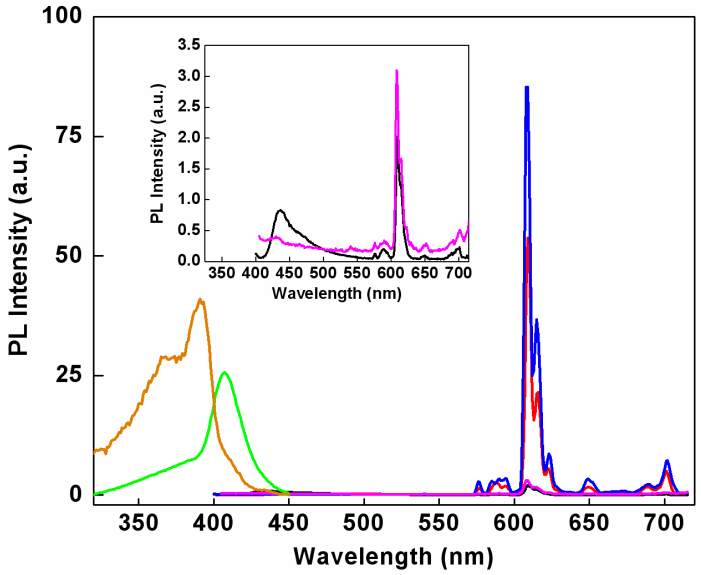

Figure 16. Excitation spectra of **2** in toluene (10^{-3} M) at RT (green) and 77 K (orange); Emission spectra of **2** in toluene at RT (black) and 77 K (red), and in the solid state at RT (purple) and 77 K (blue) with the excitation wavelength at 390 nm. The inset shows the emission spectra of **2** at RT.

emission band at 436 nm vanished completely to leave only the intense $^5D_0 \rightarrow {}^7F_{0\text{-}4}$ emission of Eu^{3+}, which was also dramatically improved for the same sample. This indicates that the ligand to Eu^{3+} energy transfer is more efficient at lower temperature. At 77 K, the $^5D_0 \rightarrow {}^7F_0$ transition of Eu^{3+} in **2** exhibits only one peak at 576 nm without any splitting, which suggests only one coordination environment for Eu^{3+} in this complex. There are two main bands to the $^7F_1$ level, corresponding to $A_1 \rightarrow A_2$ and $A_1 \rightarrow B_1$ magnetic dipole transitions, which are both allowed in C_2 symmetry. The energy gap between the levels is 7 nm. The $^5D_0 \rightarrow {}^7F_2$ transition displays three bands assigned to the allowed electronic dipole transitions, $A_1 \rightarrow A_1$, $A_1 \rightarrow B_1$ and $A_1 \rightarrow B_2$, in C_2 symmetry. The energy gaps between the levels are both 7 nm, while the total splitting is 14 nm. Especially, the $^5D_0 \rightarrow {}^7F_2$ transition splits into 3 peaks, close to J + ½, which further verified the central europium ion is located at a site of low symmetry without an

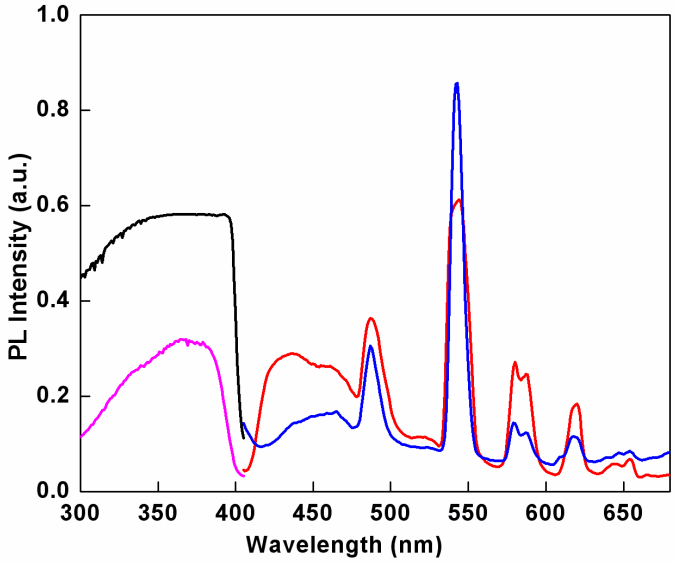

Figure 17. Excitation spectra of **3** in toluene (10^{-3} M) (orange) and in the solid state (black) at 77 K; Emission spectra of **3** in toluene (red) and in the solid state (blue) at 77 K (excited at 380 nm).

inversion center. The solid state luminescence of **2** for the Eu^{3+} centered emission shows similar behavior as that in toluene solution, except that the $^5D_0 \rightarrow {}^7F_1$ transition splits into three main bands at 77 K (Figure 16). For ligand centered emission, the peak at 436 nm was further broadened and weakened.

At room temperature, the Tb^{3+} emission from complex **3** can not be observed either in toluene solution (10^{-3} M) or in the solid state. When the sample was cooled to 77 K, the emission spectrum exhibits the characteristic transitions of the Tb^{3+} ion (Figure 17) with a small amount of ligand emission. The lines at 488, 542, 580 and 619 nm are assigned to transitions between the first exited state, $^5D_4$, and the ground multiplet $^7F_{6\text{-}3}$ for Tb^{3+} ion, respectively. The normalized excitation spectrum of **4** in toluene at 77 K, obtained by monitoring the peak of the intense $^5D_4 \rightarrow {}^7F_5$ transition of the Tb^{3+} ion, shows a broad peak in the 300 - 400 nm region. The red-shift by 25 - 50 nm (Figure 17) of the excitation maximum indicates the indirect excitation by energy transfer from the ligands to Tb^{3+} ion. We can not observe any Dy^{3+} emission from complex **4** either in the solid state or at 77 K.

Photoluminescence of Ln(DBM)$_3$L2 Complexes

The excitation spectrum of complex **5** in toluene at room temperature (Figure 18, emission monitored at 646 nm) is red shifted by 55 nm from its ground state absorption spectrum (at 350 nm). After cooling to 77 K, the excitation maximum moves to 395 nm with a long tail extended to 500 nm. Upon selective excitation at 380 nm at room temperature, the emission spectrum of complex **5** displays a broad band centered at 424 nm, derived from the coordinated ligand emission, and the characteristic sharp peaks associated with the Sm^{3+} emission at 563 nm ($^4G_{5/2} \rightarrow {}^6H_{5/2}$), 608 nm ($^4G_{5/2} \rightarrow {}^6H_{7/2}$) and 646 nm ($^4G_{5/2} \rightarrow {}^6H_{9/2}$). At 77 K, the ligand emission almost disappears, leaving only the

Sm^{3+} emission. The intensity sequence of the peaks are $I_{4G5/2\rightarrow6H9/2} > I_{4G5/2\rightarrow6H7/2} > I_{4G5/2\rightarrow6H5/2}$. The electronic dipole transition $^4G_{5/2} \rightarrow {}^6H_{9/2}$ exhibits the highest relative emission intensity. The solid state emission spectrum reveals similar behavior as that in toluene solution.

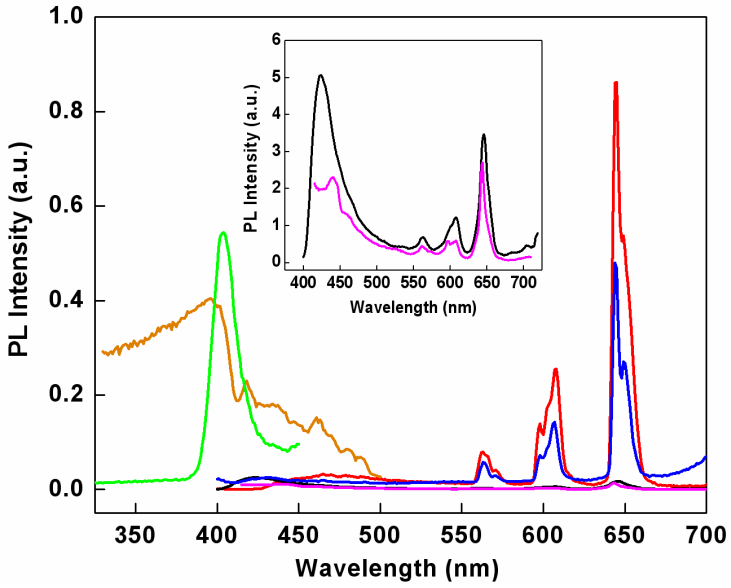

Figure 18. Excitation spectra of **5** in toluene (10^{-3} M) at RT (green) and 77 K (orange); Emission spectra of **5** in toluene at RT (black) and 77 K (red), and in the solid state at RT (purple) and 77 K (blue). The inset shows the emission spectra of **5** at RT.

Complex **6** shows strong red luminescence in solution and solid state when irradiated by UV light. When excited by light at 400 nm, the emission spectrum of **6** consists of entirely characteristic emission bands of Eu^{3+} ($^5D_0 \rightarrow {}^7F_J$, J = 0 - 4) either at room temperature or 77 K (Figure 19). Notably, the emission of **6** in toluene solution at 77 K is significantly broad. The full width at half maximum of the most intense $^5D_0 \rightarrow$

$^7F_2$ transition at 610 nm at 77 K in toluene is 20 nm while others are only several nm. The quantum yield of **6** determined at room temperature in toluene solution is 27%.

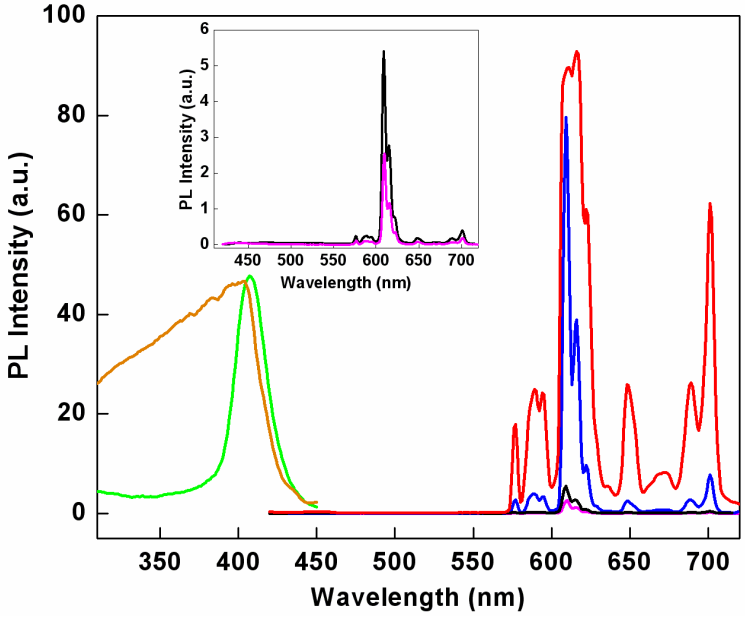

Figure 19. Excitation spectra of **6** in toluene (10^{-3} M) at RT (green) and 77 K (orange); Emission spectra of **6** in toluene at RT (black) and 77 K (red), and in the solid state at RT (purple) and 77 K (blue). The inset shows the emission spectra of **6** at RT.

Triplet Excited State Energy Levels of the Ligands

Generally, organolanthanide complex emission is originated from the excitation of the ligands. Through intersystem crossing, the energy is transferred from the singlet excited state S_1 to the triplet excited state T_1 in the ligand. The ligand then intramolecularly transfers energy from its lowest triplet excited state to the excited states of the central lanthanide ion. Finally the central lanthanide ion luminesces through radiative transitions from the excited state to the ground state.[24] According to Sato *et al.*,[25] to improve energy transfer probability from the triplet excited state of the ligand to

the resonance level of the Ln^{3+} ion, the triplet excited state of the ligand must be closely matched to or slightly above the metal ion's resonance levels. The optimum energy gap between them should be in the 2000 - 5000 cm^{-1} region. The ligands phosphorescence is clearly observed in the 77 K emission spectrum which indicates the energy of the $^3\pi\pi^*$ levels of 20 408 cm^{-1} for **L1** and 21 277 cm^{-1} for **L2**, respectively. The energy levels of the ligands' triplet excited states are higher than the excited states of Sm^{3+} (17 800 cm^{-1}) and Eu^{3+} (17 250 cm^{-1}),[26] confirming the suitability of the ligands **L1** and **L2** as sensitizers for those lanthanide ions. However, they are not suitable for Tb^{3+} (20 430 cm^{-1}) and Dy^{3+} (20 958 cm^{-1}) which possess higher excited state energies. This analysis corresponds well with the observed photophysical properties of the complexes discussed herein.

The results show that a complete energy transfer occurred from the ligand to the central Eu^{3+} ion in complex **6**. A weak ligand emission band appears in the emission spectrum of **5** due to incomplete energy transfer. Furthermore, the comparatively stronger ligand emission in **1** than that in **5** and complete lanthanide emission in **6** confirm that **L2** is a better antenna for Sm^{3+} and Eu^{3+} emission than **L1** as predicted by analysis of the triplet excited state energy levels.

Electrochemical Studies

Thiophene can be electrochemically polymerized at relatively high applied voltages when compared to other organics and thiophene derivatives.[27-29] For the design of the ligands, the 2,2'-bipyridine and 1,10-phenanthroline are incorporated directly into the polymer backbone. The thiophene residues were chosen to allow the polymer synthesis by electrochemical oxidation. CH_2Cl_2 solutions of the free ligands **L1** and **L2** (ca. 0.1 mM) are oxidatively polymerized when the potential of the electrode was swept

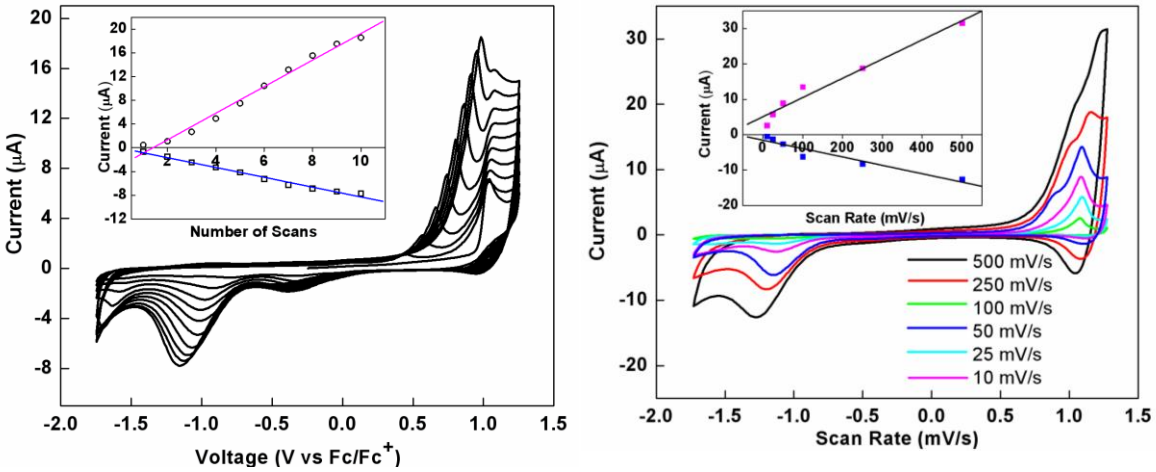

Figure 20. Left: 10 successive cyclic voltammograms of a 0.1 mM CH_2Cl_2 solution of **L1**, 0.1 M $TBAPF_6$, Pt electrode. Inset, the maximum peak current versus the number of scans. Right: Electrochemical scan rate dependence of poly-**L1** (Fc/Fc^+ is the redox couple of ferrocene). Inset: plot of linear current increase vs scan rate.

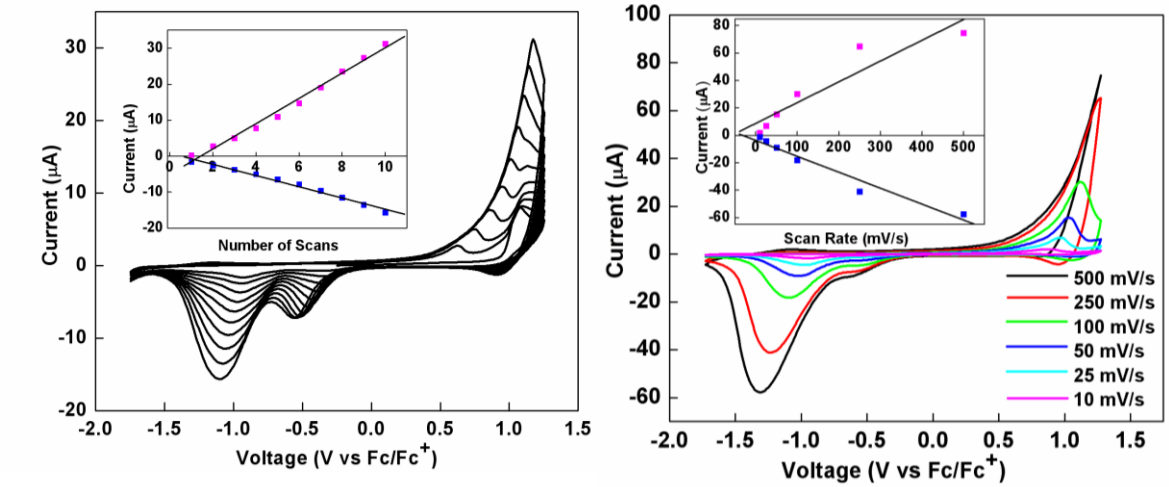

Figure 21. Left: 10 successive cyclic voltammograms of a 0.1 mM CH_2Cl_2 solution of **L2**, 0.1 M $TBAPF_6$, Pt electrode. Inset, the maximum peak current versus the number of scans. Right: Electrochemical scan rate dependence of poly-**L2** (Fc/Fc^+ is the redox couple of ferrocene). Inset: plot of linear current increase vs scan rate.

between -1.75 and +1.25 V versus Fc/Fc^+ at a scan rate of 100 mV/s. A typical electrochemical polymerization of **L1** is shown in Figure 20. For **L1**, the first polymerization scan is characterized by a relatively sharp onset of the monomer oxidation at +1.04 V followed by two reductive processes at -0.34 and -0.88 V on the return cycle. In subsequent potential sweeps, new oxidation peaks grow at +0.45 V. Repeated cycling resulted in further increased electroactivity of the electrode surface, indicative of polymer growth. A linear relationship between the maximum peak current and number of scans confirms the steady growth of the polymer film. The maximum peak current of an electrode-confined film of poly-**L1** in pure electrolyte solution varies linearly with the rate of the electrochemical scan up to 500 mV/s (Figure 20). This behavior is indicative of a strongly adsorbed electroactive thin film which is not limited by the ionic flux of the counter anions.

For **L2**, the first polymerization scan is characterized by a relatively sharp onset of the monomer oxidation at +1.08 V followed by two reductive processes at -0.35 and -0.93 V on the return cycle (Figure 21). In subsequent potential sweeps, new oxidation peaks grow in at +0.63 V. Repeated cycling resulted in further increased electroactivity of the electrode surface, indicative of polymer growth. A linear relationship between the maximum peak current and the number of scans confirms the steady growth of the polymer film. The linear relationship of the current versus scan rate is also observed, as shown in Figure 21. The resulting films of **L1** and **L2** are both golden-yellow in their reduced form.

Unfortunately, after the ligands were coordinated to the $Ln(DBM)_3(H_2O)_2$ monomers, none of them polymerized electrochemically. We observe an irreversible oxidation at +0.91 V which does not result in polymer deposition. Considering that the

$Ln(DBM)_3(H_2O)_2$ monomers are electrochemically silent within the scan window, the irreversible oxidation peak is related to **L1** or **L2**.

Lanthanide Complexes Based on L3

Crystal Structure of $Eu(DBM)_3$L3 (9)

The molecular structure of **9** (Figure 22) is the first reported structure of a complex containing both a lanthanide ion and EDOT electropolymerizable units. The eight-coordinate Eu^{3+} ion lies at the center of a slightly distorted square antiprism that is defined by the six oxygen atoms from the DBM ligands and the two nitrogen atoms from **L3**. The two square planes are almost parallel to each other, as shown by the dihedral angle of 2.3° between the two mean planes. The Eu-N_{av} bond distance (2.577(4) Å) is longer than the Eu-O_{av} bond distance (2.330(3) Å). This trend and these bond distances are consistent with the data of the complex $Eu(DBM)_3$Phen (Eu-N_{av}, 2.656 Å; Eu-O_{av} 2.359 Å).[30] In the *β*-diketone rings of **9**, all of the average carbon-carbon and carbon-oxygen bond lengths are between the single bond distance and the double bond distance. This can be explained by the fact that there exists conjugated structure between the phenyl ring and the coordinated *β*-diketonate, which leads to the delocalization of the electron density of the coordinated *β*-diketonate chelating ring. In the coordinated **L3** ligand, one of the thienyl rings is planar with an average standard deviation from planarity of the thienyl atoms of 0.014 Å, while the other thienyl ring is almost strictly planar. The C-C bond lengths in the thienyl ring are very similar to those of the corresponding C-C bond distances in free thiophene. The average C-S bond distance (1.705(5) Å) is somewhat shorter than a normal C_{sp^2}-S single bond length (1.759(8) Å), and is comparable with the corresponding C-S distance of free thiophene (1.714(1) Å).[18] Therefore, the thienyl ring structure indicates some delocalization of the π-electrons,

compared to what is found in free thiophene. The dihedral angles between the phenanthroline unit and the two thienyl rings are 14.5 and 17.6°. The six-membered dioxane ring exists in a half-chair conformation.

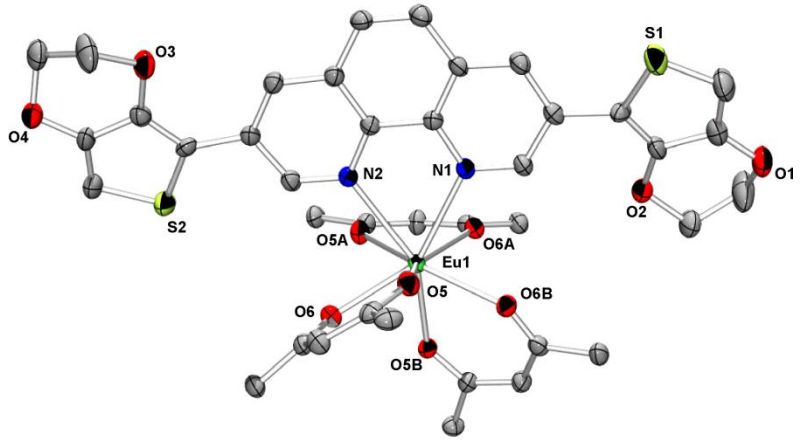

Figure 22. ORTEP diagram of **9** showing the labeling scheme of selected atoms at 30% probability level. Hydrogen atoms and phenyl rings of the dibenzoylmethanido ligands are omitted for clarity.

Crystal Structure of [Eu(BTFA)$_3$L3]·2C$_7$H$_8$ (10)

The central Eu^{3+} ion adopts an eight-coordinate geometry with six oxygen atoms from three BTFA ligands and two nitrogen atoms from **L3** (Figure 23). The coordination sphere of Eu^{3+} can be best described as a distorted dodecahedron. The Eu-O bond lengths (2.356(3) - 2.376(3) Å) are shorter than the Eu-N bond lengths (2.600(4) and 2.604(4) Å). In the BTFA rings, the distances of C1A-C4A, C1B-C4B, and C1C-C4C are 1.508(7), 1.495(6), and 1.497(6) Å, respectively, which are close to normal C-C bond. It indicates that the β-diketones do not conjugate with benzoyl group of BTFA in the complex. The C-C bond lengths in the thienyl ring are very similar to those of the corresponding C-C bond distances in free thiophene. The average C-S bond distance is 1.720(5) Å, indicating some delocalization of the π-electrons. There are two toluene solvent molecules in the

crystal structure. One of the toluene molecules was disordered. The disorder in this molecule appeared to be due to a simple rotation so that the methyl group appeared bound to two different ring carbon atoms. The ethylene bridges of the EDOT moiety were also disordered about two conformations. Additionally, the fluorine atoms of two of the trifluoromethyl groups were disordered by rotation about the C-C bond.

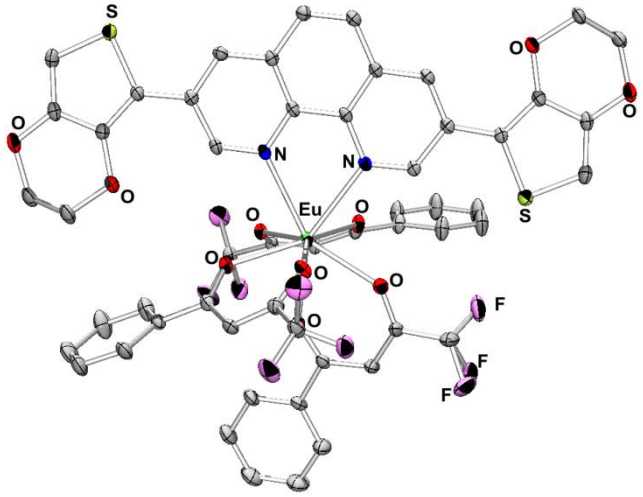

Figure 23. ORTEP diagram of **10** showing the labeling scheme of selected atoms at 30% probability level. Hydrogen atoms and solvent molecules are omitted for clarity.

Crystal Structure of [Eu(HFPD)$_3$L3]·0.5C$_7$H$_8$ (12)

There are two molecules and one toluene solvent molecule in the unit cell of the solid state structure of complex **12**. The molecular structure is shown in Figure 24. The Eu^{3+} ion is also eight-coordinate with the coordination sphere best described as a distorted dodecahedron. The Eu-O (2.368(7) – 2.426(5) Å) and Eu-N (2.549(7) and 2.569(7) Å) bond lengths follow the same trend as observed previously. The thienyl ring structure also indicates some delocalization of the π-electrons.

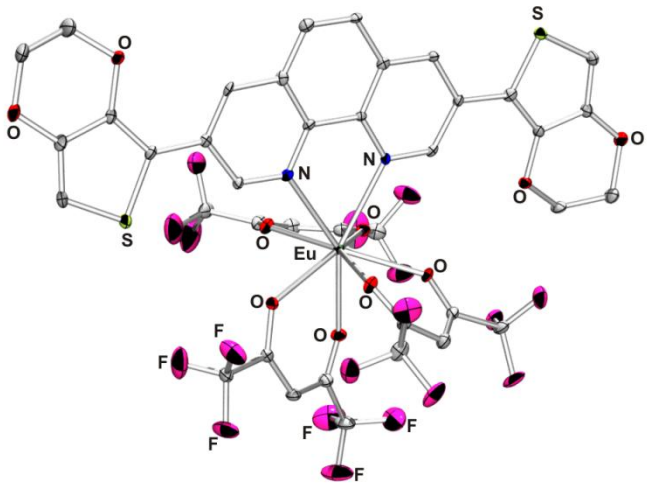

Figure 24. ORTEP diagram of **12** showing the labeling scheme of selected atoms at 25% probability level. Hydrogen atoms and solvent molecules are omitted for clarity.

UV-Vis Absorption Spectra

Absorption spectra of complexes **9** - **12** in dichloromethane at room temperature are presented in Figure 25. The absorption spectrum of **L3** displays a broad band with some vibronic structure from 325 to 400 nm (λ_{max} = 365), which is red shifted compared to Phen (λ_{max} = 290 nm) due to the extended conjugation. The UV absorption spectrum of DBM shows one π-π^* absorption peak at 350 nm.[31] The absorption spectrum of complex **9** shows one principal absorption peak at 350 nm with a molar absorption coefficient of 9.7×10^4 L mol^{-1} cm^{-1}. The ligand **L3** absorption is overlapped with the DBM absorption. The increased molar absorption coefficients of the complexes compared to the $Eu(DBM)_3(H_2O)_2$ precursor (6.9×10^4 L mol^{-1} cm^{-1}) indicate the complexation of the ligands to the metal center. The UV-Vis spectrum of complex **10** displays two main absorption bands assigned to the bound ligands BTFA and **L3**. The absorption band at 321 nm is assigned to the π-π^* transition of the conjugated system in BTFA, which is identical to the reported value.[32] Compared with free BTFA, a significant increase in

intensity of the corresponding band appears in the complex. The other absorption at 405 nm is attributed to the π-π^* transition of **L3**. The absorption spectra of complex **11** and **12** are also similar to complex **10**, containing features similar to those uncoordinated *β*-diketones and **L3**. The strong absorption at 341 and 287 nm for **11** and **12** are due to TTA and HFPD, respectively.

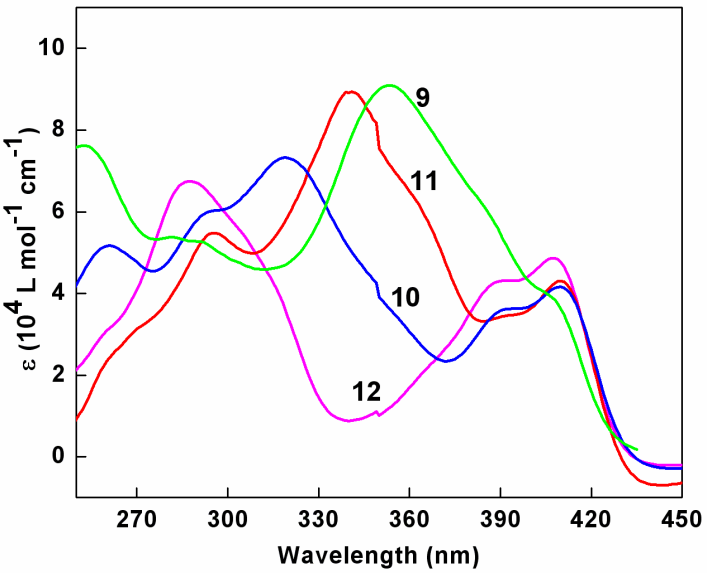

Figure 25. UV-Vis absorption spectra of complexes **9** - **12** in CH_2Cl_2 solution at RT.

Photoluminescence of Eu(β-diketonate)$_3$L3 Complexes

The normalized excitation spectrum of **9** in toluene at room temperature, obtained by monitoring the peak of the intense $^5D_0 \rightarrow {}^7F_2$ transition of the Eu^{3+} ion, shows features similar to the absorption spectrum of **9**. The room temperature normalized emission spectrum of **9** is shown in Figure 26. The emission spectrum of **9** displays a broad band centered at ca. 470 nm, derived from the coordinated ligand fluorescence, and characteristic Eu^{3+} ($^5D_0 \rightarrow {}^7F_J$, J = 0 - 4) transitions dominated by the transition from the $^7F_2$ sublevel at 610 nm. The symmetric forbidden emission $^5D_0 \rightarrow {}^7F_0$ at 576 nm can be

found in **9**. It is well known that the $^5D_0 \rightarrow {}^7F_0$ transition is strictly forbidden in a field of symmetry. Thus the above result reveals that Eu^{3+} in **9** occupies sites with low symmetry and without an inversion center. The $^5D_0 \rightarrow {}^7F_1$ transition is a magnetic dipole transition, and its intensity varies with the crystal field strength acting on Eu^{3+}. On the other hand the $^5D_0 \rightarrow {}^7F_2$ transition increases as the site symmetry of Eu^{3+} decreases. Therefore the intensity ratio of the $^5D_0 \rightarrow {}^7F_2$ transition to the $^5D_0 \rightarrow {}^7F_1$ transition is widely used as a measurement of the coordination state and the site symmetry of the rare earth elements.[23] For complex **9**, the intensity ratio $I(^5D_0 \rightarrow {}^7F_2) / I(^5D_0 \rightarrow {}^7F_1)$ is equal to ca. 10, which suggests the very low site symmetry of the Eu^{3+} in **9**.

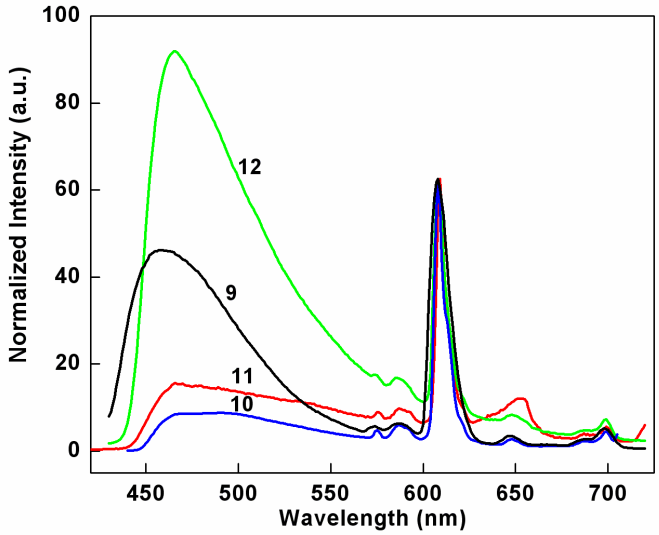

Figure 26. Emission spectra of complexes **9 - 12** in CH_2Cl_2 at RT.

For quantum yield measurements, the front face detection method was applied. A 10^{-3} M solution of complex **9** was prepared by dissolving the crystal sample of **9** in anhydrous CH_2Cl_2. The tris(dipicolinate) complex $[Eu(dpa)_3]^{3-}$ was prepared *in situ* by mixing appropriate amounts of Eu(III) and dpa in 0.1 M tris buffer (pH = 7.4). Quantum

yields Q have been calculated using the equation $Q_x/Q_r = A_x \cdot n_x^2 \cdot / A_r \cdot n_r^2$, where x refers to the sample, and r, to the reference; A is the integrated area under the emission spectrum, and n is the refractive index of the solution. $[Eu(dpa)_3^{3-}]$ in 0.1M Tris buffer (Φ = 13.5%) was used as a reference for the determination of lanthanide quantum yield. The ligand fluorescence quantum yields were determined using solutions of anthracene in ethanol as a standard reference (Φ = 28%). The overall luminescent quantum yields for the emissions from the Eu^{3+} ion and the coordinated ligand in toluene are 11.3% and 21.0%, respectively (λ_{ex} = 380 nm, room temperature). The emission spectra of complex **10**, **11** and **12** are very similar to complex **9** except that the ligand emission intensity varies with different β-diketones.

As shown in Table 1, complex **10** shows the highest Eu^{3+} emission quantum yield, while complex **12** shows the lowest Eu^{3+} quantum yield and highest liagnd emission quantum yield. The emission spectrum of the free ligand **L3** was measured at 77 K in a 2:2:1:1 mixture of ethyl iodide-ether-ethanol-toluene. We obtained the triplet excited state energy level of the ligand of 17 400 cm^{-1} which is slightly above the 4*f* resonance level of Eu^{3+} (17 250 cm^{-1}). In this way, the ligand **L3** is not a good sensitizer for lanthanide emission due to facile back energy transfer. The β-diketones play the role of antenna to excite the lanthanide. Having the β-diketones present in the complex has several advantages. First of all, the ligands shield the europium ions from residual water molecules. Secondly, the ligands help to absorb the excitation energy and to transfer it to

Table 1. The quantum yield of complexes **9** - **12** in CH_2Cl_2 at RT.

QY(%)	**9**	**10**	**11**	**12**
Eu(III)	11.3	27.4	25.2	8.1
Ligand	21	12.6	14.2	23.8

the europium ion. Indeed, it is well-known that the *f–f* transitions of the lanthanides are very weak and in order to obtain a good luminescent material one has to take advantage of the strong absorbing capacity of organic ligands with π-electrons, and the possibility of transferring the excitation energy from the triplet excited states of the ligands to the lower energy levels of the $4f^n$ configuration of the lanthanide ion. The four different *β*-diketones that we chose have the triplet excited energy level sequence of HFPD (22 200 cm^{-1}), TTA (20 400 cm^{-1}), BTFA (21 400 cm^{-1}), and DBM (19 100 cm^{-1}). The energy gap between triplet excited state of HFPD and 4*f* resonance level of Eu^{3+} is too high while the gap between triplet excited state of DBM and 4*f* resonance level of Eu^{3+} is too low. Theoretically, TTA and BTFA should be the better antennas, which is in accord with what we observed (Table 1).

Electrochemical Studies

3,4-(Ethylenedioxy)thiophene can be electrochemically polymerized at relatively low applied voltages. For the design of the ligand, the phenanthroline is incorporated directly into the polymer backbone. The 3,4-(ethylenedioxy)thiophene residues were chosen to allow the polymer synthesis by electrochemical oxidation. Cyclic voltammetry of **9** over a window between -1.25 and +1.25 V versus Fc/Fc^+ at a scan rate of 100 mV/s resulted in the growth of a polymer film that has a reversible wave with $E_{1/2}$ = -0.55 V. The first scan exhibits two oxidative peaks at ~0.4 and 1.0 V whose positions steadily become more positive with increasing scans (Figure 27). As shown in Figure 27, the maximum peak current of an electrode-confined film of poly-**9** in pure electrolyte solution varies linearly with the rate of the electrochemical scan up to 500 mV/s. This behavior is indicative of a strongly adsorbed electroactive thin film which is not limited by the ionic flux of counter anions.

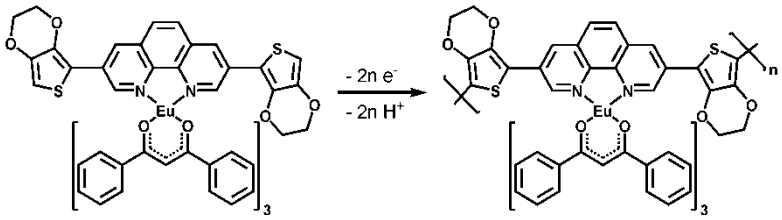

Scheme 3. Electrochemical polymerization of Europium-containing monomer to conducting metallopolymer.

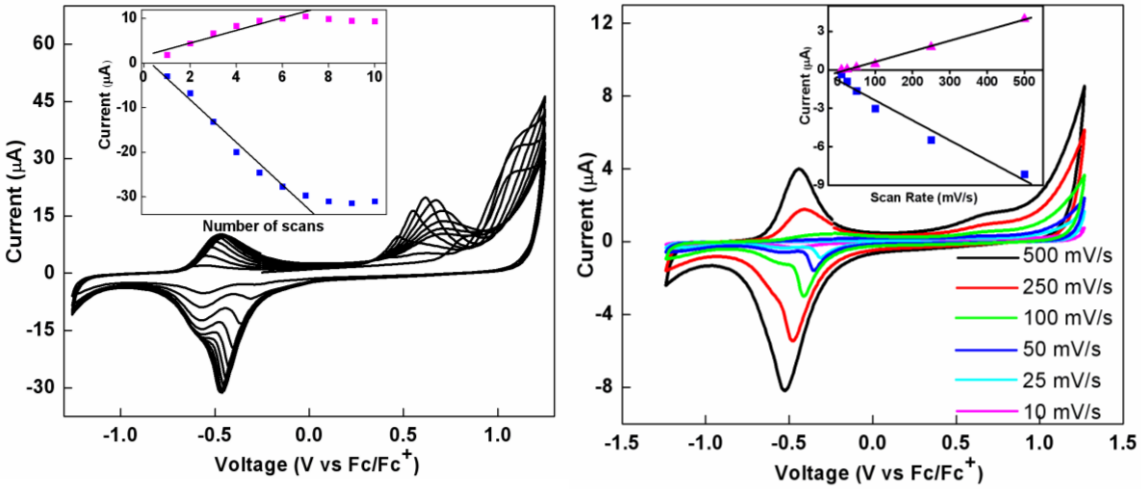

Figure 27. Left: 10 successive cyclic voltammograms of a 0.1 mM CH_2Cl_2 solution of **9**, 0.1 M $TBAPF_6$, Pt electrode. Inset, the maximum peak current versus the number of scans. Right: Electrochemical scan rate dependence of poly-**9** (Fc/Fc^+ is the redox couple of ferrocene). Inset: plot of linear current increase vs scan rate.

The XPS data were used to determine the film composition and metal coordination environment. The Eu $3d_{3/2}$ and Eu $3d_{5/2}$ peaks are observed at 1165.2 and 1135.2 eV, respectively, corresponding well to the expected values for Eu^{3+} bound to oxygen.[33] The S 2*p* peak is also found at 164.3 eV. Quantitative XPS analysis reveals that the film has an atomic ratio of Eu : S = 1 : 1.91, which is in agreement with the stoichiometric molar ratio of the monomer (1 : 2.03 by XPS) and proposed film structure

(1 : 2). The electrochemistry of complexes **10**, **11** and **12** is similar to complex **9**, and not affected by the ancillary *β*-diketones.

Quantitative XPS analysis reveals that the resulting films has an atomic ratio of Eu : S = 1 : 1.86 for **10**, and 1 : 1.87 for **11**, respectively. Corresponding polymers were prepared on ITO coated glass for the further luminescent studies.

Photoluminescence of Metallopolymers

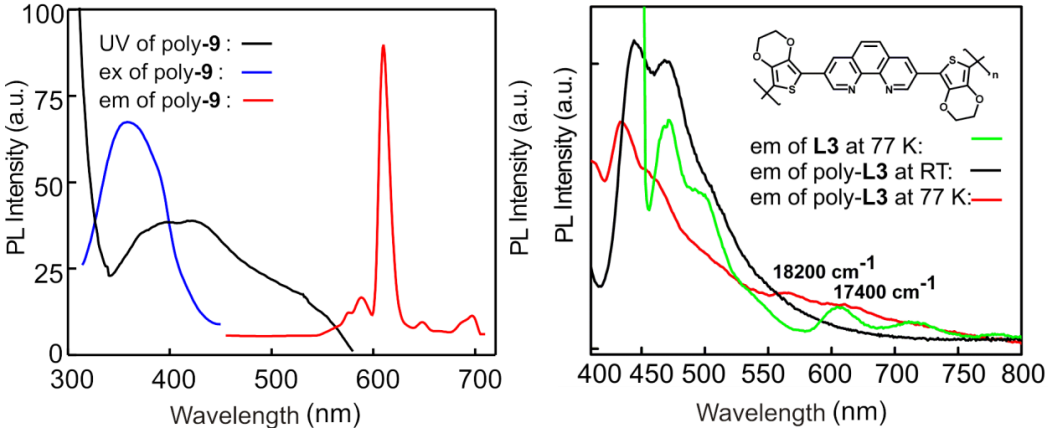

Figure 28. Left: UV-Vis absorption, excitation and emission spectra of poly-**9**. Right: Emission spectra of **L3** and poly-**L3**.

The emission spectrum of poly-**9** measured with 375 nm as the excitation wavelength is characteristic of Eu^{3+} emission as shown in Figure 28. The five expected transitions of the $^5D_0 \rightarrow {}^7F_J$ manifold are well resolved and the hypersensitive $^5D_0 \rightarrow {}^7F_2$ transition dominates the spectrum. This is indicative of a low symmetry coordination environment around the Eu^{3+}. Most notably, poly-**9**, shows exclusively the Eu^{3+} centered $^5D_0 \rightarrow {}^7F_J$ emission bands and the ligand emission from the organic backbone completely disappears, presumably indicating more efficient energy transfer. The excitation spectrum of poly-**9** is less broad and blue-shifted relative to the absorption spectrum suggesting

that the energy transfer takes place from a localized excited state. This is consistent with energy transfer from the Phen portion of the polymer backbone to the Eu^{3+}.

The more efficient energy transfer from the polymer backbone to the Eu^{3+} ion in poly-**9** can be explained by the blue shifting of the organic polymer backbone (Figure 28). The emission spectra of poly-**L3** were measured at room temperature and 77 K. The phosphorescence peak of poly-**L3** was blue shifted than that of the free ligand **L3** at 77 K, which leads to a higher triplet excited state energy level for the polymer backbone (18 200 cm^{-1}) than the free ligand (17 400 cm^{-1}). This blue shifting might be explained by the twist between the 3,4-(ethylenedioxy)thiophene and 1,10-phenanthroline in the polymer form. Such an increase of 800 cm^{-1} triplet excited state energy made the energy transfer from the polymer backbone to the 4*f* resonance level of Eu^{3+} more efficient. Similar emission properties were observed for poly-**10** and poly-**11**. However, we did not observe any emission for poly-**12**.

CONCLUSION

Three new series of lanthanide(III)-*β*-diketonate complexes (Ln = Sm, Eu, Tb, and Dy) with thiophene and 3,4-(ethylenedioxy)thiophene functionalized bidentate nitrogen donors (**L1** – **L3**) have been synthesized. The X-ray diffraction analyses and NMR studies of lanthanide complexes with these 2,2'-bipyridine and 1,10-phenanthroline derivatives end-capped with thiophene and 3,4-(ethylenedioxy)thiophene moieties are first investigated. In $Ln(DBM)_3$**L1** complexes, all the lanthanide centers are eight-coordinate with a slightly distorted square antiprism coordination sphere, while in $Ln(DBM)_3$**L2** complexes, the eight-coordinate Ln^{3+} ion adopts a dodecahedron coordination geometry. The photophysical studies show that the introduction of thiophene substituent drastically shifts the triplet excited state energy of the bpy and phen

ligands toward lower energies, resulting in a poor sensitization of Sm^{3+} and Tb^{3+} in these complexes, but allows an efficient energy transfer to Eu^{3+} in complex **6**. After coordination of **L1** and **L2** to $Ln(DBM)_3(H_2O)_2$ monomers, the complexes can not be electrochemically polymerized. Reasoning that extended thiophene units will reduce the potential at which the complexes oxidize and will stabilize the cation radicals, which are intermediates in the polymerization of thiophenes.

A further modification of thiophene substituent to 3,4-(ethylenedioxy)thiophene yields ligand 3,8-bis(3,4-(ethylenedioxy)thien-2-yl)-1,10-phenanthroline (**L3**). We focused on 1,10-phenanthroline as the metal binding moiety based on the information that 3,8-bis(thiophen-2',2''-yl)-1,10-phenanthroline (**L2**) is a better antenna for Eu^{3+} emission than 5,5'-bis(thiophen-2',2''-yl)-2,2'-bipyridine (**L1**). Four lanthanide(III)-*β*-diketonate complexes (**9 - 12**) with **L3** have been synthesized. All the lanthanide centers are eight-coordinate. The photophysical studies show that the introduction of 3,4-(ethylenedioxy)thiophene substituent drastically shifts the triplet excited state energy of the phen ligand toward lower energy. However, the choice of different diketonates efficiently sensitizes the Eu(III) emission. The complexes can be electrochemically polymerized. The resulting polymers show the pure metal-based photoluminescence via stimulated excitation, which provide promising candidates for the light emitting materials.

REFERENCES

1. Yang, L.; Gong, Z.; Nie, D.; Lou, B.; Bian, Z.; Guan, M.; Huang, C.; Lee, H. J.; Baik, W. P. *New J. Chem.* **2006**, *30*, 791.
2. *Handbook on the Physics and Chemistry of Rare Earths*; Binnemans, K., Ed.; Elsevier: Amsterdam, 2005.
3. Bellusci, A.; Barberio, G.; Crispini, A.; Ghedini, M.; Deda, M.; Pucci, D. *Inorg. Chem.* **2005**, *44*, 1818.
4. Biju, S.; Ambili Raj, D. B.; Reddy, M. L. P.; Kariuki, B. M. *Inorg. Chem.* **2006**, *45*, 10651.
5. Guan, M.; Bian, Z. Q.; Li, F. Y.; Xin, H.; Huang, C. H. *New J. Chem.* **2003**, *27*, 1731.
6. McGehee, M. D.; Bergstedt, T.; Zhang, C.; Saab, A. P.; O'Regan, M. B.; Bazan, G. C.; Srdanov, V. I.; Heeger, A. J. *Adv. Mater.* **1999**, *11*, 1349.
7. Robinson, M. R.; Ostrowski, J. C.; Bazan, G. C.; McGehee, M. D. *Adv. Mater.* **2003**, *15*, 1547.
8. Kalinowski, J.; Stampor, W.; Cocchi, M.; Virgili, D.; Fattori, V. *Appl. Phys. Lett.* **2005**, *86*, 241106.
9. Bai, X. L.; Liu, X. D.; Wang, M.; Kang, C. Q.; Gao, L. X. *Synthesis* **2005**, *3*, 458.
10. Saitoh, Y.; Koizumi, T.; Osakada, K.; Yamamoto, T. *Can. J. Chem.* **1997**, *75*, 1336.
11. Zhu, S. S.; Swager, T. M. J. *Am. Chem. Soc.* **1997**, *119*, 12568.
12. *Methods in Enzymology, 276*: *Macromolecular Crystallography, part A*; Carter, C. W., Jr.; Sweets, R. M., Eds.; 1997.
13. Altomare, A.; Burla, M. C.; Camalli, M.; Cascarano, G. L.; Giacovazzo, C.; Guagliardi, A.; Moliterni, A. G. G.; Polidori, G.; Spagna, R. *J. Appl. Cryst.* **1999**, *32*, 115.
14. Sheldrick, G. M. (**1994**) SHELXL97. Program *for the Refinement of Crystal Structures.* University of Gottingen, Germany.
15. Spek, A. L. (**1998**). *PLATON, A Multipurpose Crystallographic Tool.* Utrecht University, The Netherlands.
16. Farrugia, L. J. *J. Appl. Cryst.* **1999**, *32*. 837.
17. Charles, R. G.; Perrotto, A. *J. Inorg. Nucl. Chem.* **1964**, *26*, 373.
18. Wang, M.; Jin, L.; Liu, S.; Cai, G.; Huang, J.; Qin, W.; Huang, S. *Gaodeng Xuexiao Huaxue Xuebao* **1993**, *14*, 305.
19. Angelici, R. J. *Coord. Chem. Rev.* **1990**, *105*, 61.
20. *The Chemistry of the Lanthanides*; Moeller, T., Ed.; Pergamon Press, Oxford, 1973.
21. Araki, K.; Endo, H.; Masuda, G.; Ogawa, T. *Chem. Eur. J.* **2004**, *10*, 3331.
22. Jang, H.; Shin, C. H.; Jung, B. J.; Kim, D.; Shim, H. K.; Do, Y. *Eur. J. Inorg. Chem.* **2006**, 718.
23. Xu, Q. H.; Li, L. S.; Liu, X. S.; Xu, R. R. *Chem. Mater.* **2002**, *14*, 549.
24. Kido, J.; Okamot, Y. *Chem. Rev.* **2002**, *102*, 2357 and references therein.
25. Sato, S.; Wada, M. *Bull. Chem. Soc. Jpn*. **1970**, *43*, 1955.
26. Crosby, G. A.; Whan, R. E.; Alire, R. M. *J. Chem. Phys.* **1961**, *34*, 743.
27. Touillon, G.; Garnier, F. *J. Electroanal. Chem*. **1982**, *135*, 173.

28. Kaneto, K.; Kohno, Y.; Yoshino, K.; Inuishi, Y. *J. Chem. Soc. Chem. Commun.* **1983**, 382.
29. Roncali, J. *Chem. Rev.* **1992**, *92*, 711 and references therein.
30. Ahmed, M. O.; Liao, J. L.; Chen, X.; Chen, S. A.; Kaldis, J. H. *Acta Crystallogr.* **2003**, *E59*, m29.
31. Jang, H.; Shin, C. H.; Jung, B. J.; Kim, D.; Shim, H. K.; Do, Y. *Eur. J. Inorg. Chem.* **2006**, 718.
32. Guo, Q. L.; Zhu, W. X.; Guo, R.; Yan, X.; Wang, R. J. *Chin. J. Chem.* **2003**, *21*, 211.
33. Mercier, F.; Alliot, C.; Bion, L.; Thromat, N.; Toulhoat, P. J. *Electron Spec. Relat. Phenom.* **2006**, *150*, 21.

CRYSTALLOGRAPHIC DATA

Table 2. Crystal data and structure refinement for **2** and **3**.

	2	**3**
formula	$C_{69}H_{51}EuN_2O_6S_2$	$C_{69}H_{51}N_2O_6S_2Tb$
fw	1220.20	1227.16
T (K)	153(2)	153(2)
crystal system	Monoclinic	Monoclinic
space group	$P2_1/n$	$P2_1/n$
a (Å)	13.3826(1)	13.3888(1)
b (Å)	15.2389(1)	15.2171(2)
c (Å)	28.3442(3)	28.2634(3)
β (deg)	97.307(1)	97.161(1)
V (Å^3)	5733.46(8)	5713.43(11)
Z	4	4
ρ (g/cm^3)	1.414	1.427
μ (mm^{-1})	1.223	1.367
F(000)	2488	2496
crystal size (mm)	0.22 × 0.17 × 0.08	0.27 × 0.24 × 0.15
θ (deg)	1.97 to 27.48	1.97 to 27.47
Index ranges	-17 ≤ h ≤ 16	-17 ≤ h ≤ 16
	-19 ≤ k ≤ 19	-19 ≤ k ≤ 19
	-36 ≤ l ≤ 36	-30 ≤ l ≤ 36
Reflns collected	54768	41025
Independent reflns	13105, R_{int} = 0.0485	12823, R_{int} = 0.0722
Absorption correction	Gaussian	Gaussian
Max. and min. transmission	0.915 and 0.831	0.820 and 0.723
GOF on F^2	1.084	0.993
R_1, R_2 [I > 2σ (I)]	0.0349, 0.0770	0.0375, 0.0935
R_1, R_2 (all data)	0.0552, 0.0841	0.0556, 0.1044
Largest diff. peak and hole (e·Å^{-3})	1.268 and -0.799	1.271 and -1.927

Table 3. Selected bond lengths [Å] and angles [°] for **2**.

Bond distances (Å)			
Eu1-O2C	2.3122(17)	Eu1-N2	2.601(2)
Eu1-O1B	2.3408(18)	Eu1-N1	2.640(2)
Eu1-O2A	2.3474(18)	S1-C14	1.718(4)
Eu1-O2B	2.3515(18)	C12-C13	1.358(7)
Eu1-O1A	2.3545(19)	S2-C18	1.698(3)
Eu1-O1C	2.3592(18)	S2-C15	1.709(3)
N1-C5	1.345(3)	N1-C1	1.341(3)
Bond angles (°)			
O2C-Eu1-O1B	144.17(7)	O2A-Eu1-O1C	77.63(6)
O2C-Eu1-O2A	118.82(7)	O2B-Eu1-O1C	137.04(6)
O1B-Eu1-O2A	79.84(6)	O1A-Eu1-O1C	118.67(7)
O2C-Eu1-O2B	79.03(6)	O2C-Eu1-N2	138.00(7)
O1B-Eu1-O2B	70.95(6)	O1B-Eu1-N2	71.84(7)
O2A-Eu1-O2B	145.14(7)	O2A-Eu1-N2	79.45(7)
O2C-Eu1-O1A	77.89(6)	O2B-Eu1-N2	107.95(7)
O1B-Eu1-O1A	79.76(7)	O1A-Eu1-N2	143.05(7)
O2A-Eu1-O1A	72.57(7)	O1C-Eu1-N2	76.87(7)
O2B-Eu1-O1A	83.68(7)	O2C-Eu1-N1	83.07(7)
O2C-Eu1-O1C	71.66(6)	O1B-Eu1-N1	104.75(7)
O1B-Eu1-O1C	144.16(6)	O2A-Eu1-N1	136.14(7)

Table 4. Selected bond lengths [Å] and angles [°] for **3**.

Bond distances (Å)			
Tb1-O2C	2.287(2)	Tb1-N1	2.611(2)
Tb1-O1B	2.316(2)	S1-C14	1.694(5)
Tb1-O1A	2.325(2)	S1-C11	1.742(5)
Tb1-O2A	2.325(2)	C11-C12	1.443(12)
Tb1-O1C	2.330(2)	C11-C2	1.474(5)
Tb1-O2B	2.330(2)	S2-C18	1.706(4)
Tb1-N2	2.575(3)	S2-C15	1.711(4)
Bond angles (º)			
O2C-Tb1-O1B	144.12(7)	O1B-Tb1-O2B	71.59(7)
O2C-Tb1-O1A	77.39(8)	O1A-Tb1-O2B	82.76(8)
O1B-Tb1-O1A	79.52(8)	O2A-Tb1-O2B	145.43(8)
O2C-Tb1-O2A	118.62(8)	O1C-Tb1-O2B	137.45(7)
O1B-Tb1-O2A	79.67(8)	O2C-Tb1-N2	138.42(8)
O1A-Tb1-O2A	73.32(8)	O1B-Tb1-N2	71.86(8)
O2C-Tb1-O1C	72.39(7)	O1A-Tb1-N2	143.17(8)
O1B-Tb1-O1C	143.44(7)	O2A-Tb1-N2	79.06(8)
O1A-Tb1-O1C	119.09(8)	O1C-Tb1-N2	76.40(8)
O2A-Tb1-O1C	76.89(7)	O2B-Tb1-N2	108.72(8)
O2C-Tb1-O2B	78.54(8)	O2C-Tb1-N1	82.86(8)

Table 5. Crystal data and structure refinement for **6**.

formula	$C_{73.75}H_{55}EuN_2O_6S_2$
fw	1281.28
T (K)	153(2)
crystal system	Monoclinic
space group	$P2_1/n$
a (Å)	18.080(4)
b (Å)	15.309(3)
c (Å)	23.235(5)
β (deg)	111.45(3)
V (Å^3)	5986(2)
Z	4
ρ (g/cm^3)	1.422
μ (mm^{-1})	1.175
F(000)	2618
crystal size (mm)	0.25 × 0.22 × 0.15
θ (deg)	2.92 to 27.55
Index ranges	-22 ≤ h ≤ 23
	-19 ≤ k ≤ 17
	-30 ≤ l ≤ 30
Reflns collected	25216
Independent reflns	13729, R_{int} = 0.0357
Absorption correction	Gaussian
Max. and min. transmission	0.6788 and 0.7852
GOF on F^2	1.021
R_1, R_2 [I > 2σ (I)]	0.0534, 0.1409
R_1, R_2 (all data)	0.0773, 0.1559
Largest diff. peak and hole (e·Å^{-3})	2.371 and -1.565

Table 6. Selected bond lengths [Å] and angles [°] for **6**.

Bond distances (Å)			
Eu1-O2	2.337(3)	Eu1-O1B	2.353(3)
Eu1-O2A	2.356(3)	Eu1-O1A	2.361(3)
Eu1-O1	2.379(3)	Eu1-O2B	2.392(3)
Eu1-N2	2.634(4)	Eu1-N1	2.643(4)
S1-C1	1.673(8)	S1-C4	1.685(5)
Eu1-O2	2.337(3)	S2-C20	1.648(6)
Eu1-O2A	2.356(3)	N1-C9	1.303(6)
Bond angles (º)			
O2-Eu1-O1B	81.08(12)	O2-Eu1-O2A	87.19(12)
O1B-Eu1-O2A	144.60(11)	O2-Eu1-O1A	77.85(12
O1B-Eu1-O1A	74.16(11)	O2A-Eu1-O1A	70.74(11)
O2-Eu1-O1	71.97(11)	O1B-Eu1-O1	130.19(11)
O2A-Eu1-O1	75.78(11)	O1A-Eu1-O1	135.49(11)
O2-Eu1-O2B	105.78(12)	O1B-Eu1-O2B	71.39(11)
O2A-Eu1-O2B	143.97(11)	O1A-Eu1-O2B	144.20(11)
O1-Eu1-O2B	76.68(11)	O2-Eu1-N2	149.14(12)
O1B-Eu1-N2	77.82(12)	O2A-Eu1-N2	97.14(12)
O1A-Eu1-N2	74.89(12)	O1-Eu1-N2	138.74(12)

Table 7. Crystal data and structure refinements for complex **9**.

formula	$C_{69}H_{49}EuN_2O_{10}S_2$
fw	1282.18
T (K)	153(2)
crystal system	Monoclinic
space group	$P2_1/c$
a (Å)	19.447(4)
b (Å)	16.846(3)
c (Å)	18.629(4)
β (deg)	110.58(3)
V (Å^3)	5713(2)
Z	4
ρ (g/cm^3)	1.491
μ (mm^{-1})	1.236
F(000)	2608
crystal size (mm)	0.12 × 0.15 × 0.16
θ (deg)	2.92 to 27.50
Index ranges	$-25 \le h \le 25$
	$-21 \le k \le 21$
	$-24 \le l \le 24$
Absorption correction	Gaussian
Max. and min. transmission	0.816 and 0.853
GOF on F^2	1.042
R_1, R_2 [I > 2σ (I)]	0.0487, 0.1099
R_1, R_2 (all data)	0.1145, 0.1401
Largest diff. peak and hole (e·Å^{-3})	0.884 and -0.920

Table 8. Selected bond lengths [Å] and angles [°] of **9**.

Bond distances (Å)			
Eu1-O5	2.345(3)	Eu1-O5A	2.318(3)
Eu1-O6	2.322(3)	Eu1-O6B	2.345(3)
Eu1-O5B	2.303(3)	Eu1-O6A	2.345(3)
Eu1-N1	2.561(4)	Eu1-N2	2.593(4)
S1-C1	1.704(7)	S1-C6	1.708(5)
S2-C19	1.689(5)	S2-C24	1.719(5)
N1-C11	1.325(6)	N1-C10	1.358(6)
N2-C17	1.325(6)	N2-C18	1.350(5)
Bond angles (º)			
O5B-Eu1-O5A	83.98(11)	O5B-Eu1-O6	77.00(11)
O5A-Eu1-O6	76.40(12)	O5B-Eu1-O6B	73.60(11)
O5A-Eu1-O6B	145.74(11)	O6-Eu1-O6B	121.47(11)
O5B-Eu1-O5	113.75(11)	O5A-Eu1-O5	138.15(11)
O6-Eu1-O5	71.79(11)	O6B-Eu1-O5	75.63(12)
O5B-Eu1-O6A	78.52(11)	O5A-Eu1-O6A	72.28(11)
O6-Eu1-O6A	141.83(11)	O6B-Eu1-O6A	78.01(11)
O5-Eu1-O6A	145.81(12)	O5B-Eu1-N1	146.89(12)
O6A-Eu1-N1	76.94(12)	O5B-Eu1-N2	147.52(12)

Table 9. Crystal data and structure refinement for **10**.

formula	$C_{68}H_{50}EuF_9N_2O_{10}S_2$		
fw	1442.18		
T (K)	153(2)		
crystal system	Triclinic		
space group	P-1		
a (Å)	11.9120(2)	α (deg)	91.0520(8)
b (Å)	16.2920(4)	β (deg)	106.8070(9)
c (Å)	17.7970(6)	γ (deg)	108.6930(13)
V (Å^3)	3108.35(14)		
Z	2		
ρ (g/cm^3)	1.541		
μ (mm^{-1})	1.165		
F(000)	1456		
crystal size (mm)	0.31 × 0.04 × 0.03		
θ (deg)	1.90 to 27.45		
Index ranges	$-15 \le h \le 12$		
	$-20 \le k \le 21$		
	$-16 \le l \le 23$		
Absorption correction	Semi-empirical from equivalents		
Max. and min. transmission	0.966 and 0.899		
GOF on F^2	1.021		
R_1, R_2 [$I > 2\sigma(I)$]	0.0544, 0.0902		
R_1, R_2 (all data)	0.1060, 0.1078		
Largest diff. peak and hole (e·Å^{-3})	0.673 and -0.857		

Table 10. Selected bond lengths [Å] and angles [°] of **10**.

Bond distances (Å)			
Eu1-O1A	2.356(3)	Eu1-N1	2.604(4)
Eu1-O2C	2.365(3)	S1-C18	1.714(5)
Eu1-O1C	2.367(3)	S1-C13	1.727(5)
Eu1-O2A	2.375(3)	S2-C24	1.717(5)
Eu1-O1B	2.370(3)	S2-C19	1.723(5)
Eu1-O2B	2.376(3)	O1-C14	1.368(6)
Eu1-N2	2.600(4)	O1-C15	1.474(6)
N1-C1	1.330(5)	O1-C15A	1.475(8)
Bond angles (º)			
O1A-Eu1-O2C	74.68(12)	O1A-Eu1-N2	148.60(11)
O1A-Eu1-O1C	87.59(12)	O2C-Eu1-N2	119.86(12)
O2C-Eu1-O1C	71.61(10)	O1C-Eu1-N2	73.14(11)
O1A-Eu1-O2A	71.17(11)	O2A-Eu1-N2	79.37(12)
O2C-Eu1-O2A	130.75(12)	O1B-Eu1-N2	135.48(11)
O1C-Eu1-O2A	72.53(12)	O2B-Eu1-N2	89.87(11)
O1A-Eu1-O1B	73.84(11)	O1A-Eu1-N1	147.28(11)
O2C-Eu1-O1B	72.11(11)	O2C-Eu1-N1	83.66(11)
O1C-Eu1-O1B	142.45(11)	O1C-Eu1-N1	108.72(11)

Table 11. Crystal data and structure refinement for **12**.

formula	$C_{85}H_{46}Eu_2F_{36}N_4O_{20}S_4$		
fw	2559.42		
T (K)	153(2)		
crystal system	Triclinic		
space group	P-1		
a (Å)	12.420(3)	α (deg)	110.05(3)
b (Å)	12.636(3)	β (deg)	92.02(3)
c (Å)	15.702(3)	γ (deg)	93.67(3)
V (Å^3)	2305.8(8)		
Z	1		
ρ (g/cm^3)	1.843		
μ (mm^{-1})	1.584		
F(000)	1258		
crystal size (mm)	0.26 × 0.22 × 0.16		
θ (deg)	1.65 to 25.00		
Index ranges	$-14 \le h \le 14$		
	$-14 \le k \le 15$		
	$-18 \le l \le 18$		
Absorption correction	Gaussian		
Max. and min. transmission	0.7213 and 0.8320		
GOF on F^2	1.163		
R_1, R_2 [I > 2σ (I)]	0.0336, 0.0918		
R_1, R_2 (all data)	0.0395, 0.1132		
Largest diff. peak and hole (e·Å^{-3})	1.318 , -1.052		

Table 12. Selected bond lengths [Å] and angles [°] of **12**.

Bond distances (Å)			
Eu1-O5B	2.368(7)	Eu1-O5	2.373(5)
Eu1-O6	2.388(5)	Eu1-O6A	2.403(5)
Eu1-O6B	2.403(5)	Eu1-O5A	2.426(5)
Eu1-N2	2.549(7)	Eu1-N1	2.569(7)
Eu2-O6D	2.349(6)	Eu2-O6C	2.378(5)
Eu2-O5E	2.388(5)	Eu2-O6E	2.395(5)
Eu2-O5C	2.399(5)	Eu2-O5D	2.413(5)
Bond angles (º)			
O5B-Eu1-O5	78.0(2)	O5B-Eu1-O6	89.5(2)
O5-Eu1-O6	70.73(19)	O5B-Eu1-O6A	92.4(2)
O5-Eu1-O6A	142.81(17)	O6-Eu1-O6A	145.84(19)
O5B-Eu1-O6B	71.55(19)	O5-Eu1-O6B	136.01(18)
O6-Eu1-O6B	78.0(2)	O6A-Eu1-O6B	70.42(18)
O5B-Eu1-O5A	74.2(2)	O5-Eu1-O5A	73.34(19)
O6-Eu1-O5A	142.9(2)	O6A-Eu1-O5A	69.47(18)
O6B-Eu1-O5A	124.99(18)	O5B-Eu1-N2	147.8(2)
O5-Eu1-N2	80.02(19)	O6-Eu1-N2	105.0(2)

Chapter 3: Synthesis and Characterization of Near Infrared Emitting Lanthanide Containing Conducting Metallopolymers

INTRODUCTION

In recent decades, lanthanide-based near infrared (NIR) luminescence is attracting considerable interest in the fields of telecommunication,[1] associated lasers and LED/OLED devices,[2-4] as well as in solar energy conversion,[5,6] and bio-sciences.[7-9] The spectral range of the NIR formally encompasses from 750 nm to 2500 nm. Several trivalent visible emitting lanthanide ions also have transitions in this range, e.g. Sm^{3+} and Eu^{3+}. However, in this chapter we focus on the NIR emitting lanthanide ions mainly emitting in the NIR spectral domain, Nd^{3+}, Er^{3+} and Yb^{3+}.

The absorption spectrum of the Nd^{3+} ion displays *f-f* transition with sizeable intensity (up to $\varepsilon \approx 10 - 12\ M^{-1}cm^{-1}$) which is much higher than other lanthanide ions. The main fluorescence line of Nd^{3+} at 1.06 μm is the well known transition used in Nd : YAG (Yttrium Aluminum Garnet) lasers. This makes Nd^{3+} containing systems the most popular NIR luminescent materials for application in laser systems. The emission of Er^{3+} is both in the visible and NIR, and is the candidate of choice for telecommunications with its 1.53–1.54 μm emission line. Yb^{3+} emits at about 1 μm and is less sensitive to non-radiative deactivation in view of the large energy gap between the emitting ($^2F_{5/2}$) and ground ($^2F_{7/2}$) levels. This lanthanide ion is capturing much attention with respect to bio-applications. The relative transparency of human body tissue at ca. 1 μm suggests that *in vivo* luminescent probes of Yb^{3+} could have diagnostic value.

Our research interests are focused on the NIR lanthanide containing conducting metallopolymers as the emissive materials in polymer light-emitting diodes (PLEDs). Since the initial discovery of PLEDs, substantial developments have occurred that have led to a fundamental understanding of their operation as well as the development of

practical devices.[10,11] Although most previous investigations have focused on PLEDs emitting in the visible region, there is considerable potential for PLEDs emitting in the near infrared and infrared spectral regions.

The extension of polymer light emitting materials into the technologically important NIR region is more difficult because organic molecules usually emit only at wavelengths shorter than 1000 nm. Attempts have been made to extend organic-based light emission beyond 1000 nm by using lanthanide complexes.[12] Lanthanide ions, such as Nd^{3+}, Er^{3+}, and Yb^{3+} are known NIR emitters with excellent luminescent properties due to the characteristic *f-f* transitions, which include lifetimes in the microsecond domain and narrow, ion-specific emission in the 900 - 1600 region with pure color and potentially high efficiency. Previously, the NIR PLEDs have been prepared using blends of conjugated polymers with lanthanide chelates by vacuum deposition.[13-17] However, blending may not always give rise to uniformly dispersed and thermodynamically stable compositions. A more effective approach involves the covalent coupling of a lanthanide complex to a polymer backbone,[18-20] which rules out phase separation or aggregation during device processing/operation. Unfortunately, up to now no examples of lanthanide ions covalently incorporated into polymers for NIR emission have been reported.

From the previous study of visible lanthanide containing metallopolymers, we obtained the information that the energy can be transferred from the organic polymers to the lanthanide center. Herein we will discuss the synthesis of the well-defined conducting metallopolymers that incorporate Nd^{3+}, Er^{3+} and Yb^{3+} complexes in an inner sphere fashion. Three ligands based on the 1,10-phenanthroline (Phen) moiety serve as a metal binding group and different polymerizable groups of thiophene derivatives were prepared: 3,8-bis(thiophen-2',2''-yl)-1,10-phenanthroline (**L2**), 3,8-bis(3,4-(ethylenedioxy)thien-2-yl)-1,10-phenanthroline (**L3**), and 3,8-bis(2,2'-bithienyl-5-yl)-

1,10-phenanthroline (**L4**). The molecular structure, electropolymerization and photoluminescence of the complexes and corresponding metallopolymers have been investigated.

EXPERIMENTAL

General Methods

Air- and moisture-sensitive reactions were carried out in oven-dried glassware using standard Schlenk techniques under an inert atmosphere of dry argon. Dry DMF was used from EMD as sure-seal bottles. Bromine was obtained from EMD. 1,10-Phenanthroline and tri-*n*-butyltin chloride were purchased from Alfa Aesar. Trans-dichlorobis(triphenylphosphine)palladium(II) was obtained from STREM. THF was dried by conventional method and distilled under argon. CH_2Cl_2 was dried using a double-column anhydrous solvent system (Innovative Technologies, Newburyport, MA) and further degassed via nitrogen purge prior to use. 3,8-Dibromo-1,10-phenanthroline was prepared according to a published procedure.[21] 5-(Tributylstannyl)-2,2'-bithiophene was prepared by Swager's method.[22] 3,8-Bis(2,2'-bithienyl-5-yl)-1,10-phenanthroline (**L3**) was prepared by literature procedures.[23]

Low-res mass spectrometry was carried out by Thermo Finngan TSQ 700. Elemental analysis was performed by QTI, Whitehouse, NJ (www.qtionline.com). X-ray photoelectron spectroscopy (XPS) was carried out on a PHI 5700 XPS system equipped with a dual Mg X-ray source and monochromatic Al X-ray source complete with depth profile and angle-resolved capabilities.

Crystal Structure Determination

Suitable crystals were mounted on a glass fiber and placed in the low-temperature nitrogen stream. The data were collected on a Nonius Kappa CCD diffractometer using a

graphite monochromator with MoKα radiation (λ = 0.71073Å). Data reduction was performed using DENZO-SMN.[24] The structure was solved by direct methods using SIR97[25] and refined by full-matrix least-squares on F2 with anisotropic displacement parameters for the non-H atoms using SHELXL-97.[26] The hydrogen atoms on carbon were calculated in ideal positions with isotropic displacement parameters set to 1.2 × Ueq of the attached atom (1.5 × Ueq for methyl hydrogen atoms).

UV-Vis and Luminescent Measurements

Absorption spectra were recorded on a Varian Cary 6000i Spectrophotometer with Starna Quartz Fluorometer Cells with a pathlength of 10 mm for the ligand and 0.1 mm for the complexes. All spectroscopic data were obtained in DCM solutions unless otherwise noted. The absorption spectra of polymer films were performed on films that were fully reduced. Luminescent measurements were recorded on a Photon Technology International QM 4 spectrophotometer equipped with a 6-inch diameter K Sphere-B integrating sphere. For quantum yield measurements, the integrating sphere was used. Quantum yield was calculated by dividing the area under the emission peak of the complex by the difference between the area under the excitation peak of the sample and that of a blank solution ($A_{em\ sample}$ / ($A_{ex\ blank}$ - $A_{ex\ sample}$), where A = area under peak).[27-29]

Electrochemistry

Electrochemical syntheses and studies were performed in a dry-box under a nitrogen atmosphere using a GPES system from Eco. Chemie B. V.. All the electrochemical experiments were carried out in a three-electrode cell with a $Ag/AgNO_3$ reference electrode (silver wire dipped in a 0.01 M silver nitrate solution with 0.1 M $TBAPF_6$ in CH_3CN), a Pt button working electrode or ITO coated glass (70 – 100 Ω), and a Pt wire coil counter electrode. Potentials were relative to this 0.01 M $Ag/AgNO_3$

reference electrode. Ferrocene was used as an external reference to calibrate the reference electrode before and after experiments were performed and that value was used to correct the measured potentials. The supporting electrolyte was 0.1 M $TBAPF_6$ that was purified by recrystallization three times from hot ethanol before being dried for 3 days at 100 ^oC under active vacuum.

Synthesis

General Procedure for Complexation.

Ln(β-diketonate)$_3$(H_2O)$_2$ (0.025 mmol) was added into a suspension of ligand (0.025 mmol) in benzene, chlorobenzene or toluene (15.0 mL). The mixture was refluxed to get a clear yellow solution. After filtration, the solution was slowly cooled to room temperature and stored at the refrigerator (~ -20 °C). Crystals suitable for X-ray diffraction analysis were obtained after a few days.

[Yb(DBM)$_3$L2]·C_7H_8 (13). Light yellow crystal, yield: 6.3 mg, 19.7%. Elemental anal. calcd. (Found) for **13**, $C_{72}H_{53}N_2O_6S_2Yb$: C, 67.59 (67.60); H, 4.18 (3.97); N, 2.19 (2.37). CI-MS (CH_2Cl_2) m/z: 1188 [**13** + H - C_7H_8]$^+$. mp 286 ^oC.

[Nd(DBM)$_3$L3]·C_6H_6 (14). Yellow crystal, yield: 17.6 mg, 52%. LRMS (CI): 1275 [**14** – C_6H_6]$^+$.

Nd(BTFA)$_3$L3·2C_7H_8 (15). Yellow-green crystal, yield: 15.1 mg, 42%. LRMS (CI): 1251 [**15** + H - 2C_7H_8]$^+$. Elemental anal. calcd. (Found) for **15** - 2C_7H_8, $C_{54}H_{34}F_9N_2NdO_{10}S_2$: C, 51.88 (51.71); H, 2.74 (2.50); N, 2.24 (2.23).

Nd(TTA)$_3$L3·C_7H_8 (16). Yellow crystal, yield: 11.2 mg, 33%. LRMS (CI): 1268 [**16** - C_7H_8]$^+$. Elemental anal. calcd. (Found) for **16** - C_7H_8, $C_{48}H_{28}F_9N_2NdO_{10}S_5$: C, 45.46 (45.34); H, 2.23 (1.99); N, 2.21 (2.26).

$Er(DBM)_3L3$ (17). Light pink crystal, yield: 9.5 mg, 26%. LRMS (CI): 1297 [**17**]$^+$. Elemental anal. calcd. (Found) for **17**, $C_{69}H_{49}ErN_2O_{10}S_2$: C, 63.87 (63.93); H, 3.81 (3.57); N, 2.16 (2.24).

$Er(BTFA)_3L3 \cdot 2C_7H_8$ (18). Yellow crystal, yield: 14.1 mg, 39%. Elemental anal. calcd. (Found) for **18** - $2C_7H_8$, $C_{54}H_{34}ErF_9N_2O_{10}S_2$: C, 50.94 (50.47); H, 2.62 (2.69); N, 2.33 (2.20).

$Er(TTA)_3L3 \cdot C_7H_8$ (19). Yellow crystal, yield: 12.1 mg, 35%. Elemental anal. calcd. (Found) for **19** - C_7H_8, $C_{48}H_{28}ErF_9N_2O_{10}S_5$: C, 44.65 (45.34); H, 2.19 (1.99); N, 2.17 (2.26).

$Yb(DBM)_3L3 \cdot 3C_7H_8$ (20). Light yellow crystal, yield: 15.2 mg, 47%. LRMS (CI): 1304 [**20** + H - $3C_7H_8$]$^+$. Elemental anal. calcd. (Found) for **20**, $C_{90}H_{73}N_2O_{10}S_2Yb$: C, 68.71 (68.43); H, 4.23 (4.66); N, 2.08 (1.77).

$Yb(BTFA)_3L3$ (21). Pink crystals, yield: 12.2 mg, 38%.

$Yb(TTA)_3L3$ (22). Pink crystal, yield: 9.4 mg, 29%. Elemental anal. calcd. (Found) for **$22 \cdot 2H_2O$**, $C_{48}H_{32}F_9N_2O_{12}S_5Yb$: C, 43.24 (42.28); H, 2.42 (1.99); N, 2.10 (2.01).

$Nd(DBM)_3L4 \cdot 1.5C_7H_8$ (23). Yellow crystal, yield: 17.2 mg, 47%. LRMS (CI): 1324 [**23** + H – $1.5C_7H_8$]$^+$. Elemental anal. calcd. (Found) for **23** - $1.5C_7H_8$, $C_{73}H_{49}N_2NdO_6S_4$: C, 66.29 (66.43); H, 3.73 (3.91); N, 2.12 (2.27).

$Nd(BTFA)_3L4 \cdot C_6H_5Cl$ (24). Orange-red crystal, yield: 14.1 mg, 40%. LRMS (CI): 1299 [**24** + H - C_6H_5Cl]$^+$. Elemental anal. calcd. (Found) for **24** - **C_6H_5Cl**, $C_{58}H_{34}F_9N_2NdO_6S_4$: C, 53.65 (52.94); H, 2.64 (2.29); N, 2.16 (2.07).

$Nd(TTA)_3L4$ (25). Orange crystal, yield: 10.9 mg, 33%. LRMS (CI): 1317 [**25** + H]$^+$. Elemental anal. calcd. (Found) for **25**, $C_{52}H_{28}F_9N_2NdO_6S_7$: C, 47.44 (46.73); H, 2.14 (1.77); N, 2.13 (2.05).

Yb(DBM)$_3$L4 (26). Yellow crystal, yield: 8.8 mg, 26%. LRMS (CI): 1352 [**26** + H]$^+$. Elemental anal. calcd. (Found) for **26**, $C_{73}H_{49}N_2O_6S_4Yb$: C, 64.87 (64.22); H, 3.65 (3.97); N, 2.07 (2.26).

RESULTS AND DISCUSSION

Lanthanide Complexes Based on L2

Crystal Structure of [Yb(DBM)$_3$L2]·C$_7$H$_8$ (13)

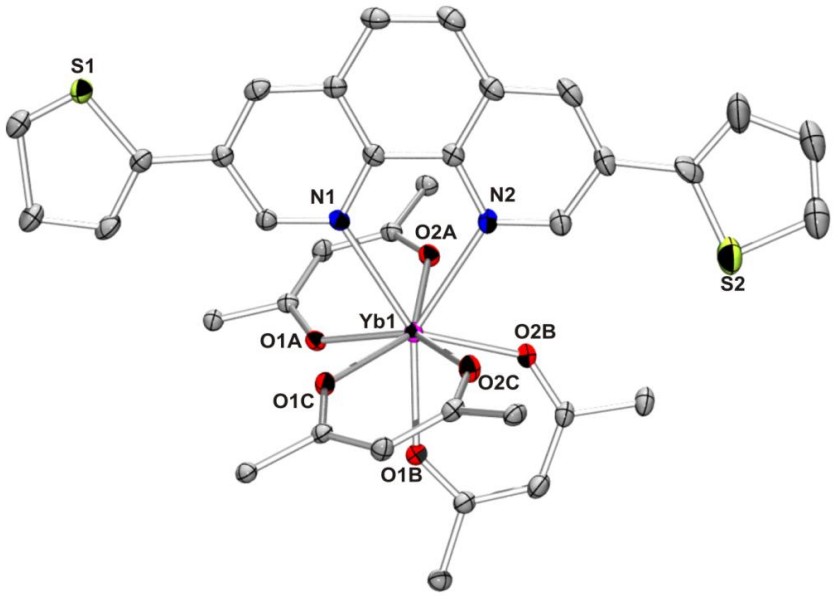

Figure 29. ORTEP diagram of **13** showing the labeling scheme of selected atoms at 30% probability level. Hydrogen atoms, solvent molecules, and phenyl rings of the dibenzoylmethanido ligands are omitted for clarity.

Complex **13** is isostructural with complex **6** (Figure 29). The phenanthroline portion is nearly planar with the largest deviation from the mean plane of 0.08 Å. The Yb-O (2.258(2) - 2.284(2) Å) and Yb-N (2.534(2) and 2.545(2) Å) bond lengths are shorter compared to those in **6**. These regular changes result from the smaller size of Yb^{3+} ion caused by the lanthanide contraction.[30] The coordination geometry of Yb^{3+} can be

described as a distorted dodecahedron. The thiophene ring structure also shows some delocalization of the π-electrons determined by the C-C and C-S bond lengths. The average C-S bond distance (1.688(8) Å) is somewhat shorter than a normal $C_{sp}{}^2$-S single bond length (1.759(8) Å), and is comparable with the corresponding C-S distance of free thiophene (1.714(1) Å).

Photophysics of 13

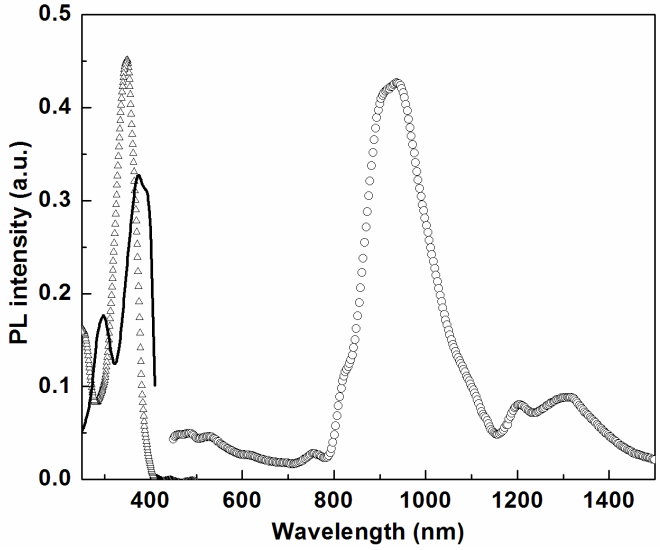

Figure 30. UV-Vis (Δ), excitation (-) and emission (o) spectra of complex **13** in CH_2Cl_2 at RT.

A high molar absorption coefficient value of complex **13** at 350 nm (9.2×10^4 L mol^{-1} cm^{-1}) is observed. The excitation spectrum of **13** (Figure 30) is obtained by monitoring the characteristic emission of Yb^{3+} ions, which is dominated by two peaks ranging from 240 to 400 nm. The excitation spectrum overlaps well with the absorption spectrum, indicating that the lanthanide luminescence is sensitized via organic ligand excitation. The emission spectrum of **13** is obtained by the excitation of 350 nm. The prominent Yb^{3+} emission band centered at 970 nm can be observed, which is assigned to

the $^2F_{5/2} \rightarrow {}^2F_{7/2}$ transition. It should be noted that the Yb^{3+} ion emission band is not a single sharp transition but an envelope of bands (ca. 1200 and 1300 nm) arising at the lower energy side of the primary band. Similar splitting has been reported previously,[31-33] and in early spectroscopic studies on ytterbium β-diketone compounds it was suggested that crystal field splitting is the origin of the structure in the emission spectra.[34]

Electrochemical Study of 13

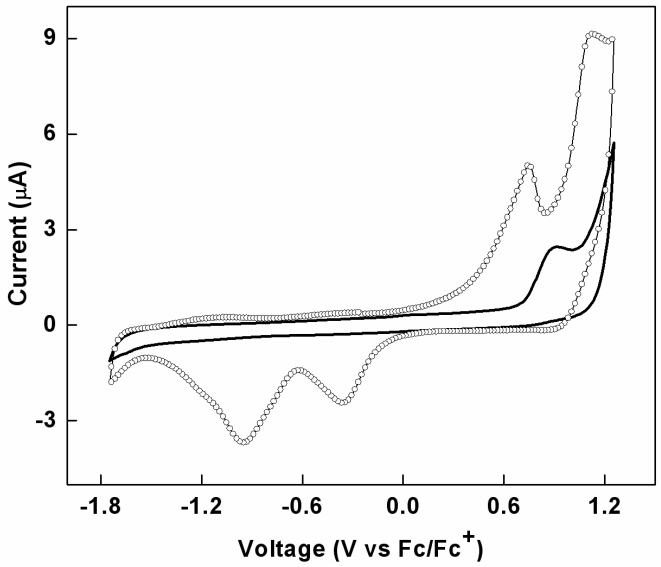

Figure 31. Cyclic voltammogram of **L2** (o) and complex **13** (solid line) in CH_2Cl_2, 0.1 M $TBAPF_6$, Pt electrode.

As we discussed in Chapter 2, **L2** can be oxidatively polymerized when the potential of the electrode was swept between -1.75 and +1.25 V versus Fc/Fc^+ at a scan rate of 100 mV/s. The cyclic voltammogram of the ligand **L2** and complex **13** are shown in Figure 31. Unfortunately, after the ligand was coordinated to the $Yb(DBM)_3(H_2O)_2$ moiety, the resulting complex **13** also can not be electrochemically polymerized. We observe an irreversible oxidation at +0.91 V which does not result in polymer deposition.

Considering that the $Yb(DBM)_3(H_2O)_2$ monomer are electrochemically silent throughout the scan window, the irreversible oxidation peak is related to **L2**.

Lanthanide Complexes Based on L3

Crystal Structure of Nd(β-diketonate)$_3$L3

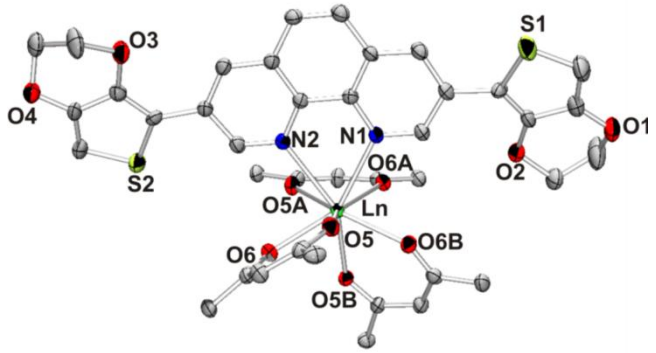

Figure 32. ORTEP plot for **14** with ellipsoids drawn at the 30% probability level. The hydrogen atoms, solvent molecules and phenyl rings of the dibenzoylmethanido ligands have been removed for clarity.

Complexes **14**, **15** and **16** are all characterized by X-ray diffraction analysis. The Nd^{3+} center is coordinated by two nitrogen atoms from **L3** and six oxygen atoms from *β*-diketonates (*β*-diketonate = DBM (**14**), BTFA (**15**) and TTA(**16**)), resulting in a coordination number of eight. Figure 32 shows the molecular structure of **14**. The coordination geometry can be described as a distorted square antiprism. The average Nd-N bond distance (2.682(2) Å) is longer than the average Nd-O bonds (2.340(18) Å). Similar geometric structures are observed for **15** and **16**.

Crystal Structure of Er(β-diketonate)$_3$L3

Complexes **18** and **19** are both characterized by X-ray diffraction analysis. The molecular structure of **18** is shown in Figure 33. As expected, in **18** the Er^{3+} ion is eight-coordinate, with six oxygen atoms from three bidentate BTFA anions and two nitrogen

atoms from a bidentate **L3** ligand. The average Er-O and Er-N distances are 2.309 (6) and 2.537(7) Å, respectively. The central Er^{3+} ion adopts a coordination geometry of distorted dodecahedron. The same coordination environment is observed in **19** with the average Er-O and Er-N distances of 2.313 (7) and 2.527(7) Å, respectively. The average bond lengths and angles of the TTA ligand are similar to those reported for other TTA complexes.[35]

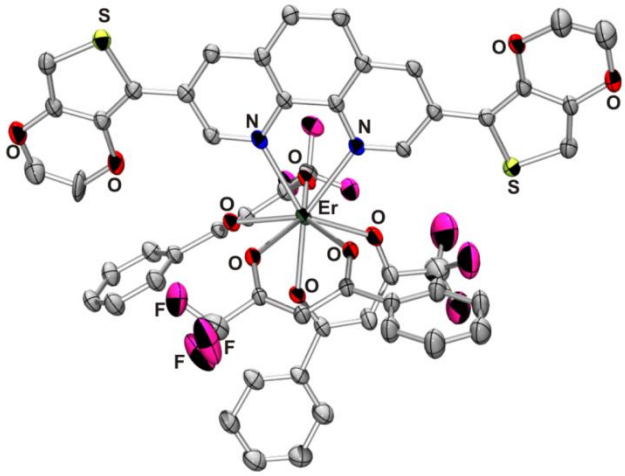

Figure 33. ORTEP plot for **18** with ellipsoids drawn at the 30% probability level. The hydrogen atoms and solvent molecules have been removed for clarity.

Crystal Structure of Yb(DBM)$_3$L3

Complex Yb(DBM)$_3$L3 (**20**) is isostructural with complex **14**. The average Yb-O and Yb-N distances are 2.276 (3) and 2.531 (3) Å, respectively, which are the shortest among the average Ln-O and Ln-N distances of complexes **14** - **20**. The six oxygen atoms and two nitrogen atoms in complex **20** lie at the apexes of a distorted dodecahedron.

The coordination geometry of the lanthanide changes from distorted square antiprism in complexes **14** - **16** to distorted dodecahedron in **18** - **20**. This geometry

change can be explained by the lanthanide contraction. The lanthanide series can be divided into three groups according to the mass: the lighter La–Pm (Group 1), the intermediate Sm–Dy (Group 2), and the heavier Ho–Lu (Group 3). Nd^{3+} ion belongs to group 1 which has the largest ionic radii, while Er^{3+} and Yb^{3+} are group 3 elements with smallest ionic radii. The decreasing size of these ions results in the coordination geometry change due to the bulky nature of the organic ligands.

Photophysics of Complexes Based on L3

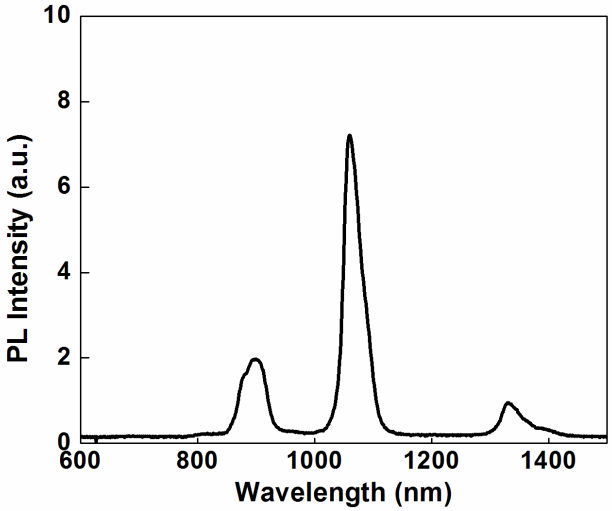

Figure 34. Emission spectrum of complex **14** in CH_2Cl_2 at RT.

At room temperature in CH_2Cl_2 solution, the emission spectrum of complex **14** (Figure 34) excited at 350 nm shows exclusively the NIR emission bands characteristic of Nd^{3+} with three lines at 896, 1061, and 1332 nm corresponding to transitions from $^4F_{3/2} \rightarrow {}^4I_{J/2}$, (J = 9, 11, 13, respectively). The excitation spectrum of complex **14**, obtained by monitoring the emission at 1061 nm, closely matched the absorption spectrum of the DBM and **L3** ligands. This indicates that, upon the photoexcitation of the organic ligands,

the excitation energy was mainly absorbed by the ligands, and then transferred to the Nd^{3+} ion.

The Er^{3+} complexes (**17** - **19**) show a strong NIR emission band at 1535 nm (Figure 35), which originates from the 4*f*–4*f* electronic transition of the first excited state ($^4I_{13/2}$) to the ground state ($^4I_{15/2}$) of the partially filled 4*f* shell. The UV-Vis absorption Spectra of complexes **17** - **19** show the absorption of *β*-diketone ligands and **L3**. Time-resolved experiments were also performed by excitation of a CH_2Cl_2 solution of complexes, and monitoring the decay of the emission of the emission band at 1535 nm resulting in a excited state lifetime of 4.8, 8.2 and 7.5 μs for complexes **17**, **18** and **19** respectively. The estimated quantum yields are calculated by the comparison of the luminescence lifetime of complexes with the natural lifetime of Er^{3+}. By using $\Phi = \tau/\tau_0$, a value of 0.6%, 1.1% and 0.92 % for the quantum yields of **17**, **18** and **19** respectively, is calculated, given a value τ_0 for the natural lifetime of Er^{3+} = 8 ms.[36]

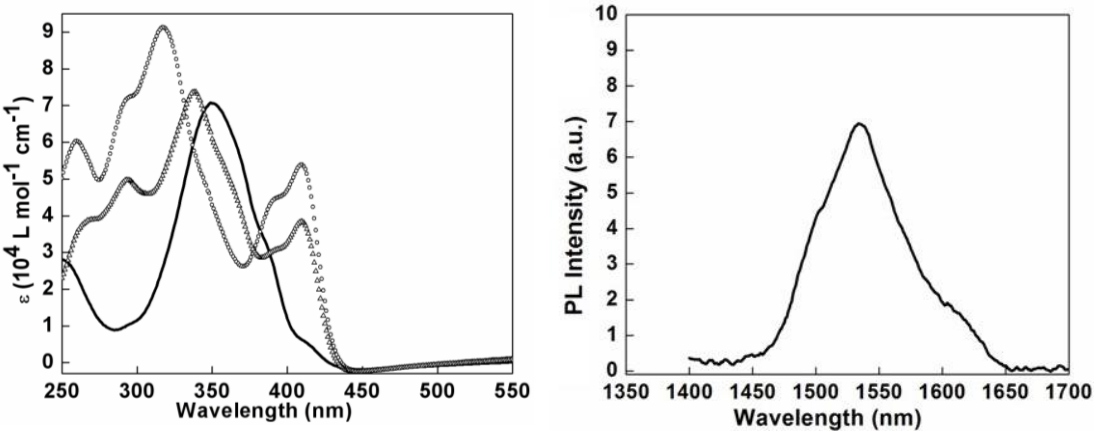

Figure 35. Left: UV-Vis absorption spectra of complexes **17** (-), **18** (o) and **19** (Δ). Right: Emission spectrum of **14**.

The luminescence of complexes **20**, **21** and **22** is characterized by emission at 972 nm (Figure 36), which is assigned to the $^2F_{5/2} \rightarrow {}^2F_{7/2}$ transition. Note that the Yb^{3+}

emission is not a single sharp transition, rather it appears as a series of bands with two other broad bands centered at 1003 and 1033 nm. Similar splitting has been reported previously and is attributed to the crystal field, or stark splitting.[17] The absolute quantum yields of **20**, **21** and **22** have been measured upon ligand excitation (350 nm) by using $[Yb(tta)_3(H_2O)_2]$ as a reference.[37] The quantum yields of **20**, **21** and **22** are 2.1%, 1.5% and 1.6%, respectively, which are relatively higher than other published data, for instance 1.8% for a bimetallic helicate in D_2O,[38] 0.5% for a terphenyl-based complex in DMSO,[39] or 0.31% for a complex with 4,4-difluoro-8-(2':2'';6'':2'''-terpyridin-4''-yl)-1,3,5,7-tetra methyl-2,6-diethyl-bora-3a,4a-diaza-s-indacene in DCM.[40] The emission lifetime of **20**, **21** and **22** were determined to be 17.3, 12.8 and 13.4 μs respectively. The quantum efficiency increasing agrees well with the corresponding lengthening of the emission lifetime as seen in other lanthanide complexes.[41]

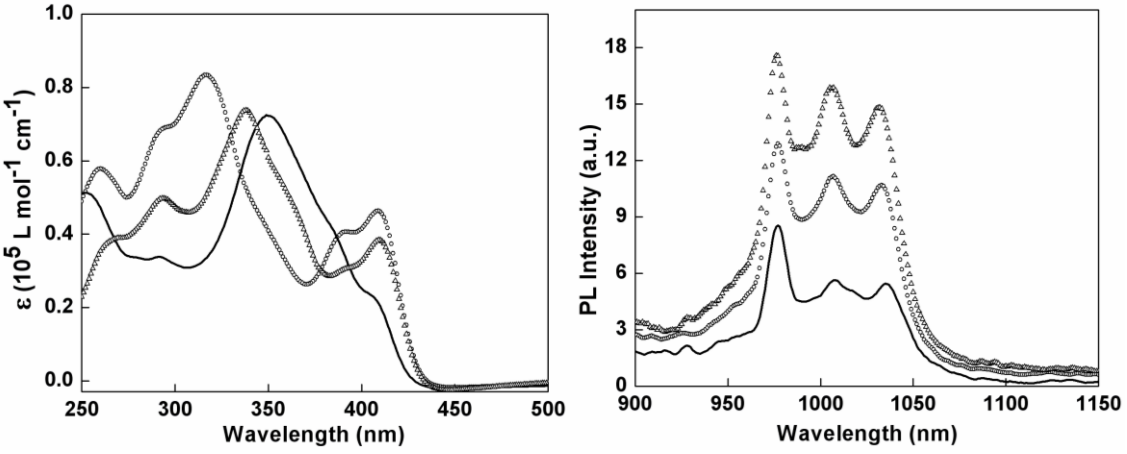

Figure 36. Left: UV-Vis absorption spectra of complexes **20** (-), **21** (o) and **22** (Δ). Right: Emission spectrum of **20** (-), **21** (o) and **22** (Δ).

Electrochemical Studies of Complexes Based on L3

3,4-(Ethylenedioxy)thiophene can be electrochemically polymerized at relatively low applied voltages. Although the same polymerizable ligand **L3** is used, complex **20**

($Yb(DBM)_3L3{\cdot}3C_7H_8$) does not electropolymerize as well as complex **9** ($Eu(DBM)_3L3$). Electropolymerization of complex **20** was performed from 2×10^{-3} M monomer solution by continuous cycling between -1.25 V and +1.25 V at a scan rate of 100 mV s^{-1} up to 10 scans. With the increasing scans, the oxidation peak quickly moves out of the solvent window. The linearity of the intensity versus number of scans failed after five scans, as shown in Figure 37.

Similar results were observed for other **L3** based complexes. Since the oxidation peak moves out of the solvent window, one way to improve the electropolymerization performance is to use polymerizable groups with even lower oxidation potential. Based on this argument, complexes with **L4** should give us better electropolymerization performance.

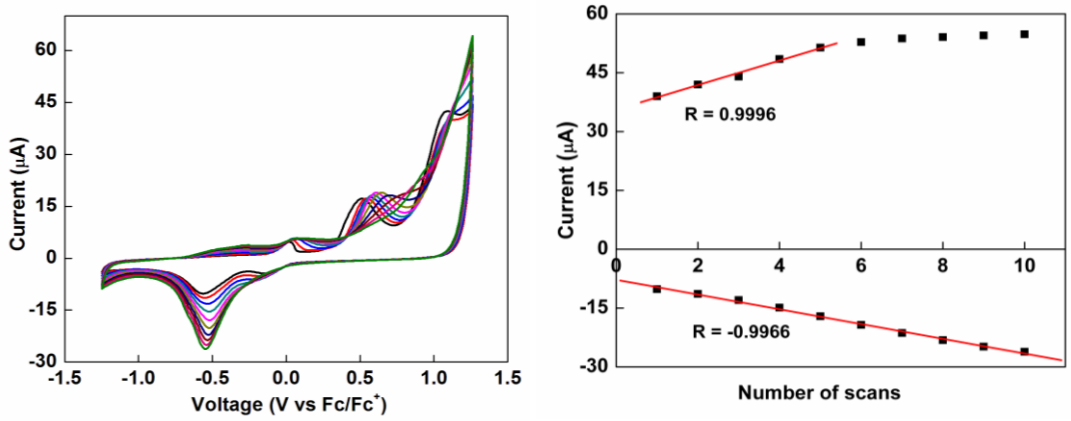

Figure 37. Left: Cyclic voltammograms of a 0.2 mM CH_2Cl_2 solution of **20**, 0.1 M $TBAPF_6$, Pt electrode. Right: The maximum peak current versus the number of scans.

Lanthanide Complexes Based on L4

Crystal Structure of Nd(β-diketonate)$_3$L4

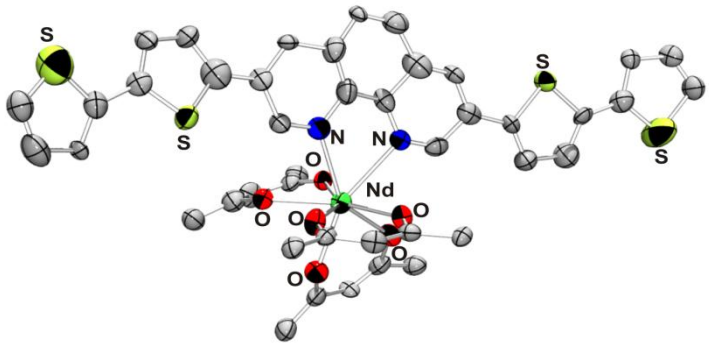

Figure 38. ORTEP diagram of **23** showing the labeling scheme of selected atoms at 30% probability level. Hydrogen atoms, solvent molecules, phenyl rings and CF_3 of the benzoyltrifluoroacetonate ligands are omitted for clarity.

The molecular structures of **23** (Figure 38) and **24** are the first reported structures of a complex containing both Nd^{3+} and BT electropolymerizable units. In complex **23**, the eight-coordinate Nd^{3+} ion lies at the center of a distorted dodecahedron that is defined by six oxygen atoms from DBM and two nitrogen atoms from **L4**. The Nd-N_{av} bond distance (2.616(18) Å) is longer than the Nd-O_{av} bond distance (2.407(3) Å) for **23**. In **24**, the central Nd^{3+} is also eight-coordinate with six oxygen atoms from BTFA and two nitrogen atoms from **L4**. In both complexes, the coordination geometry of the central lanthanide ion can be described as a distorted dodecahedron, which is different from what we observed in complex **14**. Such geometry difference can be explained by the replacement of **L3** to **L4**. As described above, the central Nd^{3+} is completely surrounded by the *β*-diketonate liagnds and the polymerizable ligand, which prevents the luminescent quenching caused by vibration and enhances the energy transfer from the ligand to the central Nd^{3+} ion.

Crystal Structure of Yb(DBM)$_3$L4

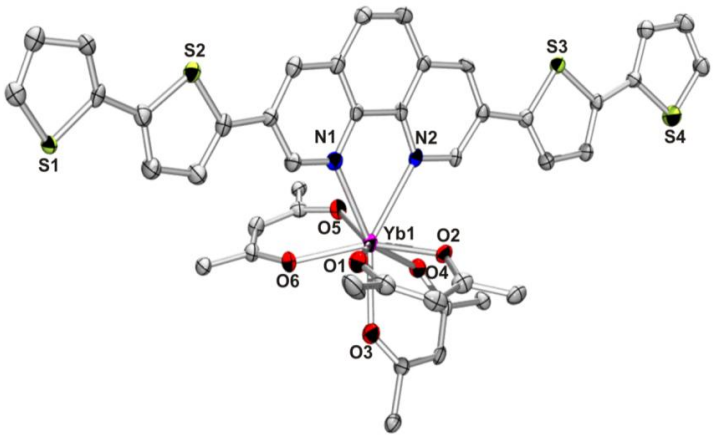

Figure 39. ORTEP diagram of **26** showing the labeling scheme of selected atoms at 30% probability level. Hydrogen atoms, solvent molecules, and phenyl rings of the dibenzoylmethanido ligands are omitted for clarity.

The coordination geometry of Yb^{3+} ion in complex **26** can be described as a distorted square antiprism (Figure 39). O3, O4, O5 and O6 form one of the two planes with the largest deviation from the planarity of 0.0814 Å for O5. The other plane is composed of N1, N2, O1, and O2 with the mean deviation from the planarity of 0.0518 Å. The dihedral angle between the two mean planes is 4.8°. The higher distortion of the square antiprism is caused by the enhanced steric hindrance from the elongated bithiophene rings compared with thiophene.

Electrochemical Studies of Complexes Based on L4

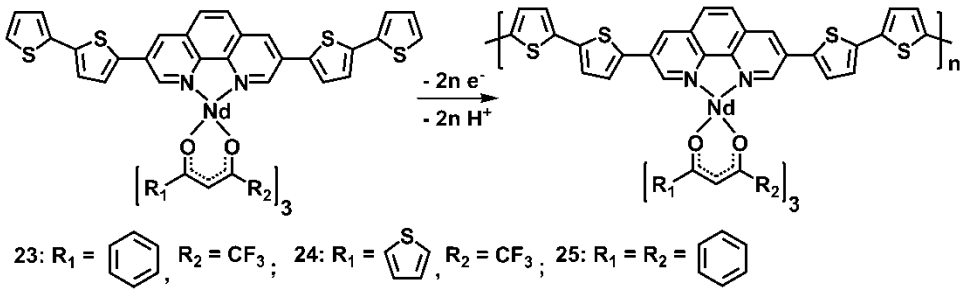

Scheme 4. Electrochemical polymerization of neodymium-containing monomer to conducting metallopolymer.

Complexes **23** - **25** have been electropolymerized to form polymers (Scheme 4) as electrode-confined films onto ITO coated glass working electrodes. Cyclic voltammetry of **23** over a window of +1.25 to -1.75 V (vs Fc/Fc^{+}) resulted in the growth of a polymer film. The first scan has monomer oxidation peaks around 0.75 and 0.9 V, and monomer reduction peaks at 0.80 and 0.56 V. A polymer reduction was observed at -0.25 and -1.1 V (Figure 40). The second scan indicates a polymer oxidation at 0.18 V. All these redox peaks grow linearly with increasing scans. The maximum peak current of an electrode-confined film of poly-**23** in pure electrolyte solution varies linearly with the rate of the electrochemical scan up to 500 mV/s. This behavior is indicative of a strongly adsorbed electroactive thin film which is not limited by the ionic flux of counter anions.

Monomers **24** and **25** exhibit similar electrochemical behavior to **23** (Figure 41). The XPS data were used to determine the film composition and metal coordination environment. The Nd $3d_{5/2}$ peak is observed at 988 eV, corresponding well to the expected values for Nd(III) bound to oxygen.[42] The S 2*p* peak is also found at 164.3 eV. Quantitative XPS analysis reveals that the films have atomic ratios of Nd : S = 1 : 4.6, 1 :

5.2 and 1 : 4.4 respectively for **23**, **24** and **25**, which is in agreement with the stoichiometric molar ratio of the proposed film structures.

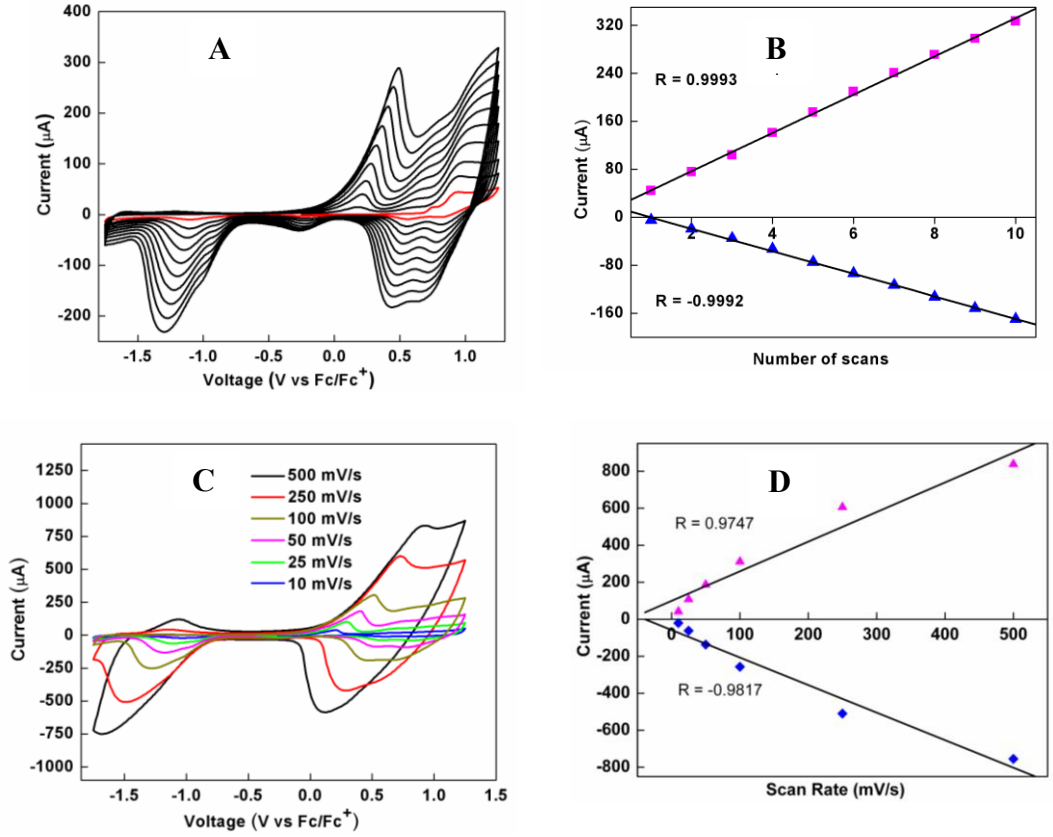

Figure 40. (A) Electrochemical polymerization of **23** (Fc/Fc^+ is the redox couple of ferrocene). (B) Plot of linear current increase vs number of scans. (C) Electrochemical scan rate dependence of poly-**23**. (D) Plot of linear current increase vs scan rate.

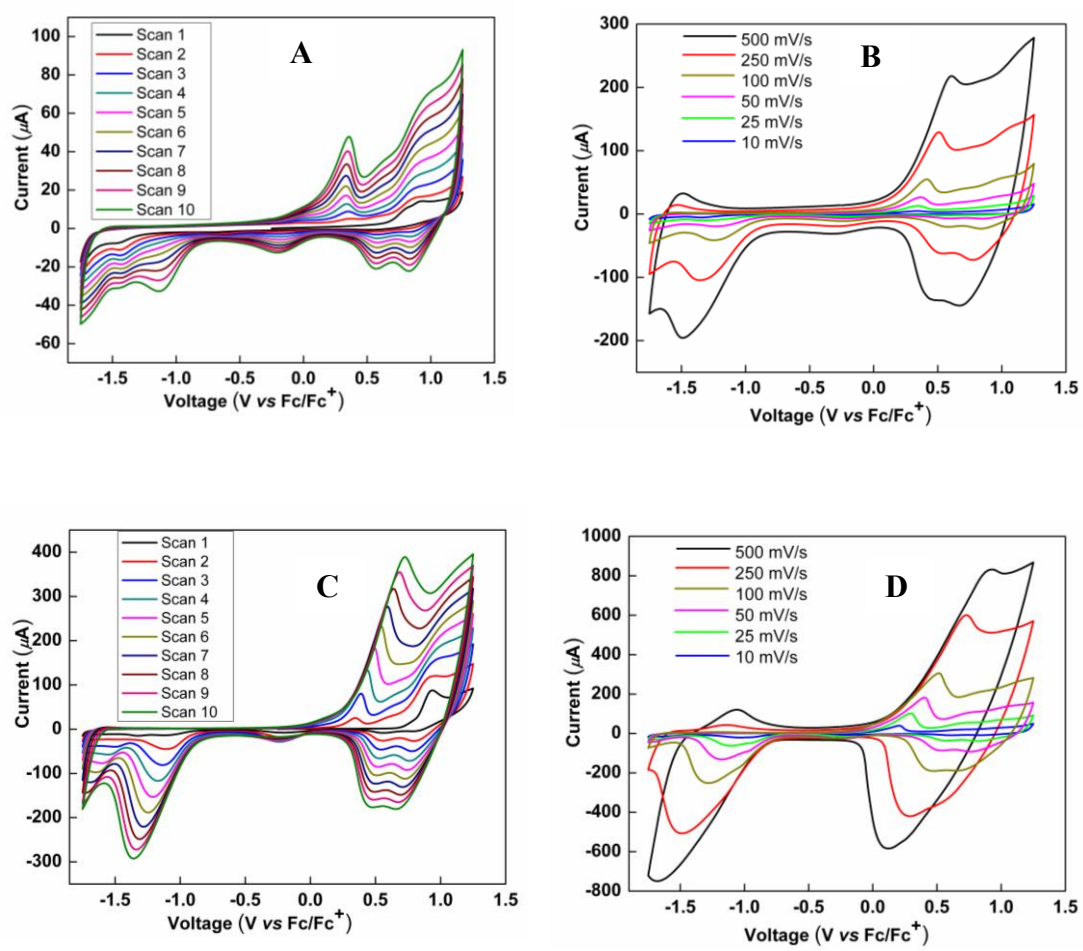

Figure 41. (A) Electrochemical polymerization of **24** (Fc/Fc+ is the redox couple of ferrocene). (B) Electrochemical scan rate dependence of poly-**24**. (C) Electrochemical polymerization of **25**. (D) Electrochemical scan rate dependence of poly-**25**.

Cyclic voltammetry of **26** over a window of +1.25 to -1.75 V (vs Fc/Fc^{+}) resulted in the growth of a polymer film, which is similar to complexes **23** - **25**. The first scan displays monomer oxidation peaks at 0.78 and 0.94 V, and monomer reduction peaks at 0.58 and 0.82 V. A polymer reduction was observed at -0.21 and -1.12 V. The subsequent scans are characterized by a polymer oxidation at 0.32 V, which increases in intensity as

the polymer is deposited. All these redox peaks grow linearly with increasing scans (Figure 42).

The maximum peak current of an electrode-confined film of poly-**26** in pure electrolyte solution varies linearly with the rate of the electrochemical scan up to 500 mV/s (Figure 42). The XPS data were used to determine the film composition and metal coordination environment. The Yb $4d_{5/2}$ peak is observed at 186.3 eV, corresponding well to the expected values for Yb(III) bound to oxygen.[43] The S $2p$ peak is also found at 163.95 eV. Quantitative XPS analysis reveals that the film has an atomic ratio of Yb : S = 1 : 4.7 for poly-**26**, which is in agreement with the stoichiometric molar ratio of the proposed film structure.

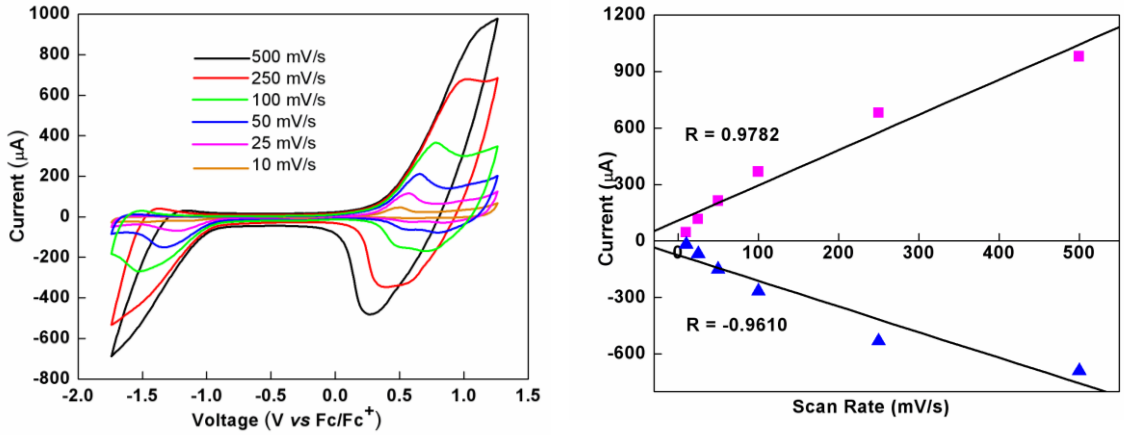

Figure 42. Electrochemical scan rate dependence of poly-**26** (left) and plot of linear current increase vs scan rate of poly-**26** (right).

Photophysics of Complexes Based on L4

The photophysical properties of **L4**, **23** - **25**, and poly-**23** - **25** have been studied under a variety of conditions. The absorption spectrum of **L4** (Figure 43) displays a broad band centered at 400 nm with a molar absorption coefficient of 6.5×10^4 L mol^{-1} cm^{-1},

which is red shifted compared to Phen (λ_{max} = 290 nm) due to the extended conjugation. The absorption spectra of **23 - 25** show singlet-singlet π–π^* transitions of **L4** maximized at 425 nm, which is red shifted compared with the free **L4** due to the geometry change caused by the coordination to the metal center. Besides the **L4** absorption, the absorption spectra of **23 - 25** also have the π–π^* transitions of β-diketones at 350, 325, and 338 nm for DBM, BTFA, and TTA, respectively.

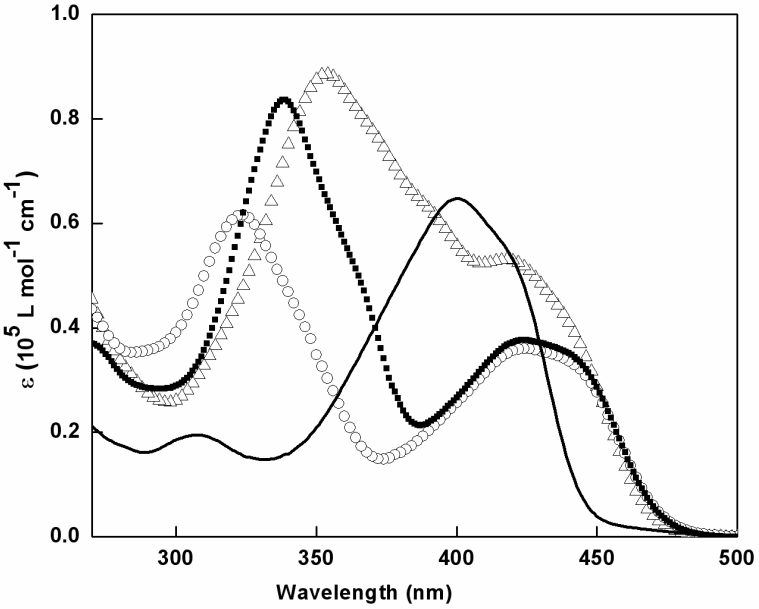

Figure 43. UV-Vis absorption spectra of **L4** (-), complexes **23** (■), **24** (o) and **25** (Δ) in CH_2Cl_2 at RT.

The emission and excitation spectra of **L4** at room temperature in CH_2Cl_2 are consistent with fluorescence emission (Φ_{fl} = 0.26) from the direct population of the singlet excited state (Figure 44). The emission spectra of **23 - 25** when excited at 425 nm show the exclusive NIR emission bands characteristic of Nd^{3+} ion. As shown in Figure 44, three lines at 899, 1053, and 1360 nm corresponding to transitions from $^4F_{3/2} \rightarrow {}^4I_{J/2}$,

(J = 9, 11, 13, respectively) were observed for **23**. The corresponding emission peaks for **24** and **25** appeared at 894, 1059, 1332 and 899, 1062, 1333 nm, respectively. The excitation spectrum of **23** was recorded by monitoring the emission intensity at 1063 nm. The observed transitions correspond to the absorption profile of the ligands thus confirming that energy transfer takes place from the ligands to the Nd^{3+} ion. The luminescent quantum yields of **23**, **24** and **25** in CH_2Cl_2 are 5.9%, 6.3% and 16.1%, respectively. The lifetimes of **23**, **24** and **25** in CH_2Cl_2 are 59, 78 and 145 μs, respectively.

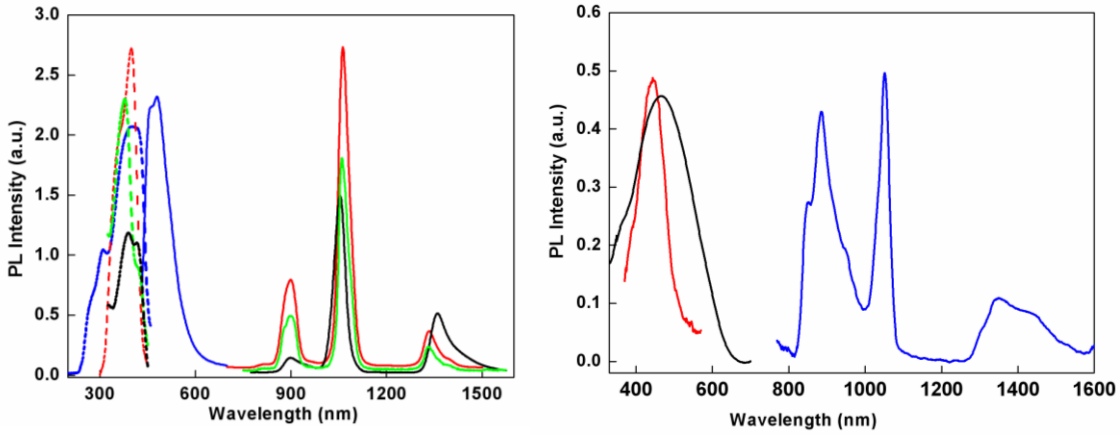

Figure 44. Left: Photophysical properties of **L4** (blue), **23** (red)**, 24** (black) and **25** (green) recorded in CH_2Cl_2 at RT, dotted line: excitation profile; solid line: emission profile. Right: Photophysical properties of poly-**25** recorded in DMF at RT. UV-Vis absorbance (black), excitation (red), and emission (blue).

The metallopolymer emission is only observed for poly-**25.** Figure 44 shows the photophysical profiles of a film of poly-**25** dissolved in DMF at RT. The UV-Vis absorbance spectroscopy displays a very broad band characteristic of the extended aromatic system of a conducting metallopolymer structure which is red-shifted from that of **L4** and **25.** The excitation spectrum of poly-**25** is less broad and blue-shifted relative to

the absorption spectrum suggesting that the energy transfer takes place from a localized excited state. This is consistent with energy transfer from the polymer backbone to the Nd^{3+}. The emission spectrum measured with 425 nm as the excitation wavelength features a manifold of two strong NIR transitions with the maxima at 884 and 1055 nm, along with a weak band at 1345 nm. The luminescent quantum yield and lifetime of poly-**25** is 1.7% and 17 μs, respectively.

When we discuss the photophysics of complex **26**, we include complex **13** and **20** as a comparison to study which ligand (**L2**, **L3** and **L4**) is the best antenna for sensitizing Yb^{3+} emission. The UV-Vis absorption spectra of the ligands show that **L4** has the highest molar absorption coefficient of 6.5×10^4 L mol^{-1} cm^{-1} with a broad band centered at 400 nm (Figure 45). From the phosphorescence spectra of the ligands in a 2:2:1:1 mixture of ethyl iodide-ether-ethanol-toluene at 77 K, the triplet excited state energy levels of the ligands were obtained (Table 13). The energy gap between the ligand triplet excited state and the 4*f* resonance level of Yb^{3+} ion (10 300 cm^{-1}) varies from 11 000 cm^{-1} for **L2** to 6 100 cm^{-1} for **L3** and 2 122 cm^{-1} for **L4**. Due to the lack of the quantum yield reports of NIR emitting lanthanide complexes, no optimum energy gap between the ligand triplet excited state and lanthanide excited state has been proposed. Herein, through varying the polymerization groups, we can adjust the triplet excited state energy levels of the organic ligands and thus find the proper energy gap for efficient NIR emission.

Table 13. Triplet excited state energy and lifetime of the ligands in a 2:2:1:1 mixture of ethyl iodide-ether-ethanol-toluene at 77 K.

Ligands	Triplet excited state energy (cm^{-1})	Lifetime (μs)
L2	21 300	39
L3	17 400	46
L4	12 422	68

The absorption spectra of **13**, **20** and **26** have the common π–π^* transitions of DBM at 350 nm. Due to the π–π^* transitions of **L3**, the absorption profile of complex **20** shows a small shoulder at 410 nm. The extended conjugation length of **L4** features the absorption spectrum of **26** with two peaks at 350 and 430 nm. The UV-Vis absorption spectra of poly-**20** and poly-**26** display very broad bands characteristic of the extended aromatic system of a conducting metallopolymer structure centered at 430 and 460 nm respectively.

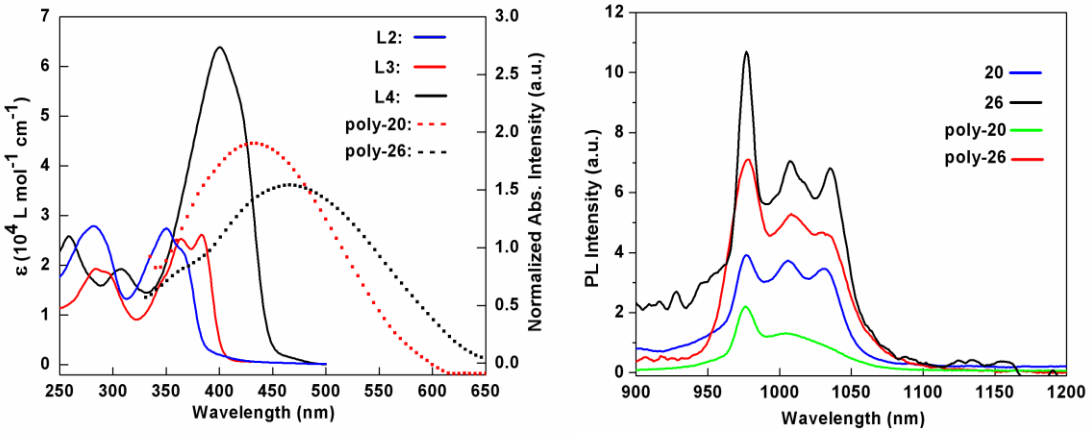

Figure 45. Left: UV-Vis of ligands in CH_2Cl_2 and polymers recorded as a thin film on ITO coated glass at RT. Right: Emission spectra of complexes in CH_2Cl_2 and polymers recorded in DMF at RT.

The emission and excitation spectra of ligands at room temperature in CH_2Cl_2 are consistent with fluorescence emission from the direct population of the singlet excited state (Figure 46). The emission spectra of complex **13**, **20** and **26** (excited at 350 nm for **13** and **20**, and 430 nm for **26**) show the exclusive NIR emission bands characteristic of Yb^{3+} ion. The prominent Yb^{3+} ion emission band centered at 970 nm is observed for all the complexes, which is assigned to the $^2F_{5/2} \rightarrow {}^2F_{7/2}$ transition. It should be noted that the Yb^{3+} ion emission band is not a single sharp transition but an envelope of bands (ca. 1000

and 1040 nm) arising at the lower energy side than the primary band, which can be explained by crystal field splitting. The metallopolymer emission is also observed for

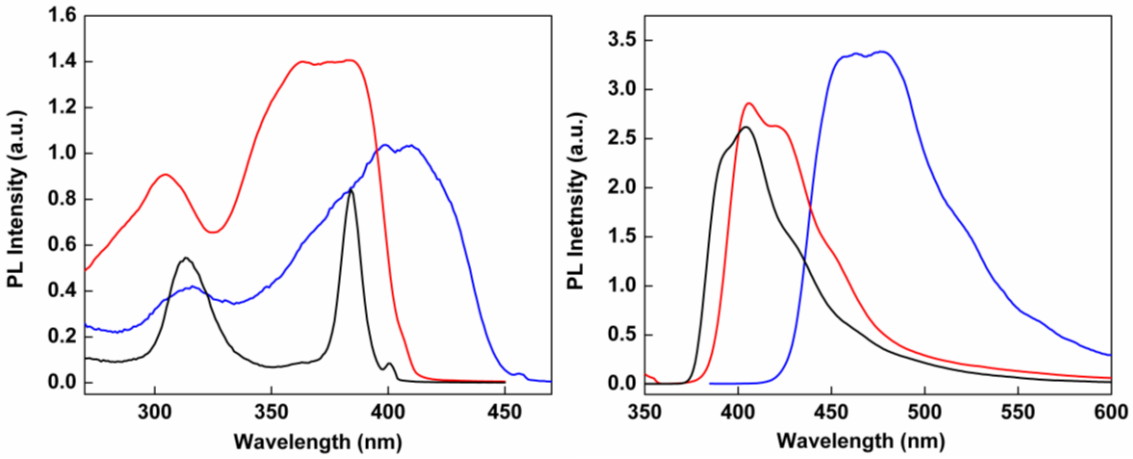

Figure 46. The excitation (left) and emission (right) spectra of the ligands in CH_2Cl_2. **L2**, black; **L3**, red; **L4**, blue.

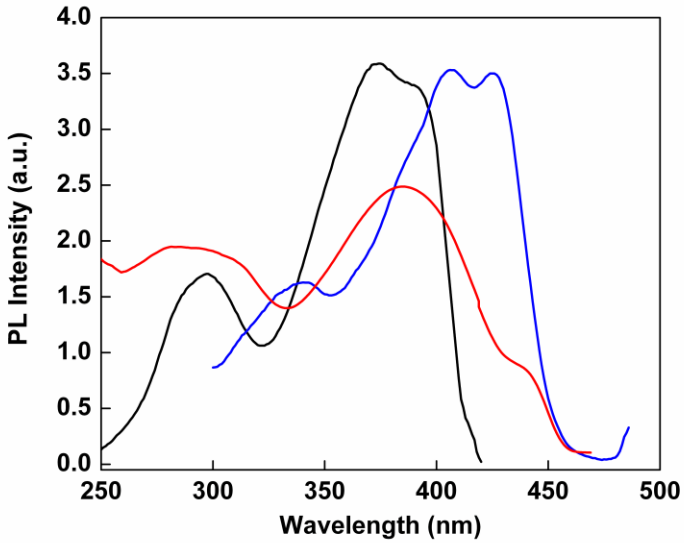

Figure 47. The excitation spectra of the complexes in CH_2Cl_2. **13**, black; **20**, red; **26**, blue.

poly-**20** and poly-**26** dissolved in DMF at RT (Figure 45). The emission spectra measured with 430 nm as the excitation wavelength feature the NIR transitions with maxima at 978 nm, along with the envelop bands at lower resolution.

The excitation spectra of complexes were recorded by monitoring the emission intensity at 978 nm, which overlapped well with their UV-Vis absorption spectra thus confirming that energy transfer takes place from the ligands to the Yb^{3+} ion (Figure 47). Photophysical studies (Table 14) show that the highest energy gap (11 000 cm^{-1}) of **13** gives the lowest quantum efficiency, and the smaller energy gap (6 100 cm^{-1}) of **20** gives the relatively higher quantum efficiency. Notably, the smallest energy gap (2 122 cm^{-1}) of **26** exhibits the highest quantum yield of 5.4% reported to date for Yb^{3+} complexes with organic ligands containing C-H bonds. The quantum yield data indicate that the energy transfer from the organic ligand to Yb^{3+} ion is favored with a small energy gap of 2 122 cm^{-1}.

Table 14. Luminescent properties of the complexes in CH_2Cl_2 and poly-**20** and poly-**26** in DMF at RT.

Compound	**13**	**20**	**26**	Poly-**20**	Poly-**26**
Quantum yield (%)	0.53	2.1	5.4	0.11	0.19
Lifetime (μs)	9.8	17.3	22.7	16.4	11.6

CONCLUSION

In summary, we have successfully demonstrated the synthesis of NIR emitting lanthanide containing conducting metallopolymers. Most of the monomer complexes have been characterized by X-ray diffraction analysis. These structures, which display pure NIR Ln^{3+}-based luminescence via stimulated excitation, are assembled from a well-characterized Ln^{3+} containing monomer via controlled electropolymerization. This new class of materials is promising to develop PLEDs which function in the NIR wavelength

region. Nd^{3+} complex **23** with DBM as the ancillary diketones shows the highest quantum yield. Yb^{3+} complexes with bis(2,2'-bithienyl-5-yl)-1,10-phenanthroline as the polymerizable ligand show the best electropolymerization performance and highest luminescent quantum yield. The triplet excited state energy measurements of a series of ligands shed light on our further study of the optimal energy gap for efficient NIR lanthanide emission, which is of great significance for the screening of potential organic antennas. Of importance here is the observation of NIR luminescence of Yb^{3+} containing metallopolymers, which has rarely been explored. The excellent NIR properties provide access to NIR luminescent polymer materials for optical applications. By changing the lanthanide centers, it should be possible to extend the emission to the 1500 nm range and thus provide low cost solutions for the 'fiber to the home' telecommunication problem.

REFERENCES

1. Bünzli, J.-C. G.; Comby, S.; Chauvin, A. S.; Vandevyver, C. D. B. *J. Rare Earths* **2007**, *25*, 257.
2. Suzuki, H. *J. Photochem. Photobiol. A* **2004**, *166*, 155.
3. Chen, Z. Q.; Bian, Z. Q.; Huang, C. H. *Adv. Mater.* **2010**, *22*, 1534.
4. Eliseeva, S. V.; Bünzli, J.-C. G. *Chem. Soc. Rev.* **2010**, *39*, 189.
5. van der Ende, B. M.; Aarts, L.; Meijerink, A. *Phys. Chem. Chem. Phys.* **2009**, *11*, 11081.
6. Shalav, A.; Richards, B. S.; Green, M. A. *Solar En. Mat. Sol. Cells* **2007**, *91*, 829.
7. Wang, F.; Banerjee, D.; Liu, Y. S.; Chen, X. Y.; Liu, X. G. *Analyst* **2010**, *135*, 1839.
8. Bünzli, J.-C. G. *Chem. Rev.* **2010**, *110*, 2729.
9. Amiot, C. L.; Xu, S. P.; Liang, S.; Pan, L. Y.; Zhao, J. X. J. *Sensors* **2008**, *8*, 3082.
10. Braun, D.; Heeger, A. J. *Appl. Phys. Lett.* **1991**, *58*, 1982.
11. Kraft, A.; Grimsdale, A. C.; Holmes, A. B. *Angew. Chem. Int. Ed. Engl.* **1998**, *37*, 402.
12. Curry, R. J.; Gillin, W. P. *Appl. Phys. Lett.* **1999**, *75*, 1380.
13. de Bettencourt-Dias, A. *Dalton Trans.* **2007**, 2229.
14. Zhang T.; Xu, Z.; Qian, L.; Tao, D. L.; Teng, F.; Gao, X.; Xu, X. R. *Chem. Phys. Lett.* **2005**, *415*, 30.
15. Kang, T. S.; Harrison, B. S.; Foley, T. J.; Knefely, A. S.; Boncella, J. M.; Reynolds, J. R.; Schanze, K. S. *Adv. Mater.* **2003**, *15*, 1093.
16. Harrison, B. S.; Foley, T. J.; Bouguettaya, M.; Boncella, J. M.; Reynolds, J. R.; Schanze, K. S. *Appl. Phys. Lett.* **2001**, *79*, 3770.
17. Kang, T. S.; Harrison, B. S.; Bouguettaya, M.; Foley, T. J.; Boncella, J. M.; Schanze, K. S.; Reynolds, J. R. *Adv. Funct. Mater.* **2003**, *13*, 205.
18. Ling Q.; Yang, M.; Wu, Z.; Zhang, X.; Wang, L.; Zhang, W. *Polymer* **2001**, *42*, 4605.
19. Lenarets, P.; Storms, A.; Mullens, J.; D'Haen, J.; Görller-Walrand, C.; Binnemans, K.; Driesen, K. *Chem. Mater.* **2005**, *17*, 5194.
20. Shunmugam, R.; Tew, G. N. *Macromol. Rapid Commun.* **2008**, *29*, 1355.
21. Saitoh, Y.; Koizumi, T.; Osakada, K.; Yamamoto, T. *Can. J. Chem.* **1997**, *75*, 1336.
22. Zhu, S. S.; Swager, T. M. *J. Am. Chem. Soc.* **1997**, *119*, 12568.
23. Sauvage, J. P.; Kern, J. M.; Bidan, D.-B.; Vidal, P.-L. *New J. Chem.* **2002**, *26*, 1287.
24. *Methods in Enzymology*, *276*: *Macromolecular Crystallography, part A*; Carter, C. W., Jr.; Sweets, R. M., Eds.; 1997.
25. Altomare, A.; Burla, M. C.; Camalli, M.; Cascarano, G. L.; Giacovazzo, C.; Guagliardi, A.; Moliterni, A. G. G.; Polidori, G.; Spagna, R. *J. Appl. Cryst.* **1999**, *32*, 115.
26. Sheldrick, G. M. (**1994**) SHELXL97. Program *for the Refinement of Crystal Structures.* University of Gottingen, Germany.
27. Aebischer, A.; Gumy, F.; Bünzli, J.- C. G. *Phys. Chem. Chem. Phys.* **2009**, *11*, 1346.
28. De Mello, J. C.; Wittmann, H. F.; Friend, R. H. *Adv. Mater.* **1997**, *9*, 230.

29. Lunstroot, K.; Nockemann, P.; Van Hecke, K.; Van Meervelt, L.; Görller-Walrand, C.; Binnemans, K.; Driesen, K. *Inorg. Chem.* **2009**, *48*, 3018.
30. *The Chemistry of the Lanthanides*; Moeller, T., Ed.; Pergamon Press, Oxford, 1973.
31. Deun, R. V.; Moors, D.; Fré, B. D.; Binnemans, K. *J. Mater. Chem.* **2003**, *13*, 1520.
32. Asano-Someda, M.; Kaizu, Y. *J. Photochem. Photobiol. A* **2001**, *139*, 161.
33. Tsvirko, M. P.; Stelmakh, G. F.; Pyatosin, V. E.; Solovyov, K. N.; Kachura, T. F. *Chem. Phys. Lett*. **1980**, *73*, 80.
34. Perkins, W. G.; Crosby, G. A. *J. Chem. Phys.* **1965**, *42*, 407.
35. Gao, L.; Guan, M.; Wang, K.; Jin, L.-P.; Huang, C.-H. *Eur. J. Inorg. Chem.* **2006**, 3731.
36. Weber, M. J. *Phys. Rev.* **1968**, *171*, 283.
37. Meshkova, S. B.; Topilova, Z. M.; Bolshoy, D. V.; Beltyukova, S. V.; Tsvirko, M. P.; Venchikov, V. Y.; Ya, V. *Acta Phys. Pol. A* **1999**, *95*, 983.
38. Gonçalves Silva, F. R.; Malta, O. L.; Reinhard, C.; Güdel, H. U.; Piguet, C.; Moser, J. E.; Bünzli, J.-C. *J. Phys. Chem. A* **2002**, *106*, 1670.
39. Klink, S. I.; Hebbink, G. A.; Grave, L.; Van Veggel, F. C. J. M.; Reinhoudt, D. N.; Slooff, L. H.; Polman, A.; Hofstraat, J. W. *J. Appl. Phys.* **1999**, *86*, 1181.
40. Ziessel, R. F.; Ulrich, G.; Charbonniere, L.; Imbert, D.; Scopelliti, R.; Bünzli, J.-C. G. *Chem. Eur. J.* **2006**, *12*, 5060.
41. Hasegawa, Y.; Kimura, Y.; Murakoshi, K.; Wada, Y.; Kim, J. H.; Nakashima, N.; Yamanaka, T.; Yanagida, S. *J. Phys. Chem.* **1996**, *100*, 10201.
42. Pizzoferrato, R; Ziller, T; Paolesse, R.; Mandoj, F.; Micozzi, A.; Ricci, A.; Lo Sterzo C. *Chem. Phys. Lett.* **2006**, *426*, 124.
43. Uwamino, Y.; Ishizuka, Y.; Yamatera, H. *J. Electron Spectrosc. Relat. Phenom.* **1984**, *34*, 67.

CRYSTALLOGRAPHIC DATA

Table 15. Crystal data and structure refinement for **13**.

formula	$C_{72}H_{53}N_2O_6S_2Yb$
fw	1279.32
T (K)	153(2)
crystal system	Monoclinic
space group	$P2_1/n$
a (Å)	17.9680(2)
b (Å)	14.3790(2)
c (Å)	24.8860(3)
β (deg)	110.8340(5)
V (Å^3)	6009.19(13)
Z	4
ρ (g/cm^3)	1.414
μ (mm^{-1})	1.681
F(000)	2596
crystal size (mm)	0.16 × 0.10 × 0.08
θ (deg)	1.86 to 27.49
Index ranges	$-23 \le h \le 23$
	$-18 \le k \le 18$
	$-32 \le l \le 32$
Reflns collected	25624
Independent reflns	13773, R_{int} = 0.0306
Absorption correction	Semi-empirical from equivalents
Max. and min. transmission	0.877 and 0.818
GOF on F^2	1.015
R_1, R_2 [I > 2σ (I)]	0.0358, 0.0836
R_1, R_2 (all data)	0.0588, 0.0898
Largest diff. peak and hole (e·Å^{-3})	1.419 and -1.030

Table 16. Selected bond lengths [Å] and angles [°] for **13**.

Bond distances (Å)			
Yb1-O1C	2.258(2)	Yb1-N2	2.545(2)
Yb1- O2C	2.259(2)	Yb1- N1	2.534(2)
Yb1- O1A	2.260(2)	C13- C14	1.374(6)
Yb1- O2B	2.266(2)	S1- C16	1.714(4)
Yb1- O2A	2.277(2)	S2- C17	1.675(5)
Yb1- O1B	2.284(2)	S2- C20	1.726(6)
Bond angles (º)			
O1C-Yb1-O2C	73.08(7)	O1A-Yb1-O2A	73.00(7)
O1C-Yb1-O1A	74.00(7)	O2B-Yb1-O2A	75.96(8)
O2C-Yb1-O1A	146.15(7)	O1C-Yb1-O1B	77.31(8)
O1C-Yb1-O2B	139.92(7)	O2C-Yb1-O1B	86.60(7)
O2C-Yb1-O2B	78.23(8)	O1A-Yb1-O1B	78.74(7)
O1A-Yb1-O2B	125.00(7)	O2B-Yb1-O1B	73.57(8)
O1C-Yb1-O2A	142.12(7)	O1C-Yb1-N1	75.34(8)
O2C-Yb1-O2A	140.66(8)	O2B-Yb1-N1	138.16(8)

Table 17. Crystal data and structure refinement for **14**.

formula	$C_{75}H_{55}N_2NdO_{10}S_2$
fw	1352.57
T (K)	153(2)
crystal system	Monoclinic
space group	$P2_1/n$
a (Å)	18.028(4)
b (Å)	17.284(4)
c (Å)	19.998(4)
β (deg)	100.11(3)
V (Å^3)	6134(2)
Z	4
ρ (g/cm^3)	1.465
μ (mm^{-1})	0.980
F(000)	2764
crystal size (mm)	0.25 × 0.22 × 0.19
θ (deg)	2.93 to 27.49
Index ranges	$-23 \le h \le 23$
	$-22 \le k \le 22$
	$-25 \le l \le 25$
Absorption correction	Gaussian
Max. and min. transmission	0.8762 and 0.6650
GOF on F^2	1.001
R_1, R_2 [$I > 2\sigma(I)$]	0.0360, 0.0883
R_1, R_2 (all data)	0.0497, 0.0945
Largest diff. peak and hole (e·Å^{-3})	1.070 and -0.805

Table 18. Selected bond lengths [Å] and angles [°] for **14**.

Bond distances (Å)			
Nd1-O5B	2.3542(18)	Nd1-O5A	2.3946(19)
Nd1-O5	2.3663(19)	Nd1-O6B	2.4029(19)
Nd1-O6A	2.3900(18)	Nd1-O6	2.4319(19)
S1-C6	1.689(3)	S1-C1	1.714(3)
Bond angles (º)			
O5B-Nd1- O5	89.54(7)	O5B-Nd1-O6A	156.88(6)
O5-Nd1-O6A	80.06(7)	O5B-Nd1-O5A	132.72(6)
O5-Nd1-O5A	110.94(7)	O6A-Nd1-O5A	70.39(7)
O5B-Nd1-O6B	70.54(6)	O5-Nd1-O6B	79.31(7)
O6A-Nd1-O6B	87.17(7)	O5A-Nd1-O6B	152.48(6)
O5B-Nd1-O6	71.56(7)	O5-Nd1-O6	70.82(7)
O6A-Nd1-O6	122.89(6)	O5A-Nd1-O6	75.81(6)
O6B-Nd1-O6	131.23(6)	O5B-Nd1-N1	74.05(7)

Table 19. Crystal data and structure refinement for **15** and **16**.

	15	**16**
formula	$C_{68}H_{50}F_9N_2NdO_{10}S_2$	$C_{55}H_{36}F_9N_2NdO_{10}S_5$
fw	1434.46	1360.40
T (K)	153(2)	153(2)
crystal system	Triclinic	Triclinic
space group	*P*-1	*P*-1
a (Å)	11.845(2)	17.058(3)
b (Å)	16.396(3)	17.578(4)
c (Å)	17.674(4)	23.377(5)
α (deg)	90.22(3)	109.64(3)
β (deg)	106.92(3)	109.22(3)
γ (deg)	108.44(2)	93.18(3)
V (Å^3)	3097.7(11)	6124(2)
Z	2	4
ρ (g/cm^3)	1.538	1.475
μ (mm^{-1})	0.995	1.100
F(000)	1450	2724
crystal size (mm)	0.19 × 0.08 × 0.06	0.13 × 0.10 × 0.06
θ (deg)	3.01 to 25.00	2.94 to 25.00
Index ranges	$-14 \le h \le 13$	$-19 \le h \le 20$
	$-18 \le k \le 19$	$-20 \le k \le 20$
	$-21 \le l \le 18$	$-25 \le l \le 27$
Absorption correction	Gaussian	Gaussian
Max. and min. transmission	0.9427 and 0.8335	0.9369 and 0.8702
GOF on F^2	1.013	1.031
R_1, R_2 [$I > 2\sigma(I)$]	0.0645, 0.1275	0.1055, 0.2821
R_1, R_2 (all data)	0.1239, 0.1528	0.1727, 0.3378
Largest diff. peak and hole (e·Å^{-3})	1.004 and -0.855	-1.491 and 5.571

Table 20. Selected bond lengths [Å] and angles [°] for **15** and **16**.

		15	
Bond distances (Å)			
Nd1-O5A	2.399(5)	Nd1-O5B	2.400(5)
Nd1-O6	2.402(4)	Nd1-O6A	2.411(5)
Nd1-O5	2.416(5)	Nd1-O6B	2.427(5)
Nd1-N2	2.641(5)	Nd1-N1	2.650(6)
Bond angles (º)			
O5A-Nd1-O5B	74.13(16)	O5A-Nd1-O6	73.75(16)
O5B-Nd1-O6	72.46(15)	O5A-Nd1-O6A	70.42(16)
O5B-Nd1-O6A	128.27(16)	O6-Nd1-O6A	128.53(16)
O5A-Nd1-O5	87.46(16)	O5B-Nd1-O5	141.98(15)
O6-Nd1-O5	70.51(15)	O6A-Nd1-O5	72.18(16)
O5A-Nd1-O6B	89.86(16)	O5B-Nd1-O6B	69.10(16)
		16	
Bond distances (Å)			
Nd1-O6A	2.390(5)	Nd1-O5	2.403(4)
Nd1-O6B	2.406(5)	Nd1-O6	2.417(5)
Nd1-O5A	2.446(4)	Nd1-N2	2.610(5)
Nd1-O5B	2.372(5)	Nd1-N1	2.648(5)
Bond angles (º)			
O5B-Nd1-O6A	125.18(16)	O5B-Nd1-O5	134.97(18)
O6A-Nd1-O5	73.54(17)	O5B-Nd1-O6B	71.65(17)
O6A-Nd1-O6B	74.34(18)	O5-Nd1-O6B	76.85(16)
O5B-Nd1-O6	73.80(16)	O6A-Nd1-O6	139.05(17)
O5-Nd1-O6	69.74(18)	O6B-Nd1-O6	80.20(18)
O5B-Nd1-O5A	79.06(17)	O6A-Nd1-O5A	69.96(16)

Table 21. Crystal data and structure refinement for **18** and **19**.

	18	**19**
formula	$C_{68}H_{50}ErF_9N_2O_{10}S_2$	$C_{55}H_{36}ErF_9N_2O_{10}S_5$
fw	1457.48	1383.42
T (K)	153(2)	153(2)
crystal system	Triclinic	Triclinic
space group	*P*-1	*P*-1
a (Å)	11.969(2)	12.054(2)
b (Å)	16.260(3)	16.384(3)
c (Å)	17.851(4)	17.382(4)
α (deg)	91.68(3)	77.74(3)
β (deg)	106.70(3)	70.37(4)
γ (deg)	109.06(2)	71.05(3)
V (Å^3)	3115.8(11)	3037.3(12)
Z	2	2
ρ (g/cm^3)	1.554	1.513
μ (mm^{-1})	1.502	1.636
F(000)	1466	1378
crystal size (mm)	0.20 × 0.18 × 0.15	0.18 × 0.15 × 0.10
θ (deg)	3.03 to 25.00	1.71 to 25.00
Index ranges	$-14 \le h \le 12$	$-13 \le h \le 14$
	$-19 \le k \le 19$	$-19 \le k \le 19$
	$-20 \le l \le 21$	$-20 \le l \le 20$
Absorption correction	Gaussian	Gaussian
Max. and min. transmission	0.8060 and 0.7532	0.8535 and 0.7572
GOF on F^2	1.029	1.072
R_1, R_2 [$I > 2\sigma(I)$]	0.0750, 0.1902	0.0813, 0.2195
R_1, R_2 (all data)	0.1104, 0.2176	0.0970, 0.2394
Largest diff. peak and hole (e·Å^{-3})	3.305 and -1.160	3.044 and -2.122

Table 22. Selected bond lengths [Å] and angles [°] for **18** and **19**.

		18	
Bond distances (Å)			
Er1-O5A	2.283(6)	Er1-O6	2.308(6)
Er1-O6A	2.310(7)	Er1-O5	2.315(7)
Er1-O5B	2.316(6)	Er1-O6B	2.326(7)
Er1-N1	2.536(7)	Er1-N2	2.537(8)
Bond angles (º)			
O5A-Er1-O6	75.3(2)	O5A-Er1-O6A	73.0(2)
O6-Er1-O6A	134.0(2)	O5A-Er1-O5	86.8(2)
O6-Er1-O5	72.7(2)	O6A-Er1-O5	73.1(3)
O5A-Er1-O5B	73.3(2)	O6-Er1-O5B	71.6(2)
O6A-Er1-O5B	127.4(3)	O5-Er1-O5B	142.4(2)
O5A-Er1-O6B	95.0(2)	O6-Er1-O6B	143.0(2)
		19	
Bond distances (Å)			
Er1-O5	2.302(7)	Er1-O6A	2.304(7)
Er1-O6	2.308(7)	Er1-O5B	2.310(7)
Er1-O6B	2.320(7)	Er1-O5A	2.328(7)
Er1-N2	2.520(8)	Er1-N1	2.534(7)
Bond angles (º)			
O5-Er1-O6A	124.0(3)	O5-Er1-O6	73.8(3)
O6A-Er1-O6	73.3(3)	O5-Er1-O5B	138.3(3)
O6A-Er1-O5B	74.3(3)	O6-Er1-O5B	77.9(3)
O5-Er1-O6B	73.9(3)	O6A-Er1-O6B	140.8(3)
O6-Er1-O6B	80.8(3)	O5B-Er1-O6B	71.8(3)
O5-Er1-O5A	74.1(3)	O6A-Er1-O5A	72.8(2)

Table 23. Crystal data and structure refinement of **20**.

formula	$C_{90}H_{73}N_2O_{10}S_2Yb$
fw	1579.66
T (K)	153(2)
crystal system	Monoclinic
space group	$P2_1/c$
a (Å)	18.587(3)
b (Å)	18.122(2)
c (Å)	22.505(2)
β (deg)	91.57(1)
V (Å^3)	7577.7(16)
Z	4
ρ (g/cm^3)	1.385
μ (mm^{-1})	1.352
F(000)	3236
crystal size (mm)	0.32 × 0.26 × 0.20
θ (deg)	2.91 to 27.48
Index ranges	$-22 \le h \le 22$
	$-21 \le k \le 20$
	$-26 \le l \le 26$
Absorption correction	Gaussian
Max. and min. transmission	0.6552 and 0.7561
GOF on F^2	1.084
R_1, R_2 [I > 2σ (I)]	0.0383, 0.0848
R_1, R_2 (all data)	0.0621, 0.0954
Largest diff. peak and hole (e.Å^{-3})	0.929 and -1.052

Table 24. Selected bond lengths [Å] and angles [°] of **20**.

Bond distances (Å)			
Yb1-O5	2.257(3)	Yb1-O6A	2.262(3)
Yb1-O6	2.265(3)	Yb1-O5A	2.277(3)
Yb1-O5B	2.287(3)	Yb1-O6B	2.305(3)
Yb1-N1	2.517(3)	Yb1-N2	2.543(4)
S1-C1	1.720(5)	S1-C6	1.724(5)
S2-C20	1.717(6)	S2-C19	1.724(5)
N1-C11	1.324(5)	N1-C10	1.361(5)
Bond angles (º)			
O5-Yb1-O6A	82.70(11)	O5-Yb1-O6	73.36(11)
O6A-Yb1-O6	77.94(11)	O5-Yb1-O5A	78.31(11)
O6A-Yb1-O5A	74.42(10)	O6-Yb1-O5A	142.45(10)
O5-Yb1-O5B	146.48(11)	O6A-Yb1-O5B	76.91(10)
O6-Yb1-O5B	76.51(11)	O5A-Yb1-O5B	120.21(11)
O5-Yb1-O6B	139.94(11)	O6A-Yb1-O6B	118.44(11)
O6-Yb1-O6B	140.67(10)	O5A-Yb1-O6B	75.98(10)
O5B-Yb1-O6B	73.58(11)	O5-Yb1-N1	105.65(11)
O6A-Yb1-N1	144.06(11)	O6-Yb1-N1	71.55(11)
O5-Yb1-N2	74.59(11)	O6B-Yb1-N1	77.64(10)
O5B-Yb1-N1	77.89(11)	O5A-Yb1-N1	141.18(11)
O6A-Yb1-N2	148.57(11)	O6-Yb1-N2	114.76(11)

Table 25. Crystal data and structure refinement for **23** and **24**.

	23	**24**
formula	$C_{167}H_{122}N_4Nd_2O_{12}S_8$	$C_{64}H_{39}ClF_9N_2NdO_6S_4$
fw	2921.65	1410.90
T (K)	153(2)	153(2)
crystal system	triclinic	triclinic
space group	P-1	P-1
a (Å)	14.0286(2)	12.00700(10)
b (Å)	17.0151(3)	14.3083(2)
c (Å)	17.0821(4)	18.8278(2)
α (deg)	104.7895(7)	71.2200(10)
β (deg)	107.3236(7)	77.1200(10)
γ (deg)	107.8097(10)	73.6600(10)
V (Å^3)	3426.34(11)	2907.37(6)
Z	1	2
ρ (g/cm^3)	1.416	1.612
μ (mm^{-1})	0.937	1.167
F(000)	1496	1414
crystal size (mm)	0.35 × 0.30 × 0.25	0.23 × 0.12 × 0.08
θ (deg)	2.97 to 25	1 to 27.5
Index ranges	$-16 \le h \le 16$	$-15 \le h \le 15$
	$-19 \le k \le 20$	$-18 \le k \le 18$
	$-19 \le l \le 20$	$-24 \le l \le 19$
Absorption correction	Gaussian	Multi-scan
Max. and min. transmission	0.5987 and 0.6892	0.72 and 0.91
GOF on F^2	0.911	1.046
R_1, R_2 [I > 2σ (I)]	0.0780, 0.1863	0.0296, 0.0625
R_1, R_2 (all data)	0.1216, 0.2232	0.0391, 0.0667
Largest diff. peak and hole (e·Å^{-3})	3.910 and -0.870	1.003 and -0.824

Table 26. Selected bond lengths [Å] and angles [°] of **23**.

Bond distances (Å)			
Nd1-O1B	2.291(9)	Nd1 O2B	2.372(9)
Nd1-O1	2.342(9)	Nd1-O2	2.372(9)
Nd1-O2A	2.440(9)	Nd1-O1A	2.434(10)
Nd1-N1	2.645(11)	Nd1-N2	2.668(11)
S1-C1	1.714(15)	S1-C4	1.754(19)
S2-C8	1.646(15)	S2-C5	1.759(16)
Bond angles (º)			
O1B-Nd1-O1	144.9(3)	O1B-Nd1-O2B	71.1(3)
O1-Nd1-O2B	73.9(3)	O1B-Nd1-O2	143.4(3)
O1-Nd1-O2	71.1(3)	O2B-Nd1-O2	144.7(3)
O1B-Nd1-O2A	80.6(3)	O1-Nd1-O2A	128.1(3)
O2B-Nd1-O2A	134.3(3)	O2-Nd1-O2A	73.9(3)
O1B-Nd1-O1A	102.4(3)	O1-Nd1-O1A	74.5(3)
O2B-Nd1-O1A	81.1(3)	O2-Nd1-O1A	93.5(3)
O2A-Nd1-O1A	70.7(3)	O1B-Nd1-N1	70.5(3)
O1-Nd1-N1	127.9(3)	O2B-Nd1-N1	120.5(3)
O2-Nd1-N1	79.5(3)	O2A-Nd1-N1	80.1(3)
O1A-Nd1-N1	150.7(3)	O1B-Nd1-N2	93.9(3)
O1-Nd1-N2	76.2(3)	O2B-Nd1-N2	78.2(3)

Table 27. Selected bond lengths [Å] and angles [°] of **24**.

Bond distances (Å)			
Nd1-O6	2.3763(15)	Nd1-O2	2.3837(15)
Nd1-O4	2.4065(16)	Nd1-O5	2.4199(16)
Nd1-O1	2.4228(15)	Nd1-O3	2.4325(16)
Nd1-N2	2.5970(17)	Nd1-N1	2.6359(18)
S3-C20	1.719(2)	S3-C17	1.732(2)
S2-C5	1.727(2)	S2-C8	1.728(2)
Bond angles (º)			
O6-Nd1-O2	79.16(6)	O6-Nd1-O4	77.71(6)
O2-Nd1-O4	73.83(5)	O6-Nd1-O5	70.03(5)
O2-Nd1-O5	86.57(6)	O4-Nd1-O5	144.88(5)
O6-Nd1-O1	130.31(5)	O2-Nd1-O1	70.82(5)
O4-Nd1-O1	127.10(5)	O5-Nd1-O1	69.53(6)
O6-Nd1-O3	146.31(6)	O2-Nd1-O3	86.29(5)
O4-Nd1-O3	69.06(5)	O5-Nd1-O3	139.61(5)
O1-Nd1-O3	70.58(6)	O6-Nd1-N2	118.10(6)
O2-Nd1-N2	151.01(5)	O4-Nd1-N2	130.20(5)
O5-Nd1-N2	78.98(5)	O1-Nd1-N2	80.58(5)
O3-Nd1-N2	88.64(5)	O6-Nd1-N1	83.61(5)
O2-Nd1-N1	145.90(5)	O4-Nd1-N1	73.86(5)

Table 28. Crystal data and structure refinement of **26**.

formula	$C_{73}H_{49}N_2O_6S_4Yb$
fw	1351.42
T (K)	153(2)
crystal system	Triclinic
space group	P-1
a (Å)	12.136(5)
b (Å)	16.461(5)
c (Å)	17.892(4)
α (deg)	91.682(5)
β (deg)	109.646(6)
γ (deg)	90.502(5)
V (Å^3)	3364(2)
Z	2
ρ (g/cm^3)	1.334
μ (mm^{-1})	1.565
F(000)	1366
crystal size (mm)	0.15 × 0.08 × 0.05
θ (deg)	2.91 to 27.48
Index ranges	$-14 \le h \le 14$
	$-19 \le k \le 19$
	$-21 \le l \le 20$
Absorption correction	Gaussian
Max. and min. transmission	0.7991 and 0.9258
GOF on F^2	0.989
R_1, R_2 [I > 2σ (I)]	0.0931, 0.1904
R_1, R_2 (all data)	0.1887, 0.2222
Largest diff. peak and hole (e.Å^{-3})	1.331 and -0.697

Table 29. Selected bond lengths [Å] and angles [°] of **26**.

Bond distances (Å)			
Yb1-O2	2.238(7)	Yb1-O4	2.263(7)
Yb1-O5	2.266(8)	Yb1-O3	2.267(8)
Yb1-O6	2.277(7)	Yb1-O1	2.283(8)
Yb1-N1	2.513(9)	Yb1-N2	2.548(8)
S1-C1	1.647(16)	S1-C4	1.679(17)
S2-C8	1.711(12)	S2-C5	1.719(11)
Bond angles (º)			
O2-Yb1-O4	74.3(3)	O2-Yb1-O5	137.8(3)
O4-Yb1-O5	73.8(3)	O4-Yb1-O3	74.2(3)
O2-Yb1-O3	81.9(3)	O5-Yb1-O3	114.6(3)
O2-Yb1-O6	148.0(3)	O4-Yb1-O6	123.9(3)
O5-Yb1-O6	74.0(3)	O3-Yb1-O6	79.2(3)
O2-Yb1-O1	72.8(3)	O4-Yb1-O1	138.9(3)
O5-Yb1-O1	146.3(3)	O3-Yb1-O1	77.4(3)
O6-Yb1-O1	78.0(3)	O2-Yb1-N1	105.3(3)
O4-Yb1-N1	141.6(3)	O5-Yb1-N1	83.9(3)
O3-Yb1-N1	144.1(3)	O6-Yb1-N1	77.0(3)
O3-Yb1-N2	147.8(3)	O5-Yb1-N2	74.9(3)
O1-Yb1-N1	71.8(3)	O2-Yb1-N2	72.9(3)

Chapter 4: Electrogenerated Chemiluminescence of Conducting Metallopolymers Incorporating Cyclometalated Pt(II) Complexes

INTRODUCTION

Electrogenerated Chemiluminescence (ECL)

Electrogenerated chemiluminescence (ECL) is the process whereby species generated at electrodes undergo high-energy electron-transfer reactions to form excited states that emit light.[1-6] ECL was first reported in the 1960s through the use of rubrene, 9,10-diphenylanthracene (DPA), and related compounds.[7,8] Then in the 1970s, ECL was observed by reacting electrogenerated $[Ru(bpy)_3]^{3+}$ (where bpy refers to 2,2'-bipyridine) with tri-*n*-propylamine (TPrA) to create an electronically excited state that emits at approximately 610 nm which has found broad applications in commercial ECL immunoassays and DNA analyses.[9] ECL based on $Ru(bpy)_3^{2+}$ and its derivatives has been mostly studied due to their good stability and high ECL efficiency in aqueous media, favorable electrochemical properties, and compatibility with a wide range of analytes. $Ru(bpy)_3^{2+}$ ECL has been widely used for the determination of numerous coreactants such as oxalate,[10] alkylamines,[11,12] amino acids,[13] ascorbic acid,[14] and many pharmaceutical compounds.[15] More importantly, the $Ru(bpy)_3^{2+}$/TPrA ECL system could provide extremely sensitive label detection at subpicomolar concentration as well as an extremely wide dynamic range of greater than six orders of magnitude. After more than 40 years of study, ECL has now become a very powerful analytical technique and been widely used in the areas of, for example, immunoassay, food and water testing, and biowarfare agent detection.[4] ECL has also been successfully exploited as a detector of flow injection analysis (FIA), high-performance liquid chromatography (HPLC), capillary electrophoresis, and micro total analysis.[4]

There are two dominant pathways through which ECL can be produced, namely the annihilation and coreactant pathways. Although modern ECL applications are almost exclusively based on coreactant ECL, the early ECL studies originated with ion annihilation ECL. In the annihilation pathway (Scheme 5), both oxidized (D^+) and reduced species (A^-) are produced on the electrode surface by a potential step or sweep. These species then undergo high energy electron transfer reactions to produce a ground (D) state and an electronically excited state (A^*) which then relaxes by emission.

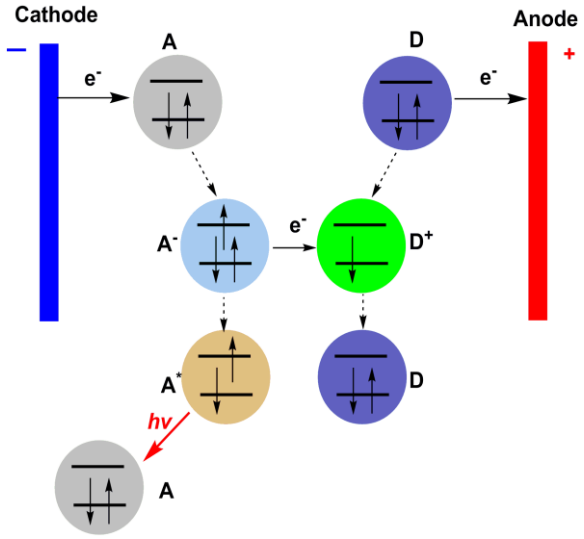

Scheme 5. Ion annihilation pathway of ECL. A and D could be the same species. Adapted from reference 4.

At present, all commercially available ECL analytical instruments are based on coreactant ECL technology. Therefore, understanding the ECL mechanisms of the relevant systems is important. Unlike ion annihilation ECL, in which electrolytic generation of both the oxidized and reduced ECL precursors are required, coreactant ECL is usually generated by one directional potential scanning on the electrode in the presence

of both the luminophore and a deliberately added reagent (coreactant). Depending on the polarity of the applied potential, both the luminophore and the coreactant species can be first oxidized or reduced at the electrodes to form radicals. The intermediates arised from the coreactant then decompose to produce a powerful reducing or oxidizing species that reacts with the oxidized or reduced luminophore to produce the excited states that emit light. For example, oxalate ion ($C_2O_4^{2-}$) is the first coreactant discovered.[10] ECL of $Ru(bpy)_3^{2+}$/oxalate system is produced as follows.

$$Ru(bpy)_3^{2+} - e^- \longrightarrow Ru(bpy)_3^{3+}$$

$$Ru(bpy)_3^{3+} + C_2O_4^{2-} \longrightarrow Ru(bpy)_3^{2+} + C_2O_4^{\bullet -}$$

$$C_2O_4^{\bullet -} \longrightarrow CO_2^{\bullet -} + CO_2$$

$$Ru(bpy)_3^{3+} + CO_2^{\bullet -} \longrightarrow Ru(bpy)_3^{2+*} + CO_2$$

$$Ru(bpy)_3^{2+} + CO_2^{\bullet -} \longrightarrow Ru(bpy)_3^{+} + CO_2$$

$$Ru(bpy)_3^{3+} + Ru(bpy)_3^{+} \longrightarrow Ru(bpy)_3^{2+} + Ru(bpy)_3^{2+*}$$

$$Ru(bpy)_3^{2+*} \longrightarrow Ru(bpy)_3^{2+} + h\nu$$

Scheme 6. Coreactant ECL of $Ru(bpy)_3^{2+}$. Adapted from reference 1.

In an aqueous solution, $Ru(bpy)_3^{2+}$ is first oxidized at the electrode to the $Ru(bpy)_3^{3+}$ cation, which is then capable of oxidizing the oxalate ($C_2O_4^{2-}$) in the diffusion layer close to the electrode surface to form an oxalate radical anion ($C_2O_4^{\bullet -}$). This radical anion can rapidly form a highly reducing radical anion ($CO_2^{\bullet -}$), which then either reduces the $Ru(bpy)_3^{3+}$ complex to from excited state ($Ru(bpy)_3^{2+*}$) or reduces $Ru(bpy)_3^{2+}$ to form $Ru(bpy)_3^{+}$ that reacts with $Ru(bpy)_3^{3+}$ to generate the excited state. The excited state emits light with $\lambda_{max} \sim 620$ nm.

ECL is a form of chemiluminescence (CL). CL is the emission of light with limited emission of heat (luminescence), as the result of a chemical reaction. There are numerous reactions where the decomposition of the species results in the production of excited states and emission. In contrast, the excited state and emission in ECL is initiated and controlled by changing an electrode potential. As an analytical tool, ECL has several advantages: (1) we can have time and position control. (2) The generation of the excited states in ECL can be selectively controlled by varying the electrode potentials, which makes ECL more selective than CL. (3) ECL is usually a nondestructive technique. The ECL emitters can be regenerated after the ECL emission. Since ECL is a combination between electrochemical and spectroscopic methods, it has many distinct advantages over other spectroscopy-based detection systems. For example, ECL does not need a light source which excludes a background optical signal.

ECL of Metal Complexes

Metal complexes are important in the rapid development of ECL from a laboratory curiosity to a useful analytical technique. In particular, $Ru(bpy)_3^{2+}$ and its derivatives have played a pivotal role because of their excellent properties in photochemistry, electrochemistry, and spectroscopic qualities required of ECL luminophores.[2,16,17] In early 1980s a method for the binding of $Ru(bpy)_3^{2+}$ to target biomolecules (e.g. antibodies, proteins, and nucleic acids) triggered the renewed interest in discovering new ECL luminophores. Although $Ru(bpy)_3^{2+}$ is an ideal luminophore for selective and sensitive analytical methods, it would be useful to have other ECL labels with a wide range of wavelengths so that simultaneous determination of several species in a single sample is possible.

$Ru(bpy)_3^{2+}$ has become the most thoroughly studied ECL molecule for a number of reasons: (1) Strong luminescence. (2) Strong solubility in both aqueous and nonaqueous solution at room temperature. (3) Reversible one-electron transfer reactions at easily attainable potentials. (4) Stable reduced and oxidized species. $Ru(bpy)_3^{2+}$ has a photoluminescence efficiency of 6.82% and an ECL efficiency of 5%.[1] Different organic ligands bound to Ru^{2+} have been studied, such as 2-(2-pyridyl)-benzimidazole (PBIm-H), 2-(2-pyridyl)-*N*-methylbenzimidazole (PBIm-Me), 4,4′-dimethyl-2,2′-bipyridyl (dmbpy), and 1,10-phenanthroline (phen).[1] The ECL efficiency generally increases as fewer electron-donating ligands are introduced to the complexes. Because the donor property of the ligands increases in the order of phen < bpy < dmbpy , PBIm-Me < PBIm-H, the ECL efficiency of the Ru(II) complexes decreases in the order of phen > bpy > dmbpy > PBIm-Me > PBIm-H.

The extension of $Ru(bpy)_3^{2+}$ ECL to the osmium system has been limited due to the large spin-orbit coupling in the osmium system which causes shorter excited state lifetime and lower emission efficiencies. The first report of osmium ECL was $Os(phen)_3^{2+}$ in DMF which has an ECL efficiency of 40% using $Ru(bpy)_3^{2+}$ at 100% as a relative standard.[18]

Extremely efficient ECL from cyclometalated Ir^{3+} complexes has been recently reported, in which the ECL efficiency values from some chelates were even higher than the corresponding photoluminescence efficiencies.[19] The first group of complexes have a common formula of $(pq)_2Ir(L)$, in which pq is a 2-phenylquinoline anion and L is a monoanionic bidentate ligand, e.g. acetylacetonate (acac) and picolinate (pico). Their electrochemical and spectroscopic behaviors are similar to those of $Ru(bpy)_3^{2+}$. $[(ppy)_2Ir(L)]^+$, where ppy = 2-phenylpyridine anion and L = bpy and phen, show maximum emissions from photoluminescence and ECL all close to 605 nm. The TPrA

coreactant ECL intensities of $[(ppy)_2Ir(L)]^+$ are 2 (L = bpy) and 4 (L = phen) times of the $Ru(bpy)_3^{2+}$/TPrA system, respectively.[20]

Compared with Ru^{2+} and Ir^{3+} complexes, the ECL study of Pt^{2+} complexes are relatively rare. ECL emission from $Pt(q)_2$ (q = 8-quinolato) was generated by a terminal voltage of 4 V. The source of ECL was annihilation of the $Pt(q)_2^+$ and $Pt(q)_2^-$ species.[21] ECL of Pt(II) octaethyl porphyrin, PtOEP, was generated by the recombination of radical cation and anion of PtOEP with a low efficiency.[22]

ECL of Polymer Films

There are limited studies dealing with ECL from pure active materials deposited as solid films on electrodes. The ECL properties of the metallopolymer $[Ru(bpy)_2(PVP)_{10}]^{2+}$, where PVP is poly(4-vinylpyridine), have been studied in detail predominantly through the use of oxalate, TPrA, and other small molecules as coreactants.[23] The concentrations of luminophores in thin films are much higher than those in solution phase, typically micromolar in solution compared to molar concentrations within films. The high concentrations found in thin films may limit the overall luminescence efficiency by self-absorbance in light-stimulated emission. However, surface immobilization may bring significant positive benefits. For example, the overall efficiency of the ECL for the metallopolymer film is almost four times higher than that for $[Ru(bpy)_2(PVP)_{10}]^{2+}$ dissolved in solution.

ECL of tris(4-vinyl-4'-methyl-2,2'-bipyridyl)ruthenium(II) has been reported by electropolymerization of ruthenium monomer complex on the electrode. When the potential is pulsed between +1.5 and -1.5 V (vs SCE) in an acetonitrile electrolyte, the modified electrodes exhibit an orange luminescence (650 nm).[24]

ECL of polymers is attractive for light-emitting devices, but there are still many issues for practical application. The operation theory and degradation mechanism are still under investigation.

Scope of Our Research

Although a large body of literature regarding electrophosphorescent heavy-metal complexes has been reported, utilization of Pt(II) complexes in conducting polymers for PLEDs application has not been widely studied. In particular, the ECL study of conducting metallopolymers is rather rare. To advance the development of novel Pt(II)-containing conducting metallopolymers to fill this gap, I take advantage of the luminescence of cyclometalated Pt(II) complexes coupled with the electrically conducting character of polythiophene systems. Three new ligands, 2,6-di(thiophen-2-yl)pyridine (**L5**), 1,3-bis[5-(3,4-dibutyl-2,2':5,2''-terthiophene)-pyridine-2-yl]benzene (**L6**), and 1,3-bis(4-(3,4-dioctyl-2,2':5',2''-terthiophene)-1H-pyrazol-1-yl)benzene (**L7**) were prepared. I have chosen the cyclometalated Pt(II) complexes of the N^C^N- and S^N^C-coordinating ligands considering the strong ligand field influence of the aromatic carbon atom, which increases the energy gap of the metal centered excited states, thus preventing the quenching by fast radiationless decay through the metal centered states.[25] The cyclometalated Pt(II) complexes have been prepared and characterized. Conducting metallopolymer films have been prepared through electropolymerization. The photophysical properties and ECL of the Pt(II) complexes and their corresponding polymers have been studied.

EXPERIMENTAL

General Methods

Air- and moisture-sensitive reactions were carried out in oven-dried glassware using standard Schlenk techniques under an inert atmosphere of dry argon. Dry DMF was used from EMD as sure-seal bottles. Bromine was obtained from EMD. 3,4-Dibromothiophene was purchased from Oakwood. Magnesium turnings were purchased from J. T. Baker. Tri-*n*-butyltin chloride and 1,3-benzenediboronic acid were purchased from Alfa Aesar. 1,3-Bis(diphenylphosphino)propane nickel(II) chloride and trans-dichlorobis(triphenylphosphine)palladium(II) were obtained from Strem. Toluene, diethyl ether and CH_2Cl_2 were dried using a double-column anhydrous solvent system (Innovative Technologies, Newburyport, MA) and further degassed via nitrogen purge prior to use. Other reagents were used as received from Aldrich. NMR spectra were recorded with Varian 400 MHz (^1H and $^{13}C\{^1H\}$) spectrometer. High- and low-res mass spectrometry was carried out by Thermo Finngan TSQ 700 and Waters Autospec Ultima. Elemental analysis was performed by QTI, Whitehouse, NJ (www.qtionline.com). X-ray photoelectron spectroscopy (XPS) was carried out on a PHI 5700 XPS system equipped with a dual Mg X-ray source and monochromatic Al X-ray source complete with depth profile and angle-resolved capabilities. The microwave assisted reaction was performed in a CEM Discover reactor.

Crystal Structure Determination

A suitable crystal was mounted on a glass fiber and placed in the low-temperature nitrogen stream. The data were collected on a Nonius Kappa CCD diffractometer using a graphite monochromator with MoKα radiation (λ = 0.71073Å). Data reduction was performed using DENZO-SMN.[26] The structure was solved by direct methods using

SIR97[27] and refined by full-matrix least-squares on F^2 with anisotropic displacement parameters for the non-H atoms using SHELXL-97.[28]

Electrochemistry

Electrochemical syntheses and studies were performed in a dry-box under a nitrogen atmosphere using a GPES system from Eco. Chemie B. V.. All the electrochemical experiments were carried out in a three-electrode cell with a $Ag/AgNO_3$ reference electrode (silver wire dipped in a 0.01 M silver nitrate solution with 0.1 M $TBAPF_6$ in CH_3CN), a Pt button working electrode, and a Pt wire coil counter electrode. Potentials were relative to this 0.01 M $Ag/AgNO_3$ reference electrode. Ferrocene was used as an external reference to calibrate the reference electrode before and after experiments were performed and that value was used to correct the measured potentials. The supporting electrolyte was 0.1 M $TBAPF_6$ that was purified by recrystallization three times from hot ethanol before being dried for 3 days at 100 ^oC under active vacuum.

Photoluminescent Measurements

Absorption spectra were recorded on a Varian Cary 6000i spectrophotometer with Starna Quartz Fluorometer Cells with a pathlength of 10 mm. Luminescent measurements were recorded on a Photon Technology International QM 4 spectrophotometer equipped with a 6-inch diameter K Sphere-B integrating sphere. Quantum yields Q have been calculated using the equation $Q_x/Q_r = A_x \cdot n_x^2 \cdot / A_r \cdot n_r^2$, where x refers to the sample, and r, to the reference; A is the integrated area under the emission spectrum, and n is the refractive index of the solution. All photoluminescent measurements of polymer films were performed on films that were fully reduced.

Electrogenerated Chemiluminescence Measurements

The electrochemical cell is composed of an ITO working electrode, a Ag wire quasireference electrode in non-aqueous solution and a Pt wire counter electrode. Cyclic voltammograms (CVs) were recorded on a model 660 electrochemical workstation (CH Instruments, Austin, TX). Faradaic current and ECL transients were simultaneously recorded using an Autolab electrochemical workstation (Eco Chemie, The Netherlands) coupled with a photomultiplier tube (PMT, Hammamatsu R4220p, Japan) held at -750 V with a high-voltage power supply (Kepco, Flushing, NY). The photocurrent produced at the PMT was converted to a voltage signal with an electrometer/high resistance system (Keithley, Cleveland, OH) and fed into the external input channel of an analog-to-digital converter (ADC) of the Autolab.

Synthesis

Synthesis of 2,6-Di(thiophen-2-yl)pyridine (L5)

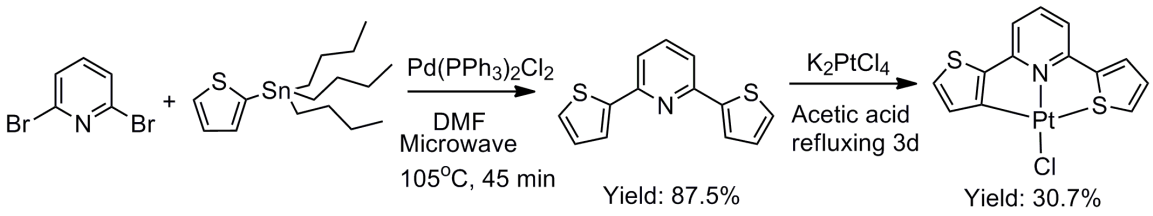

Scheme 7. Synthesis of **L5** and **27**.

2,6-Dibromopyridine (1.42 g, 6.0 mmol), 2-(tributylstannyl)thiophene (5.00 g, 13.4 mmol) and $Pd(PPh_3)_2Cl_2$ (280.8 mg, 0.4 mmol) were combined in DMF (30 mL) in an 80 mL microwave reaction vessel. The reaction was run in the microwave reactor for 45 min at 300 W and 105 ºC. The reaction mixture was dissolved in CH_2Cl_2 and washed with water (3 × 100 mL). The organic phase was dried over Na_2SO_4 and reduced to dryness. The product was purified by column chromatography (silica gel, CH_2Cl_2 :

hexanes = 2 : 1) to yield a light yellow solid (1.49 g, 87.5%). ^{1}H NMR (400 MHz, $CDCl_3$): δ (ppm) = 7.69 (t, *J* = 8.0, 1H), 7.63 (dd, *J* = 1.2, 3.6, 2H), 7.50 (d, = 7.6, 2H), 7.41 (dd, *J* =1.2, 5.2, 2H), 7.13 (t, *J* = 4.4, 2H). ^{13}C{^{1}H} NMR (100 MHz, $CDCl_3$): δ (ppm) = 151.1, 143.8, 136.3, 126.9, 126.8, 123.7, 115.7.

Synthesis of PtL5Cl (27)

A mixture of **L5** (0.122 g, 0.5 mmol) and K_2PtCl_4 (0.208 g, 0.5 mmol) in acetic acid (30.0 mL) was refluxed for three days. After cooling, the solid was filtered out and washed with methanol and diethyl ether. Slow evaporation of the resulting orange powder in tetrahydrofuran at room temperature affords red crystals (74.9 mg, 30.7%) suitable for X-ray diffraction analysis. ^{1}H NMR (400 MHz, DMSO-d_6): δ (ppm) = 7.64 (d, *J* = 8.0, 1H), 7.59 (d, *J* = 4.8, 1H), 7.51 (t, *J* = 7.6, 1H), 7.22 (d, *J* = 6.0, 1H), 7.12 - 7.15 (m, 2H), 7.01 (d, *J* = 6.0, 1H), 6.90 (d, *J* = 7.6, 1H). CI-MS (CH_2Cl_2) m/z: 473 [**27**]$^{+}$. Elemental anal. calcd. (Found) for **27·0.5THF**, $C_{16}H_{15}ClNO_{0.5}PtS_2$: C, 36.68 (36.25); H, 2.89 (2.02); N, 2.67 (3.13).

Synthesis of PtL5Pz (28)

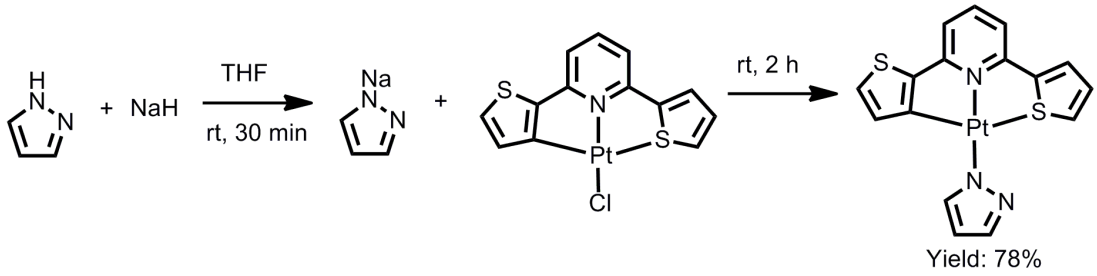

Scheme 8. Synthesis of **28**.

NaH (9.6 mg, 0.4 mmol) was added to a schlenk flask. Dry THF (20.0 mL) was transferred under Ar. Pyrazole (27.2 mg, 0.4 mmol) was added to the solution under Ar slowly with bubbles forming. The mixture was stirred at room temperature for 30 min to

get a clear solution. Complex **27** (146.1 mg, 0.3 mmol) was added to the above solution. Orange solution was obtained after another two hours of stirring. The reaction mixture was dissolved in CH_2Cl_2 and washed with $NH_4Cl_{(aq)}$ and water (3 × 100 mL). The organic phase was dried over Na_2SO_4 and reduced to dryness. The product was purified by column chromatography (silica gel, CH_2Cl_2 : hexanes = 2 : 1) to yield a yellow powder (118 mg, 78 %). ^{1}H NMR (400 MHz, $CDCl_3$): δ (ppm) = 7.87 (br, 1H), 7.77 (t, *J* = 7.6, 1H), 7.45 (d, *J* = 4.8, 1H), 7.40 (dd, *J* = 1.2, 7.6, 1H), 7.24 (dd, *J* = 1.2, 4.8, 1H), 7.20 (dd, *J* = 1.6, 7.6, 1H), 7.13 (dd, *J* = 0.8, 2.4, 1H), 7.03 (dd, *J* = 0.8, 2.4, 1H), 6.89 (t, *J* = 4.4, 1H), 6.85 (d, *J* = 4.4, 1H), 5.77 (t, *J* = 2.0, 1H). CI-MS (CH_2Cl_2) m/z: 505 [**28**]$^+$. Elemental anal. calcd. (Found) for **28**, $C_{16}H_{11}N_3PtS_2$: C, 38.09 (38.18); H, 2.20 (2.15); N, 8.33 (8.20).

Synthesis of 1,3-Bis[5-(3,4-dibutyl-2,2':5,2''-terthiophene)-pyridine-2-yl]benzene (L6) and 29

3,4-Dibutyl-2,2':5',2''-terthiophene was prepared according to the literature.[29]

5-(Tributylstannyl)-3,4-dibutyl-2,2':5',2''-terthiophene. A 50 mL THF solution of 3,4-dibutyl-2,2':5',2''-terthiophene (3.606 g, 10.0 mmol) was cooled in a dry ice/acetone bath, and 6.875 mL of *n*-butyllithium (11.0 mmol, 1.6 M solution in hexane) was added. After stirring for one hour, the cooling bath was removed. Tributyltin chloride (3.584 g, 11.0 mmol) was added. The mixture was stirred at room temperature for one hour, then quenched with saturated ammonium chloride solution. The mixture was extracted with hexanes. The organic phase was washed with brine, dried over Na_2SO_4 and evaporated to give the crude product, which was further purified by vacuum distillation to get the target product (yield: 5.527 g, 85%). ^{1}H NMR (400 MHz, CD_2Cl_2): *δ* (ppm) = 7.29 (dd, *J* = 5.2, 1.2, 1H), 7.26 (dd, *J* = 3.2, 1.6, 1H), 7.13 (dd, *J* = 3.6, 1.2, 1H), 7.11 (dd, *J* = 3.6, 2.4, 1H), 7.06 (dd, *J* = 3.6, 1.2, 1H), 7.29 (dd, *J* = 5.2, 1.2, 1H),

2.17 (m, CH_2, 10H), 1.36 (m, CH_2, 10H), 1.11 (m, CH_2, 10H), 0.97 (m, CH_3, 15H). $^{13}C\{^1H\}$ NMR (100 MHz, CD_2Cl_2): δ (ppm) = 141.5, 140.0, 139.5, 135.6, 129.3, 127.3, 126.8, 126.6, 125.7, 125.1, 32.9, 28.9, 27.6, 27.0, 22.7, 14.0, 13.7, 10.9.

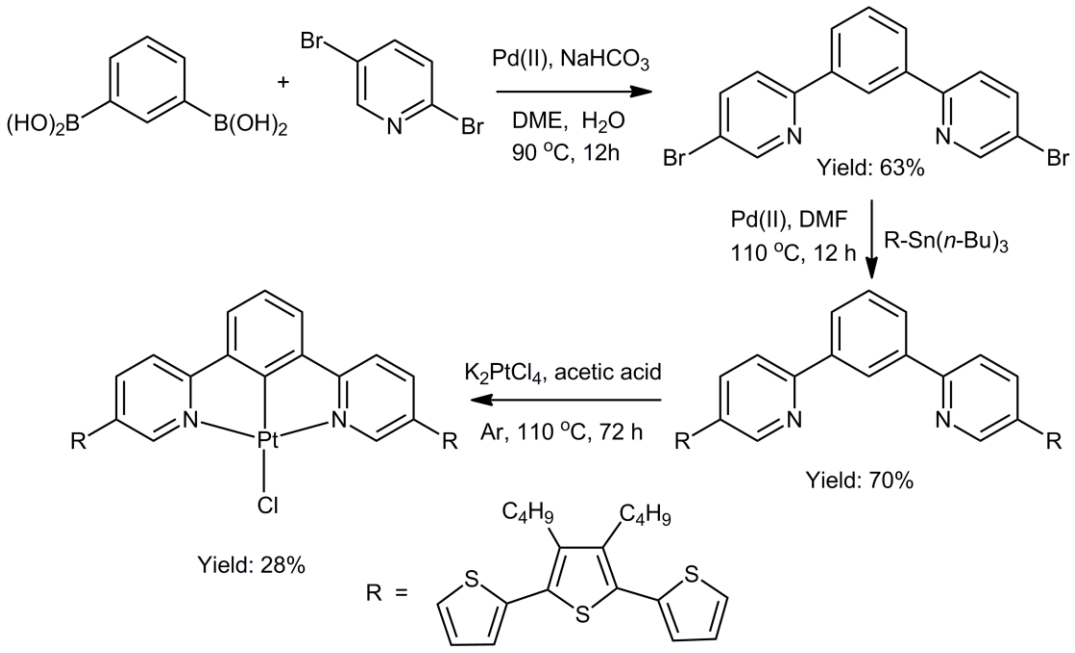

Scheme 9. Synthesis of **L6** and **29**.

1,3-Bis(2-bromopyridine-5-yl)benzene. 2,5-Dibromopyridine (1.422 g, 6.0 mmol), $Pd(PPh_3)_4$ (0.306 g, 0.264 mmol) and dimethoxylethane (20.0 mL) were added to a 100 mL three-necked flask. N_2 was bubbled through the mixture for 20 min, then 1,3-phenyldibronic acid (0.332 g, 2.0 mmol) and N_2 bubbled $NaHCO_{3(aq)}$ (1.0 M, 13.0 mL) were added. The resulting solution was refluxed at 90 ^oC for 12 h. After cooling, 100 mL of CH_2Cl_2 was added to the resulting red solution. The solution was then washed with saturated $NH_4Cl_{(aq)}$, $NaCl_{(aq)}$, and H_2O. The separated organic phase was dried over Na_2SO_4 and evaporated to give the crude product. Further purification on silica gel column using CH_2Cl_2 / hexanes (2 : 1) as eluent yields the white powder (0.490 g, 63%).

^{1}H NMR (400 MHz, $CDCl_3$): δ (ppm) = 8.76 (dd, J = 2.2, 0.6, 2H), 8.62 (t, J = 2.0, 1H), 8.05 (dd, J = 8.0, 1.6, 2H), 7.89 (dd, J = 8.4, 2.0, 2H), 7.74 (dd, J = 8.4, 0.8, 2H), 7.58 (t, J = 7.6, 1H). ^{13}C{^{1}H} NMR (100 MHz, $CDCl_3$): δ (ppm) = 155.6, 151.0, 139.7, 139.1, 129.7, 127.8, 125.4, 122.0, 119.9. Elemental anal. calcd. (Found) for $C_{16}H_{10}Br_2N_2$: C, 49.27 (49.02); H, 2.58 (2.53); N, 7.18 (6.97).

1,3-Bis[5-(3,4-dibutyl-2,2':5,2''-terthiophene)-pyridine-2-yl]benzene (L6). 1,3-Bis(2-bromopyridine-5-yl)benzene (0.390 g, 1.0 mmol) and 5-(tributylstannyl)-3,4-dibutyl-2,2':5',2''-terthiophene (1.03 g, 2.4 mmol) were added to a 100 mL three-necked flask. The flask was evacuated and filled with N_2. Anhydrous DMF (30 mL) was transferred followed by the addition of $Pd(PPh_3)_2Cl_2$ (35.5 mg, 0.05 mmol) under N_2. The resulting mixture was stirred at 95 ^{o}C for 12 h. After cooling, the mixture was extracted with CH_2Cl_2, then washed with saturated $NH_4Cl_{(aq)}$, $NaCl_{(aq)}$, and H_2O. The separated organic phase was dried over Na_2SO_4 and evaporated to give the crude product. Further purification on silica gel column using CH_2Cl_2 as eluent yields the pure product (0.664 g, 70%). ^{1}H NMR (400 MHz, CD_2Cl_2): δ (ppm) = 9.00 (d, J = 2.4, 2H), 8.80 (s, 1H), 8.11 (dd, J = 2.0, 8.0, 2H), 7.98 (dd, J = 2.0, 8.0, 2H), 7.90 (d, J = 8.0, 2H), 7.59 (t, J = 8.0, 1H), 7.42 (d, J = 3.6, 2H), 7.35 (dd, J = 2.4, 3.6, 2H), 7.17 (m, 4H), 7.09 (m, 2H), 2.17 (m, CH_2, 8H), 1.43 (m, CH_2, 8H), 1.01 (m, CH_2, 8H), 0.90 (m, CH_3, 8H). ^{13}C{^{1}H} NMR (100 MHz, CD_2Cl_2): δ (ppm) = 155.8, 146.8, 141.0, 140.8, 140.1, 139.6, 137.2, 136.4, 133.5, 130.5, 129.8, 129.6, 129.1, 127.8, 127.5, 127.1, 126.3, 125.9, 125.3, 124.9, 120.6, 33.2, 28.3, 23.4, 14.0. Elemental anal. calcd. (Found) for $C_{56}H_{56}N_2S_6$: C, 70.84 (70.32); H, 5.95 (5.73); N, 2.95 (2.79).

PtL6Cl (29). A mixture of **L6** (0.475 g, 0.5 mmol) and K_2PtCl_4 (0.208 g, 0.5 mmol) in acetic acid (30.0 mL) was refluxed for 72 h. After cooling, the solid was filtered out and washed with water, methanol and diethyl ether. The resulting yellow

powder was redissolved in CH_2Cl_2, purified on neutral Al_2O_3 column with 2 : 1 of CH_2Cl_2/hexanes as eluent to afford yellow product (0.330 g, 28%). Red crystals suitable for X-ray diffraction analysis were obtained by slow diffusion of diethyl ether into the CH_2Cl_2 solution of the product. ^{1}H NMR (400 MHz, CD_2Cl_2): δ (ppm) = 9.55 (d, J = 2.0, 2H), 8.05 (dd, J = 2.0, 8.4, 2H), 7.65 (d, J = 8.0, 2H), 7.51 (d, J = 4.0, 2H), 7.44 (m, 4H), 7.27 (t, J = 7.6, 1H), 7.23 (dd, J = 1.2, 3.6, 2H), 7.21 (d, J = 3.6, 2H), 7.16 (m, 2H), 2.80 (m, 8H), 1.59 (m, 8 H), 1.22 (t, J = 6.8, 12 H), 1.08 (m, 8H). ^{13}C{^{1}H} NMR (100 MHz, CD_2Cl_2): δ (ppm) = 165.1, 148.6, 141.1, 140.6, 138.7, 137.8, 136.2, 134.6, 130.6, 130.1, 129.4, 127.7, 126.9, 126.2, 125.9, 125.7, 119.5, 33.0, 32.9, 28.2, 28.0, 23.2, 23.2, 13.9, 13.8. HRMS (CI): calcd. for $C_{56}H_{55}ClN_2PtS_6$ m/z 1178.2028 (**29**$^+$), found 1178.2053. Elemental anal. calcd. (Found) for $C_{56}H_{55}ClN_2PtS_6$: C, 57.05 (56.85); H, 4.70 (4.44); N, 2.38 (2.49).

Synthesis of 1,3-Bis(4-(3,4-dioctyl-2,2':5',2''-terthiophene)-1H-pyrazol-1-yl)benzene (L7) and 30

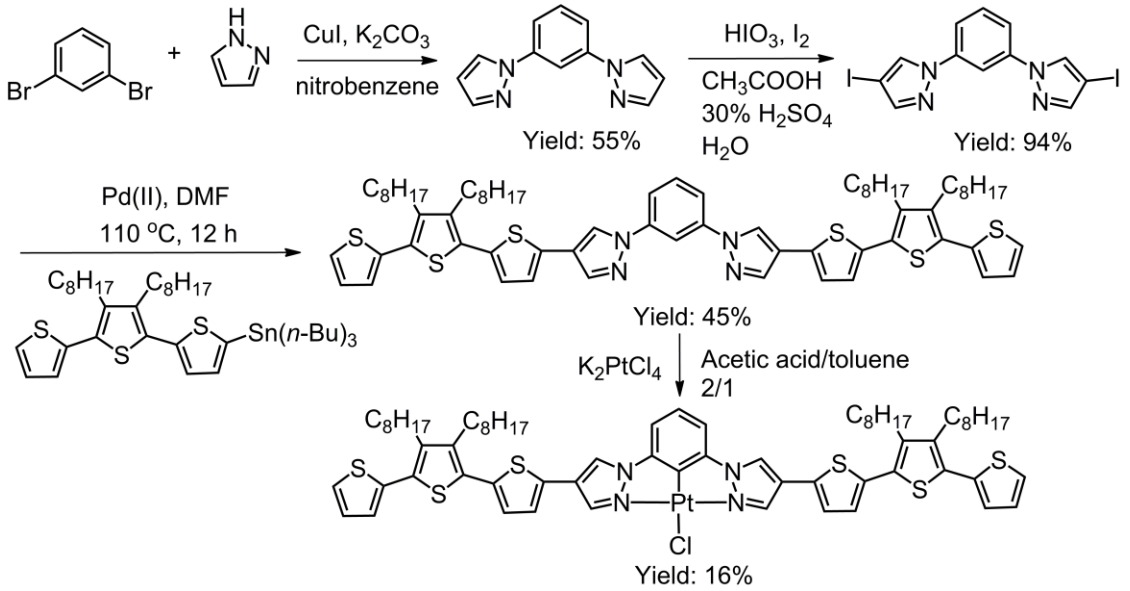

Scheme 10. Synthesis of **L7** and **30**.

1,3-Di(1H-pyrazol-1-yl)benzene was prepared according to the literature.[30]

1,3-Bis(4-iodo-1H-pyrazol-1-yl)benzene. 1,3-Di(1H-pyrazol-1-yl)benzene (1.15 g, 5.5 mmol) in a round bottom flask was treated under argon with acetic acid (16 mL), water (2 mL) and H_2SO_4 (30% in water, 2 mL) and heated to 60 °C. A separately prepared deep violet acetic acid solution (60 mL) containing HIO_3 (0.408 g, 2.33 mmol), I_2 (1.18 g, 4.64 mmol) and five drops of concentrated H_2SO_4 was added to the solution of 1,3-di(1H-pyrazol-1-yl)benzene dropwisely. The mixture was then stirred under argon at 60 °C overnight. After cooling to room temperature, aqueous solution of $Na_2S_2O_3$ was added to quench the pale purple color. The white solid was filtered out, washed with Na_2CO_3 solution and water. The solid was redissolved in CH_2Cl_2, washed with $NH_4Cl_{(aq)}$ and water. The organic phase was dried over Na_2SO_4, then evaporated to yield the target product (2.38 g, 94%). ^{1}H NMR (400 MHz, CD_2Cl_2): δ (ppm) = 7.98 (s, 2H), 7.97 (d, J = 2.0, 1H), 7.67 (s, 2H), 7.52 (t, J = 2.4, 1H), 7.50 (d, J = 2.0, 1H), 7.48 (t, J = 8.0, 1H). ^{13}C{^{1}H} NMR (100 MHz, CD_2Cl_2): δ (ppm) = 146.3, 140.4, 131.4, 130.7, 116.8, 109.6, 59.6.

1,3-Bis(4-(3,4-dioctyl-2,2':5',2''-terthiophene)-1H-pyrazol-1-yl)benzene (L7). 1,3-Bis(4-iodo-1H-pyrazol-1-yl)benzene (1.38 g, 3 mmol), 5-(tributylstannyl)-3,4-dioctyl-2,2':5',2''-terthiophene (5.33 g, 7 mmol), LiCl (1.26 g, 30.0 mmol) were added into a three-necked flask. DMF (30 mL) was transferred into the flask under Ar. $Pd(PPh_3)_2Cl_2$ (210 mg, 0.3 mmol) was added to the above mixture. The reaction was refluxed at 110 °C under Ar for 12 h. The reaction mixture was dissolved in CH_2Cl_2 and washed with water (3 × 100 mL). The organic phase was dried over Na_2SO_4 and reduced to dryness. The product was purified by column chromatography (silica gel, CH_2Cl_2 : hexanes = 2 : 1) to yield a yellow solid (1.55 g, 45%). ^{1}H NMR (400 MHz, $CDCl_3$): δ (ppm) = 8.19 (s, 2H), 8.17 (t, J = 2.0, 1H), 7.96 (s, 2H), 7.67 (t, J = 1.2, 1H), 7.65 (d, J =

1.6, 1H), 7.56 (t, *J* = 7.6, 1H), 7.32 (dd, *J* = 1.2, 5.2, 2H), 7.15 (dd, *J* = 1.2, 4.0, 2H), 7.13 (d, *J* = 3.6, 2H), 7.08 (m, 4H), 2.72 (m, 8H), 1.63 (m, 12H), 1.45 - 1.27 (m, 36H), 0.98 (t, *J* = 6.8, 12H). $^{13}C\{^{1}H\}$ NMR (100 MHz, $CDCl_3$): δ (ppm) = 140.8, 140.2, 140.1, 139.1, 136.2, 134.6, 133.7, 130.6, 129.9, 129.7, 127.4, 126.4, 125.9, 125.3, 123.5, 123.1, 119.1, 116.5, 109.5, 34.7, 31.9, 29.9, 29.3, 29.2, 26.6, 22.7, 14.1. CI-MS (CH_2Cl_2) m/z: 1151 [**L7**]$^+$. Elemental anal. calcd. (Found) for **L7**, $C_{68}H_{86}N_4S_6$: C, 70.91 (70.45); H, 7.53 (7.31); N, 4.86 (5.02).

PtL7Cl (30). A mixture of **L7** (0.461 g, 0.4 mmol) and K_2PtCl_4 (0.166 g, 0.4 mmol) in a mixture of acetic acid/toluene (2 : 1, 30.0 mL) was refluxed for 72 h. After cooling, the solid was filtered out and washed with water, methanol and diethyl ether. The resulting deep yellow powder was redissolved in CH_2Cl_2, purified on neutral Al_2O_3 column with 2 : 1 CH_2Cl_2/hexanes as eluent to afford yellow product (0.089 g, 16%). ^1H NMR (400 MHz, CD_2Cl_2): *δ* (ppm) = 8.63 (s, 2H), 7.98 (t, *J* = 9.2, 1H), 7.87 (d, *J* = 1.6, 1H), 7.84 (d, *J* = 1.6, 1H), 7.77 (s, 2H), 7.59 (t, *J* = 7.6, 2H), 7.32 (dd, *J* = 1.2, 5.2, 2H), 7.15 – 7.13 (m, 2H), 7.09 (m, 4H), 2.77 (m, 8H), 1.64 (m, 12H), 1.56 - 1.28 (m, 36H), 0.90 (t, *J* = 6.8, 12H). CI-MS (CH_2Cl_2) m/z: 1395 [**30**]$^+$. Elemental anal. calcd. (Found) for $C_{69}H_{88}ClN_4PtS_6$: C, 59.35 (58.76); H, 6.35 (5.79); N, 4.01 (3.64).

RESULTS AND DISCUSSION

Structure Determination

Crystal Structure of PtL5Cl (27)

Constable *et al*. reported the synthesis of **L5** by three-step reactions from 2-acetylthiophene in a total yield of 29.6%.[31] **L5** has the potential for a variety of coordination modes, such as N,C-, N,S-, and C,N,S-. Constable's study of the coordination chemistry of **L5** with K_2PtCl_4 in 2-methoxyethanol by NMR spectroscopy

reveals the coordination of **L5** to Pt(II) in a C,N,S-tridentate mode. However, it is not possible to eliminate the dimeric structure such as (**L5**)Pt(μ-Cl)$_2$Pt(**L5**) only on the basis of the NMR spectrum. We modify the synthesis of **L5** by one-step stille coupling of 2,6-dibromopyridine and 2-(tributylstannyl)thiophene with an improved yield of 87.5%. The complexation is done in glacial acetic acid. Single crystals of Pt**L5**Cl (**27**) were obtained from slow evaporation of tetrahydrofuran solution at room temperature. The crystal structure is shown in Figure 48.

The X-ray analysis reveals that **L5** coordinates with the Pt(II) in a tridentate fashion by the formation of one Pt-N bond, one Pt-S bond, and one Pt-C bond. The formation of the Pt-C bond is a common structure feature for cyclometalated Pt(II) complexes in which the anionic carbon donor center is generated by the deprotonation of the C-H bond. The coordination geometry around the Pt(II) is slightly distorted square planar. The Pt-C bond length (1.994(2) Å) is similar to values reported in other Pt(thpy)$_2$

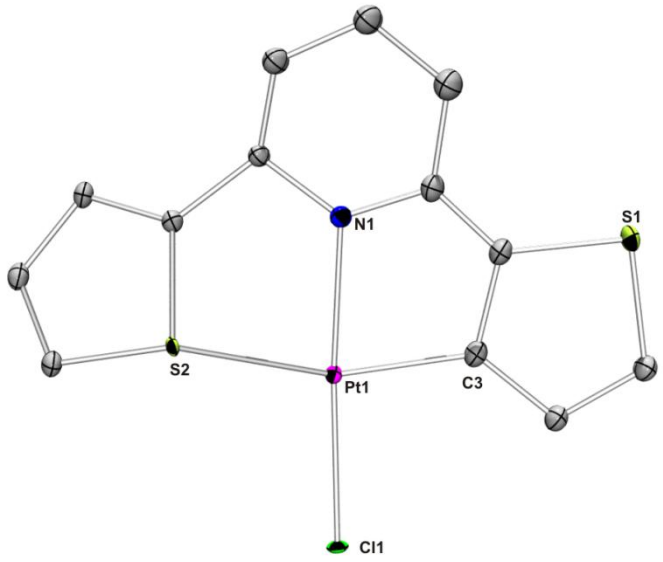

Figure 48. ORTEP diagram of **27** showing the labeling scheme of selected atoms at 30% probability level. Hydrogen atoms are omitted for clarity.

(thpy = 2-(2'-thienyl)pyridine) complexes (1.989(6) to 1.953(7) Å); whereas the Pt-N bond length (2.105(6) Å) is slightly longer to values from other Pt(thpy)$_2$ complexes.[32,33] The Pt-Cl bond distance is 2.311(3) Å, which is normal for such a bond *trans* to N. The Pt-S bond length (2.442(6) Å) is longer than that of other Pt complexes,[34] which can be explained by the *trans* effect exerted by the carbanion ligand. The bond angles and lengths for the **L5** ligand are similar to those reported for related 2-(2'-thienyl)pyridine ligands.[32,33] The dihedral angles between the middle pyridine ring and the thiophene rings containing S1 and S2 are 4.2 and 29.5°, respectively. The dihedral angle between the two thiophene rings is 30.8°.

Complex **27** forms a stacked dimer in the crystal lattice with a weak Pt···Pt interaction. The Pt···Pt distance is 4.167(5) Å (Figure 49), which is longer than the Pt···Pt distances documented in the literature.[35]

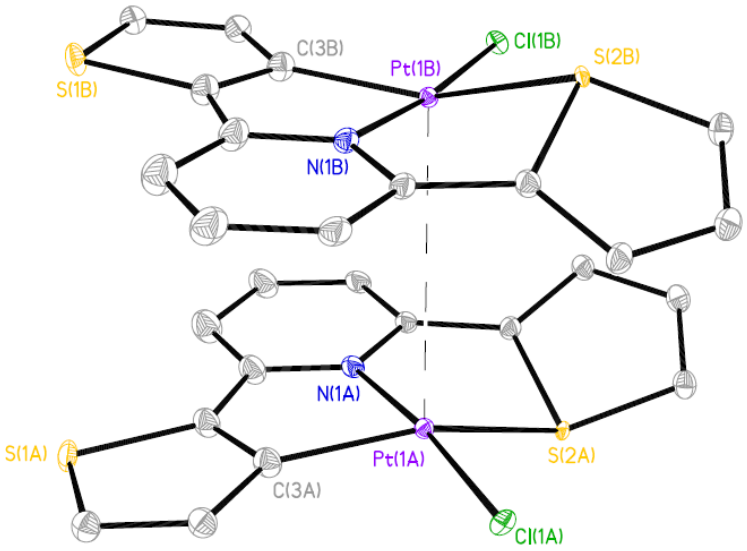

Figure 49. Stacking structure for **27**. Weak contact is depicted by the dotted line.

Crystal Structure of PtL6Cl (29)

Single crystals were obtained by slow diffusion of diethyl ether into the CH_2Cl_2 solution of **29**. The molecular structure of **29** (Figure 50) is the first reported structure of a cyclometalated Pt(II) with terthiophene electropolymerizable units. The Pt(II) center is four-coordinate in an approximately square planar environment, all the atoms attached to Pt(II) center being essentially coplanar (the largest mean deviation is 0.1333 Å). At the platinum center the chloride atom is *trans* to the carbon atom. The long Pt-Cl bond length (2.401(3) Å) confirms the *trans* influence of the cyclometalated carbon atom. The Pt-C bond distance (1.914(9) Å) lies in the range observed for Pt(II) complexes of related N, C, N terdentate ligands (1.90 - 1.94 Å).[36] The C-Pt-Cl axis is almost linear (177.9(3)°), whereas N1-Pt-N2 is more distorted at 161.0(3)°, probably as a consequence of chelate ring strain. The thiophene rings are not coplanar. The dihedral angles, ranging from 15.3 to 41.9°, are larger than those found in terthiophene at 6 - 9°, due to the presence of

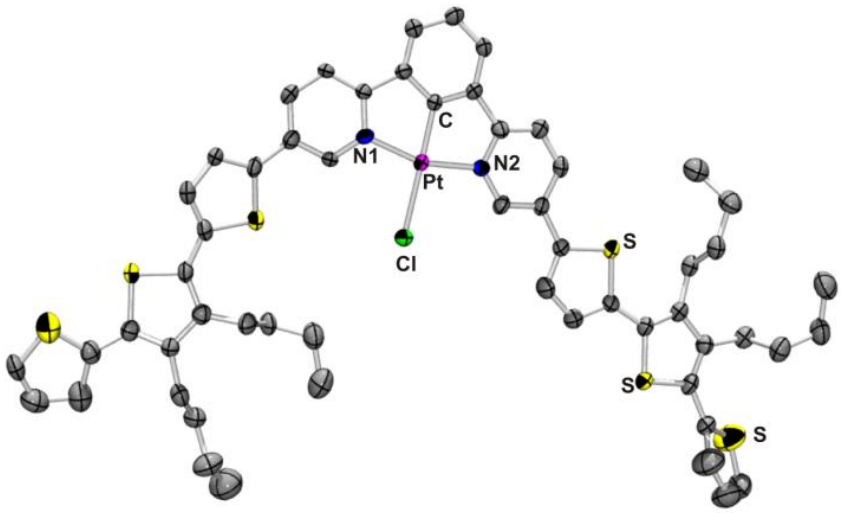

Figure 50. ORTEP diagram of **29** showing the labeling scheme of selected atoms at 30% probability level. Hydrogen atoms are omitted for clarity.

n-butyl groups.[36] Different from the 3,4-dibutyl-2,2':5,2''-terthiophene structure, only one *n*-butyl side chain is fully extended adopting a *s*-trans conformation.[38] No Pt···Pt interaction is observed in this molecule. The shortest Pt···Pt distance is 4.990 Å.

Electrochemical Studies

Pt(II) Complex 27 and 28 with L5

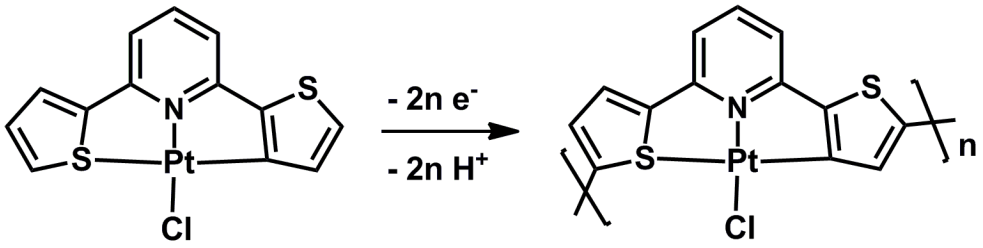

Scheme 11. Electrochemical polymerization of Pt(II)-containing monomer to conducting metallopolymer.

The electrochemistry of complex **27** and **28** is similar with the same polymerizable ligand **L5**. The replacement of chloride by pyrazole in **28** does not affect the electrochemical performance. As shown in Figure 51, cyclic voltammetry of **27** over a window of +1.25 to -1.75 V (vs Fc/Fc^+) resulted in the growth of a polymer film. The first scan shows an oxidation peak at 0.9 V associated with the thiophene oxidation. A reduction peak was observed at -0.83 V, which moves negatively with the increasing scans. A linear relationship of the maximum peak current with the number of scans was also observed. The maximum peak current of an electrode-confined film of poly-**27** in pure electrolyte solution varies linearly with the electrochemical scan rate up to 500 mV/s.

The XPS data were used to determine the film composition. The Pt 4*f* peak is observed at 72.2 eV, corresponding well to the expected value for Pt(II). The S 2*p* peak is

also found at 164.1 eV. Quantitative XPS analysis reveals that the films of poly-**27** and poly-**28** have an atomic ratio of Pt : S = 1 : 1.81 and 1 : 2.23, respectively, which is in agreement with the stoichiometric molar ratio of the monomer (1 : 2) and the proposed film structure.

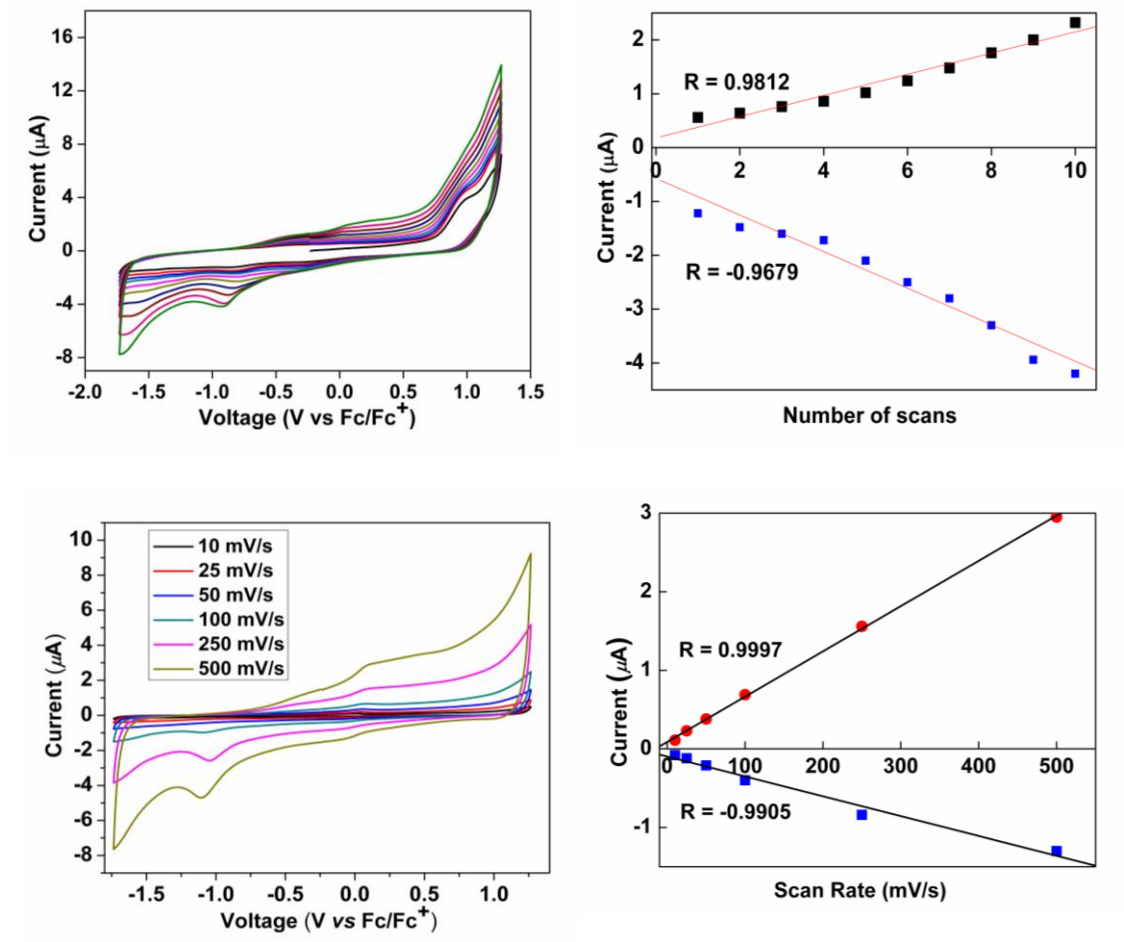

Figure 51. Top left: Electrochemical polymerization of **27** in CH_2Cl_2 at RT (Fc/Fc^+ is the redox couple of ferrocene). Top right: plot of linear current increase vs number of scans. Bottom left: Electrochemical scan rate dependence of poly-**27**. Bottom right: Plot of linear current increase vs scan rate.

Pt(II) Complex 29 with L6

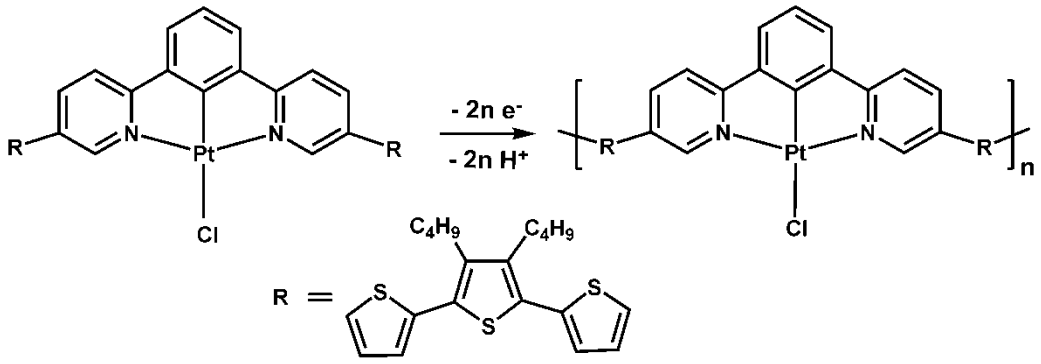

Scheme 12. Electrochemical polymerization of monomer **29** to conducting metallopolymer poly-**29**.

Complex **29** has been electropolymerized to form poly-**29** (Scheme 12) as an electrode-confined film onto a variety of working electrode surfaces. Cyclic voltammetry of **29** over a window of +1.0 to - 0.25 V (vs Fc/Fc^+) resulted in the growth of a polymer film. The positive scan exhibits two oxidation peaks at 0.40 and 0.68 V vs Fc/Fc^+ whose positions steadily become more positive with the increasing scans (Figure 52), due to the growing of the polymer film on the surface of the working electrode and the increasing resistance accordingly. The reduction peaks were observed at 0.3 and 0.48 V. The resulting electroactive polymer film was characterized using electrochemical methods and X-ray photoelectron spectroscopy (XPS). As shown in Figure 52, the maximum peak current of an electrode-confined film of poly-**29** in pure electrolyte solution varies linearly with the scan rate up to 500 mV/s. This behavior is indicative of a strongly adsorbed electroactive thin film which is not limited by the ionic flux of counter anions. The XPS data were used to determine the film composition. The Pt 4*f* peak is observed at 72.3 eV, corresponding well to the expected value for Pt(II). The S 2*p* peak is also found at 163.25 eV. Quantitative XPS analysis reveals that the film has an atomic ratio of Pt : S

= 1 : 6.8, which is in agreement with the stoichiometric molar ratio of the monomer (1 : 5.57 by XPS) and the proposed film structure (1 : 6).

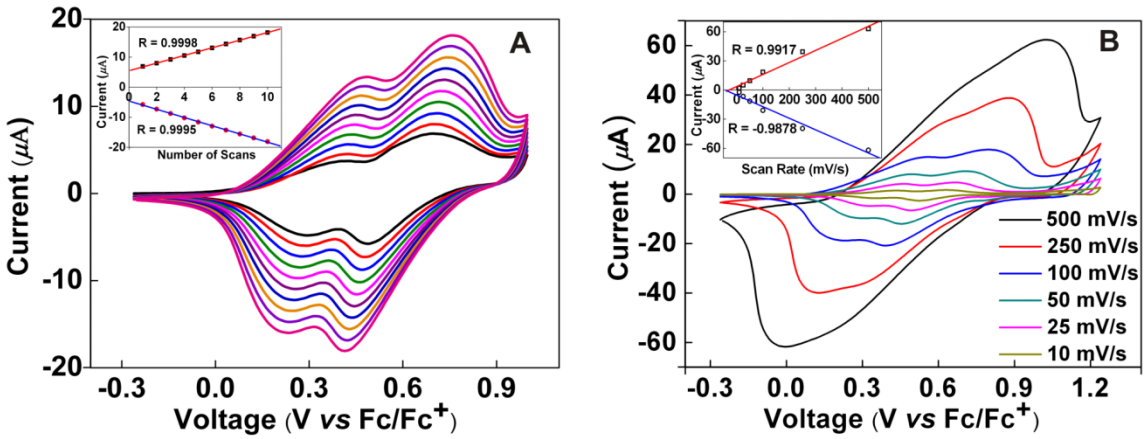

Figure 52. (A) Electropolymerization of **29** in CH_2Cl_2 ($TBAPF_6$) at RT. Inset: plot of linear current increase vs scan times. (B) Electrochemical scan rate dependence of poly-**29**. Inset: plot of linear current increase vs scan rate (Fc/Fc^+ is the redox couple of ferrocene).

Pt(II) Complex 30 with L7

Ligand **L7** has the similar polymerization groups, alkylated terthiophene, as ligand **L6**, which leads to a similar electrochemical behavior of complex **30** and **29**. Cyclic voltammetry of **30** over a window of +1.25 to -1.75 V (vs Fc/Fc^+) resulted in the growth of a polymer film. The positive scan has three oxidation peaks around 0.47, 0.68 and 1.17 V. The first two oxidation peaks merge into one peak with the increasing scans. The reduction peaks were observed at 0.40 and 0.99 V. All these redox peaks grow linearly with the increasing scans. The maximum peak current of an electrode-confined film of poly-**30** in pure electrolyte solution varies linearly with the electrochemical scan rate up to 500 mV/s. This behavior is indicative of a strongly adsorbed electroactive thin film which is not limited by the ionic flux of counter anions.

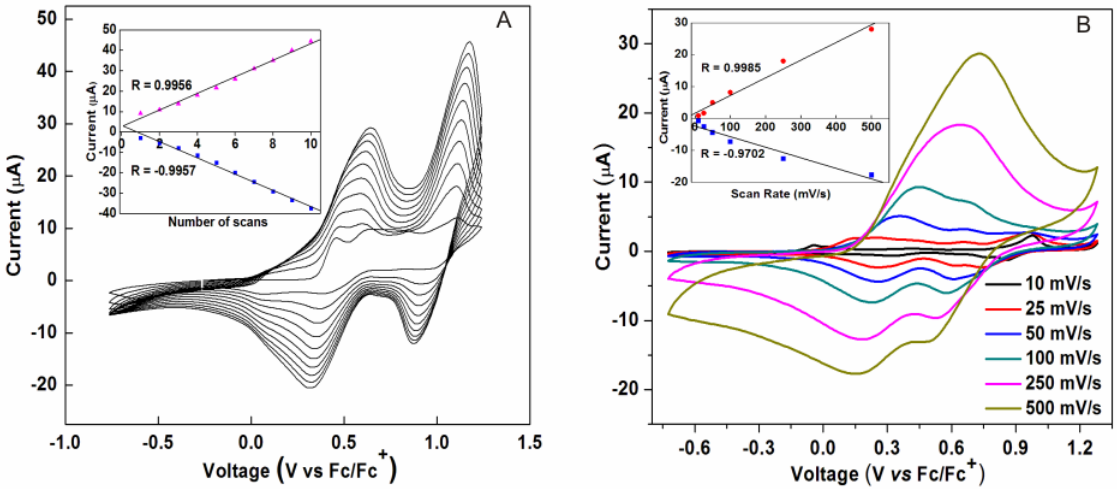

Figure 53. (A) Electropolymerization of **30** in CH_2Cl_2 ($TBAPF_6$) at RT. Inset: plot of linear current increase vs scan times. (B) Electrochemical scan rate dependence of poly-**30**. Inset: plot of linear current increase vs scan rate (Fc/Fc^+ is the redox couple of ferrocene).

Photophysical Properties

Recently cyclometalated complexes have attracted strong research interest as emitting components in electroluminescent (EL) devices.[37-39] The phosphorescent metal complexes allow for the utilization of both singlet and triplet excitons which are generated upon charge injection from the electrodes. Consequently, internal quantum efficiencies approaching 100% may be achieved. Many examples of electrophosphorescent metal complexes based on iridium, osmium, platinum and rare earth metal complexes are known. For example, Che *et al*. described the vapor deposition of Pt-salen complexes as efficient electrophosphorescent dyes in multilayer OLED devices with a maximum luminous efficiency of 31 Cd A^{-1}.[40] However there are still limited examples of electrophosphorescent polymers as single-component PLED materials. Here we study the photophysical properties of the cyclometalated Pt(II)

complexes and their corresponding metallopolymers for the potential application of light emitting materials in PLED.

Pt(II) Complex 27 and 28 with L5

The absorption spectra of **L5** and **27** in CH_2Cl_2 at room temperature are shown in Figure 54A. **L5** shows a structured absorption spectrum (250 to 350 nm), which are mainly assigned as π-π^* transitions. Complex **27** exhibits an intense absorption at 306 nm which is associated with ligand π-π^* transitions. Thus it can be assigned as mainly ligand centered (LC) transitions of the **L5** ligand. The corresponding electronic state is largely of ^{1}LC character. A weak absorption at a longer wavelength (~440 nm), is attributed to the direct population of a triplet excited state, following previous assignments in Pt(II) complexes.[41-43]

Figure 54B shows the emission of **L5** in CH_2Cl_2 solution at room temperature and in 2-methyltetrahydrofuran at 77 K, respectively. **L5** has a strong blue emission at 375 nm at room temperature with a quantum yield of 77.8%. At 77K, this emission peak shows fine structures at the same wavelength. Two new emission peaks at 500 and 542 nm with low intensity are observed. Considering the long lifetime of 22 μs, we attribute the emission bands at 500 and 542 nm to the electronic transition between the lowest triplet excited state T_1 and the singlet ground state S_0 of **L5**.

The emission of the complex **27** at room temperature is also shown in Figure 54B. The emission profile of **27** is characterized with two emission peaks at 561 and 605 nm. These two peaks are red shifted by 61 nm compared with the phosphorescence of **L5** at 500 and 543 nm. The lifetime of the emission, 17.3 μs, is also comparable with the ligand phosphorescence emission. Quantum yield of the emission is 23.6%. The emission peaks of **27** at 561 and 605 nm remain at the same position in different solvents with polarity

index increases from 1.6 (CCl_4) to 6.4 (DMF), as shown in Figure 55 A. The absence of solvatochromism effect also proves that the complex emission is not a charge transfer peak. The concentration dependence of the emission spectrum of **27** is depicted in Figure 55B. The new peak which appeared at 720 nm and red shifted to 750 nm with increasing concentration, arises from the emissive dimer formed in solution with high concentration. This is in accord with our previous discussion of the Pt···Pt interactions in the solid state crystal structure.

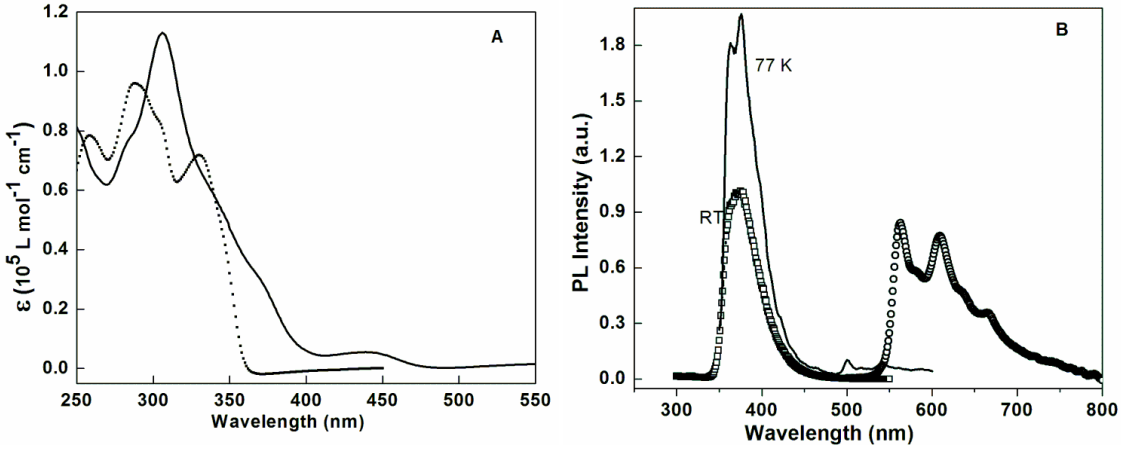

Figure 54. A: UV-Vis absorption spectra of free ligand **L5** (dotted line) and complex **27** (solid line) in CH_2Cl_2. B: Emission spectra of **L5** at RT in CH_2Cl_2 (square) and 77 K in 2-methyltetrahydrofuran (solid line) and complex **27** (circle) at RT in CH_2Cl_2 under the excitation of 320 nm.

Complex **28** has a very similar emission profile as complex **27**. In CH_2Cl_2 at low concentration of 5×10^{-6} M, the emission spectrum of **28** shows two emission peaks at 572 and 612 nm. With the increasing concentration a new peak at 750 nm appears. The high energy emission peak at 572 and 612 nm totally disappear at the high concentration of 1×10^{-3} M. This is probably due to the replacement of Cl by pyrazole in **28** which leads to a short Pt···Pt interactions in the dimer. The lifetime and quantum yield of **28** is

25.7 μs and 39.1%, respectively. The higher quantum yield of **28** than that of **27** may also due to the replacement of Cl with pyrazole.

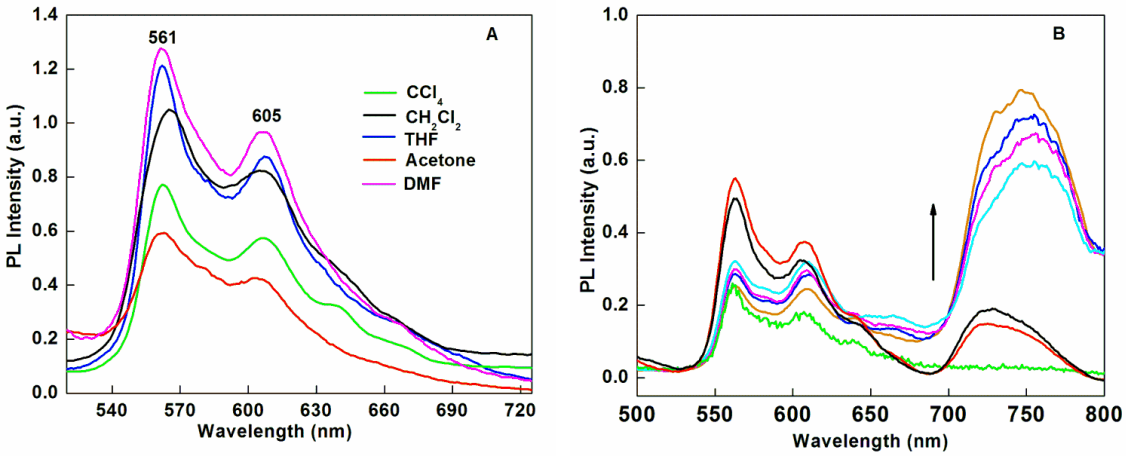

Figure 55. A: Emission spectra of **27** in different solvents at RT with the concentration of 1×10^{-5} M under the excitation of 320 nm. B: Concentration dependence of **27** in CH_2Cl_2 from 1×10^{-4} M to 6.4×10^{-3} M with concentration doubled for each measurement under the excitation of 320 nm.

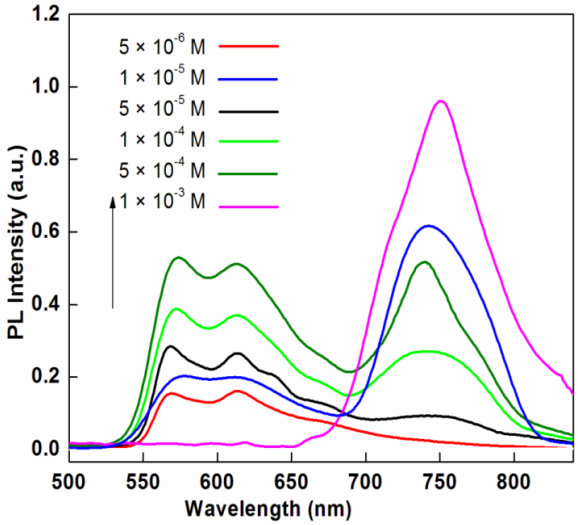

Figure 56. Emission spectra of **28** in different concentration from 5×10^{-6} M to 1×10^{-3} M under the excitation of 320 nm.

Pt(II) Complex 29 with L6

The photophysical properties of **L6**, **29**, and corresponding polymers have been studied under a variety of conditions. The absorption spectrum of **L6** (Figure 57A) displays a peak at 387 nm, while the complex **29** shows a broad absorption at ca. 400 nm. Both poly-**L6** and poly-**29** show a red shifted absorption at ca. 500 nm. Upon selective excitation at 420 nm, the emission profile of **29** displays a broad and unstructured band centered at 560 nm with half-height width of 170 nm (Figure 57B). The emission spectrum of ligand **L6** at 77 K in 2-methyltetrahydrofuran solution is featured with a more structured band at the same wavelength of the emission at room temperature (Figure 58A). The concentration dependence study of the emission spectra of **29** is shown in Figure 58B. With the increasing concentration, the emission intensity grows while maintaining the same emission color. At higher concentration (above 10^{-3} M), the emission intensity decreases due to the trival quenching. In order to determine whether the complex **29** emission is ligand centered emission or charge transfer emission,

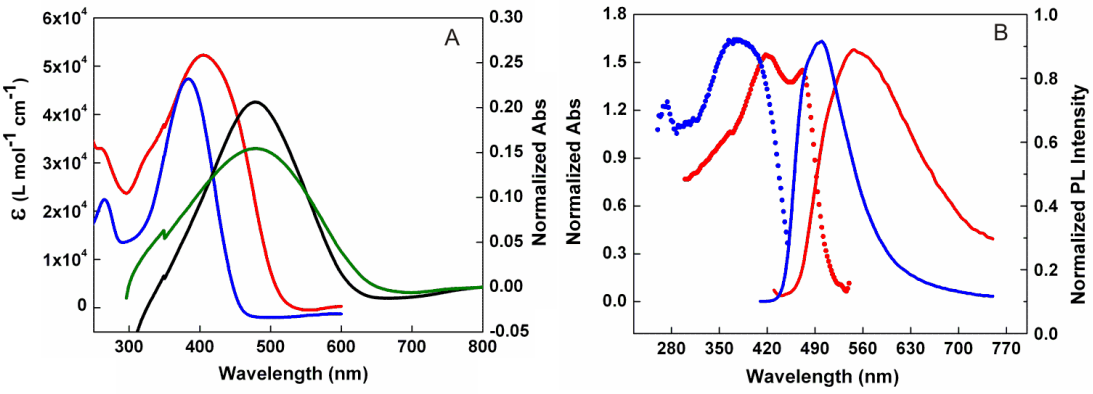

Figure 57. A: UV-Vis of **L6** (blue line), poly-**L6** (black line), complex **29** (red line), and poly-**29** (green line) in CH_2Cl_2. B: Excitation spectra of **L6** (blue dotted line) and **29** (red dotted line) and emission spectra of **L6** (blue line) and **29** (red line) in CH_2Cl_2 at RT.

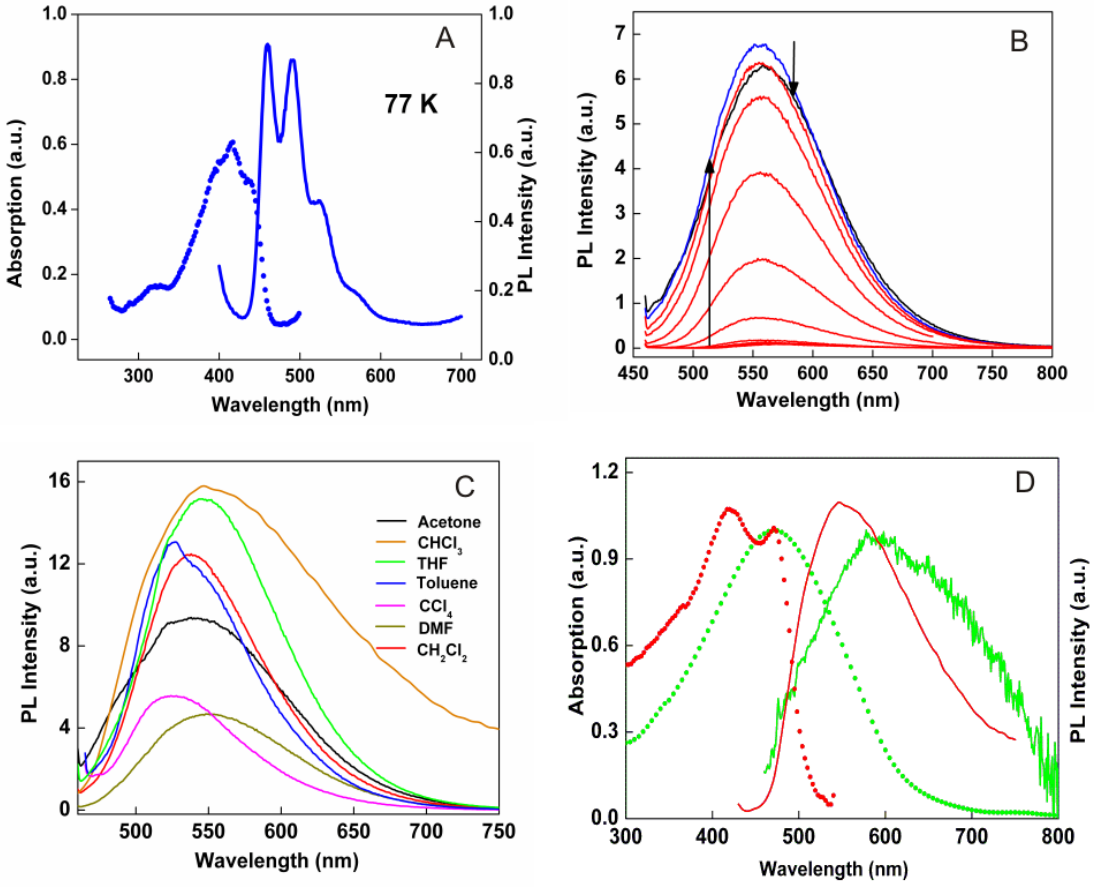

Figure 58. A: Excitation (dotted line) and emission (solid line) spectra of **L6** at 77 K in 2-methyltetrahydrofuran. B: Emission spectra of **29** in different concentration from 1×10^{-6} M to 1×10^{-2} M in CH_2Cl_2. C: Emission spectra of **29** in different solvents at RT. D: Excitation (red dotted line) and emission (red line) of **29** recorded in CH_2Cl_2 at RT and excitation (green dotted line) and emission (green line) of poly-**29** on ITO coated glass.

I measured the emission spectra of **29** in different solvents. The polar index of these solvents varies from 1.6 (CCl_4) to 6.4 (DMF). As shown in Figure 58C, the emission peak moves from 529 nm in CCl_4, to 536 nm in CH_2Cl_2, to 546 nm in THF and 547 nm in DMF. The energy of the emission peak decreases with increasing polarity of the solvent indicates a positive solvatochromism, which shows the emission of **29** is of charge transfer character. Further evidence in support of this assignment comes from the

relatively long lifetime of **29**, 9.1 μs. The luminescent quantum yield of **29** in a degassed CH_2Cl_2 solution is 3.5%.

The photophysical properties of poly-**29** deposited on ITO-coated glass as a thin film have also been investigated. The absorption spectrum displays a very broad band characteristic of the extended aromatic system of a conducting metallopolymer structure which is red shifted from that of **L6** and **29**. The emission of poly-**29** is observed as a broad band peaked at 590 nm measured with 480 nm as the excitation wavelength (Figure 58D).

Pt(II) Complex 30 with L7

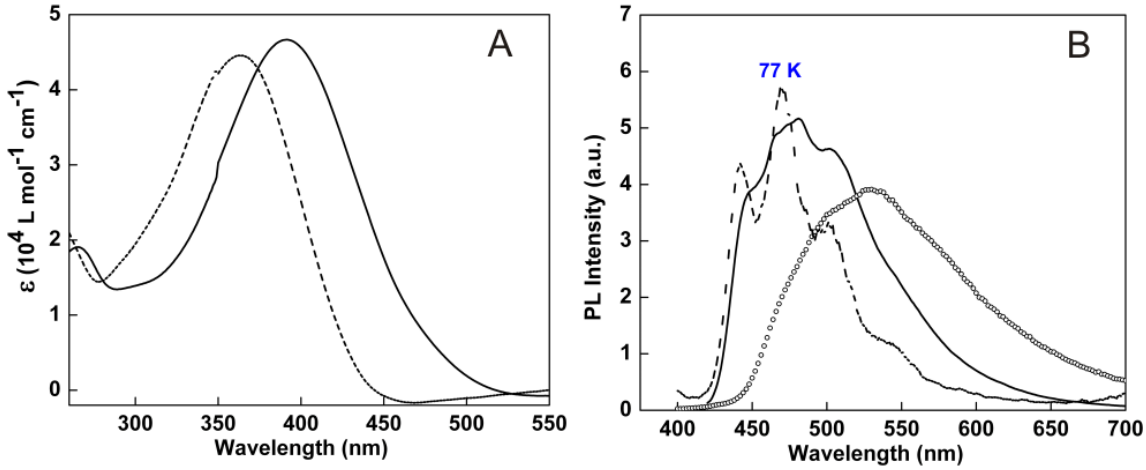

Figure 59. A: UV-Vis of **L7** (dotted line) and **30** (solid line) in CH_2Cl_2 at RT. B: Emission spectra of **L7** at RT in CH_2Cl_2 (dotted line) and 77 K in 2-methyltetrahydrofuran (solid line) under the excitation of 390 nm, and **30** in CH_2Cl_2 at RT (circle) under the excitation of 400 nm.

The UV-Vis absorption spectra of **L7** and complex **30** are shown in Figure 59A. **L7** has an absorption band at ca. 363 nm associated with the π-π^* transition. After complexation with Pt(II), the absorption band of **30** is red shifted by 27 nm with an enhanced absorptivity. The emission properties of the ligand and complex are also

investigated (Figure 59B). **L7** in CH_2Cl_2 at room temperature emits violet-blue light with the wavelength centered at 480 nm. Low temperature measurement of **L7** in 2-methyltetrahydrofuran provides a more structured spectrum at the same position. The emission spectrum of **30** is featured with a broad band centered at 530 nm. To identify the nature of the emission, we measured the emission spectra of **30** in solvents with polarity index varying from 1.6 to 6.4 (Figure 60)

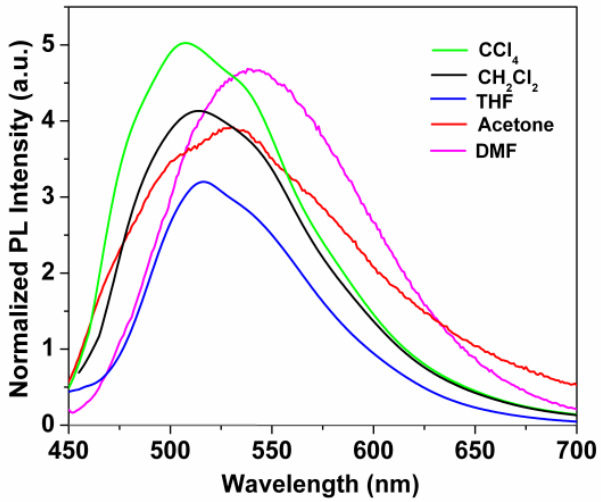

Solvent	Emission (nm)	Polarity index
CCl_4	508	1.6
CH_2Cl_2	513	3.1
THF	517	4.0
Acetone	532	5.1
DMF	541	6.4

Figure 60. Emission spectra of **30** in different solvents at RT. The maximum of the emission wavelength is listed in the table.

The results in Figure 60 indicate that the emission peak of **30** shifts to the long wavelength with the increasing polarity of the solvent. This positive solvatochromism proves that the emission of **30** is a charge transfer peak.

Electrogenerated Chemiluminescence (ECL)

Poly-**27** and poly-**28** produce coreactant ECL in acetonitrile solution under the presence of 0.1 M $TBAPF_6$ as a supporting electrolyte and 100 mM of tri-*n*-propylamine

(TPrA) as a coreactant (Figure 61). The working electrode of the ECL measurement is poly-**27** or **28** films on ITO coated glass. Electrosyntheses of the films were performed from 1×10^{-3} M monomer solutions by continuous cycling between -1.75 V and +1.25 V at a scan rate of 100 mV s^{-1}. The films obtained were then copiously washed with fresh CH_2Cl_2 before using as a working electrode in ECL measurements. In scanning the working electrode to the positive side, both the film and TPrA are oxidized. TprA, upon oxidizing electrochemically, produces a strong reducing agent, which can react with the polymer to produce polymer anions or react directly with the oxidized polymer to produce the excited state. ECL light was emitted by the degradation of the excited state to the ground state.

Figure 61 shows the i-t-ECL of the metallopolymer deposited on ITO electrode in acetonitrile solution. The working electrode was pulsed between zero to 1.2 V, in which both polymer and TPrA are oxidized completely.

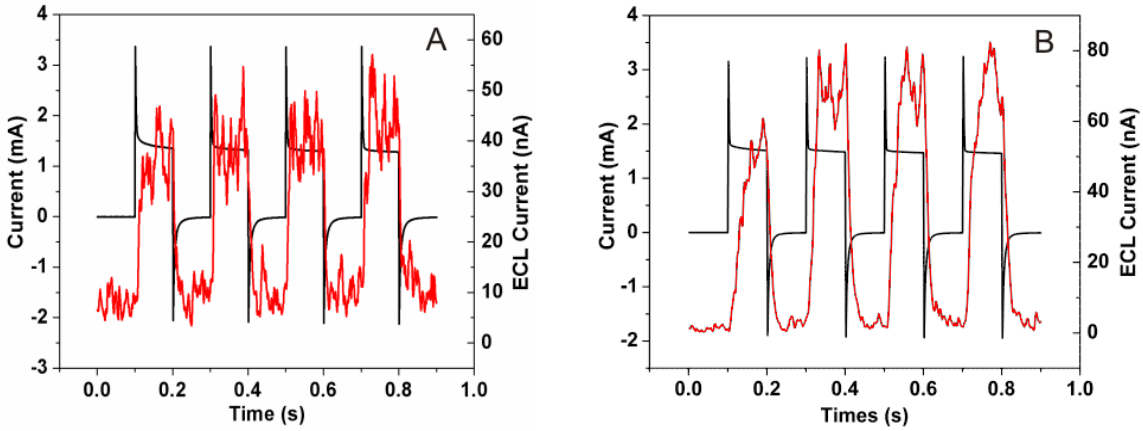

Figure 61. I-t-ECL for poly-**27** (A) and poly-**28** (B), pulsing between zero to +1.2 V vs Ag/Ag^{+} (pulse width, 0.1 second).

The mechanism of ECL production is proposed to be emitted after oxidizing of the polymer to form polymer cation radical on the film, then reacting with TPrA radical to form the excited state of the polymer. The schematic diagram could be summarized as follows:

$$\text{Polymer} - e \rightarrow [\text{polymer}]^{+\bullet}$$

$$\text{TPrAH} - e \rightarrow \text{TPrAH}^{+\bullet} \rightarrow \text{TPrA}^{\bullet} + H^{+}$$

$$[\text{polymer}]^{+\bullet} + \text{TPrA}^{\bullet} \rightarrow [\text{Polymer}]^{*} \rightarrow \text{Polymer} + h\nu$$

ECL of the poly-**29** was taken in the acetonitrile solution in the presence of 0.1 M $TBAPF_6$ as a supporting electrolyte and 100 mM of TPrA as a coreactant (Figure 62A). In scanning the working electrode to the positive side, the ECL light was observed when both the film and TPrA are oxidized. However, pulsing for longer time (ca. 1500 ms), the ECL light decreased, that is might be due to the dissolution of the polymer (oxidized polymer) in solution. Since the polymer film is not stable under pulsing for long time, and the ECL signal is weak, the ECL spectrum could not be recorded using CCD camera even after integrating for 20 min. However, a qualitative spectrum was taken using long pass cut-off filters and pulsing for very short time (0.5 sec) and using sensitive PMT as a

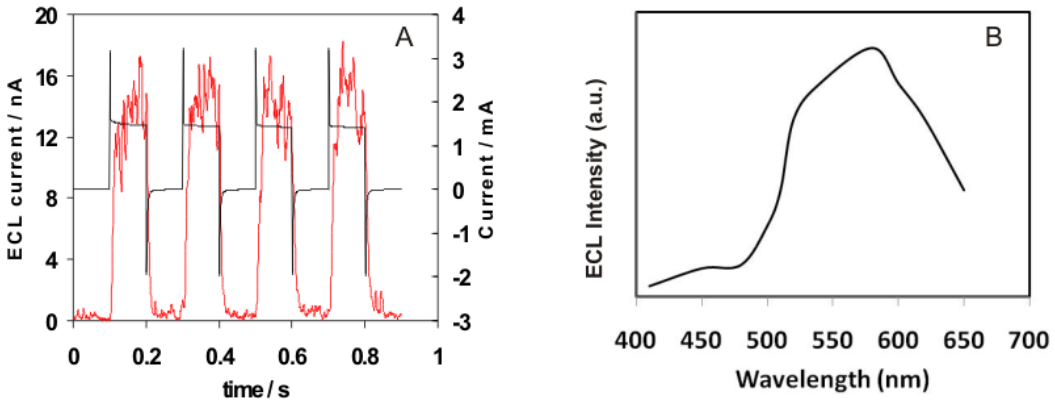

Figure 62. A: I-t-ECL of poly-**29**, pulsing between zero to +1.3 V vs Ag/Ag^{+} (pulse width 0.1 second). B: ECL spectrum of the metallopolymer using cut-off filters.

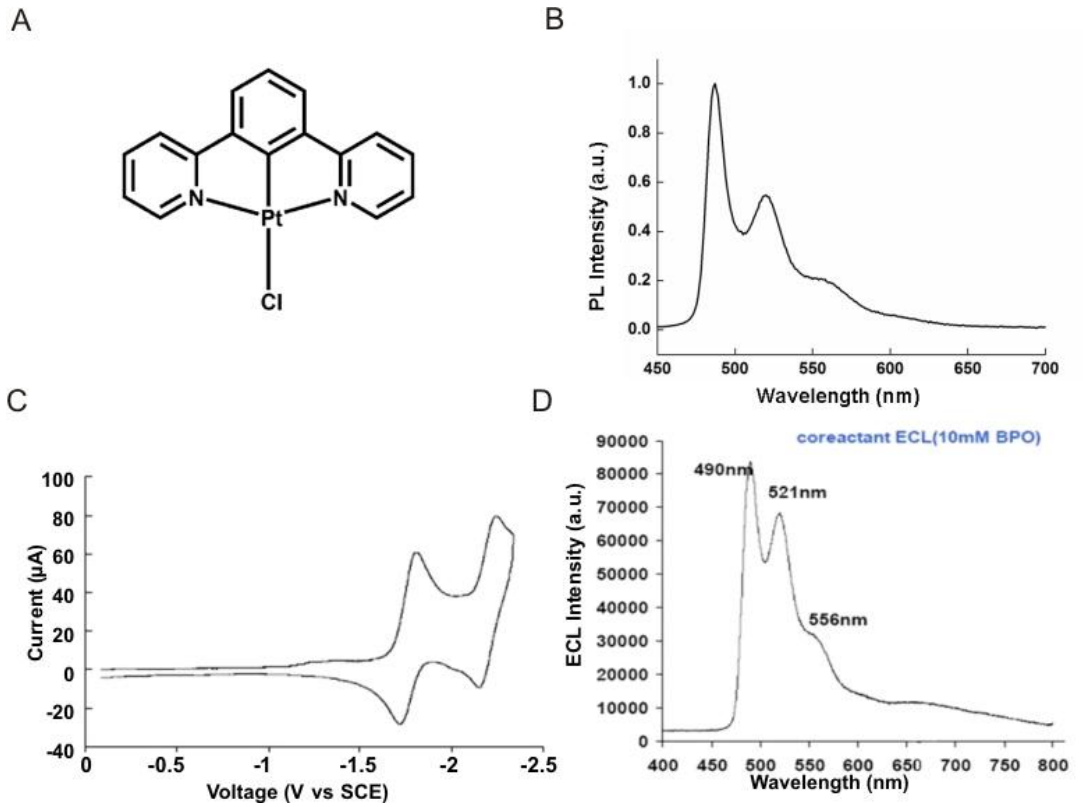

Figure 63. A: Molecular structure of model complex Pt[1,3-di(pyridin-2-yl)benzene]Cl. B: Photoluminescence spectrum of model complex at RT in CH_2Cl_2. C: Cyclic voltammetry of model complex. D: ECL spectrum of model complex pulsing between zero to -2.5 V vs Ag/Ag^+.

detector. Figure 62B shows the ECL spectrum of the metallopolymer which ECL maximum peaks at ~590 nm, the same as photoluminescence. Matching of the photoluminescence and ECL spectra indicates that in both cases the same emission state is formed.

In our previous photophysical studies, the emission of complex **29** is considered to be of charge transfer. In order to identify this charge transfer peak in detail, a model complex, Pt[1,3-di(pyridin-2-yl)benzene]Cl was prepared. The cyclic voltammetry of the model complex shows two redox peaks at -1.7 and -2.2 V. In CH_2Cl_2 solution, this

complex emits in the region of 480 - 550 nm. Benzoyl peroxide (BPO) was used as a coreactant for reductive ECL. BPO, upon reducing electrochemically, produces a strong oxidizing agent, which can react with the radical anion of model complex populating the excited state. Under these conditions, strong ECL was observed (Figure 63).

From the ECL study of the model complex, we get the information that the metal binding portion of poly-**29** can be reduced (green box in Scheme 13). The cyclic voltammetry scan of poly-**29** on ITO coated glass in acetonitrile solution with 0.1 M $TBAPF_6$ as a supporting electrolyte shows that poly-**29** can be oxidized at ca. 1.0 V due to the oxidation of the alkylated terthiophene portion (purple ellipse in Scheme 13). Based on the above information, the ECL emission of poly-**29** is considered to be an intraligand charge transfer, positive charge is formed on the terthiophene end when an electron is transferred to the Pt[1,3-di(pyridin-2-yl)benzene]Cl middle portion.

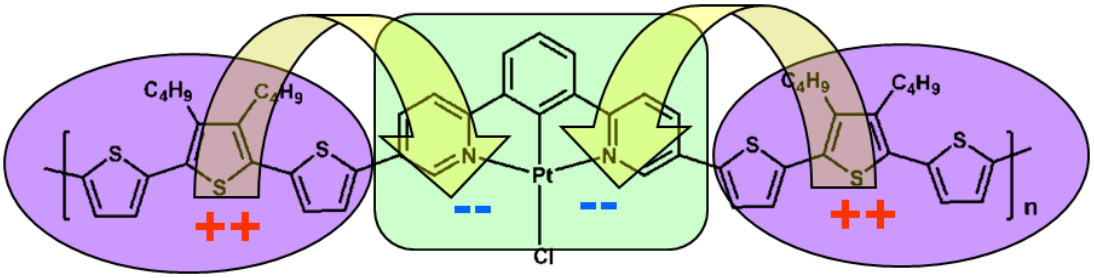

Scheme 13. Schematric presentation of the intraligand charge transfer in poly-**29**.

Poly-**30** also gives ECL signal in the presence of 0.1 M $TBAPF_6$ as a supporting electrolyte and 100 mM of TPrA as a coreactant. As shown in Figure 64, the intensity of the ECL current is in the same order as that of poly-**29**. The cyclic voltammetry of poly-**30** has a very similar feature with that of poly-**29**, oxidation at the terthiophene end and

reduction in the middle metal coordination portion. Thus we can also explain the ECL emission of poly-**30** as an intraligand charge transfer.

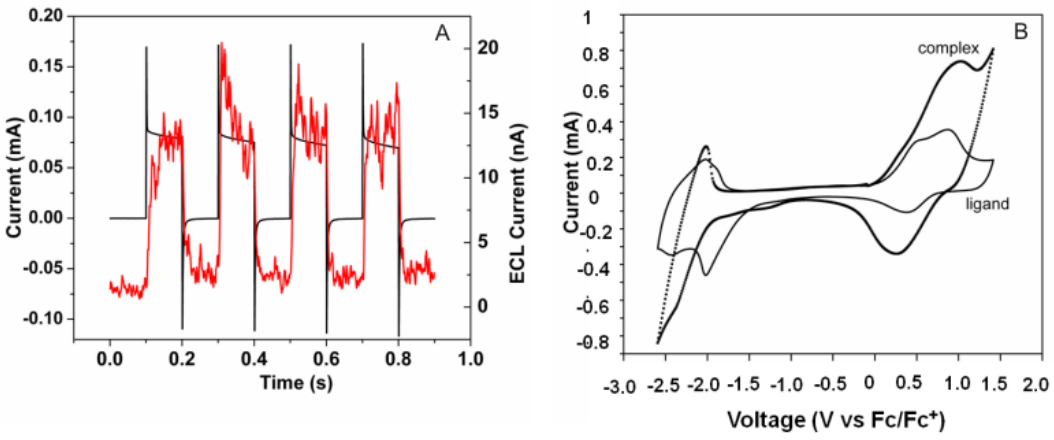

Figure 64. A: I-t-ECL of poly-**30**, pulsing between zero to +1.2 V vs Ag/Ag^+ (pulse width 0.1 second). B: Cyclic voltammetry scan of the complex polymer (dotted line) and ligand polymer (solid line).

CONCLUSION

In summary, we have demonstrated the synthesis of three different ligand systems with polymerizable thiophene and its derivatives. Four cyclometalated Pt(II) complexes with these ligands have been prepared. Photoluminescent properties of the organic ligands, cyclometalated Pt(II) complexes and corresponding Pt(II) containing conducting metallopolymers have been investigated. All the cyclometalated complexes can be electropolymerized to form metallopolymers. The resulting metallopolymers show ECL emission in the presence of TPrA as coreactant. Notably, these polymers represent the first observation of ECL from conducting metallopolymers with cyclometalated Pt(II). The replacement of Cl anion with pyrazole in complex **28** leads to a higher luminescent quantum yield. However, the ECL intensity of poly-**28** is not improved dramatically. Our preliminary results bode well for a new type of phosphorescent material for potential

application of ECL. Furthermore, this approach represents a novel perspective on the use of phosphorescent conducting metallopolymers for a wide range of light-emitting applications.

REFERENCES

1. *Electrogenerated Chemiluminescence*; Bard, A. J., ed.; Marcel Dekker, New York, 2004.
2. Richter, M. M.; *Chem. Rev.* **2004**, *104*, 3003.
3. Pyati, R.; Richter, M. M. *Annu. Rep. Prog. Chem., Sect. C* **2007**, *103*, 12.
4. Miao, W. J. *Chem. Rev.* **2008**, *108*, 2506.
5. Marquette, C. A.; Blum, L. J. *Anal. Bioanal. Chem.* **2008**, *390*, 155.
6. Forster, R. J.; Bertoncello, P.; Keyes, T. E. *Annu. Rev. Anal. Chem.* **2009**, *2*, 359.
7. Visco, R.; Chandross, E. *J. Am. Chem. Soc.* **1964**, *86*, 350.
8. Santhanam, K.; Bard, A. J. *J. Am. Chem. Soc.* **1965**, *87*, 139.
9. Tokel-Takvoryan, N.; Hemingway, R.; Bard, A. J. *J. Am. Chem. Soc.* **1973**, *95*, 6582.
10. Chang, M. M.; Saji, T.; Bard, A. J. *J. Am. Chem. Soc.* **1977**, *99*, 5399.
11. Wightman, R. M.; Forry, S. P.; Maus, R.; Badocco, D.; Pastore, P. *J. Phys. Chem. B* **2004**, *108*, 19119.
12. Zu, Y. B.; Bard, A. J. *Anal. Chem.* **2000**, *72*, 3223.
13. Skotty, D. R.; Lee, W. Y.; Nieman, T. A. *Anal. Chem.* **1996**, *68*, 1530.
14. Zorzi, M.; Pastore, P.; Magno, F. *Anal. Chem.* **2000**, *72*, 4934.
15. Shi, L. H.; Liu, X. Q.; Li, H. J.; Xu, G. B. *Anal. Chem.* **2006**, *78*, 7330.
16. Balzani, V.; Juris, A. *Coord. Chem. Rev.* **2001**, *211*, 97.
17. Juris, A.; Balzani, V.; Barigelletti, F.; Campagna, S.; Belser, P.; Von Zelewsky, A. *Coord. Chem. Rev.* **1988**, *84*, 85.
18. Bolletta, B.; Ciano, T.; Balzani, V.; Serpone, N. *Inorg. Chim. Acta* **1982**, *62*, 207.
19. Shin, I.-S.; Kim, J. I.; Kwon, T.-H.; Hong, J.-I.; Lee, J.-K.; Kim, H. *J. Phys. Chem. C* **2007**, *111*, 2280.
20. Kim, J. I.; Shin, I.-S.; Kim, H.; Lee, J.-K. *J. Am. Chem. Soc.* **2005**, *127*, 1614.
21. *High Energy Processes in Organometallic Chemistry*; Vogler, A.; Kunkely, H., Eds.; Am. Chem. Soc., Washington D. C., 1987.
22. Gross, E. M.; Armstrong, N. R.; Wightman, R. M. *J. Electrochem. Soc.* **2002**, *149*, E137.
23. Dennany, L.; Hogan, C.; Keyes, T.; Forster, R. J. *Anal. Chem.* **2006**, *78*, 1412.
24. Abruna, H. D.; Bard, A. J. *J. Am. Chem. Soc.* **1982**, *104*, 2641.
25. Terheijden, J.; van Koten, G.; van Beek, J. A. M. *Organometallics* **1987**, *6*, 89.
26. *Methods in Enzymology, 276*: *Macromolecular Crystallography, part A*; Carter, C. W., Jr.; Sweets, R. M., Eds.; 1997.
27. Altomare, A.; Burla, M. C.; Camalli, M.; Cascarano, G. L.; Giacovazzo, C.; Guagliardi, A.; Moliterni, A. G. G.; Polidori, G.; Spagna, R. *J. Appl. Cryst.* **1999**, *32*, 115.
28. Sheldrick, G. M. (**1994**) SHELXL97. Program *for the Refinement of Crystal Structures.* University of Gottingen, Germany.
29. Araki, K.; Endo, H.; Masuda, G.; Ogawa, T. *Chem. Eur. J.* **2004**, *10*, 3331.
30. Willison, S. A.; Krause, J. A.; Connick, W. B. *Inorg. Chem.* **2008**, *47*, 1258.
31. Constable, E. C.; Henney, R. P. G.; Tocher, D. A. *J. Chem. Soc. Dalton Trans.* **1992**, 2467.

32. Brooks, J.; Babayan, Y.; Lamansky, S.; Djurovich, P. I.; Tsyba, I.; Bau, R.; Thompson, M. E. *Inorg. Chem.* **2002**, *41*, 3055.
33. Thomas III, S. W.; Venkatesan, K.; Müller, P.; Swager, T. M. *J. Am. Chem. Soc.* **2006**, *128*, 16641.
34. Godbert, N.; Pugliese, T.; Aiello, I.; Bellusci, A.; Crispini, A.; Ghedini, M. *Eur. J. Inorg. Chem.* **2007**, 5105.
35. Wadas, T. J.; Wang, Q.-M.; Kim, Y. J.; Flaschenreim, C.; Blanton, T. N.; Eisenberg, R. *J. Am. Chem. Soc.* **2004**, *126*, 16841, and references therein.
36. DeWitt, L.; LeGoff, E.; Benz, M . E.; Liao, J. H.; Kanatzidis, M. G. *J. Am. Chem. Soc.* **1993**, *115*, 12158.
37. Gong, X.; Ostrowski, J. C.; Bazan, G. C.; Moses, D.; Heeger, A. J.; Liu, M. S.; Jen, A. K. Y. *Adv. Mater.* **2003**, *15*, 45.
38. Bagnich, S. A.; Im, C.; Bässler, H.; Neher, D.; Scherf, U. *Chem. Phys.* **2004**, *299*, 11.
39. Yang, X. H.; Neher, D. *Appl. Phys. Lett.* **2004**, *84*, 2476.
40. Che, C.-M.; Chan, S.-C.; Xiang, H. F.; Chan, M. C. W.; Liu, Y.; Wang, Y. *Chem. Commun.* **2004**, 1484.
41. Lai, S. W.; Lam, H. W.; Lu, W.; Cheung, K. K.; Che, C. M. *Organometallics* **2002**, *21*, 226.
42. Berenguer, J. R.; Lalinde, E.; Torroba, J. *Inorg. Chem.* **2007**, *46*, 9919.
43. Develay, S.; Blackburn, O.; Thompson, A. L.; Williams, J. A. G. *Inorg. Chem.* **2008**, *47*, 11129.

CRYSTALLOGRAPHIC DATA

Table 30. Crystal data and structure refinement of **27**.

formula	$C_{13}H_8ClNPtS_2$
fw	472.88
T (K)	293(2)
crystal system	Monoclinic
space group	P-1
a (Å)	7.159(5)
b (Å)	18.671(5)
c (Å)	9.441(5)
α (deg)	90.000(5)
β (deg)	95.150(5)
γ (deg)	90.000(5)
V (Å^3)	1256.8(12)
Z	4
ρ (g/cm^3)	2.494
μ (mm^{-1})	11.685
F(000)	876
crystal size (mm)	0.03 × 0.05 × 0.13
θ (deg)	2.91 to 30.51
Index ranges	$-7 \le h \le 9$
	$-24 \le k \le 24$
	$-12 \le l \le 12$
GOF on F^2	1.165
R_1, R_2 [I > 2σ (I)]	0.0635, 0.1660
R_1, R_2 (all data)	0.0640, 0.1662
Largest diff. peak and hole (e.Å^{-3})	3.694 and -3.785

Table 31. Crystal data and structure refinement of **29**.

formula	$C_{56}H_{55}ClN_2PtS_6$
fw	1178.92
T (K)	153(2)
crystal system	Triclinic
space group	P-1
a (Å)	8.890(5)
b (Å)	17.166(6)
c (Å)	18.043(5)
α (deg)	112.215(4)
β (deg)	101.180(5)
γ (deg)	91.193(5)
V (Å^3)	2487.2(17)
Z	2
ρ (g/cm^3)	1.574
μ (mm^{-1})	3.167
F(000)	1192
crystal size (mm)	0.05 × 0.05 × 0.15
θ (deg)	2.91 to 27.48
Index ranges	$-9 \le h \le 10$
	$-17 \le k \le 20$
	$-21 \le l \le 21$
Absorption correction	Gaussian
Max. and min. transmission	0.6480 and 0.8577
GOF on F^2	1.026
R_1, R_2 [I > 2σ (I)]	0.0665, 0.1412
R_1, R_2 (all data)	0.1083, 0.1613
Largest diff. peak and hole (e.Å^{-3})	4.923 and -1.266

Table 32. Selected bond lengths [Å] and angles [°] for **27** and **29**.

		27	
Bond distances (Å)			
Pt1-C3	1.99(2)	Pt1-Cl1	2.311(3)
Pt1-N1	2.105(16)	Pt1-S2	2.442(6)
S1-C1	1.74(2)	S1-C4	1.79(2)
Bond angles (º)			
C3- Pt1-S2	147.5(6)	N1-Pt1-S2	78.6(4)
Cl1-Pt1-S2	103.58(17)	C3-Pt1-N1	79.0(7)
C3-Pt1- Cl1	96.9(6)	N1-Pt1-Cl1	174.4(4)
		29	
Bond distances (Å)			
Pt1-C31	1.914(9)	Pt1-N1	2.034(7)
Pt1-N2	2.042(7)	Pt1-Cl1	2.401(3)
S1-C3	1.656(13)	S1-C4	1.683(11)
Bond angles (º)			
C31-Pt1-N1	80.8(3)	N1-Pt1-N2	161.0(3)
C31-Pt1-N2	80.4(3)	C31-Pt1-Cl1	177.9(3)
N1-Pt1-Cl1	98.2(2)	N2-Pt1-Cl1	100.7(2)
C3-S1-C4	94.2(6)	C16-S2-C5	92.7(5)
C25-N1-Pt1	125.3(6)	C24-N1-Pt1	114.8(6)
C36-N2-C32	120.4(8)	C36-N2-Pt1	125.5(7)
C32-N2-Pt1	114.1(6)	C2-C1-C4	101.7(11)
C8-C7-C6	115.0(8)	C11-C12-C13	117.1(8)

Chapter 5: Magnetic and Conductivity Studies of Conducting Metallopolymers

INTRODUCTION

Conducting Polymer Magnetism

In the late 1970's,[1,2] conjugated polymers were proclaimed as futuristic new materials that would lead to the next generation of electronic and optical devices. It now appears that with the discoveries of polymer light-emitting diodes and organic transistors new technologies are imminent. In particular, polythiophenes are an important representative class of conjugated and electrically conducting polymers that form some of the most environmentally and thermally stable materials. Polythiophene possesses unique properties that have been used in many device applications including electrical conductors, nonlinear optical devices, sensors, batteries, and new types of memory devices. Creative design and development strategies of novel polythiophenes are still under way to obtain interesting materials and enhanced performance in certain devices. In addition to the various physical phenomena currently related to conjugated polymers, magnetism is one of the latest properties found in polymers.

Magnetism traditionally has been restricted to compounds containing metal ions. The first conjugated organic magnet was reported in 2001.[3] Compared to discrete organic radicals, in conducting polymers, the magnetic moments are created upon doping. The possibility of ferromagnetic behavior in conducting polymers has been theoretically addressed[4,5] and evidence of this interaction has been reported.[6,7] However, the majority of such materials are spinless bipolarons, or π-dimers with low spin concentrations in doped conjugated polymers. This lack of spin has limited the applications of these structures as magnetic materials and further development of bi-functional materials.

These drawbacks stimulate us to synthesize new types of magnetic conducting metallopolymers which are both magnetic and electrically conductive. Our strategy is inspired by the previous investigations of molecular magnets, where an inorganic approach has been followed by Kahn *et al*.[8] and Drillon *et al*.,[9] using metal ions bridged by closed-shell organic ligands. Herein, one-dimensional ferrimagnets were obtained, which in some cases ordered ferromagnetically at low temperature. Later on Gatteschi developed the idea by choosing ligands which contain free radicals and investigated the interaction between metal ions and organic radicals.[10] By following Gatteschi's method an extraordinary $V^{II}(TCNE)_x \cdot y(CH_2Cl_2)$ complex with T_c above room temperature was prepared.[11] Since then quite a few interesting research reports were published about the coexistence of conducting electrons and localized spins from metals, which leads to numerous intriguing phenomena, such as paramagnetic superconductivity,[12] antiferromagnetic superconductivity,[13] magnetic-field induced superconductivity,[14] and conducting molecular antiferromagnetic behavior.[15] These exciting results promote us to the idea of directly binding metal ions to conducting polymers, which produce polarons upon doping. In this chapter, our goal is to prepare magnetic conducting metallopolymers with a polythiophene backbone by taking advantage both of transition metal *d* spins and polaronic ferromagnetism in conducting polymers. A promising strategy for creating this type of bi-functionality focuses on a variety of polydentate nitrogen donor ligands with thiophene groups, where the nitrogen atoms chelate the metal ions while the thiophene groups act as the polymerizable portion. This type of intimate interaction between metal center and polymer backbone in an inner sphere mode will lead to a magnetic conducting metallopolymer architecture. As such, the inorganic metal centers can interact magnetically due to the relatively strong magnetic interaction through π-conjugated system as compared to the through-space interaction. Also, the polymer backbone can

simultaneously have a structuring effect and bring an additional property such as conductivity, luminescence, or optical activity.

Spin Crossover (SCO) Background

Considering the striking and fascinating behavior of SCO compounds and the rich literature base on this class of complexes, we chose 3*d* transition metal Fe(II) for our initial studies. The incorporation of Fe(II) into the polymer backbone offers the possibility of: (a) increased cooperativity thus leading to steep and wide hysteresis loop for the purpose of memory device; (b) attenuating the conducting properties by switching on the bi-stable SCO center (switchable SCO polymer conductors).

As a consequence of the energy splitting of the *d* orbitals into the t_{2g} and e_g sets in a ligand field, octahedral complexes of certain transition metal ions with configurations d^4 to d^7, may exist in either the high-spin (HS) or low-spin (LS) state, depending on the nature of the ligand field about the metal ion.[16-20] Although spin transitions have been observed for all the configurations listed above for the first transition series and a very limited number of the second transition series, Fe(II) is the most commonly reported one. For the d^6 ion of Fe(II), for example, the two states are illustrated by $[Fe(H_2O)_6]^{2+}$, which, with the configuration $t_{2g}^4 e_g^2$, has four unpaired electrons and thus is strongly paramagnetic ($^5T_{2g}$ state in octahedral symmetry), and $[Fe(CN)_6]^{4-}$ ($t_{2g}^6 e_g^0$) which has no unpaired electrons ($^1A_{1g}$ state). SCOs are found in many natural systems where they play a vital role in controlling biological functions.[21] They are also observed in certain minerals and in geological processes where the relationship between pressure and spin-state is particularly intriguing.[22] Although in the synthetic systems, SCO was first recognized in 1931 and has been investigated extensively since the mid-1970s, only during the 1980s, however, was it realized that SCO compounds could be used as active

elements in memory devices.[23-25] The basic principle of this type of memory device lies on the hysteresis effect of the SCO complexes. The fundamental origin of the SCO phenomenon is molecular, but the shape of the temperature dependence of the high-spin molar fraction, $x_{HS} = f(T)$, depends strongly on intermolecular interactions. The more pronounced these intermolecular interactions are, the steeper the $x_{HS} = f(T)$ curve around $T_{1/2}$ (the temperature at which two spin states are present in the ration 1 : 1). When the magnitude of these intermolecular interactions overcomes a threshold value, the SCO phenomenon may become cooperative, which, if pronounced, may lead to a thermal hysteresis loop. In this case, the temperature of the LS → HS transition in the warming mode, $T_c\uparrow$, is higher than the temperature of the HS → LS transition in the cooling mode, $T_c\downarrow$. Between $T_c\uparrow$ and $T_c\downarrow$, the state of the system, LS or HS, depends on its history, and hence on the information which has been stored, conferring a memory effect on the system. The loop width and steepness are related to the strength of the cooperative interactions. For a given system, allowing SCO centers to communicate via covalently bound chemical bridges, i. e. in a polymeric species, is an important strategy to enhance cooperativity.[26,27] Our approach to a novel conducting metallopolymer structure includes direct bonding of Fe(II) to the backbone of the polymer, which guarantees a polymeric structure for the effective communication of SCO centers. This arrangement will lead to increased control of metal complex spacing. Furthermore, the polymer backbone brings the additional property of conduction. Besides, the use of electrodeposition provides easy fabrication of thin films of controlled thickness, which is very important for the practical application of these materials.

With the recognition that SCO compounds bear the potential for practical application in switching and display devices, recent activities in this field have been mostly devoted to the design of new SCO compounds in which SCO properties may be

combined with other physical or chemical properties in a synergic fashion, e.g. magnetic exchange, liquid crystalline properties, host-guest chemistry, non-linear optics, electrical conductivity and ligand isomerization.[28-36] Such synergic cooperative systems with two or more phase transitions of different physical nature may lead to a number of advantages in practical applications, e.g. enhancement of spin transition signals, switching and sensing in different temperature regimes. Among them, pioneering work on the coexistence of SCO and electrical conductivity has been reported by Faulmann *et al*.,[37-39] where the cooperativity in SCO cations was enhanced via the control of π-packing, a supramolecular synthetic strategy.

Scope of Our Research

Four different ligand systems, **L8 - L11** (Scheme 14) have been synthesized, in which the nitrogen donor moiety serves as a metal binding group and thiophene or its derivatives as polymerizable groups. Generally, we chose the polydentate nitrogen donor environment systems which have been shown to favor SCO in the literature, then install the polymerizable groups into those ligands. According to different synthetic strategies, we can either attach the polymerizable groups in the last step, or install the polymerizable groups at the beginning.

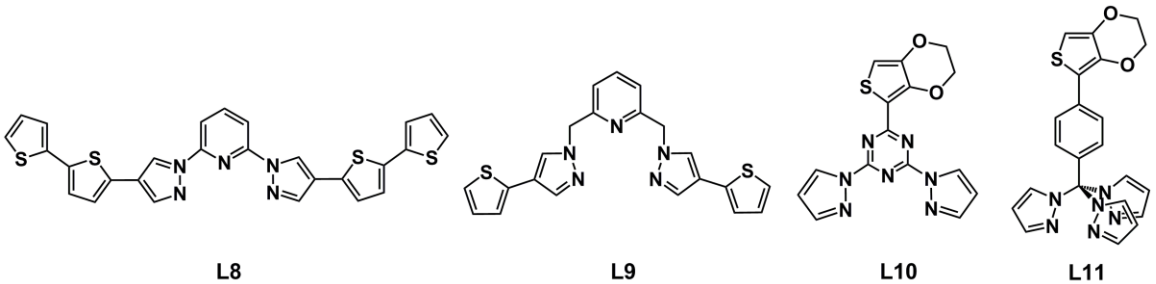

Scheme 14. Molecular structure of **L8 - L11**.

This kind of ligand design also minimizes spinless bipolaron formation as the polymer structure only consists of comparatively short two-ring or four-ring spin containing units. Our polymers are anticipated to have a much stronger effect on the SCO centers through covalent bonds. Equally, when the metal centers undergoes cooperative SCO behavior, the electronic transport in the conducting backbone will also be affected dramatically, which suggests a promising precursor for the synthesis of switchable SCO polymer conductors.

All complexes have been characterized by X-ray diffraction analysis and elemental analysis. Variable temperature electron paramagnetic resonance (EPR) spectroscopy and magnetic susceptibility were measured to monitor the spin state change of the Fe(II) system. The conductivities of films containing transition metals have also been measured.

EXPERIMENTAL

General Methods

Air- and moisture-sensitive reactions were carried out in oven-dried glassware using standard Schlenk techniques under an inert atmosphere of dry argon. Dry DMF and 1,4-dioxane were used from EMD as sure-seal bottles. Iodine was purchased from J. T. Baker. Tri-*n*-butyltin chloride, sodium amide, thiophene-2-acetonitrile, ethyl formate, cyanuric chloride, pyridine, and 2,6-dibromopyridine were purchased from Alfa Aesar. 3,4-Ethylenedioxythiophene was obtained from AK Scientific. Hydrazine and 4-(trifluoromethyl)phenol were purchased from Sigma-Aldrich. Sodium hydride and raney nickel (slurry in water) were purchased from Aldrich. *Trans*-dichlorobis(triphenylphosphine)palladium(II) and tetrakis(triphenylphosphine)palladium(0) were obtained from Strem. 2,6-

Bis(chloromethyl)pyridine and trifluoromethanesulfonic anhydride were purchased from TCI. Toluene, tetrahydrofuran, diethyl ether and CH_2Cl_2 were dried using a double-column anhydrous solvent system (Innovative Technologies, Newburyport, MA) and further degassed via nitrogen purge prior to use.

NMR spectra were recorded with Varian 400 MHz (^1H and $^{13}C\{^1H\}$) spectrometer. Low-res mass spectrometry was carried out by Thermo Finngan TSQ 700. Elemental analysis was performed by QTI, Whitehouse, NJ (www.qtionline.com). X-ray photoelectron spectroscopy (XPS) was carried out on a PHI 5700 XPS system equipped with a dual Mg X-ray source and monochromatic Al X-ray source complete with depth profile and angle-resolved capabilities. The dc magnetization was measured with a commercial superconducting quantum interference device (SQUID) magnetometer. X-band EPR spectra were recorded on a Bruker EMX Plus spectrometer equipped with a nitrogen flow cryostat.

Crystal Structure Determination

A suitable crystal was mounted on a glass fiber and placed in the low-temperature nitrogen stream. The data were collected on a Nonius Kappa CCD diffractometer using a graphite monochromator with MoKα radiation (λ = 0.71073Å). Data reduction was performed using DENZO-SMN.[40] The structure was solved by direct methods using SIR97[41] and refined by full-matrix least-squares on F^2 with anisotropic displacement parameters for the non-H atoms using SHELXL-97.[42]

Electrochemistry

Electrochemical syntheses and studies were performed in a dry-box under a nitrogen atmosphere using a GPES system from Eco. Chemie B. V.. All the electrochemical experiments were carried out in a three-electrode cell with a $Ag/AgNO_3$

reference electrode (silver wire dipped in a 0.01 M silver nitrate solution with 0.1 M $TBAPF_6$ in CH_3CN), a Pt button working electrode or an ITO coated glass electrode, and a Pt wire coil counter electrode. Potentials were relative to this 0.01 M $Ag/AgNO_3$ reference electrode. Ferrocene was used as an external reference to calibrate the reference electrode before and after experiments were performed and that value was used to correct the measured potentials. The supporting electrolyte was 0.1 M $TBAPF_6$ that was purified by recrystallization three times from hot ethanol before being dried for 3 days at 100 ^oC under active vacuum.

Film Thickness

Film thickness was determined using a Veeco Dektak Profilomter. Films were prepared on interdigitated microelectrode that was first treated by successive sonnication in deionized water, ethanol, acetone, and methylene chloride. Electropolymerization was performed for 5 and 10 cycles at a scan rate of 100 mV/s.

In Situ Conductivity

In situ conductivity measurements were carried out at a scan rate of 10 mV/s with a 40mV offset potential between the two working electrodes. The conductivity (σ) was then calculated by the equation $\sigma = (i_D/V_D)(D/nTL)$, where i_D is the drain current, V_D is the offset potential, and T is the polymer thickness; with a 5 μm gap, D; n = 99 gaps; and 0.5 cm electrode length, L. The conductivity was then calculated from the value of the drain current by applying geometrical factors.

Synthesis

Synthesis of 2,6-Bis[4-(2,2'-bithienyl-5-yl)pyrazol-1-yl]pyridine (L8)

5-(Tributylstannyl)-2,2'-bithiophene was prepared by Swager's method.[43] 2,6-Bis(4-iodopyrazol-1-yl)pyridine was prepared using the procedure described by Zoppellaro.[44]

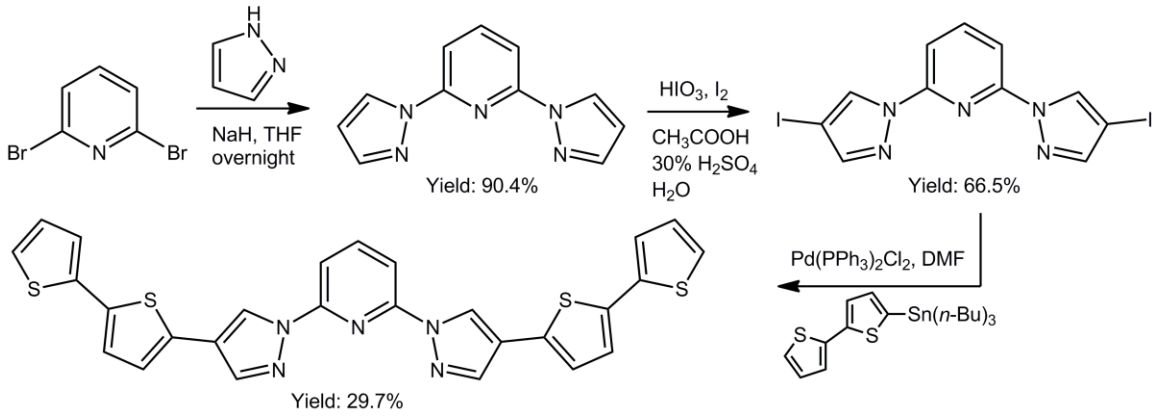

Scheme 15. Synthesis of **L8**.

2,6-Bis(pyrazol-1-yl)pyridine. Sodium hydride (2.4 g, 0.1 mol) was added to a 250 mL of 3-necked flask. Dry THF (50 mL) was transferred to the flask. Pyrazole (6.8 g, 0.1 mol) was slowly added to the above solution under N_2. The mixture was stirred at room temperature for 30 min until all bubbles evolved and the solution became clear. After the addition of 2,6-dibromopyridine (11.8 g, 0.0496 mol), the mixture was stirred at 60 °C overnight. The solvent was evaporated, and the residue was suspended in 300 mL of $NH_4Cl_{(aq)}$. The white solid was filtered out, washed with water and methanol, dried under vacuum to get 9.47 g product (Yield = 90.4%). Purity and composition were confirmed by comparing ^{1}H NMR spectroscopy data to literature values.[45]

2,6-Bis[4-(2,2'-bithienyl-5-yl)pyrazol-1-yl]pyridine (L8). 2,6-Bis(4-iodopyrazol-1-yl)pyridine (1.15 g, 2.48 mmol) and $Pd(PPh_3)_2Cl_2$ (0.305 g, 0.44 mmol) were added into a 3-necked flask. The mixture was evacuated under vacuum for 20 min, then dry DMF was cannula transferred into the flask followed by 5-(tributylstannyl)-2,2'-

bithiophene (2.28 g, 5 mmol). After the mixture was heated at 120 °C for four hours, another portion of 5-(tributylstannyl)-2,2'-bithiophene (2.28 g, 5 mmol) was added. The reaction mixture was heated at 120 °C overnight. After cooling, 100 mL of CH_2Cl_2 was added. The resulting solution was washed with $NH_4Cl_{(aq)}$, $NaF_{(aq)}$ and water. The organic phase was evaporated. The crude product was purified on silica gel column with CH_2Cl_2 as eluent to yield a yellow solid (0.396 g, 29.6%). ^{1}H NMR (400 MHz, $CDCl_3$): δ (ppm) = 8.65 (d, *J* = 0.8, 2H), 7.88 (m, 3H), 7.82 (d, *J* = 0.4, 1H), 7.81 (d, *J* = 0.8, 1H), 7.17 (dd, *J* = 1.2, 5.2, 2H), 7.14 (dd, *J* = 1.2, 5.2, 2H), 7.08 (m, 4H), 6.98 (dd, *J* = 3.2, 5.2, 2H). CI-MS (CH_2Cl_2) m/z: 540 [**L8**]$^+$. Elemental anal. calcd. (Found) for **L8**, $C_{27}H_{17}N_5S_4$: C, 60.08 (59.21); H, 3.17 (2.66); N, 12.98 (12.54).

Synthesis of 2,6-Bis((4-(thiophen-2-yl)-1H-pyrazol-1-yl)methyl)pyridine (L9)

Thienyl-2-malonaldehydonitrile and 4-(thiophen-2-yl)-1H-pyrazole were prepared according to literature methods.[46,47]

NaH (72.0 mg, 3.0 mmol) was added to a 3-necked flask. Dry THF was transferred into the flask under Ar. 4-(Thiophen-2-yl)-1H-pyrazole (450.6 mg, 3.0 mmol) was slowly added to the above mixture under Ar. The mixture was stirred at room temperature for 30 min until all bubbles evolved and the solution became clear. After the addition of 2,6-bis(chloromethyl)pyridine (176.0 mg, 1.0 mmol), the mixture was refluxed for 18 h. The solvent was evaporated, the residue was suspended in $NH_4Cl_{(aq)}$ to obtain a white precipitate. The solid was collected by filtration, washed with plenty of water, dried under vacuum at 70 °C overnight to get the target product (177.6 mg, 44%). ^{1}H NMR (400 MHz, CD_3Cl): δ (ppm) = 7.82 (t, *J* = 8.0, 1H), 7.79 (s, 2H), 7.68 (s, 2H), 7.20 (d, *J* = 8.0, 2H), 7.09 (dd, *J* = 0.8, 5.2, 2H), 7.00 (dd, *J* = 0.8, 5.2, 2H), 6.94 (dd, *J* = 3.6, 5.2, 2H), 5.63 (s, 4H). ^{13}C{^{1}H} NMR (100 MHz, $CDCl_3$): δ (ppm) = 155.8, 139.6,

137.7, 135.0, 127.9, 127.3, 123.3, 122.8, 121.9, 117.8, 56.8. CI-MS (CH_2Cl_2) m/z: 404 [**L9**]$^+$. Elemental anal. calcd. (Found) for **L9**, $C_{21}H_{17}N_5S_2$: C, 62.51 (62.57); H, 4.25 (4.76); N, 17.36 (17.11).

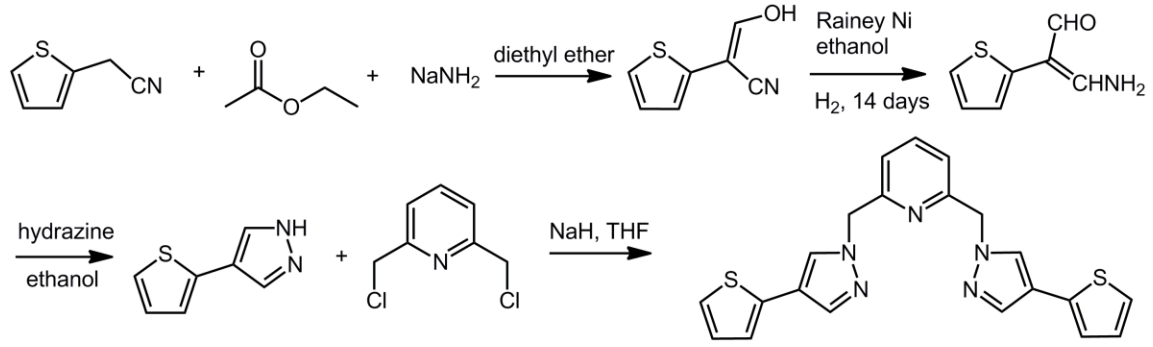

Scheme 16. Synthesis of **L9**.

Synthesis of 2-(3,4-(Ethylenedioxy)thien-2-yl)-4,6-di(1H-pyrazol-1-yl)-1,3,5-triazine (L10)

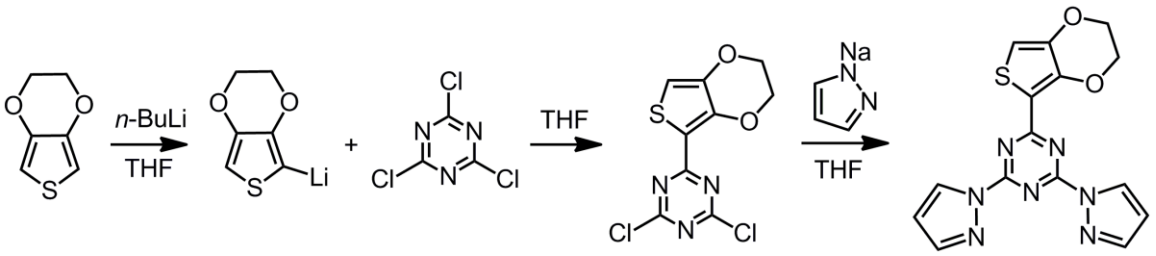

Scheme 17. Synthesis of **L10**.

2,4-Dichloro-6-(3,4-(ethylenedioxy)thien-2-yl)-1,3,5-triazine. 3,4-Ethylenedioxythiophene (1.42 g, 10.0 mmol) was added to dry THF in a 100 mL schlenk flask. *n*-BuLi (1.6 M in hexanes, 6.87 mL) was added dropwise to the above solution at -78 °C. After stirring at -78 °C for one hour, the resulting solution was cannula transferred to a THF solution of cyanuric chloride (1.84 g, 10.0 mmol) at -78 °C. The mixture was stirred at -78 °C for two hours, then the temperature was increased to room temperature. After stirring overnight at room temperature, 200 mL of CH_2Cl_2 was added.

The organic phase was washed with $NH_4Cl_{(aq)}$ and water, dried over $MgSO_4$, then evaporated. The crude product was purified on silica gel column with CH_2Cl_2 as eluent to get pale yellow product (1.19 g, 41%). ^{1}H NMR (400 MHz, CD_3Cl): δ (ppm) = 6.82 (s, 1H), 4.48 (t, *J* = 4.0, 2H), 4.29 (t, *J* = 4.0, 2H). $^{13}C\{^1H\}$ NMR (100 MHz, $CDCl_3$): δ (ppm) = 171.3, 169.4, 148.4, 142.9, 113.0, 111.8, 66.0, 64.3. CI-MS (CH_2Cl_2) m/z: 290 $[M]^+$. Elemental anal. calcd. (Found) for $C_9H_5Cl_2N_3O_2S$: C, 37.26 (36.98); H, 1.74 (2.01); N, 14.48 (14.72).

2-(3,4-(Ethylenedioxy)thien-2-yl)-4,6-di(1H-pyrazol-1-yl)-1,3,5-triazine (L10). NaH (211.2 mg, 8.8 mmol) was added to a 3-necked flask. Dry THF (50 mL) was transferred into the flask under Ar. Pyrazole (598.4 mg, 8.8 mmol) was slowly added to the above mixture under Ar. The mixture was stirred at room temperature for 30 min until all bubbles evolved and the solution became clear. After the addition of 2,4-dichloro-6-(3,4-(ethylenedioxy)thien-2-yl)-1,3,5-triazine (1.16 g, 4.0 mmol), the mixture was refluxed overnight. The solvent was evaporated, the residue was redissolved in CH_2Cl_2. The organic phase was washed with $NH_4Cl_{(aq)}$ and water, dried over $MgSO_4$, then evaporated. The crude product was purified on silica gel column with CH_2Cl_2 : MeOH (10 : 1) as eluent to get pale yellow product (925 mg, 65.4%). ^{1}H NMR (400 MHz, CD_3Cl): δ (ppm) = 8.73 (dd, *J* = 0.8, 3.2, 2H), 7.92 (dd, *J* = 0.8, 1.6, 2H), 6.76 (s, 1H), 6.54 (dd, *J* = 1.2, 2.8, 2H), 4.54 (m, 2H), 4.31 (m, 2H). $^{13}C\{^1H\}$ NMR (100 MHz, $CDCl_3$): δ (ppm) = 168.8, 161.4, 146.1, 144.4, 141.6, 129.3, 113.3, 108.8, 108.2, 64.7, 63.1. CI-MS (CH_2Cl_2) m/z: 353 [**L10**]$^+$. Elemental anal. calcd. (Found) for **L10**, $C_{15}H_{11}N_7O_2S$: C, 50.99 (51.24); H, 3.14 (3.68); N, 27.75 (26.98).

Synthesis of 1,1',1''-((4-(3,4-(Ethylenedioxy)thien-2-yl)phenyl)methanetriyl)tris(1H-pyrazole) (L11)

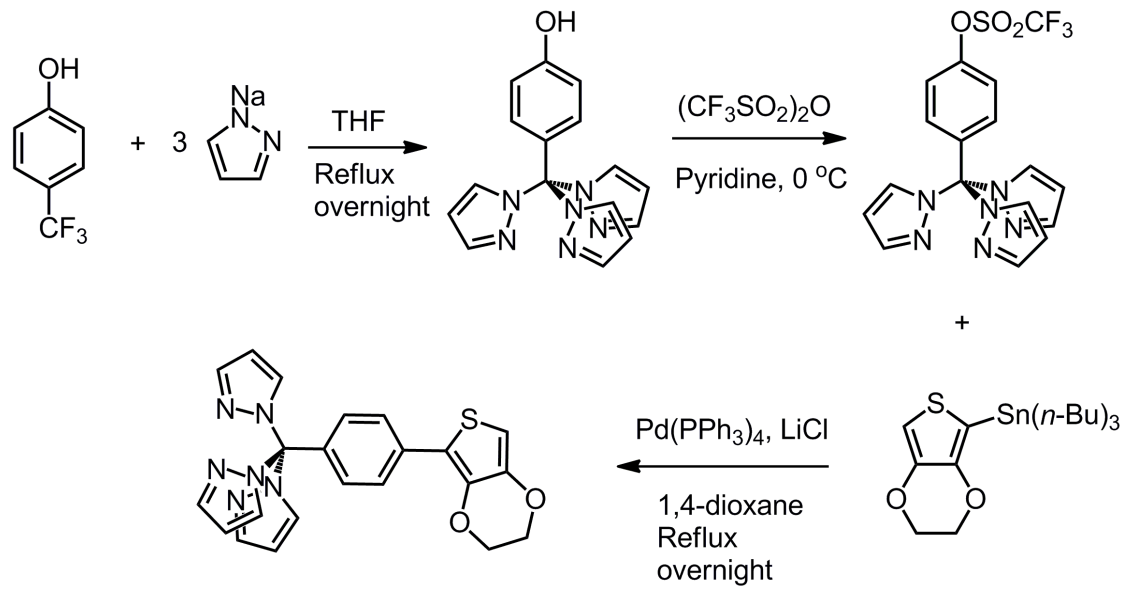

Scheme 18. Synthesis of **L11.**

4-(Tri(1H-pyrazol-1-yl)methyl)phenol. NaH (1.92 mg, 80 mmol) was added to a 3-necked flask. Dry THF (100 mL) was transferred into the flask under Ar. Pyrazole (5.44 g, 80 mmol) was slowly added to the above mixture under Ar. The mixture was stirred at room temperature for 30 min until all bubbles evolved and the solution became clear. After the addition of 4-(trifluoromethyl)phenol (3.24 g, 20 mmol), the mixture was refluxed for 18 h. The solvent was evaporated to get the residue, which was collected by filtration, washed with diethyl ether. The crude product was dissolved in water, dilute HCl (10%) was added dropwise to precipitate the product until the pH = 7. The white precipitate was collected by filtration, washed with water, then dried under vacuum to give the target product (3.61 g, 59%). ^{1}H NMR (400 MHz, CD_3Cl): δ (ppm) = 7.72 (dd, *J* = 0.8, 1.6, 3H), 7.50 (dd, *J* = 0.4, 1.2, 3H), 7.14 (s, 1H), 6.90 (dd, *J* = 2.4, 6.8, 2H), 6.64 (dd, *J* = 2.4, 6.8, 2H), 6.35 (dd, *J* = 2.0, 2.8, 3H). ^{13}C{^{1}H} NMR (100 MHz, CD_3OD): δ

(ppm) = 159.5, 141.1, 132.3, 130.2, 128.0, 114.7, 106.2, 93.3. CI-MS (CH_2Cl_2) m/z: 306 $[M]^+$.

4-(Tri(1H-pyrazol-1-yl)methyl)phenyl trifluoromethanesulfonate. 4-(Tri(1H-pyrazol-1-yl)methyl)phenol (712 mg, 2.0 mmol) was added to a schlenk flask. Dry pyridine (20 mL) was added into the flask at 0 °C. Trifluoromethanesulfonic anhydride (705 mg, 2.5 mmol) in dry pyridine (10 mL) was added dropwise to the above solution at 0 °C under Ar. After stirring at 0 °C for another two hours, the solution was stirred at room temperature overnight. The mixture was poured into 100 mL of diethyl ether, then washed with water and dilute HCl (10%). The organic phase was evaporated to get a yellow solid (695 mg, 79.3%). ^{1}H NMR (400 MHz, CD_3Cl): δ (ppm) = 7.66 (dd, *J* = 0.8, 1.6, 3H), 7.32 (d, *J* = 9.2, 2H), 7.25 (dd, *J* = 0.8, 2.8, 3H), 7.23 (d, *J* = 14, 2H), 6.32 (d, *J* = 1.6, 2.8, 3H). ^{13}C{^{1}H} NMR (100 MHz, CD_3Cl): δ (ppm) = 150.7, 142.0, 137.9, 132.3, 131.8, 121.2, 107.2, 92.6.

1,1',1''-((4-(3,4-(Ethylenedioxy)thien-2-yl)phenyl)methanetriyl)tris(1H-pyrazole) (L11). 4-(Tri(1H-pyrazol-1-yl)methyl)phenyl trifluoromethanesulfonate (438.4 mg, 1.0 mmol), LiCl (127.2 mg, 3.0 mmol), and 2-(tributylstannyl)-3,4-(ethylenedioxy)thiophene (860.2 mg, 2.0 mmol) were added into a 3-necked flask. The chemicals were dried under vacuum for 30 min, then 1,4-dioxane (50 mL) was transferred into the flask. $Pd(PPh_3)_4$ (69.5 mg, 0.06 mmol) was added under N_2. The mixture was refluxed overnight. The solvent was evaporated to get the crude product, which was further purified on silica gel column with CH_2Cl_2 as eluent to get 235 mg of product, yield: 54.3%. ^{1}H NMR (400 MHz, CD_3Cl): δ (ppm) = 7.75 (t, *J* = 2.0, 3H), 7.73 (dd, *J* = 2.0, 2.8, 2H), 7.54 (dd, *J* = 0.8, 2.8, 3H), 7.09 (dd, *J* = 2.0, 2.8, 2H), 6.36 (dd, *J* = 1.6, 2.8, 2H), 6.34 (s, 1H), 4.30 (m, 2H), 4.25 (m, 2H). ^{13}C{^{1}H} NMR (100 MHz, CD_3OD): δ (ppm) = 142.5, 141.6, 139.4, 135.6, 135.2, 132.6, 129.2, 125.6, 116.5, 106.7,

99.0, 93.3, 65.0, 64.6. CI-MS (CH_2Cl_2) m/z: 432 [**L11**]$^+$. Elemental anal. calcd. (Found) for **L11**, $C_{22}H_{18}N_6O_2S$: C, 61.38 (61.66); H, 4.21 (4.69); N, 19.52 (19.14).

Synthesis of [FeL8(CH$_3$OH)$_3$](ClO$_4$)$_2$·CH$_3$OH·0.5H$_2$O (31)

Ferrous perchlorate hydrate (25.5 mg, 0.1 mmol) dissolved in MeOH was slowly diffused into the **L8** (54.0 mg, 0.1 mmol) solution in CH_2Cl_2. After a few weeks, yellow crystals suitable for X-ray diffraction analysis were found (54.0 mg, 29%). Elemental anal. calcd. (Found) for **31 - CH$_3$OH - 0.5 H$_2$O**, $C_{30}H_{29}Cl_2FeN_5O_{11}S_4$: C, 40.46 (40.11); H, 3.28 (3.73); N, 7.86 (7.45).

Synthesis of Fe(L9)$_2$(ClO$_4$)$_2$·2CH$_3$OH ·H$_2$O (32)

Ferrous perchlorate hydrate (25.5 mg, 0.1 mmol) dissolved in MeOH (5 mL) was added to **L9** (80.7 mg, 0.2 mmol) solution in CH_2Cl_2 (10 mL). The resulting yellow solution was stirred at room temperature under N_2 for 2 h. Diethyl ether was slowly diffused into the above solution to get colorless crystals (26.3 mg, 23%). Elemental anal. calcd. (Found) for **32 - 2CH$_3$OH - H$_2$O**, $C_{42}H_{34}Cl_2FeN_{10}O_8S_4$: C, 47.51 (47.19); H, 3.23 (3.37); N, 13.19 (13.41).

Synthesis of Fe(L9)$_2$(BF$_4$)$_2$·C$_3$H$_6$O (33)

Ferrous tetrafluoroborate hexahydrate (6.8 mg, 0.02 mmol) in acetone (2 mL) was slowly diffused into the **L9** (8.1 mg, 0.02 mmol) solution in CH_2Cl_2 (5 mL) in a sealed tube. After one week, green crystals were found (6.7 mg, 31%). Elemental anal. calcd. (Found) for **33 - C$_3$H$_6$O**, $C_{42}H_{34}B_2F_8FeN_{10}S_4$: C, 48.67 (48.22); H, 3.31 (3.49); N, 13.51 (12.98).

Synthesis of $Fe(L9)_2(BF_4)_3 \cdot C_3H_6O$ (34)

Ferrous tetrafluoroborate hexahydrate (33.8 mg, 0.1 mmol) in acetone (10 mL) was added into the **L9** (80.7 mg, 0.2 mmol) solution in CH_2Cl_2 (20 mL). The mixture was stirred under N_2 for several hours, then filtered. The filtration was stored at the refrigerator (~ -20 °C). Yellow crystals suitable for X-ray diffraction analysis were obtained after a few days (30.7 mg, 26%). Elemental anal. calcd. (Found) for **34 - C_3H_6O**, $C_{42}H_{34}B_3F_{12}FeN_{10}S_4$: C, 44.91 (45.17); H, 3.05 (2.63); N, 12.47 (13.02).

Synthesis of $Fe(L10)_2(ClO_4)_2 \cdot CH_3OH$ (35)

Ferrous perchlorate hydrate (25.5 mg, 0.1 mmol) dissolved in MeOH (5 mL) was added to **L10** (70.7 mg, 0.2 mmol) solution in CH_2Cl_2 (10 mL). The resulting orange solution was stirred at room temperature under N_2 for a few hours. Diethyl ether was slowly diffused into the above solution to get red crystals (34.8 mg, 35%). Elemental anal. calcd. (Found) for **35 - CH_3OH**, $C_{30}H_{22}Cl_2FeN_{14}O_{12}S_2$: C, 37.48 (36.89); H, 2.31 (2.54); N, 20.40 (20.76).

Synthesis of $Cu_2(L11)_2(SO_4)_2(CH_3OH)_2 \cdot 2CH_3OH$ (36)

$CuSO_4 \cdot 5H_2O$ (25.0 mg, 0.1 mmol) in MeOH (10 mL) was added to **L11** (43.0 mg, 0.1 mmol) solution in CH_2Cl_2 (10 mL). The mixture was stirred at room temperature under N_2 overnight. The solution was filtered, the filtration stood at room temperature for a couple of days to get yellow crystals (61.5 mg, 47%). Elemental anal. calcd. (Found) for **36**, $C_{48}H_{52}Cu_2N_{12}O_{16}S_4$: C, 44.06 (43.19); H, 4.01 (3.27); N, 12.85 (13.03).

RESULTS AND DISCUSSION

Structure Determination

Crystal Structure of $[FeL8(CH_3OH)_3](ClO_4)_2 \cdot CH_3OH \cdot 0.5H_2O$ (31)

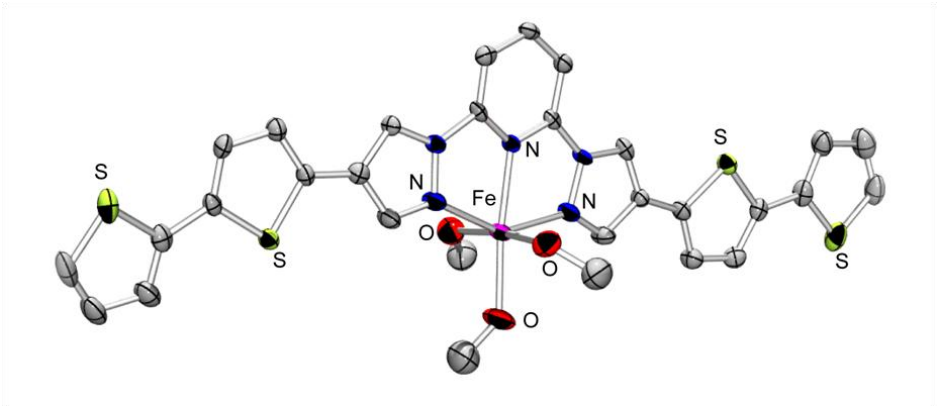

Figure 65. ORTEP diagram of **31** showing the labeling scheme of selected atoms at 30% probability level. Hydrogen atoms, perchlorate anions and solvent molecules are omitted for clarity.

In one unit cell of the solid state structure of **31**, there are two $[Fe\mathbf{L8}(CH_3OH)_3]^{2+}$ cations, four perchlorate anions, two methanol solvent molecules and one water molecule. An ORTEP perspective view of the cationic moiety of **31** is shown in Figure 65. The Fe(II) center is six-coordinate in a distorted octahedral geometry. One **L8** ligand is bound to Fe(II) with two nitrogen atoms from the pyrazole rings and one nitrogen atom from the pyridine ring. The Fe-N distances involving the pyrazole unit are longer (2.184(7) Å) than the pyridine one (2.134(7) Å). However, these Fe-N bond lengths are typical for high-spin iron(II) centers.[48] The other three coordination sites are completed by three oxygen atoms from the coordinated methanol molecules with average Fe-O bond length of 2.107(7) Å, which are in the normal range of Fe-O(methanol) bond distances.[49] The N-Fe-O is almost linear with the average angle of 173.5°. The two pyrazole rings are almost coplanar with the pyridine rings. The dihedral angles between two pyrazole rings and pyridine ring are 2.4° and 5.4°. The thiophene rings in this molecule are also parallel to the bis(pyrazol-1-yl)pyridine portion with the largest dihedral angle of 9.3°. That the

ligand to metal ratio is not the common 2 : 1 for Fe(II) bis(pyrazol-1-yl)pyridine complex can be explained by the large steric hindrance of the ligand.

Crystal Structure of 32 - 34

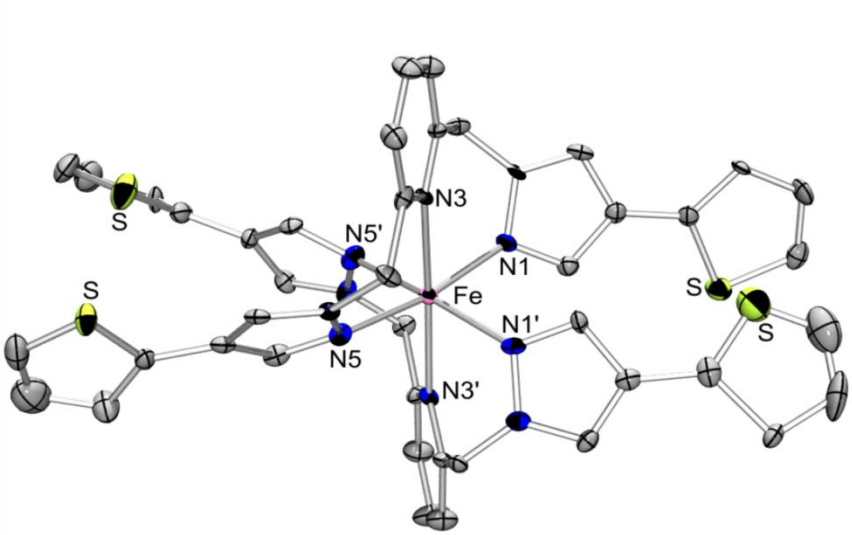

Figure 66. ORTEP diagram of the cationic structure of **32** showing the labeling scheme of selected atoms at 30% probability level. Hydrogen atoms, perchlorate anions and solvent molecules are omitted for clarity.

32 crystallizes in the triclinic space group *P*-1. To the best of our knowledge, it is the first time that the structure of complexes containing the 2,6-bis[(pyrazol-1-yl)methyl]pyridine derivatives with Fe(II) has been reported. The triclinic unit cell of the solid state structure contains one Fe(**L9**)$_2^{2+}$ cation, two perchlorate anions, two methanol molecules and one water molecule. Two **L9** ligands coordinate with one Fe(II) center. The Fe-N1 and Fe-N5 distances are 2.149(7) and 2.169(8) Å, respectively, which are typical of those observed with other complexes of Fe(II) with nitrogen containing heterocycles as ligands in high-spin state.[50] The pyridyl nitrogen is also connected to the iron atom, but the distance is longer (2.281(7) Å). The slightly longer Fe-N distances

involve the pyridine rings indicate that the geometry around iron is best described as a slightly elongated octahedron. There is a *trans* arrangement of the pyrazolyl rings, which orient above and below the plane of the central pyridyl ring, as pictured in Figure 66. The dihedral angles between two pyrazole rings with the pyridine ring are 55.6 and 63.9°. This arrangement has been published before for those metal complexes with 2,6-bis[(pyrazol-1-yl)methyl]pyridine.[51] In **L9**, the dihedral angles between the thiophene rings and pyrazole ring are 11.7 and 15.4°. The cationic units are associated into one-dimensional (1D) supramolecular chains based on S···S interactions (3.513 Å) as shown in Figure 67.

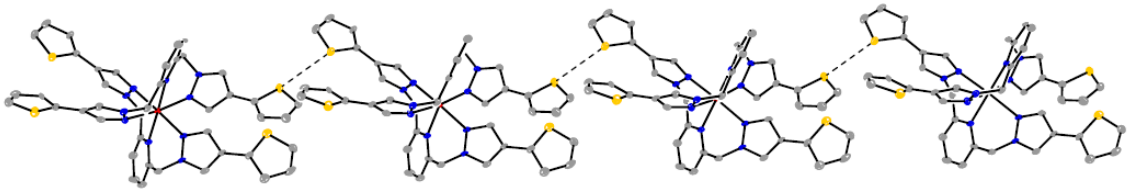

Figure 67. Association of the cationic units in **32** into 1D supramolecular chains based on the S···S interactions of thiophene rings between neighboring molecules.

Complex **33** and **34** have the same cationic structure as that of complex **32**. In complex **33**, the coordination geometry of Fe(II) is also an elongated octahedron with longer Fe-N(pyridine) bond length of 2.272(10) Å and shorter Fe-N(pyrazole) bond lengths of 2.150(9) and 2.162(9) Å. The dihedral angles of two pyrazole rings and pyridine ring (60.6 and 73.2°) are larger than those in **32**. Complex **34** crystallizes in monoclinic space group *C*2/*c*. There are one Fe(**L9**)$^{3+}$ cation, three tetrafluoroborate anions and one acetone solvent molecule in the unit cell. Due to the oxidation state change of the Fe metal center from +2 to +3, the Fe-N bond lengths in **34** are shorter than those in complex **32** and **33**. The long Fe-N(pyridine) (2.117(5) Å) and short Fe-

N(pyrazole) (2.106(5) Å) bonds compose the elongated octahedral geometry of Fe(III). The bond length shortening also leads to the decreased dihedral angles between the pyrazole rings and pyridine ring (53.7 and 58.8°).

Crystal Structure of $Fe(L10)_2(ClO_4)_2 \cdot CH_3OH$ (35)

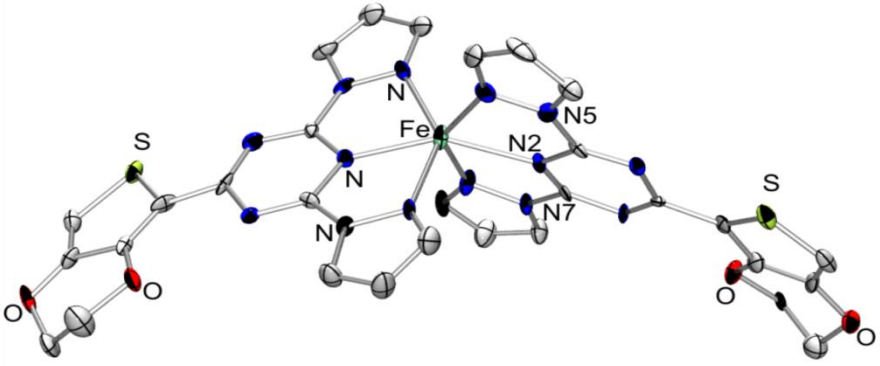

Figure 68. ORTEP diagram of the cationic structure of **35** showing the labeling scheme of selected atoms at 30% probability level. Hydrogen atoms, perchlorate anions and solvent molecules are omitted for clarity.

Ligand **L10** is a modification of 2,4,6-tris(pyrazolyl)-1,3,5-triazine. EDOT polymerizable group is first attached to the triazine through stille coupling. The other two Cl atoms are substituted by pyrazole later. The coordination chemistry of 2,4,6-tris(pyrazolyl)-1,3,5-triazine and Fe(II) has never been explored before. As a derivative of 2,4,6-tris(pyrazolyl)-1,3,5-triazine, **L10** may adopt various coordination modes with metal ions, such as tridentate terpyridine-like and bidentate bipyridine-like modes. Crystal structure analysis shows that in complex **35**, **L10** adopts the tridentate mode with three nitrogens coordinating with the Fe(II) (Figure 68). The Fe-N(triazine) bond distance (2.076(13) Å) is shorter than the Fe-N(pyrazole) bond distances (2.262(16) and 2.283(14) Å), which makes a compressed octahedral geometry for Fe(II). The triazine ring C-N

distances of C8-N2 (1.383(18) Å) and C7-N1 (1.41(2) Å) are typical single-bond values, and the remaining four C-N distances are narrowly spread in the double-bond range (between 1.31(2) and 1.345(19) Å). Two pyrazole rings are almost coplanar with the triazine ring with the dihedral angles of 3.3 and 5.0°. The dihedral angle between the thiophene ring and the triazine ring is 11.8°.

Crystal Structure of $Cu_2(L11)_2(SO_4)_2(CH_3OH)_2 \cdot 2CH_3OH$ (36)

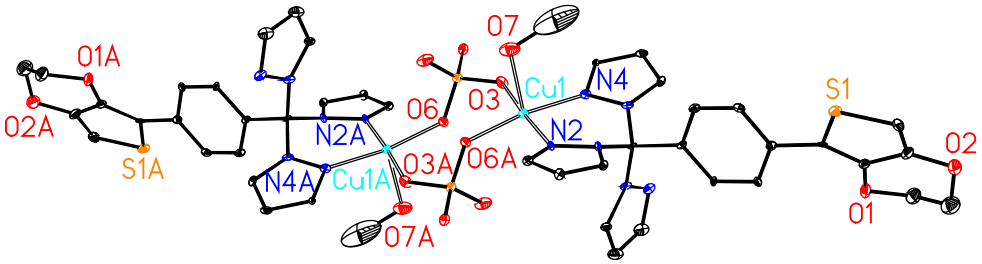

Figure 69. ORTEP diagram of **36** showing the labeling scheme of selected atoms at 30% probability level. Hydrogen atoms and solvent molecules are omitted for clarity.

The isoelectronic tris(pyrazolyl)methane ligand is formally derived from the tris(pyrazolyl)borate ligand by replacing the central boron anion with a carbon atom, which has received less attention.[52,53] The coordination chemistry of tris(pyrazolyl)methane with transition metals typically reveals a tridentate coordination mode. However, in the molecular structure of complex **36** (shown in Figure 69), the tris(pyrazolyl)methyl unit acts as a bidentate ligand. The two Cu(II) centers are bridged by sulfate anions. Two out of three pyrazole rings coordinate with Cu(II) with the Cu-N bond length of 1.991(10) Å. The Cu(II) is five-coordinate with the coordination geometry of square pyramidal. The equatorial plane is composed of two nitrogen atoms and two

oxygen atoms from the bridged sulfate anions (Cu-O bond lengths of 1.948(8) and 1.923(8) Å) with the mean deviation of 0.0813 Å. The Cu1 atom is 0.0895 Å out of this plane. The axial position of the square pyramid is occupied by the oxygen atom from the coordinated methanol molecule with the Cu-O bond length of 2.299(10) Å. The sulfate anions act as a bidentate bridge to connect two Cu(II) atoms with a distance of 4.830 Å. The hydrogen bonds between the oxygen atoms of sulfate anions and the oxygen atoms of coordinated methanol (O···H-O distance of 2.726 Å) connect the dinuclear units into 1D structure (Figure 70).

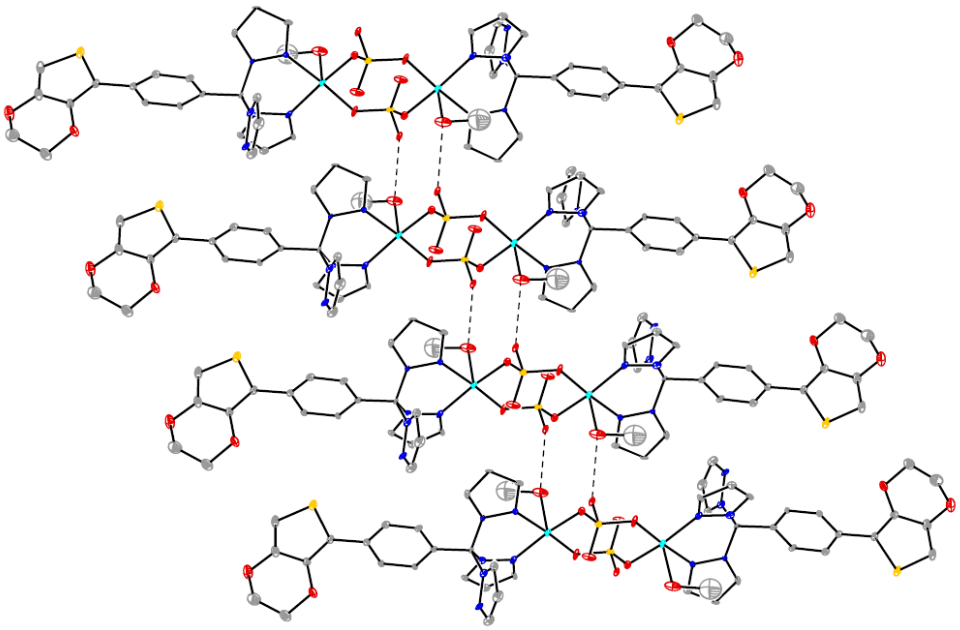

Figure 70. Association of the dinuclear units of **36** into 1D supramolecular chain based on the hydrogen bonds between neighboring molecules.

Electrochemical Studies

Cyclic voltammetry of **31** over a window of +1.25 to -1.5 V (vs Fc/Fc^+) resulted in the growth of a polymer film (Figure 71). The first scan has oxidation peaks around 0.8 and 1.1 V, and reduction peaks at 0.74 and 0.49 V. With increasing scans, the oxidation and reduction peaks merge into one broad peak. All these redox peaks grow linearly with increasing scans. The XPS data were used to determine the film composition and metal coordination environment. The Fe 2*p* peak is observed at 709.7 eV. The S 2*p* peak is found at 162.65 eV. Quantitative XPS analysis reveals that the film has an atomic ratio of Fe : S = 1 : 4.8, which is in agreement with the stoichiometric molar ratio of the proposed film structure (Fe : S = 1 : 4).

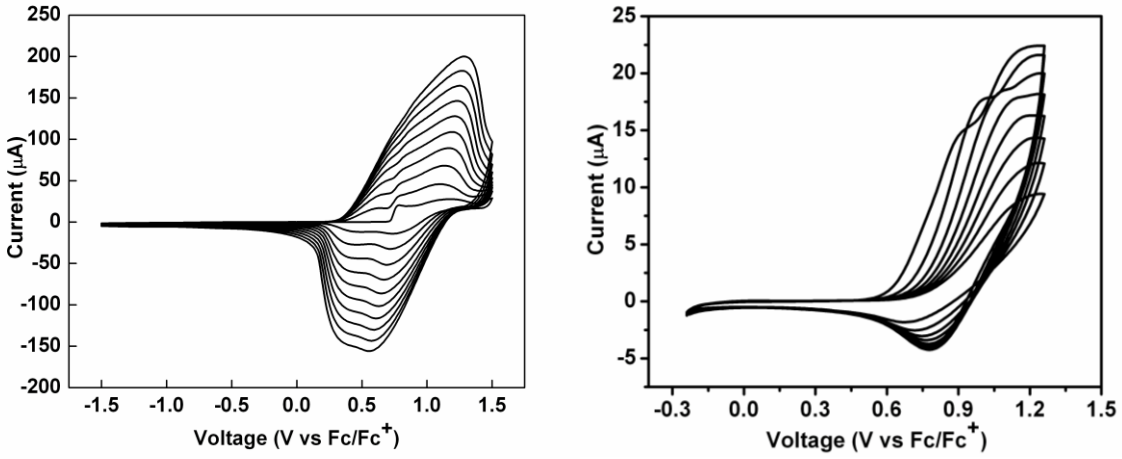

Figure 71. Electrochemical polymerization of **31** (left) and **32** (right). Fc/Fc^+ is the redox couple of ferrocene.

The electrochemical behavior of **33** and **34** is similar to that shown for **32** in Fighure 71. When the potential of the electrode was swept between -0.25 and +1.25 V versus Fc/Fc^+ at a scan rate of 100 mV/s, complex **32** is oxidatively polymerized. A typical electrochemical polymerization of **32** is shown in Figure 71. For **32**, the first polymerization scan is characterized by a thiophene oxidation at ca. +1.1 V followed by

the reductive process at 0.78 V on the return cycle. However, the reduction peak stops growing after four scans.

Electropolymerization of complex **35** was performed from 2×10^{-3} M monomer solution in CH_2Cl_2 by continuous cycling between -1.75 V and +1.25 V (Figure 72). The first scan shows an oxidation peak at ca. 0.9 V, which increase linearly with increasing scans. Different from other electropolymnerization behavior of EDOT containing ligand, such as complex **9**, the oxidation peak does not move with increasing scans. A reduction peak is found at -1.45 V. The XPS data were used to determine the film composition and metal coordination environment for poly-**35**. The Fe 2*p* peak is observed at 711.9 eV. The S 2*p* peak is found at 163.75 eV. Quantitative XPS analysis reveals that the film has an atomic ratio of Fe : S = 1 : 2.16, which is in agreement with the stoichiometric molar ratio of the proposed film structure (Fe : S = 1 : 2).

Complex **36** can not be electropolymerized. It may be due to the dissociation of the dinuclear structure in solution.

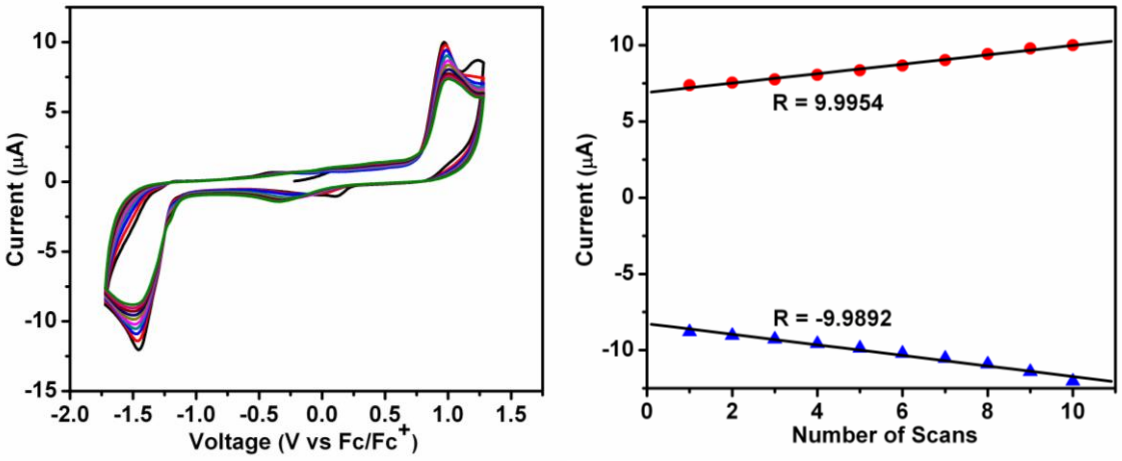

Figure 72. Left: Electrochemical polymerization of **35** (Fc/Fc^+ is the redox couple of ferrocene). Right: Plot of linear current increase vs number of scans.

Magnetic Studies

Magnetic susceptibility measurements show that only the Fe(II)/(III) complexes **32 - 34** with **L9** ligand exhibit the SCO transition. Complex **32** is measured as light yellow microcrystalline powders. The magnetic moment versus temperature data for **32** are shown in Figure 73. The effective magnetic moment of **32** at room temperature, 5.28 μ_B, typical of high spin iron(II) with a small orbital contribution to the spin only magnetic moment of 4.90 μ_B with g = 2.0.[54] Upon cooling, the sample undergoes abrupt spin state transitions to a populated S = 0 low-spin form. This transition is centered at 265 K and shows a hysteresis loop of 4 K. The effective magnetic moment of **32** at 5 K is 0.56 μ_B indicating the almost complete transition of the metal center.

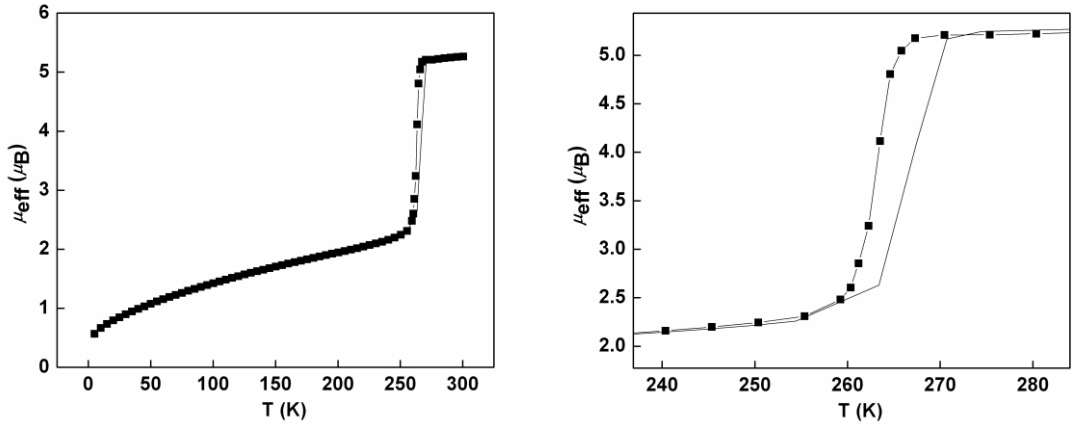

Figure 73. Left: Variation of effective magnetic moment as a function of the temperature for **32**. Right: Enlargement of temperature dependence of the effective magnetic moment showing the hysteresis loop.

The SCO transition is further supported by the X-band EPR spectrum at various temperatures. Complex **32** was measured as a powder sample diluted with anhydrous KBr at the concentration of 10^{-5} M. When Fe(II) is in high spin state, it has four unpaired electrons and is EPR active. Whereas in low spin state, Fe(II) has no unpaired electrons

and is EPR silent. Variable temperature X-band EPR spectra of **32** were recorded in Figure 74. At 90 K, complex **32** is in low spin state, no EPR signal is observed. With increasing temperature, a small signal at g = 4.1 is observable from 210 K. An abrupt increase in the signal intensity is found between 270 and 280 K. At 290 K, the dominant signal in the spectrum is a single isotropic signal with no observable hyperfine interactions.

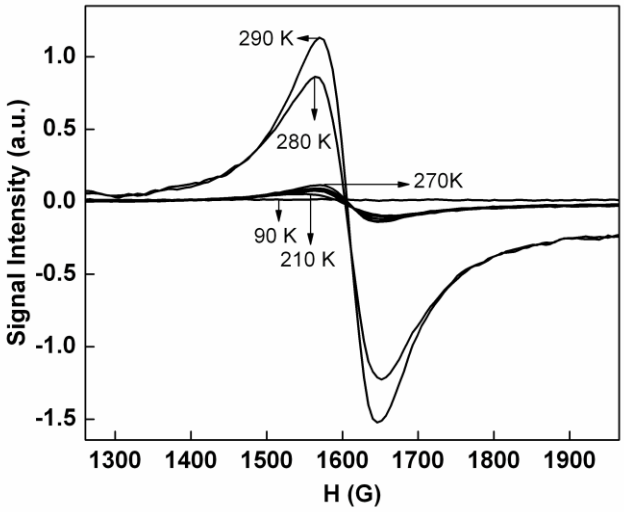

Figure 74. Temperature dependence of the EPR spectra on heating for **32**.

The magnetic measurements of complex **33** were carried out on its powder and in acetone solution (10^{-2} M). At room temperature, the effective magnetic moment in the solid state (5.08 μ_B) is close to that in solution (5.0 μ_B). As shown in Figure 75, complex **33** displays a very broad SCO transition with the effective magnetic moment of 5.08 μ_B at 300 K, typical of the high spin state, to effective magnetic moment of 1.3 μ_B in acetone solution and 0.8 μ_B in solid state at 100 K, typical of the low spin state. There is no

thermal hysteresis in the SCO region. The $T_{1/2}$ of **33** in the solid state and acetone solution is 245 and 256 K, respectively.

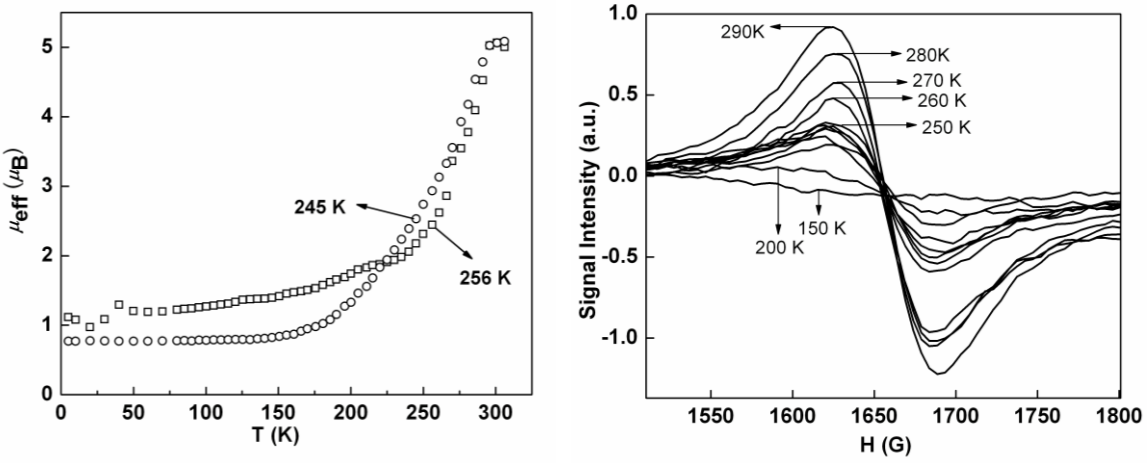

Figure 75. Left: Temperature dependence of the effective magnetic moment of **33** in solid state (□) and acetone solution (○). Right: Temperature dependence of the EPR spectra on heating for **33**.

The SCO transition is also verified by the variable temperature EPR spectra. A small signal at g = 4.2 is observable from 210 K. Different from the sharp intensity change of the EPR signal in complex **32**, the EPR intensity of **33** increases steadily with increasing temperature indicating the gradual SCO transition.

The effective magnetic moment of **34** (5.81 μ_B) at room temperature is close to the spin only value of high spin Fe(III) (5.92 μ_B). Complex **34** exhibits a partial SCO transition from fully high spin Fe(III) above ca. 200 K to two-thirds of high spin and one-third of low spin iron(III) at 75 K. The behavior is reversible as the samples are heated and recooled. The inverse molar magnetic susceptibility, $1/\chi_M$, is linear between 200 and 300 K and a linear least squares fit yields a Curie constant of 4.60 emu K/mol and a Weiss temperature, of -6.3 K. Also $1/\chi_M$ of **34** is linear between 2 and 120 K and yields a

Curie constant of 3.41 emu K/mol and a Weiss temperature of -3.3 K. The small observed Weiss temperatures indicate that, as expected, complex **34** is a dilute, fully paramagnetic complex between 2 and 300 K. The decrease in the moments below ca. 20 K is a result of zero field splitting of the high spin iron(III) ground state.

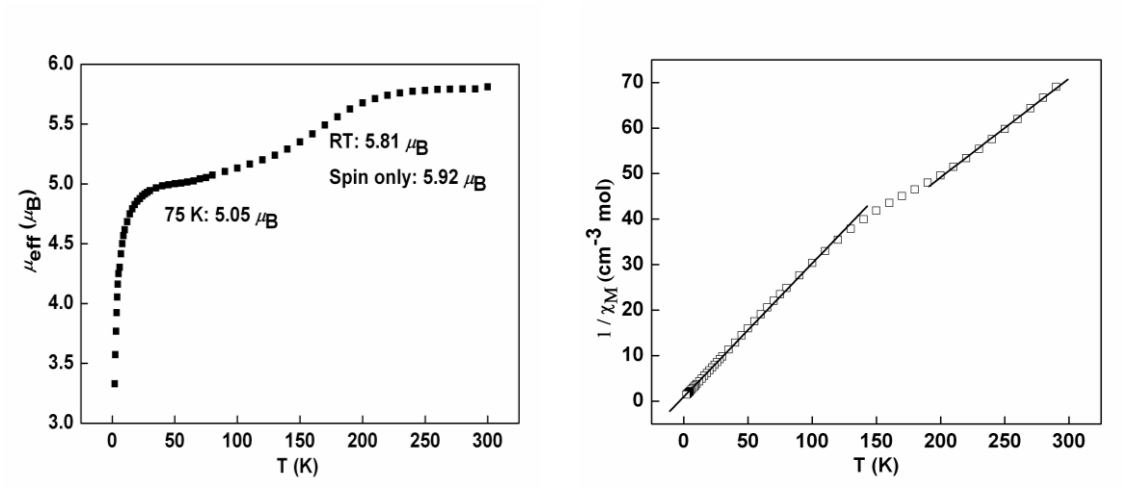

Figure 76. Left: Temperature dependence of the effective magnetic moment of **34**. Right: Temperature dependence of the inverse molar magnetic susceptibility of **34**.

The magnetic susceptibility of complex **36** has been measured in the temperature range of 5 - 300 K. The temperature dependence of χ_M and $\chi_M T$ product of the Cu_2 unit is shown in Figure 77. Upon cooling, χ_M increases, reaching a maximum of 0.154 cm^3 mol^{-1} around 5 K. The $\chi_M T$ value at room temperature of 0.79 cm^3 K mol^{-1} is slightly larger than the spin only value of 0.76 cm^3 K mol^{-1} expected for two isolated copper(II) ions (S = 1/2) assuming g = 2.00. As the temperature is lowered, $\chi_M T$ decreases steadily to 0.69 cm^3 K mol^{-1} at ca. 27 K, and then increases again to 0.78 cm^3 K mol^{-1} upon cooling to 5 K. This is characteristic magnetic behavior of antiferromagnetic coupling in the dinuclear centers. The increase of $\chi_M T$ at low temperature region may be due to the intermolecular ferromagnetic interaction and monomeric impurity. To estimate the magnitude of the

antiferromagnetic coupling, the magnetic susceptibility data (5 - 300 K) were fitted to the modified Bleaney-Bowers equation for two interacting copper(II) ions (S = 1/2) with the Hamiltonian in the form of $H = -JS_1 \cdot S_2$. Then an intermolecular ferromagnetic interaction was considered, the susceptibility equation can be written as follows[55]

$$\chi = \frac{2Ng^2\beta^2}{k(T-\theta)}[3+\exp(-J/kT)]^{-1}(1-\rho)+\frac{Ng^2\beta^2}{2kT}\rho + N_\alpha$$

where N, g, β and ρ parameters in the equation bear their usual meaning. A temperature independent susceptibility term (N_α) was also included and set as 1.2×10^{-4} cm^3 mol^{-1}. The result of the fit, shown as the solid line in Figure 77, was: $g = 2.06$, $J = -7.9$ cm-1, $\theta = 3.0$ K, $\rho = 0.012$, and $R = 1.8 \times 10^{-3}$ ($R = \Sigma[(\chi_M)^{obs} - (\chi_M)^{calc}]^2/[(\chi_M)^{obs}]^2$). The negative sign of J confirmed the weak antiferromagnetic coupling between adjacent copper(II) ions through the bridging sulfate anions.

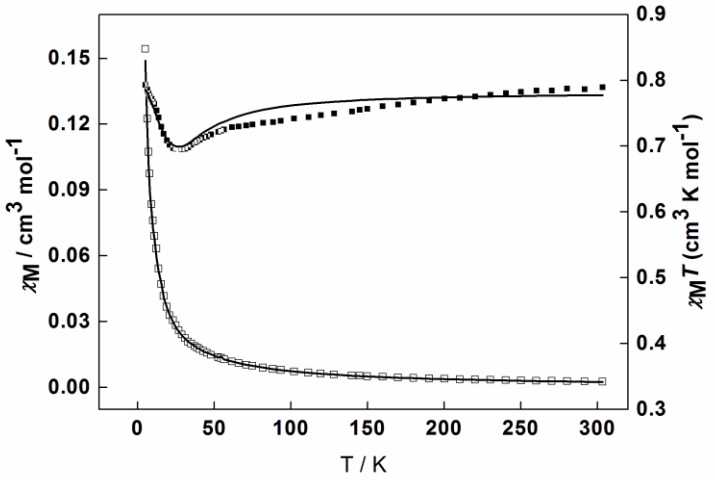

Figure 77. Plots of χ_M (□) and $\chi_M T$ (■) versus the temperature for **36**. The solid line represents the theoretical curve with the best fit parameters.

In Situ Conductivity

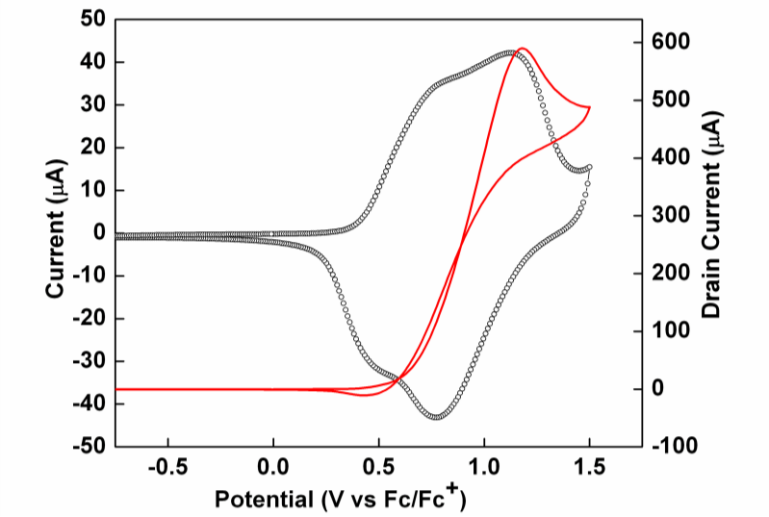

Figure 78. CV (circle) and drain current (solid line) profile (5 mV/s, offset potential of 40 mV; solid line) of poly-**31** on interdigitated Pt microelectrodes in CH_2Cl_2 with 0.1 M $TBAPF_6$ as a supporting electrolyte.

To probe the conduction properties of the obtained metallopolymers, we utilized methods developed by Wrighton and co-workers[56-59] to investigate polymer conductivity as a function of oxidation potential. Complex **31** was electropolymerized on interdigitated microelectrode to form poly-**31**, which connected the two sets of electrodes. After a small potential difference (V_D) was applied between the two electrodes, typically 40 mV, both electrodes were scanned versus the reference electrode. The drain current (i_D) that flowed between the two sets of electrodes, source and drain, is then observed as a function of the applied potential, Figure 78. This drain current can be related directly to absolute conductivity ($\sigma = (i_D/V_D)(D/nTL)$). Poly-**31** displays a rapid increase in drain current upon initial polymer oxidation followed by a subsequent decrease and eventually reaches a plateau. The maximum in situ conductivity at 1.1 V is 9.93×10^{-3} S/cm with the film thickness of 1.5×10^{-5} cm. We correct this conductivity by a known standard, poly(3-

methylthiophene) films grown on the same electrode. For the poly(3-methylthiophene) film, the maximum drain current is 1.1×10^{-2} A and the film thickness is 2.8×10^{-5} cm. The conductivity of poly(3-methylthiophene) was determined to be 0.098 S/cm. The literature published conductivity of poly(3-methylthiophene) is 60 S/cm.[60] The relation used to correct the conductivity of poly-**31** follows as: $\sigma_{(\text{poly-}\mathbf{31}\text{)(corr.)}} = (\sigma_{(\text{poly-}\mathbf{31}\text{)}} / \sigma_{(\text{poly(3-methylthiophene)})}) \times 60$ S/cm. For the aforementioned values, the corrected conductivity of poly-**31** is calculated as 6.1 S/cm.

CONCLUSION

Four different types of ligand systems with polydentate nitrogen donors have been designed and synthesized. The coordination chemistry for these novel ligands with transition metals has been investigated. Six complexes with Fe(II)/(III) and Cu(II) have been characterized by single crystal X-ray diffraction analysis. Variable temperature magnetic susceptibility measurements show that Fe(II)/(III) complexes with **L9** have the SCO transition. The highest $T_{1/2}$ is observed for complex **31** at 265 K, which is promising for further synthesis of complexes with $T_{1/2}$ near room temperature. The variable temperature EPR spectra further verify the spin state change in the Fe(II) systems. Although complexes with **L9** can be electropolymerized, we can not get film thick enough for the in situ conductivity measurements. Further modification needs to be done to achieve better electrochemical performance. The conductivity for poly-**31** was measured as 6.1 S/cm when oxidized. Further studies in the spectral, magnetic and electrical properties changes caused by covalently bonded metals to the conducting polymer systems should be useful not only for information storage but also for various devices.

REFERENCES

1. Shirakawa, H.; Louis, E. J.; MacDiarmid, A. G.; Chiang, C. K.; Heeger, A. J. *J. Chem. Soc. Chem. Commun.* **1977**, 579.
2. Chiang, C. K.; Fischer, C. R.; Park, Y. W.; Heeger, A. J.; Shirakawa, H.; Louis, E. J.; Gau, S. C.; MacDiarmid, A. G. *Phys. Rev. Lett.* **1977**, *39*, 1098.
3. Rajca, A.; Wongsriratanakul, J.; Rajca, S. *Science* **2001**, *294*, 1503.
4. Fukutome, H.; Takahashi, A.; Ozaki, M. *Chem. Phys. Lett.* **1987**, *133*, 34.
5. Macedo, A. M. S.; dos Santos, M. C.; Coutinho-Filho, M. D.; Macedo, C. A. *Phys. Rev. Lett.* **1995**, *74*, 1851.
6. Yoshizawa, K.; Tanaka, K.; Yamato, T.; Yamauchi, J. *J. Chem. Phys.* **1992**, *96*, 5516.
7. Devine, J. N.; Crayston, J. A.; Walton, J. C. *Synth. Met.* **1999**, *103*, 2294.
8. Pei, Y.; Verdaguer, M.; Kahn, O.; Sletten, J.; Renard, J. P. *J. Am. Chem. Soc.* **1986**, *108*, 7428.
9. Georges, R.; Cursly, J.; Drillon, M. *J. Appl. Phys.* **1985**, *58*, 914.
10. Caneschi, A.; Gatteschi, D.; Sessoli, R.; Rey, P. *Acc. Chem. Res.* **1989**, *22*, 392.
11. Manriquez, J. M.; Yee, G. T.; McLean, R. S.; Epstein, A. J.; Miller, J. S. *Science* **1991**, *252*, 1415.
12. Kurmoo, M.; Day, A. W. Graham. P.; Coles, S. J.; Hursthouse, M. B.; Caulfield, J. L.; Singleton, J.; Pratt, F. L.; Ducasse, W. Hayes. L.; Guionneau, P. *J. Am. Chem. Soc.* **1995**, *117*, 12209.
13. Ojima, E.; Fujiwara, H.; Kato, K.; Kobayashi, H. *J. Am. Chem. Soc.* **1999**, *121*, 5581.
14. Coronado, E.; Galan-Mascaros, J. R.; Gomez-Garcia, C. J.; Laukhin, V. N. *Nature* **2000**, *408*, 447.
15. Uii, S.; Shinagawa, H.; Terashima, T.; Yakabe, T.; Terai, Y.; Tokumoto, M.; Kobayashi, A.; Tanaka, H.; Kobayashi, H. *Nature* **2001**, *410*, 908.
16. *Spin Crossover in Transition Metal Compounds I, II and III*, *Top. Curr. Chem.*; Gütlich, P.; Goodwin, H. A., Eds.; Springer-Verlag, Berlin, 2004.
17. Krivokapic, I.; Zerara, M.; Daku, M. L.; Vargas, A.; Enachescu, C.; Ambrus, C.; Tregenna-Piggott, P.; Amstutz, N.; Krausz, E.; Hauser, A. *Coord. Chem. Rev.* **2007**, *251*, 364.
18. Hauser, A.; Enachescu, C.; Daku, M. L.; Vargas, A.; Amstutz, N. *Coord. Chem. Rev.* **2006**, *250*, 1642.
19. Gaspar, A. B.; Ksenofontov, V.; Seredyuk, M.; Gütlich, P. *Coord. Chem. Rev.* **2005**, *249*, 2661.
20. Kahn, O.; Martinez, C. J. *Science* **1998**, *279*, 44.
21. Scheidt, W. R.; Reed, C. A. *Chem. Rev.* **1981**, *81*, 543.
22. Womes, M.; Jumas, J. C.; Olivier-Fourcade, J.; Aubertin, F.; Gonser, U. *Chem. Phys. Lett.* **1993**, *201*, 555.
23. Kahn, O.; Kröber, J.; Jay, C. *Adv. Mater.* **1992**, *4*, 718.
24. Hauser, A.; Spiering, H. *Angew. Chem., Int. Ed. Engl.* **1994**, *33*, 2024.
25. Gütlich, P.; Hauser, A. *Coord. Chem. Rev.* **1990**, *97*, 1.
26. Codjovi, E.; Sommier, L.; Kahn, O.; Jay, C. *New J. Chem.* **1996**, *20*, 503.

27. Garcia, Y.; Kahn, O.; Rabardel, L.; Chansou, B.; Salmon, L.; Tuchagues, J. P. *Inorg. Chem.* **1999**, *38*, 4663.
28. Letard, J.-F.; Montant, S.; Guionneau, P.; Martin, P.; Le Calvez, A.; Freysz, E.; Chasseau, D.; Lapouyade, R.; Kahn, O. *Chem. Commun.* **1997**, 745.
29. Real, J. A.; Andres, E.; Munoz, M. C.; Julve, M.; Granier, T.; Bousseksou, A.; Varret, F. *Science* **1995**, *268*, 265.
30. Halder, G. J.; Kepert, C. J.; Moubaraki, B.; Murray, K. S.; Cashion, J. D. *Science* **2002**, *298*, 1762.
31. Fujigaya, T.; Jiang, D.-L.; Aida, T. *J. Am. Chem. Soc.* **2003**, *125*, 14690.
32. Galyametdinov, Y.; Ksenofontov, V.; Prosvirin, A.; Ovchinnikov, I.; Ivanova, G.; Gütlich, P.; Haase, W. *Angew. Chem., Int. Ed.* **2001**, *40*, 4269.
33. Niel, V.; Thompson, A. L.; Munoz, M. C.; Galat, A.; Goeta, A. E.; Real, J. A. *Angew. Chem., Int. Ed.* **2003**, *42*, 3760.
34. Sunatsuki, Y.; Ikuta, Y.; Matsumoto, N.; Ohta, H.; Kojima, M.; Iijima, S.; Hayami, S.; Maeda, Y.; Kaizaki, S.; Dahan, F.; Tuchagues, J.-P. *Angew. Chem., Int. Ed.* **2003**, *42*, 1614.
35. Galet, A.; Niel, V.; Munoz, M. C.; Real, J. A. *J. Am. Chem. Soc.* **2003**, *125*, 14224.
36. Niel, V.; Thompson, A. L.; Goeta, A. E.; Enachescu, C.; Hauser, A.; Galet, A.; Munoz, M. C.; Real, J. A. *Chem. Eur. J.* **2005**, *11*, 2047.
37. Faulmann, C.; Jacob, K.; Dorbes, S.; Lampert, S.; Malfant, I.; Doublet, M. L.; Valade, L.; Real, J. A. *Inorg. Chem.* **2007**, *46*, 8548.
38. Faulmann, C.; Dorbes, S.; de Bonneval, W. G.; Molnar, G.; Bousseksou, A.; Gomez-Garcia, C. J.; Coronado, E.; Valade, L. *Eur. J. Inorg. Chem.* **2005**, 3261.
39. Dorbes, S.; Valade, L.; Real, J. A.; Faulmann, C. *Chem. Commun.* **2005**, 69.
40. *Methods in Enzymology*, *276*: *Macromolecular Crystallography, part A*; Carter, C. W., Jr.; Sweets, R. M., Eds.; 1997.
41. Altomare, A.; Burla, M. C.; Camalli, M.; Cascarano, G. L.; Giacovazzo, C.; Guagliardi, A.; Moliterni, A. G. G.; Polidori, G.; Spagna, R. *J. Appl. Cryst.* **1999**, *32*, 115.
42. Sheldrick, G. M. (**1994**) SHELXL97. Program *for the Refinement of Crystal Structures.* University of Gottingen, Germany.
43. Zhu, S. S.; Swager, T. M. *J. Am. Chem. Soc.* **1997**, *119*, 12568.
44. Zoppellaro, G.; Baumgarten, M. *Eur. J. Org. Chem.* **2005**, 2888.
45. Jameson, D. L.; Goldsby, K. A. *J. Org. Chem.* **1990**, *55*, 4992.
46. Gronowitz, S.; Liljefors, S. *Chemica Scripta.* **1978-79**, *13*, 39.
47. Liljefors, S.; Gronowitz, S. *Chemica Scripta.* **1980**, *15*, 102.
48. Elhaïk, J.; Kilner, C. A.; Halcrow, M. A. *Dalton Trans.* **2006**, 823.
49. Roux, C.; Zarembowitch, J.; Gallois, B.; Bolte, M. *New J. Chem.* **1992**, *16*, 671.
50. Holland, J. M.; McAllister, J. A.; Kilner, C. A.; Thornton-Pett, M.; Bridgeman, A. J.; Halcrow, M. A. *J. Chem. Soc., Dalton Trans.* **2002**, 548.
51. Reger, D. L.; Semeniuc, R. F.; Smith, M. D. *Crystal Growth & Design* **2005**, *5*, 1182.
52. Kitajima, N.; Moro-oka, Y. *Chem. Rev.* **1994**, *94*, 737.
53. Kimani, M. M.; Brumaghim, J. L.; VanDerveer, D. *Inorg. Chem.* **2010**, *49*, 9200.

54. O'Connor, C. J. *Prog. Inorg. Chem.* **1982**, *29*, 203.
55. *Molecular Magnetism*; Kahn, O., Ed.; VCH Publishers, New York, 1993.
56. Paul, E. W.; Ricco, A. J.; Wrighton, M. S. *J. Phys. Chem.* **1985**, *89*, 1441.
57. Thackeray, J. W.; White, H. S.; Wrighton, M. S. *J. Phys. Chem.* **1985**, *89*, 5133.
58. Kittlesen, G. P.; White, H. S.; Wrighton, M. S. *J. Am. Chem. Soc.* **1984**, *106*, 7389.
59. Ofer, D.; Crooks, R. M.; Wrighton, M. S. *J. Am. Chem. Soc.* **1990**, *112*, 7869.
60. Schiavon, G.; Sitran, S.; Zotti, G. *Synth. Met.* **1989**, *32*, 209.

CRYSTALLOGRAPHIC DATA

Table 33. Crystal data and structure refinement of **31**.

formula	$C_{62}H_{68}Cl_4Fe_2N_{10}O_{25}S_8$
fw	1863.24
T (K)	153(2)
crystal system	Triclinic
space group	P-1
a (Å)	10.335(2)
b (Å)	17.206(3)
c (Å)	22.190(4)
α (deg)	86.93(3)
β (deg)	82.88(3)
γ (deg)	85.16(3)
V (Å^3)	3898.0(13)
Z	2
ρ (g/cm^3)	1.587
μ (mm^{-1})	0.806
F(000)	1916
crystal size (mm)	0.20 × 0.18 × 0.15
θ (deg)	2.97 to 25.00
Index ranges	$-12 \le h \le 10$
	$-20 \le k \le 19$
	$-26 \le l \le 25$
Absorption correction	Gaussian
Max. and min. transmission	0.8601 and 0.8188
GOF on F^2	1.087
R_1, R_2 [I > 2σ (I)]	0.0921, 0.1932
R_1, R_2 (all data)	0.1370, 0.2161
Largest diff. peak and hole (e.Å^{-3})	2.086 and -0.802

Table 34. Selected bond lengths [Å] and angles [°] of **31**.

Bond distances (Å)			
Fe1-O1	2.081(7)	Fe1-O2	2.101(7)
Fe1-O3	2.139(7)	Fe1-N2	2.174(7)
Fe1-N3	2.134(6)	Fe1-N5	2.194(7)
Bond angles (º)			
O1-Fe1-O2	87.5(3)	O2-Fe1-N5	88.6(3)
O1-Fe1-N3	173.5(3)	N3-Fe1-N5	73.7(2)
O2-Fe1-N3	97.6(3)	O3-Fe1-N5	88.8(3)
O1-Fe1-O3	86.0(3)	N2-Fe1-N5	147.6(3)
O2-Fe1-O3	171.7(3)	O2-Fe1-N5	88.6(3)
N3-Fe1-O3	89.2(2)	O1-Fe1-N2	101.8(3)
O2-Fe1-N2	93.9(3)	O3-Fe1-N2	92.5(3)
N3-Fe1-N2	74.0(2)	O1-Fe1-N5	110.5(3)

Table 35. Crystal data and structure refinement of **32**.

formula	$C_{44}H_{42}Cl_2FeN_{10}O_{11}S_4$
fw	1141.87
T (K)	153(2)
crystal system	Triclinic
space group	P-1
a (Å)	11.180(2)
b (Å)	15.348(3)
c (Å)	17.002(3)
α (deg)	101.40(3)
β (deg)	94.67(4)
γ (deg)	111.19(3)
V (Å^3)	2629.0(11)
Z	2
ρ (g/cm^3)	1.442
μ (mm^{-1})	0.613
F(000)	1176
crystal size (mm)	0.17 × 0.12 × 0.08
θ (deg)	2.91 to 27.48
Index ranges	$-13 \le h \le 13$
	$-13 \le k \le 18$
	$-20 \le l \le 18$
Absorption correction	Gaussian
Max. and min. transmission	0.9526 and 0.9029
GOF on F^2	1.038
R_1, R_2 [I > 2σ (I)]	0.0983, 0.2346
R_1, R_2 (all data)	0.1547, 0.2346
Largest diff. peak and hole (e.Å^{-3})	1.932 and -1.844

Table 36. Selected bond lengths [Å] and angles [°] of **32**.

Bond distances (Å)			
Fe1-N1	2.149(7)	Fe1-N5	2.169(8)
Fe1-N1'	2.182(7)	Fe1-N5'	2.192(7)
Fe1-N3'	2.278(7)	Fe1-N3	2.281(7)
Bond angles (º)			
N1-Fe1-N5	174.3(3)	N1'-Fe1-N3'	85.6(3)
N1-Fe1-N1'	85.6(3)	N5'-Fe1-N3'	87.4(3)
N5-Fe1-N1'	97.0(3)	N1-Fe1-N3	87.4(3)
N1-Fe1-N5'	90.9(3)	N5-Fe1-N3	87.5(3)
N5-Fe1-N5'	87.2(3)	N1'-Fe1-N3	90.2(3)
N1'-Fe1-N5'	171.9(3)	N5'-Fe1-N3	97.0(3)
N1-Fe1-N3'	93.9(3)	N3'-Fe1-N3	175.4(3)

Table 37. Crystal data and structure refinement of **33** and **34**.

	33	**34**
formula	$C_{45}H_{40}B_2F_8FeN_{10}OS_4$	$C_{45}H_{40}B_3F_{12}FeN_{10}OS_4$
fw	1094.58	1181.38
T (K)	153(2)	153(2)
crystal system	Triclinic	Monoclinic
space group	P-1	C2/c
a (Å)	10.397(2)	11.846
b (Å)	12.684(3)	30.598
c (Å)	19.641(4)	13.996
α (deg)	86.08(3)	90.00
β (deg)	77.76(3)	94.23
γ (deg)	84.35(3)	90.00
V (Å^3)	2516.1(9)	5059.4
Z	2	4
ρ (g/cm^3)	1.445	1.572
μ (mm^{-1})	0.542	0.558
F(000)	1120	2436
crystal size (mm)	0.27 × 0.18 × 0.15	0.18 × 0.15 × 0.10
θ (deg)	3.21 to 25.00	3.21 to 25.00
Index ranges	$-12 \le h \le 12$	$-14 \le h \le 14$
	$-14 \le k \le 11$	$-28 \le k \le 36$
	$-22 \le l \le 22$	$-16 \le l \le 16$
Absorption correction	Gaussian	Gaussian
Max. and min. transmission	0.9232 and 0.8675	0.9463 and 0.9062
GOF on F^2	1.068	1.031
R_1, R_2 [I > 2σ (I)]	0.0849, 0.2107	0.0913, 0.1964
R_1, R_2 (all data)	0.1337, 0.2463	0.1985, 0.2376
Largest diff. peak and hole (e.Å^{-3})	1.486 and -0.555	1.336 and -0.540

Table 38. Selected bond lengths [Å] and angles [°] for **33** and **34**.

		33	
Bond distances (Å)			
Fe1-N5	2.150(9)	Fe1-N1'	2.159(11)
Fe1-N1	2.162(9)	Fe1-N5'	2.193(10)
Fe1-N3	2.272(10)	Fe1-N3'	2.291(11)
Bond angles (º)			
N5-Fe1-N1'	89.3(4)	N5-Fe1-N1	171.1(3)
N1'-Fe1-N1	87.0(4)	N5-Fe1-N5'	87.8(4)
N1'-Fe1-N5'	171.7(4)	N1-Fe1-N5'	96.9(3)
N5-Fe1-N3	87.2(4)	N1'-Fe1-N3	94.7(4)
N1-Fe1-N3	85.0(4)	N5'-Fe1-N3	92.9(4)
		34	
Bond distances (Å)			
Fe1-N5	2.106(5)	S1-C3'	0.534(14)
Fe1-N1	2.117(5)	S1-C1	1.737(8)
Fe1-N3	2.203(4)	S1-C4	1.752(7)
Bond angles (º)			
N5-Fe1-N5'	88.4(2)	N5-Fe1-N1	94.24(17)
N5-Fe1-N1'	172.54(17)	N1-Fe1-N1'	84.0(3)
N5-Fe1-N3	93.46(17)	N5-Fe1-N3'	86.73(17)
N1-Fe1-N3	86.14(17)	N1-Fe1-N3'	93.65(17)

Table 39. Crystal data and structure refinement of **35** and **36**.

	35	**36**
formula	$C_{31}H_{26}Cl_2FeN_{14}O_{13}S_2$	$C_{48}H_{52}Cu_2N_{12}O_{16}S_4$
fw	993.53	1308.34
T (K)	153(2)	153(2)
crystal system	Monoclinic	Monoclinic
space group	*I*a	*C*2/c
a (Å)	17.375(4)	24.872(5)
b (Å)	8.9651(18)	6.9504(14)
c (Å)	24.759(5)	32.552(7)
β (deg)	90.60(3)	106.16(3)
V (Å^3)	3856.4(13)	5404.9(19)
Z	4	4
ρ (g/cm^3)	1.711	1.608
μ (mm^{-1})	0.724	1.023
F(000)	2024	2696
crystal size (mm)	0.10 × 0.08 × 0.05	0.15 × 0.08 × 0.05
θ (deg)	3.03 to 25.00	3.05 to 24.99
Index ranges	$-20 \le h \le 20$	$-29 \le h \le 29$
	$-10 \le k \le 10$	$-8 \le k \le 8$
	$-29 \le l \le 29$	$-38 \le l \le 37$
Absorption correction	Gaussian	Gaussian
Max. and min. transmission	0.9647 and 0.9311	0.9506 and 0.8616
GOF on F^2	1.060	1.137
R_1, R_2 [I > 2σ (I)]	0.0613, 0.1075	0.0968, 0.2000
R_1, R_2 (all data)	0.1355, 0.1352	0.1917, 0.2310
Largest diff. peak and hole (e.Å^{-3})	0.585 and -0.404	1.016 and -0.863

Table 40. Selected bond lengths [Å] and angles [°] for **35** and **36**.

		35	
Bond distances (Å)			
Fe1-N2	2.076(13)	Fe1-N2'	2.140(13)
Fe1-N7'	2.225(16)	Fe1-N5'	2.242(15)
Fe1-N7	2.262(16)	Fe1-N5	2.283(14)
Bond angles (º)			
N2-Fe1-N2'	151.25(19)	N2-Fe1-N7'	126.9(5)
N2'-Fe1-N7'	70.0(5)	N2-Fe1-N5'	92.0(5)
N2'-Fe1-N5'	72.5(5)	N7'-Fe1-N5'	140.8(6)
N2-Fe1-N7	74.0(5)	N2'-Fe1-N7	125.5(5)
N7'- Fe1-N7	111.10(18)	N5'-Fe1-N7	82.1(5)
N2-Fe1-N5	69.8(5)	N2'-Fe1-N5	91.7(5)
		36	
Bond distances (Å)			
Cu1-O6	1.923(8)	Cu1-O3	1.948(8)
Cu1-N4	1.991(10)	Cu1-N2	1.991(9)
Cu1-O7	2.299(10)	S1-C4	1.701(15)
Bond angles (º)			
O6-Cu1-O3	94.6(4)	O6-Cu1-N4	169.9(4)
O3-Cu1-N4	86.7(4)	O6-Cu1-N2	89.1(4)
O3-Cu1-N2	176.2(4)	N4-Cu1-N2	89.5(4)
O6-Cu1-O7	95.4(4)	O3-Cu1-O7	90.9(4)
N4-Cu1-O7	94.5(4)	N2-Cu1-O7	89.5(4)

REFERENCES

Chapter 1

Natta, G.; Mazzanti, G.; Corradini, P. *Atti. Acad. Naz. Lincei, Cl. Sci. Fis. Mat. Rend.* **1958**, *25*, 3.

Chiang, C. K.; Fincher, Jr., C. R.; Park, Y. W.; Heeger, A. J.; Shirakawa, H.; Louis, E. J.; Gau, S. C.; MacDiarmid, A. G. *Phys. Rev. Lett.* **1977**, *39*, 1098.

Burroughes, J. H.; Bradley, D. D. C.; Brown, A. R.; Marks, R. N.; MacKay, K.; Friend, R. H.; Burn, P. L.; Holmes, A. B. *Nature* **1990**, *347*, 539.

Duan, Y.; Liu, S.; Guan, H. *Sci. Technol. Adv. Mater.* **2005**, *6*, 513.

Nambiar, S.; Yeow, J. T. W. *Biosens Bioelectron* **2011**, *26*, 1825.

Conjugated Polymers: Processing and Applications; Skotheim, T. A.; Reynolds, J. R., Eds.; Hoboken CRC Press, 2006.

Frontiers in Transition Metal-Containing Polymers; Abd-El-Aziz, A. S.; Manners, I., Eds.; John Wiley & Sons, Inc, New Jersey, 2007.

Synthetic Metal-Containing Polymers; Manners, I., Ed.; Wiley-VCH, New York, 2004.

Supramolecular Chemistry-Concepts and Prospectives; Lehn, J.-M., Ed.; VCH, Weinheim, 1995.

McGehee, M. D.; Bergstedt, T.; Zhang, C.; Saab, A. P.; O'Regan, M. B.; Bazan, G. C.; Srdanov, V. I.; Heeger, A. J. *Adv. Mater.* **1999**, *11*, 1349.

Slooff, L. H.; Polman, A.; Cacialli, F.; Friend, R. H.; Hebbink, G. A.; van Veggel, F. C. J. M.; Reinhoudt, D. N. *Appl. Phys. Lett.* **2001**, *78*, 2122.

Li, H. R.; Fu, L. S.; Lin, J.; Zhang, H. J. *Thin Solid Films* **2002**, *416*, 197.

Du, C. X.; Ma, L.; Xu, Y.; Li, W. L. *J. Appl. Polym. Sci.* **1997**, *66*, 1405.

Strek, W.; Legendziewicz, J.; Lukowiak, E.; Maruszewski, K.; Sokolnicki, J.; Boiko, A. A.; Borzechowska, M. *Spectrochim. Acta, Part A* **1998**, *54*, 2215.

Wang, Q. M.; Yan, B. *J. Mater. Chem.* **2004**, *14*, 2450.

Shunmugam, R.; Tew, G. N. *Maccromol. Rapid Commun.* **2008**, *29*, 1355.

Shunmugam, R.; Tew, G. N. *J. Am. Chem. Soc.* **2005**, *127*, 13567.

Balzani, V.; Juris, A.; Venturi, M.; Campagna, S.; Serroni, S. *Chem. Rev.* **1996**, *96*, 759.

Holliday, B. J.; Swager, T. M. *Chem. Commun.* **2005**, 23.

Handbook on the Physics and Chemistry of Rare Earths; Gschneidner, K. A.; Eyring, L., Eds.; Elsevier Science Publisher, New York, 1987.

Lanthanide and Actinide Chemistry; Cotton, S., Ed.; John Wiley & Sons, Ltd., 2007.

Complexes of the Rare Earth; Sinha, S. P., Ed.; Progamon: London, 1966.

Moore, E. G.; Samuel, A. P. S.; Raymond, K. N. *Acc. Chem. Res.* **2009**, *42*, 542.

Segal, M.; Baldo, M. A.; Holmes, R. J.; Forrest, S. R.; Soos, Z. G. *Phys. Rev. B* **2003**, *68*, 075211/1.

D'Aleo, A.; Picot, A.; Beeby, A.; Williams, J. A. G.; Le Guennic, B.; Andraud, C.; Maury, O. *Inorg. Chem.* **2008**, *47*, 10258.

Kido, J.; Okamoto, Y. *Chem. Rev.* **2002**, *102*, 2357.

Kido, J.; Nagai, K.; Ohashi, Y. *Chem. Lett.* **1990**, 657.

Kido, J.; Nagai, K.; Okamoto, Y.; Skotheim, T. *Chem. Lett.* **1991**, 1267.

Takada, N.; Tsutsui, T.; Saito, S. *Jpn. J. Appl. Phys.* **1994**, *33*, 863.
Lanthanide Probes in Life, Chemical and Earth Sciences - Theory and Practice; Bünzli, J.-C. G.; Choppin, G. R., Eds.; Elsevier, Amsterdam, 1989.
Solid State Luminescence - Theory, Materials and Devices; Kitai, A. H., Ed.; Chapman & Hall, London, 1993.
Luminescent Materials; Blasse, G.; Grabmaier, B. C., Eds.; Springer Verlag, Berlin, New York, 1994.
Armelao, L.; Quici, S.; Barigelletti, F.; Accorsi, G.; Bottaro, G.; Cavazzini, M.; Tondello, E. *Coord. Chem. Rev.* **2010**, *254*, 487.
Binnemans, K. *Chem. Rev.* **2009**, *109*, 4283.
Binnemans, K. *Chem. Rev.* **2005**, *105*, 4148.
Hemmila, I. J. *Alloys Compd.* **1995**, *225*, 480.
Selvin, P. R. *Annu. Rev. Biophys. Biomol. Struct.* **2002**, *31*, 275.
Tremblay, M. S.; Zhu, Q.; Marti, A. A.; Dyer, J.; Halim, M.; Jockusch, S.; Turro, N. J.; Sames, D. *Org. Lett.* **2006**, *8*, 2723.
Sculimbrene, B. R.; Imperiali, B. *J. Am. Chem. Soc.* **2006**, *128*, 7346.
Mondry, A.; Janicki, R. *Dalton Trans.* **2006**, 4702.
Wang, B. S.; Andrejco, M. J. *Proc. SPIE-Int. Soc. Opt. Eng.* **2005**, *6019*, 601911.
Weissleder, R.; Tung, C.-H.; Mahmood, U.; Bogdanov, A. *Nat. Biotechnol.* **1999**, *17*, 375.
Hebbink, G. A.; Stouwdam, J. W.; Reinhoudt, D. N.; Van Veggel, F. C. J. M. *Adv. Mater.* **2002**, *14*, 1147.
Shah, K. *Cancer Biol. Ther.* **2005**, *4*, 518.
Zimmer, J. P.; Kim, S.-W.; Ohnishi, S.; Tanaka, E.; Frangioni, J. V.; Bawendi, M. G. *J. Am. Chem. Soc.* **2006**, *128*, 2526.
Ennen, H.; Pomrenke, G.; Axmann, A.; Eisele, K.; Haydl, W.; Schneider, J. *App. Phys. Lett.* **1985**, *46*, 381.
Kawamura, Y.; Wada, Y.; Hasegawa, Y.; Iwamuro, M.; Kitamura, T.; Yanagida, S. *Appl. Phys. Lett.* **1999**, *74*, 3245.
Gillin, W. P.; Curry, R. J. *Appl. Phys. Lett.* **1999**, *74*, 798.
Kang, T.-S.; Harrison, B. S.; Bouguettaya, M.; Foley, T. J.; Boncella, J. M.; Schanze, K. S.; Reynolds, J. R. *Adv. Funct. Mater.* **2003**, *13*, 205.
Wang, D.; Zhang, J.; Lin, Q.; Fu, L.; Zhang, H.; Yang, B. *J. Mater. Chem.* **2003**, *13*, 2279.
Chen, J.; Liu, X.; Fan, X.; Lin, Q.; Gu, P.; Tang, J. *Proc. SPIE-Int. Soc. Opt. Eng.* **2000**, *4220*, 255.
Zheng, L.; Yang, M.; Wu, P.; Ye, H.; Liu, X. *Synth. Met.* **2004**, *144*, 259.
Chen, X. Y.; Yang, X. P.; Holliday, B. J. *J. Am. Chem. Soc.* **2008**, *130*, 1548.
Hagfeldt, A.; Grätzel, M. *Acc. Chem. Res.* **2000**, *33*, 269.
Kuciauskas, D.; Freund, M. S.; Gray, H . B.; Winkler, J. R.; Lewis, N. S. *J. Phys. Chem. B.* **2001**, *105*, 392.
Tai, W. P.; Inoue, K.; Oh, J. H. *Sol. Energy Mater.* **2002**, *71*, 553.
Demas, J. N.; DeGraff, B. A. *Coord. Chem. Rev.* **2001**, *211*, 317.

Buss, C. E.; Mann, K. R. *J. Am. Chem. Soc.* **2002**, *124*, 1031.
Higgins, B.; DeGraff, B. A. *Inorg. Chem.* **2005**, *44*, 6662.
Photofunctional Transition Metal Cmplexes; Yam, V. W. W.; Balch, A. L., Eds.; Springer Verlag, Berlin; New York, 2007.
Lu, W.; Mi, B. X.; Chan, M. C. W.; Hui, Z.; Zhu, N.; Lee, S. T.; Che, C. M. *Chem. Commun.* **2002**, 206.
Lu, W.; Mi, B. X.; Chan, M. C. W.; Hui, Z.; Che, C. M.; Zhu, N.; Lee, S. T. *J. Am. Chem. Soc.* **2004**, *126*, 4958.
Baldo, M. A.; O'Brien, D. F.; You, Y.; Shoustikov, A.; Sibley, S.; Thompson, M. E.; Forrest, S. R. *Nature* **1998**, *395*, 151.
Adachi, C.; Baldo, M. A.; Forrest, S. R.; Lamansky, S.; Thompson, M. E.; Kwong, R. C. *Appl. Phys. Lett.* **2001**, *78*, 1622.
Brooks, J.; Babayan, Y.; Lamansky, S.; Djurovich, P. I.; Tsyba, I.; Bau, R.; Thompson, M. E. *Inorg. Chem.* **2002**, *41*, 3055.
Adachi, C.; Baldo, M. A.; Thompson, M. E.; Forrest, S. R. *J. Appl. Phys.* **2001**, *90*, 5048.
Ikai, M.; Tokito, S.; Sakamoto, Y.; Suzuki, T.; Taga, Y. *Appl. Phys. Lett.* **2001**, *79*, 156.
Nazeeruddin, M. K.; Humphry-Baker, R. *J. Am. Chem. Soc.* **2003**, *125*, 8790.
D'Andrade, B. W.; Brooks, J.; Adamovich, V.; Thompson, M. E.; Forrest, S. R. *Adv. Mater.* **2002**, *14*, 1032.
Kwok, C.-C.; Yu, S.-C.; Sham, I. H. T.; Che, C.-M. *Chem. Commun.* **2004**, 2758.
Holliday, B. J.; Stanford, T. B.; Swager, T. M. *Chem. Mater.* **2006**, *18*, 5649.
Choi, T. L.; Lee, K. H.; Joo, W. J.; Lee, S.; Lee, T. W.; Chae, M. Y. *J. Am. Chem. Soc.* **2007**, *129*, 9842.
Ling, Q. D.; Song, Y.; Ding, S. J.; Zhu, C. X.; Chan, D. S. H.; Kwong, D. L.; Kang, E. T.; Neoh, K. G. *Adv. Mater.* **2005**, *17*, 455.
Köhler, A.; Wittmann, H. F.; Friend, R. H.; Khan, M. S.; Lewis, J. *Synth. Met.* **1996**, *77*, 147.
Wong, W. Y.; Wang, X. Z.; He, Z.; Djurisic, A. B.; Yip, C. T.; Cheung, K. Y.; Wang, H.; Mak, C. S. K.; Chan, W. K. *Nat. Mater.* **2007**, *6*, 521.
Rajca, A.; Wongsriratanakul, J.; Rajca, S. *Science* **2001**, *294*, 1503.
Kosaka, Y.; Yamamoto, H. M.; Nakao, A.; Tamura, M.; Kato, R. *J. Am. Chem. Soc.* **2007**, *129*, 3054.
Fukutome, H.; Takahashi, A.; Ozaki, M. *Chem. Phys. Lett.* **1987**, *133*, 34.
Yoshizawa, K.; Tanaka, K.; Yamato, T.; Yamauchi, J. *J. Chem. Phys.* **1992**, *96*, 5516.
Devine, J. N.; Crayston, J. A.; Walton, J. C. *Synth. Met.* **1999**, *103*, 2294.
Murray, M. M.; Kaszynski, P.; Kaisaki, D. A.; Chang, W.; Dougherty, D. A. *J. Am. Chem. Soc.* **1994**, *116*, 8152.
van Haare, J. A. E. H.; van Boxtel, M.; Janssen, R. A. *J. Chem. Mater.* **1998**, *10*, 1166.
Hill, M. G.; Mann, K. R.; Miller, L. L.; Penneau, J.-P. *J. Am. Chem. Soc.* **1992**, *114*, 2728.
Bäuerle, P.; Segelbacher, U.; Gaudl, K. U.; Huttenlocher, D.; Mehring, M. *Angew. Chem., Int. Ed. Engl.* **1993**, *32*, 76.

van Haare, J. A. E. H.; Groenendaal, L.; Havinga, E. E.; Jassen, R. A. J.; Meijer, E. W. *Angew. Chem., Int. Ed. Engl.* **1996**, *35*, 638.
Takahashi, K.; Cui, H.-B.; Okano, Y.; Kobayashi, H.; Einaga, Y.; Sato, O. *Inorg. Chem.* **2006**, *45*, 5739.
O'Sullivan, T. J.; Djukic, B.; Dube, P. A.; Lemaire, M. T. *Chem. Commun.* **2009**, *14*, 1903.
Djukic, B.; Lemaire, M. T. *Inorg. Chem.* **2009**, *48*, 10489.

Chapter 2

Yang, L.; Gong, Z.; Nie, D.; Lou, B.; Bian, Z.; Guan, M.; Huang, C.; Lee, H. J.; Baik, W. P. *New J. Chem.* **2006**, *30*, 791.
Handbook on the Physics and Chemistry of Rare Earths; Binnemans, K., Ed.; Elsevier: Amsterdam, 2005.
Bellusci, A.; Barberio, G.; Crispini, A.; Ghedini, M.; Deda, M.; Pucci, D. *Inorg. Chem.* **2005**, *44*, 1818.
Biju, S.; Ambili Raj, D. B.; Reddy, M. L. P.; Kariuki, B. M. *Inorg. Chem.* **2006**, *45*, 10651.
Guan, M.; Bian, Z. Q.; Li, F. Y.; Xin, H.; Huang, C. H. *New J. Chem.* **2003**, *27*, 1731.
McGehee, M. D.; Bergstedt, T.; Zhang, C.; Saab, A. P.; O'Regan, M. B.; Bazan, G. C.; Srdanov, V. I.; Heeger, A. J. *Adv. Mater.* **1999**, *11*, 1349.
Robinson, M. R.; Ostrowski, J. C.; Bazan, G. C.; McGehee, M. D. *Adv. Mater.* **2003**, *15*, 1547.
Kalinowski, J.; Stampor, W.; Cocchi, M.; Virgili, D.; Fattori, V. *Appl. Phys. Lett.* **2005**, *86*, 241106.
Bai, X. L.; Liu, X. D.; Wang, M.; Kang, C. Q.; Gao, L. X. *Synthesis* **2005**, *3*, 458.
Saitoh, Y.; Koizumi, T.; Osakada, K.; Yamamoto, T. *Can. J. Chem.* **1997**, *75*, 1336.
Zhu, S. S.; Swager, T. M. J. *Am. Chem. Soc.* **1997**, *119*, 12568.
Methods in Enzymology, *276*: *Macromolecular Crystallography, part A*; Carter, C. W., Jr.; Sweets, R. M., Eds.; 1997.
Altomare, A.; Burla, M. C.; Camalli, M.; Cascarano, G. L.; Giacovazzo, C.; Guagliardi, A.; Moliterni, A. G. G.; Polidori, G.; Spagna, R. *J. Appl. Cryst.* **1999**, *32*, 115.
Sheldrick, G. M. (**1994**) SHELXL97. Program *for the Refinement of Crystal Structures.* University of Gottingen, Germany.
Spek, A. L. (**1998**). *PLATON, A Multipurpose Crystallographic Tool.* Utrecht University, The Netherlands.
Farrugia, L. J. *J. Appl. Cryst.* **1999**, *32*. 837.
Charles, R. G.; Perrotto, A. *J. Inorg. Nucl. Chem.* **1964**, *26*, 373.
Wang, M.; Jin, L.; Liu, S.; Cai, G.; Huang, J.; Qin, W.; Huang, S. *Gaodeng Xuexiao Huaxue Xuebao* **1993**, *14*, 305.
Angelici, R. J. *Coord. Chem. Rev.* **1990**, *105*, 61.
The Chemistry of the Lanthanides; Moeller, T., Ed.; Pergamon Press, Oxford, 1973.
Araki, K.; Endo, H.; Masuda, G.; Ogawa, T. *Chem. Eur. J.* **2004**, *10*, 3331.

Jang, H.; Shin, C. H.; Jung, B. J.; Kim, D.; Shim, H. K.; Do, Y. *Eur. J. Inorg. Chem.* **2006**, 718.
Xu, Q. H.; Li, L. S.; Liu, X. S.; Xu, R. R. *Chem. Mater.* **2002**, *14*, 549.
Kido, J.; Okamot, Y. *Chem. Rev.* **2002**, *102*, 2357 and references therein.
Sato, S.; Wada, M. *Bull. Chem. Soc. Jpn*. **1970**, *43*, 1955.
Crosby, G. A.; Whan, R. E.; Alire, R. M. *J. Chem. Phys.* **1961**, *34*, 743.
Touillon, G.; Garnier, F. *J. Electroanal. Chem*. **1982**, *135*, 173.
Kaneto, K.; Kohno, Y.; Yoshino, K.; Inuishi, Y. *J. Chem. Soc. Chem. Commun.* **1983**, 382.
Roncali, J. *Chem. Rev.* **1992**, *92*, 711 and references therein.
Ahmed, M. O.; Liao, J. L.; Chen, X.; Chen, S. A.; Kaldis, J. H. *Acta Crystallogr.* **2003**, *E59*, m29.
Jang, H.; Shin, C. H.; Jung, B. J.; Kim, D.; Shim, H. K.; Do, Y. *Eur. J. Inorg. Chem.* **2006**, 718.
Guo, Q. L.; Zhu, W. X.; Guo, R.; Yan, X.; Wang, R. J. *Chin. J. Chem.* **2003**, *21*, 211.
Mercier, F.; Alliot, C.; Bion, L.; Thromat, N.; Toulhoat, P. J. *Electron Spec. Relat. Phenom.* **2006**, *150*, 21.

Chapter 3

Bünzli, J.-C. G.; Comby, S.; Chauvin, A. S.; Vandevyver, C. D. B. *J. Rare Earths* **2007**, *25*, 257.
Suzuki, H. *J. Photochem. Photobiol. A* **2004**, *166*, 155.
Chen, Z. Q.; Bian, Z. Q.; Huang, C. H. *Adv. Mater.* **2010**, *22*, 1534.
Eliseeva, S. V.; Bünzli, J.-C. G. *Chem. Soc. Rev.* **2010**, *39*, 189.
van der Ende, B. M.; Aarts, L.; Meijerink, A. *Phys. Chem. Chem. Phys.* **2009**, *11*, 11081.
Shalav, A.; Richards, B. S.; Green, M. A. *Solar En. Mat. Sol. Cells* **2007**, *91*, 829.
Wang, F.; Banerjee, D.; Liu, Y. S.; Chen, X. Y.; Liu, X. G. *Analyst* **2010**, *135*, 1839.
Bünzli, J.-C. G. *Chem. Rev.* **2010**, *110*, 2729.
Amiot, C. L.; Xu, S. P.; Liang, S.; Pan, L. Y.; Zhao, J. X. J. *Sensors* **2008**, *8*, 3082.
Braun, D.; Heeger, A. J. *Appl. Phys. Lett.* **1991**, *58*, 1982.
Kraft, A.; Grimsdale, A. C.; Holmes, A. B. *Angew. Chem. Int. Ed. Engl.* **1998**, *37*, 402.
Curry, R. J.; Gillin, W. P. *Appl. Phys. Lett.* **1999**, *75*, 1380.
de Bettencourt-Dias, A. *Dalton Trans.* **2007**, 2229.
Zhang T.; Xu, Z.; Qian, L.; Tao, D. L.; Teng, F.; Gao, X.; Xu, X. R. *Chem. Phys. Lett.* **2005**, *415*, 30.
Kang, T. S.; Harrison, B. S.; Foley, T. J.; Knefely, A. S.; Boncella, J. M.; Reynolds, J. R.; Schanze, K. S. *Adv. Mater.* **2003**, *15*, 1093.
Harrison, B. S.; Foley, T. J.; Bouguettaya, M.; Boncella, J. M.; Reynolds, J. R.; Schanze, K. S. *Appl. Phys. Lett.* **2001**, *79*, 3770.
Kang, T. S.; Harrison, B. S.; Bouguettaya, M.; Foley, T. J.; Boncella, J. M.; Schanze, K. S.; Reynolds, J. R. *Adv. Funct. Mater.* **2003**, *13*, 205.
Ling Q.; Yang, M.; Wu, Z.; Zhang, X.; Wang, L.; Zhang, W. *Polymer* **2001**, *42*, 4605.

Lenarets, P.; Storms, A.; Mullens, J.; D'Haen, J.; Görller-Walrand, C.; Binnemans, K.; Driesen, K. *Chem. Mater.* **2005**, *17*, 5194.
Shunmugam, R.; Tew, G. N. *Macromol. Rapid Commun.* **2008**, *29*, 1355.
Saitoh, Y.; Koizumi, T.; Osakada, K.; Yamamoto, T. *Can. J. Chem.* **1997**, *75*, 1336.
Zhu, S. S.; Swager, T. M. *J. Am. Chem. Soc.* **1997**, *119*, 12568.
Sauvage, J. P.; Kern, J. M.; Bidan, D.-B.; Vidal, P.-L. *New J. Chem.* **2002**, *26*, 1287.
Methods in Enzymology, *276*: *Macromolecular Crystallography, part A*; Carter, C. W., Jr.; Sweets, R. M., Eds.; 1997.
Altomare, A.; Burla, M. C.; Camalli, M.; Cascarano, G. L.; Giacovazzo, C.; Guagliardi, A.; Moliterni, A. G. G.; Polidori, G.; Spagna, R. *J. Appl. Cryst.* **1999**, *32*, 115.
Sheldrick, G. M. (**1994**) SHELXL97. Program *for the Refinement of Crystal Structures.* University of Gottingen, Germany.
Aebischer, A.; Gumy, F.; Bünzli, J.- C. G. *Phys. Chem. Chem. Phys.* **2009**, *11*, 1346.
De Mello, J. C.; Wittmann, H. F.; Friend, R. H. *Adv. Mater*. **1997**, *9*, 230.
Lunstroot, K.; Nockemann, P.; Van Hecke, K.; Van Meervelt, L.; Görller-Walrand, C.; Binnemans, K.; Driesen, K. *Inorg. Chem.* **2009**, *48*, 3018.
The Chemistry of the Lanthanides; Moeller, T., Ed.; Pergamon Press, Oxford, 1973.
Deun, R. V.; Moors, D.; Fré, B. D.; Binnemans, K. *J. Mater. Chem.* **2003**, *13*, 1520.
Asano-Someda, M.; Kaizu, Y. *J. Photochem. Photobiol. A* **2001**, *139*, 161.
Tsvirko, M. P.; Stelmakh, G. F.; Pyatosin, V. E.; Solovyov, K. N.; Kachura, T. F. *Chem. Phys. Lett*. **1980**, *73*, 80.
Perkins, W. G.; Crosby, G. A. *J. Chem. Phys.* **1965**, *42*, 407.
Gao, L.; Guan, M.; Wang, K.; Jin, L.-P.; Huang, C.-H. *Eur. J. Inorg. Chem.* **2006**, 3731.
Weber, M. J. *Phys. Rev.* **1968**, *171*, 283.
Meshkova, S. B.; Topilova, Z. M.; Bolshoy, D. V.; Beltyukova, S. V.; Tsvirko, M. P.; Venchikov, V. Y.; Ya, V. *Acta Phys. Pol. A* **1999**, *95*, 983.
Gonçalves Silva, F. R.; Malta, O. L.; Reinhard, C.; Güdel, H. U.; Piguet, C.; Moser, J. E.; Bünzli, J.-C. *J. Phys. Chem. A* **2002**, *106*, 1670.
Klink, S. I.; Hebbink, G. A.; Grave, L.; Van Veggel, F. C. J. M.; Reinhoudt, D. N.; Slooff, L. H.; Polman, A.; Hofstraat, J. W. *J. Appl. Phys.* **1999**, *86*, 1181.
Ziessel, R. F.; Ulrich, G.; Charbonniere, L.; Imbert, D.; Scopelliti, R.; Bünzli, J.-C. G. *Chem. Eur. J.* **2006**, *12*, 5060.
Hasegawa, Y.; Kimura, Y.; Murakoshi, K.; Wada, Y.; Kim, J. H.; Nakashima, N.; Yamanaka, T.; Yanagida, S. *J. Phys. Chem.* **1996**, *100*, 10201.
Pizzoferrato, R; Ziller, T; Paolesse, R.; Mandoj, F.; Micozzi, A.; Ricci, A.; Lo Sterzo C. *Chem. Phys. Lett.* **2006**, *426*, 124.
Uwamino, Y.; Ishizuka, Y.; Yamatera, H. *J. Electron Spectrosc. Relat. Phenom*. **1984**, *34*, 67.

Chapter 4

Electrogenerated Chemiluminescence; Bard, A. J., ed.; Marcel Dekker, New York, 2004.
Richter, M. M.; *Chem. Rev.* **2004**, *104*, 3003.
Pyati, R.; Richter, M. M. *Annu. Rep. Prog. Chem., Sect. C* **2007**, *103*, 12.

Miao, W. J. *Chem. Rev.* **2008**, *108*, 2506.
Marquette, C. A.; Blum, L. J. *Anal. Bioanal. Chem.* **2008**, *390*, 155.
Forster, R. J.; Bertoncello, P.; Keyes, T. E. *Annu. Rev. Anal. Chem.* **2009**, *2*, 359.
Visco, R.; Chandross, E. *J. Am. Chem. Soc.* **1964**, *86*, 350.
Santhanam, K.; Bard, A. J. *J. Am. Chem. Soc.* **1965**, *87*, 139.
Tokel-Takvoryan, N.; Hemingway, R.; Bard, A. J. *J. Am. Chem. Soc.* **1973**, *95*, 6582.
Chang, M. M.; Saji, T.; Bard, A. J. *J. Am. Chem. Soc.* **1977**, *99*, 5399.
Wightman, R. M.; Forry, S. P.; Maus, R.; Badocco, D.; Pastore, P. *J. Phys. Chem. B* **2004**, *108*, 19119.
Zu, Y. B.; Bard, A. J. *Anal. Chem.* **2000**, *72*, 3223.
Skotty, D. R.; Lee, W. Y.; Nieman, T. A. *Anal. Chem.* **1996**, *68*, 1530.
Zorzi, M.; Pastore, P.; Magno, F. *Anal. Chem.* **2000**, *72*, 4934.
Shi, L. H.; Liu, X. Q.; Li, H. J.; Xu, G. B. *Anal. Chem.* **2006**, *78*, 7330.
Balzani, V.; Juris, A. *Coord. Chem. Rev.* **2001**, *211*, 97.
Juris, A.; Balzani, V.; Barigelletti, F.; Campagna, S.; Belser, P.; Von Zelewsky, A. *Coord. Chem. Rev.* **1988**, *84*, 85.
Bolletta, B.; Ciano, T.; Balzani, V.; Serpone, N. *Inorg. Chim. Acta* **1982**, *62*, 207.
Shin, I.-S.; Kim, J. I.; Kwon, T.-H.; Hong, J.-I.; Lee, J.-K.; Kim, H. *J. Phys. Chem. C* **2007**, *111*, 2280.
Kim, J. I.; Shin, I.-S.; Kim, H.; Lee, J.-K. *J. Am. Chem. Soc.* **2005**, *127*, 1614.
High Energy Processes in Organometallic Chemistry; Vogler, A.; Kunkely, H., Eds.; Am. Chem. Soc., Washington D. C., 1987.
Gross, E. M.; Armstrong, N. R.; Wightman, R. M. *J. Electrochem. Soc.* **2002**, *149*, E137.
Dennany, L.; Hogan, C.; Keyes, T.; Forster, R. J. *Anal. Chem.* **2006**, *78*, 1412.
Abruna, H. D.; Bard, A. J. *J. Am. Chem. Soc.* **1982**, *104*, 2641.
Terheijden, J.; van Koten, G.; van Beek, J. A. M. *Organometallics* **1987**, *6*, 89.
Methods in Enzymology, *276*: *Macromolecular Crystallography, part A*; Carter, C. W., Jr.; Sweets, R. M., Eds.; 1997.
Altomare, A.; Burla, M. C.; Camalli, M.; Cascarano, G. L.; Giacovazzo, C.; Guagliardi, A.; Moliterni, A. G. G.; Polidori, G.; Spagna, R. *J. Appl. Cryst.* **1999**, *32*, 115.
Sheldrick, G. M. (**1994**) SHELXL97. Program *for the Refinement of Crystal Structures.* University of Gottingen, Germany.
Araki, K.; Endo, H.; Masuda, G.; Ogawa, T. *Chem. Eur. J.* **2004**, *10*, 3331.
Willison, S. A.; Krause, J. A.; Connick, W. B. *Inorg. Chem.* **2008**, *47*, 1258.
Constable, E. C.; Henney, R. P. G.; Tocher, D. A. *J. Chem. Soc. Dalton Trans.* **1992**, 2467.
Brooks, J.; Babayan, Y.; Lamansky, S.; Djurovich, P. I.; Tsyba, I.; Bau, R.; Thompson, M. E. *Inorg. Chem.* **2002**, *41*, 3055.
Thomas III, S. W.; Venkatesan, K.; Müller, P.; Swager, T. M. *J. Am. Chem. Soc.* **2006**, *128*, 16641.
Godbert, N.; Pugliese, T.; Aiello, I.; Bellusci, A.; Crispini, A.; Ghedini, M. *Eur. J. Inorg. Chem.* **2007**, 5105.

Wadas, T. J.; Wang, Q.-M.; Kim, Y. J.; Flaschenreim, C.; Blanton, T. N.; Eisenberg, R. *J. Am. Chem. Soc.* **2004**, *126*, 16841, and references therein.
DeWitt, L.; LeGoff, E.; Benz, M . E.; Liao, J. H.; Kanatzidis, M. G. *J. Am. Chem. Soc.* **1993**, *115*, 12158.
Gong, X.; Ostrowski, J. C.; Bazan, G. C.; Moses, D.; Heeger, A. J.; Liu, M. S.; Jen, A. K. Y. *Adv. Mater.* **2003**, *15*, 45.
Bagnich, S. A.; Im, C.; Bässler, H.; Neher, D.; Scherf, U. *Chem. Phys.* **2004**, *299*, 11.
Yang, X. H.; Neher, D. *Appl. Phys. Lett.* **2004**, *84*, 2476.
Che, C.-M.; Chan, S.-C.; Xiang, H. F.; Chan, M. C. W.; Liu, Y.; Wang, Y. *Chem. Commun.* **2004**, 1484.
Lai, S. W.; Lam, H. W.; Lu, W.; Cheung, K. K.; Che, C. M. *Organometallics* **2002**, *21*, 226.
Berenguer, J. R.; Lalinde, E.; Torroba, J. *Inorg. Chem.* **2007**, *46*, 9919.
Develay, S.; Blackburn, O.; Thompson, A. L.; Williams, J. A. G. *Inorg. Chem.* **2008**, *47*, 11129.

Chapter 5

Shirakawa, H.; Louis, E. J.; MacDiarmid, A. G.; Chiang, C. K.; Heeger, A. J. *J. Chem. Soc. Chem. Commun.* **1977**, 579.
Chiang, C. K.; Fischer, C. R.; Park, Y. W.; Heeger, A. J.; Shirakawa, H.; Louis, E. J.; Gau, S. C.; MacDiarmid, A. G. *Phys. Rev. Lett.* **1977**, *39*, 1098.
Rajca, A.; Wongsriratanakul, J.; Rajca, S. *Science* **2001**, *294*, 1503.
Fukutome, H.; Takahashi, A.; Ozaki, M. *Chem. Phys. Lett.* **1987**, *133*, 34.
Macedo, A. M. S.; dos Santos, M. C.; Coutinho-Filho, M. D.; Macedo, C. A. *Phys. Rev. Lett.* **1995**, *74*, 1851.
Yoshizawa, K.; Tanaka, K.; Yamato, T.; Yamauchi, J. *J. Chem. Phys.* **1992**, *96*, 5516.
Devine, J. N.; Crayston, J. A.; Walton, J. C. *Synth. Met.* **1999**, *103*, 2294.
Pei, Y.; Verdaguer, M.; Kahn, O.; Sletten, J.; Renard, J. P. *J. Am. Chem. Soc.* **1986**, *108*, 7428.
Georges, R.; Cursly, J.; Drillon, M. *J. Appl. Phys.* **1985**, *58*, 914.
Caneschi, A.; Gatteschi, D.; Sessoli, R.; Rey, P. *Acc. Chem. Res.* **1989**, *22*, 392.
Manriquez, J. M.; Yee, G. T.; McLean, R. S.; Epstein, A. J.; Miller, J. S. *Science* **1991**, *252*, 1415.
Kurmoo, M.; Day, A. W. Graham. P.; Coles, S. J.; Hursthouse, M. B.; Caulfield, J. L.; Singleton, J.; Pratt, F. L.; Ducasse, W. Hayes. L.; Guionneau, P. *J. Am. Chem. Soc.* **1995**, *117*, 12209.
Ojima, E.; Fujiwara, H.; Kato, K.; Kobayashi, H. *J. Am. Chem. Soc.* **1999**, *121*, 5581.
Coronado, E.; Galan-Mascaros, J. R.; Gomez-Garcia, C. J.; Laukhin, V. N. *Nature* **2000**, *408*, 447.
Uii, S.; Shinagawa, H.; Terashima, T.; Yakabe, T.; Terai, Y.; Tokumoto, M.; Kobayashi, A.; Tanaka, H.; Kobayashi, H. *Nature* **2001**, *410*, 908.
Spin Crossover in Transition Metal Compounds I, II and III, *Top. Curr. Chem.*; Gütlich, P.; Goodwin, H. A., Eds.; Springer-Verlag, Berlin, 2004.

Krivokapic, I.; Zerara, M.; Daku, M. L.; Vargas, A.; Enachescu, C.; Ambrus, C.; Tregenna-Piggott, P.; Amstutz, N.; Krausz, E.; Hauser, A. *Coord. Chem. Rev.* **2007**, *251*, 364.
Hauser, A.; Enachescu, C.; Daku, M. L.; Vargas, A.; Amstutz, N. *Coord. Chem. Rev.* **2006**, *250*, 1642.
Gaspar, A. B.; Ksenofontov, V.; Seredyuk, M.; Gütlich, P. *Coord. Chem. Rev.* **2005**, *249*, 2661.
Kahn, O.; Martinez, C. J. *Science* **1998**, *279*, 44.
Scheidt, W. R.; Reed, C. A. *Chem. Rev.* **1981**, *81*, 543.
Womes, M.; Jumas, J. C.; Olivier-Fourcade, J.; Aubertin, F.; Gonser, U. *Chem. Phys. Lett.* **1993**, *201*, 555.
Kahn, O.; Kröber, J.; Jay, C. *Adv. Mater.* **1992**, *4*, 718.
Hauser, A.; Spiering, H. *Angew. Chem., Int. Ed. Engl.* **1994**, *33*, 2024.
Gütlich, P.; Hauser, A. *Coord. Chem. Rev.* **1990**, *97*, 1.
Codjovi, E.; Sommier, L.; Kahn, O.; Jay, C. *New J. Chem.* **1996**, *20*, 503.
Garcia, Y.; Kahn, O.; Rabardel, L.; Chansou, B.; Salmon, L.; Tuchagues, J. P. *Inorg. Chem.* **1999**, *38*, 4663.
Letard, J.-F.; Montant, S.; Guionneau, P.; Martin, P.; Le Calvez, A.; Freysz, E.; Chasseau, D.; Lapouyade, R.; Kahn, O. *Chem. Commun.* **1997**, 745.
Real, J. A.; Andres, E.; Munoz, M. C.; Julve, M.; Granier, T.; Bousseksou, A.; Varret, F. *Science* **1995**, *268*, 265.
Halder, G. J.; Kepert, C. J.; Moubaraki, B.; Murray, K. S.; Cashion, J. D. *Science* **2002**, *298*, 1762.
Fujigaya, T.; Jiang, D.-L.; Aida, T. *J. Am. Chem. Soc.* **2003**, *125*, 14690.
Galyametdinov, Y.; Ksenofontov, V.; Prosvirin, A.; Ovchinnikov, I.; Ivanova, G.; Gütlich, P.; Haase, W. *Angew. Chem., Int. Ed.* **2001**, *40*, 4269.
Niel, V.; Thompson, A. L.; Munoz, M. C.; Galat, A.; Goeta, A. E.; Real, J. A. *Angew. Chem., Int. Ed.* **2003**, *42*, 3760.
Sunatsuki, Y.; Ikuta, Y.; Matsumoto, N.; Ohta, H.; Kojima, M.; Iijima, S.; Hayami, S.; Maeda, Y.; Kaizaki, S.; Dahan, F.; Tuchagues, J.-P. *Angew. Chem., Int. Ed.* **2003**, *42*, 1614.
Galet, A.; Niel, V.; Munoz, M. C.; Real, J. A. *J. Am. Chem. Soc.* **2003**, *125*, 14224.
Niel, V.; Thompson, A. L.; Goeta, A. E.; Enachescu, C.; Hauser, A.; Galet, A.; Munoz, M. C.; Real, J. A. *Chem. Eur. J.* **2005**, *11*, 2047.
Faulmann, C.; Jacob, K.; Dorbes, S.; Lampert, S.; Malfant, I.; Doublet, M. L.; Valade, L.; Real, J. A. *Inorg. Chem.* **2007**, *46*, 8548.
Faulmann, C.; Dorbes, S.; de Bonneval, W. G.; Molnar, G.; Bousseksou, A.; Gomez-Garcia, C. J.; Coronado, E.; Valade, L. *Eur. J. Inorg. Chem.* **2005**, 3261.
Dorbes, S.; Valade, L.; Real, J. A.; Faulmann, C. *Chem. Commun.* **2005**, 69.
Methods in Enzymology, *276*: *Macromolecular Crystallography, part A*; Carter, C. W., Jr.; Sweets, R. M., Eds.; 1997.
Altomare, A.; Burla, M. C.; Camalli, M.; Cascarano, G. L.; Giacovazzo, C.; Guagliardi, A.; Moliterni, A. G. G.; Polidori, G.; Spagna, R. *J. Appl. Cryst.* **1999**, *32*, 115.

Sheldrick, G. M. (**1994**) SHELXL97. Program *for the Refinement of Crystal Structures.* University of Gottingen, Germany.
Zhu, S. S.; Swager, T. M. *J. Am. Chem. Soc.* **1997**, *119*, 12568.
Zoppellaro, G.; Baumgarten, M. *Eur. J. Org. Chem.* **2005**, 2888.
Jameson, D. L.; Goldsby, K. A. *J. Org. Chem.* **1990**, *55*, 4992.
Gronowitz, S.; Liljefors, S. *Chemica Scripta.* **1978-79**, *13*, 39.
Liljefors, S.; Gronowitz, S. *Chemica Scripta.* **1980**, *15*, 102.
Elhaïk, J.; Kilner, C. A.; Halcrow, M. A. *Dalton Trans.* **2006**, 823.
Roux, C.; Zarembowitch, J.; Gallois, B.; Bolte, M. *New J. Chem.* **1992**, *16*, 671.
Holland, J. M.; McAllister, J. A.; Kilner, C. A.; Thornton-Pett, M.; Bridgeman, A. J.; Halcrow, M. A. *J. Chem. Soc., Dalton Trans.* **2002**, 548.
Reger, D. L.; Semeniuc, R. F.; Smith, M. D. *Crystal Growth & Design* **2005**, *5*, 1182.
Kitajima, N.; Moro-oka, Y. *Chem. Rev.* **1994**, *94*, 737.
Kimani, M. M.; Brumaghim, J. L.; VanDerveer, D. *Inorg. Chem.* **2010**, *49*, 9200.
O'Connor, C. J. *Prog. Inorg. Chem.* **1982**, *29*, 203.
Molecular Magnetism; Kahn, O., Ed.; VCH Publishers, New York, 1993.
Paul, E. W.; Ricco, A. J.; Wrighton, M. S. *J. Phys. Chem.* **1985**, *89*, 1441.
Thackeray, J. W.; White, H. S.; Wrighton, M. S. *J. Phys. Chem.* **1985**, *89*, 5133.
Kittlesen, G. P.; White, H. S.; Wrighton, M. S. *J. Am. Chem. Soc.* **1984**, *106*, 7389.
Ofer, D.; Crooks, R. M.; Wrighton, M. S. *J. Am. Chem. Soc.* **1990**, *112*, 7869.
Schiavon, G.; Sitran, S.; Zotti, G. *Synth. Met.* **1989**, *32*, 209.